Development of Tandem Solid-State Dye-Sensitised Solar Cells via Interfacial Engineering

Amy Neild

A thesis submitted for the degree of

Doctor of Philosophy

School of Natural and Environmental Sciences

Newcastle University

December 2023

Declaration:

The following results were obtained by or with the assistance of other researchers:

1. Transient Absorption Spectroscopy measurements performed by Dr Owen Woodford
2. Scanning Electron Microscopy and Energy-Dispersive X-ray spectroscopy measurements performed by Dr Isabel Arce Garcia
3. Atomic layer deposition of alumina performed by Dr Konstantin Vasilevskiy
4. Synthesis of N^3,N^4-bis(4-(bis(4-methoxyphenyl)amino)phenyl)thiophene-3,4-dicarboxamide (TPABT) performed by Miriam Fsadni and Benjamin Vella
5. LEG4/L0 co-sensitised TiO_2 solid-state dye sensitised solar cells fabricated and characterised by Norman Zweig, supervised by the author

All other work was performed by the author.

Abstract

Dye-sensitised solar cells (DSCs) are an attractive photovoltaic (PV) technology due to their low cost, light weight and simple fabrication process using earth abundant materials. Specifically, organic dyes offer tuneable optical properties and high absorption coefficients. However, a limiting factor on the power conversion efficiency (PCE) is that organic dyes suffer from relatively narrow spectral absorption in comparison to other PV technologies, thus limiting the light-harvesting ability of the cells. Implementing a tandem structure in which two photoactive electrodes are incorporated for enhanced light collection represents a promising approach. However, fundamental stability issues surrounding the liquid electrolyte pose concern for the commercialisation of such devices. Therefore, the work in this thesis aims to improve the stability of tandem DSCs by establishing a proof of concept for p-n tandem solid-state DSCs (ssDSCs) where the liquid electrolyte is replaced with solid charge transporting materials. The PCE of ssDSCs is generally much lower that of liquid DSCs. Therefore an amide-based hole transporting material (HTM) with improved conductivity was tested in n-type ssDSCs with the aim to enhance device performance. Further efforts to broaden the spectral absorption of ssDSCs through co-sensitisation of the TiO_2 photoanode was also conducted.

This thesis presents the design, fabrication and optimisation of both n-type and p-type ssDSCs. For n-type ssDSCs, the co-sensitisation of LEG4 with L0 resulted in a notable 7% increase in PCE due to the extension of the absorption region to lower wavelengths. Employment of the amide-based HTM (termed TPABT) highlighted that further aging compared with Spiro-OMeTAD based ssDSCs was essential for dye regeneration to allow for oxidation of the TPABT. This indicated the different oxidation pathway compared with Spiro-OMeTAD, which was attributed to the closer molecular packing of TPABT. Additionally, it was found that TPABT devices exhibited significant hysteresis. However, after performing a light soaking treatment the efficiency of TPABT based devices improved from 0.33% to 1.48% and hysteresis was no longer observed. It was hypothesised that the light soaking treatment led to Li^+ ion migration from coordinates inside the pores toward the TiO_2/LEG4 interface. Here, it is thought the Li^+ ions screen conduction band electrons after injection, resulting in enhanced photocurrents and solar cell performance.

Additionally, a study on mitigating interfacial charge recombination in p-type ssDSCs was undertaken where three NiO surface treatments were tested to reduce recombination at the ETM/electrode interface. Atomic layer deposition of alumina and an aluminium alkoxide solution treatment were employed onto the NiO surface, and a chenodeoxycholic acid treatment employed both as a surface treatment onto sensitised NiO and as a co-adsorbent to P1 were conducted. Current density-voltage (J-V) measurements signified resistive behaviour in the devices, and transient absorption spectroscopy (TAS) measurements revealed charge carrier lifetimes in the sub-picosecond timescale. This was attributed to hole shallow-trapping, where the existence of excess Ni^{3+} states on the NiO surface trap a hole to "Ni^{4+}" – a mixed valence state of Ni higher than 3. Therefore, it is believed that the p-type ssDSCs presented in this thesis exhibit fast recombination and inefficient hole injection into the NiO, leading to poor device performances.

To assemble the tandem ssDSC a charge recombination layer (CRL) was employed between the n-type and p-type subcells to enable charge transfer from one subcell to another, and the subcells were pressed together with clamps. Efforts were dedicated to fabricating a CRL that formed an ohmic contact to minimise energy barriers for the charge carriers to flow across the CRL. A CRL composed of Spiro-OMeTAD/Ag/PEI/PCBM:PEI demonstrated the establishment of an ohmic connection. However, when employed into tandem ssDSCs the poor performance of the p-type ssDSC coupled with the low current measured through the CRL significantly inhibited the performance of the tandem device. A further study testing the mechanical adhesion of a Spiro-OMeTAD/PEDOT:PSS/PEI/PCBM:PEI CRL using a transparent conductive adhesive (TCA) showed both electrical and mechanical connection of the CRL, where UV epoxy was used to secure the glass substrates in place. When employed in tandem ssDSCs, this will eliminate the necessity to apply clamping or pressure on the subcells for operation.

Overall, this thesis highlights the significance of additional research required on the p-type electrode to overcome the associated charge recombination issues encountered in p-type ssDSCs. Additionally, the importance of obtaining high electrical conductivity in the CRL was highlighted. Despite this, a tandem ssDSC exhibiting a V_{OC} of 0.88 V and J_{SC} of 0.005 mA cm^{-2} was achieved, underscoring the potential of the tandem ssDSC configuration and the ability to utilise the collective open-circuit voltages of the component devices.

Acknowledgements

First and foremost, I would like to express my sincerest gratitude to my supervisors, Prof. Elizabeth Gibson and Dr Pablo Docampo. Libby, thank you everything – for every piece of advice and assistance, for your constant motivation, and for instilling confidence in me when I needed it the most. Pablo, thank you for believing in my abilities and for pushing me out of my comfort zone. I would not be the scientist I am today without either of you. I would also like to extend my thanks to Dr Konstantin Vasilevskiy for teaching me how to operate the equipment in the clean rooms and for always maintaining such a pleasant work environment.

Working in the Energy Materials Lab at Newcastle University has been an enriching experience and this work would not have been achievable without the friendly company, helpful assistance, and positive encouragement from every member of our group, both past and present. Abbi, Ella, Miriam, Heather and Jayne, thank you for always keeping me smiling since day one. Lawrence and Cathal, I have valued every p-type discussion and your knowledge was highly appreciated. Linah, Mashaer, Matar, Abdo, Rishan, Delowar and Bening, thank you for every coffee, catch up and chemistry chat. Iacopo, Kezia, Natalie, Timo, Giovanni, Harvey, and David, I am grateful for the many insightful discussions and friendly conversations that took place in the cell building and characterisation labs. Norman, thank you for taking the time to test the Automated Spray Pyrolysis Machine and bring my baby to life. I would especially like to thank Dr Joshua Karlsson and Dr Susana Stephens for your support and assistant in the lab during my earlier years as a PhD student, and Dr Susana Iglesias Porras and Dr Matthew Royle for every passionate and thought-provoking conversation we have had discussing our work.

My special thanks go to my most amazing friends, Toby, Luke, Georgia, Joe, Olive and Immie. What an adventure these years have been. Your support and guidance, even though our PhD topics differ, meant the world to me. Yet, beyond that, the friendship and memories you have gifted me mean the most. You have no idea how appreciated you were during tough times.

I would like to thank my parents for providing me with never-ending love and support, which has enabled me to succeed to the highest degree throughout my journey of higher education. You have afforded me with independence and courage to accomplish my goals, for which I am forever grateful. Lastly, my heartfelt thanks go to Josh. Thank you for your unwavering support throughout this journey and for teaching me that happiness fuels greater accomplishments.

Contents

Abbreviations

A	absorption
ALD	atomic layer deposition
AM	air mass
At%	atomic weight percentage
a.u.	arbitrary units
a-Si	amorphous silicon
CB	conduction band
CdTe	cadmium telluride
CIGS	copper indium gallium selenide
CRL	charge recombination layer
CV	cyclic voltammetry
c-Si	single-crystal silicon
D	ground state of the dye
D*	excited state of the dye
D+	oxidised state of the dye
DSC	dye-sensitised solar cell
E_{CB}	conduction band energy
E_F	Fermi level energy
E_g	band gap energy
E_{VB}	valence band energy
EDX	energy-dispersive X-ray spectroscopy
ETL	electron transporting layer

ETM	electron transporting material
FF	fill factor
G-code	geometric code
HOMO	highest occupied molecular orbital
HTM	hole transporting material
IPCE	incident photon-to-current conversion efficiency
J-V	current density-voltage
J_{SC}	short-circuit current
λ_{max}	wavelength of maximum absorption
mc-Si	multi-crystalline silicon
NHE	normal hydrogen electrode
n-ssDSC	n-type solid-state dye-sensitised solar cell
p-ssDSC	p-type solid-state dye-sensitised solar cell
PCE	power conversion efficiency
PIA	photoinduced absorption spectroscopy
PV	photovoltaic
SEM	scanning electron microscopy
ssDSC	solid-state dye-sensitised solar cell
τ	lifetime
T	transmittance
t-DSC	tandem dye-sensitised solar cell
t-ssDSC	tandem solid-state dye-sensitised solar cell
TAS	transient absorption spectroscopy
TCA	transparent conductive adhesive

UV-Vis	ultraviolet-visible spectroscopy
VB	valence band
V_{OC}	open-circuit voltage

Chemical abbreviations:

BCP	bathocuproine
CDCA	chenodeoxycholic acid
F108	poly(ethylene glycol)-*block*-poly*(*propylene glycol*)*-*block*-poly(ethylene glycol)
FTO	fluorine-doped tin oxide
LiTFSI	lithium bis(trifluoromethanesulfonyl)imide
PEI	polyethylenimine
PCBM	phenyl C_{61} butyric acid methyl ester
PEDOT:PSS	poly(3,4-ethylenedioxythiophene) polystyrene sulfonate
tBP	4-*tert*-butylpyridine

Chapter 1.
Introduction

1.1 The Climate Crisis

Climate change is the greatest threat to our existence on this planet. We are witnessing ever more frequent extreme weather events around the world, as wildfires, storms and floods are tragically becoming a common occurrence. If we continue like so we risk the collapse of everything that gives us security – food production, access to fresh water, and habitable ambient temperature.

"We are the first generation to feel the impact of climate change and the last generation that can do something about it." – U.S. Senator Jay Inslee

Primarily driven by human activities, the most prominent cause of climate change is the increase in greenhouse gas emissions. These gases, such as carbon dioxide (CO_2), methane (CH_4) and water vapour (H_2O), trap heat near the Earth's surface and maintain an average temperature of 15°C.[1] However, in the last century as we entered the modern industrial era, activities such as burning of fossil fuels, deforestation, industrial and agricultural processes, and our ever-increasing energy consumption have significantly elevated the concentration of greenhouse gases in the atmosphere, especially CO_2. This has led to an increase in global average surface temperature of around 1.1°C since the pre-industrial era (1880-1900).[2] This is termed global warming.

Governments and Policymakers around the world have a significant role in addressing the climate crisis by implementing policies and regulations that minimise our impact on the climate. To avert the worst impacts of climate change, global temperature increase needs to

be limited to 1.5°C above pre-industrial levels. Above 1.5°C and we approach climatic tipping points such as the melting of arctic permafrost, which could result in the release of millennia of stored greenhouse gases and the loss of control of our climate for good.[3] On 12th December 2015, 196 Parties at the UN Climate Change Conference (COP21) entered a legally binding international treaty on climate change, known as the Paris Agreement, that's overarching goal was to limit the temperature increase to well below 2°C above pre-industrial levels and pursue efforts to limit the temperature increase to 1.5°C above pre-industrial levels.[4] Such a landmark in the multilateral climate change process saw, for the first time, nations come together to address climate change through international cooperation.

Since 2020, countries that are parties to the Paris Agreement have been submitting their Nationally Determined Contributions (NDCs) that outline their climate action plans and targets, communicating the actions they will take to reduce their greenhouse gas emissions in order to reach the Paris Agreement temperature goal. In December 2020, the UK communicated in its NDC that the UK commits to reducing economy-wide greenhouse gas emissions by at least 68% by 2030, compared to 1990 levels, and achieve net zero greenhouse emissions by 2050.[5]

A Net Zero Strategy was published by the UK government in October 2021 that included policies and proposals for a transition into the new Green Industrial Revolution. The strategy highlights that a clean, reliable power system is the foundation of a productive net zero economy, and promises in the first key policy that, "By 2035 the UK will be powered entirely by clean electricity, subject to security of supply".[3] The power system is said to consist of abundant, cheap British renewables. This transition will subsequently decrease our reliance on fossil fuels and, as a result, eliminate the primary source of carbon emissions.

1.2 Renewable Energy

Fossil fuels such as coal, oil, and gas are non-renewable energy resources that take hundreds of millions of years to form and have been the dominant source of energy for centuries due to their energy density and relative ease of extraction. Nonetheless, they are by far the largest contributor to climate change, as they account for over 75% of global greenhouse gas emissions and almost 90% of all carbon dioxide emissions.[6] On the contrary, renewable energy

such as hydropower, biomass, solar, wind, and geothermal energy refers to energy derived from natural sources that are typically abundant and can be harnessed without depleting them. As well as this, renewable energy sources produce little to no direct carbon emissions during electricity generation. Hence, the transition away from fossil fuels to renewable energy sources is vital to mitigate the adverse effects of climate change. Since the Paris Agreement was adopted in 2015 investments in renewable energy sources have surpassed those in fossil fuels (Figure 1.1),[7] showing an encouraging indication of the ongoing transition and reflecting the growing commitment to sustainable and renewable energy.

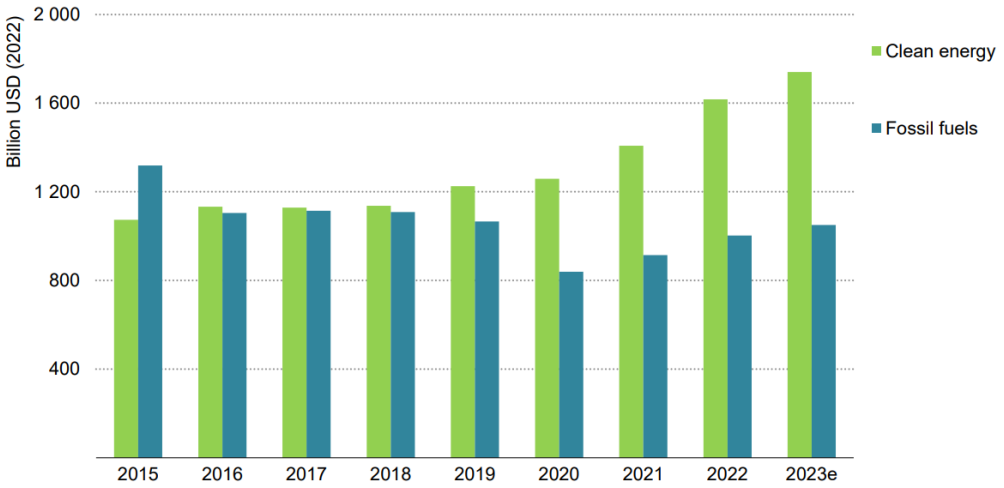

Figure 1.1: Global energy investment in clean energy and in fossil fuels, 2015-2023e (2023e = estimated values for 2023). Figure obtained from IEA World Energy Investment 2023 report.

1.2.1 Solar Energy

Solar energy, the radiant energy emitted from the sun, is the most abundant of all renewable and non-renewable energy resources and can even be harnessed in cloudy weather.[8] The amount of solar energy that strikes the Earth over 80 minutes is more than all the energy consumed globally in a year. Therefore, with the right infrastructure in place, capturing and converting solar energy into usable electrical energy could provide ample power for the entire world.

There are two primary ways of utilising solar energy. One way is through capturing the sun's heat and converting it into usable thermal energy through Solar Thermal Systems, and the other way is through converting sunlight directly into electricity using Photovoltaics.

The technology that converts sunlight directly into electricity is termed photovoltaics (PV), originating from the Greek words 'phos' meaning light and 'volt' referring to electricity. Photovoltaic devices are known as solar cells. The solar PV power generation has increased from 251 TWh in 2015 to 1293 TWh in 2022. To meet the requirements of the International Energy Agency Net Zero Scenario the solar PV power generation should be at 8255 TWh by 2030 (Figure 1.2).[9]

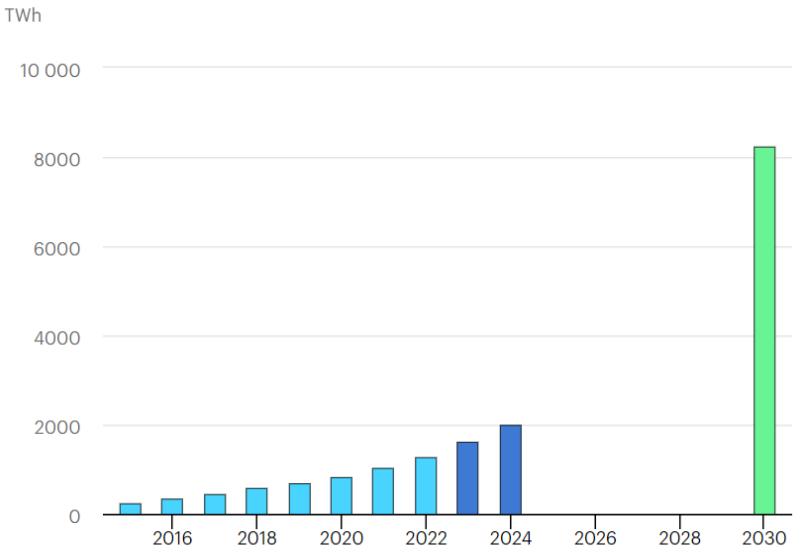

Figure 1.2: Solar PV power generation in the Net Zero Scenario, 2015-2030. Figure obtained from IEA data and statistics, 2015-2030.

1.2.2 Ambient light harvesting

One way to significantly increase PV power generation is to harness ambient light using photovoltaics compatible with such lighting. Not all countries are subjected to the same amount of sunlight, as many countries experience cloudy climates. This could hinder the deployment of PV in such countries, as policymakers and investors might question whether the solar power potential is good enough to take advantage of in those locations. However, certain types of photovoltaic devices perform better than others in these low light environments. For example, dye-sensitised solar cells (DSCs) have shown promising performance in ambient light compared with other photovoltaic technologies.[10] Advancing research and development in these categories of solar cells could allow for better utilisation of solar energy in cloudy or overcast regions, as well as during dusk and dawn when sunlight intensity is lower, allowing solar energy to become more accessible to a broader range of

geographic locations and environments. This is a crucial step in the journey to net zero greenhouse emissions by 2050.

1.2.3 Powering the Internet of Things

The Internet of Things (IoT) is a world-spanning network of interconnected objects, devices, sensors, and everyday items that can communicate over the internet. Such devices span various domains, from remotely controlled lighting, security cameras, and thermostats in smart homes, to wearable devices that monitor vital signs in healthcare. In the future, nearly half of IoT devices will be integrated into buildings or in indoor applications,[11] many of which have artificial light on for 24 hours a day, such as hospitals, airports, offices and factories. DSCs have also shown to work exceptionally well under fluorescent lighting and a prototype of a fully self-powered intelligent IoT node using dye-sensitised light harvesters has already been demonstrated.[12] By integrating indoor photovoltaics we can reduce the dependence on external energy grids, aligning with the goals of the Net Zero Scenario by promoting clean and locally generated energy.

1.3 Fundamentals of Photovoltaics

1.3.1 The Solar Spectrum

The spectrum of the sun's radiation is close to that of a black body at a temperature of 5800 K, emitting light across a wide range of wavelengths known as the solar spectrum. By understanding the light that we are provided with we can design solar cells that can efficiently capture energy across this range of wavelengths.

The solar spectrum consists of various wavelengths of light, from ultraviolet (UV) to infrared (IR), as shown in Figure 1.3. The key to highly efficient solar cells is absorbing as broad a range of photons from the solar spectrum as possible.

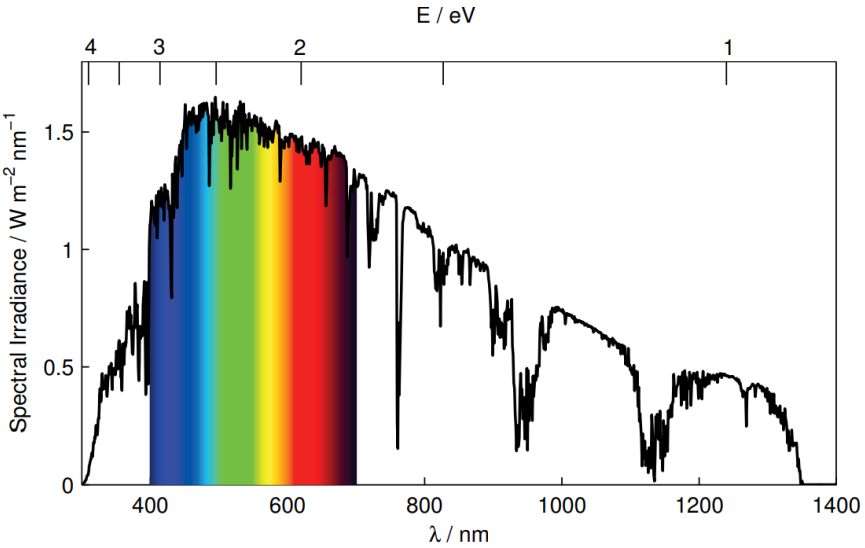

Figure 1.3: Solar irradiance at the surface of the Earth with the visible part of the spectrum indicated by its colours (from 380 – 700 nm).

1.3.2 Semiconductors and Junctions

A solar cell generates a voltage and a current when exposed to sunlight by a process known as the photovoltaic effect. Semiconductors are materials that are particularly effective in exhibiting the photovoltaic effect, therefore they are the fundamental material for the construction of most solar cells. They are able to convert light into electricity due to an energy difference between the valence band (the highest occupied energy levels) and the conduction band (the lowest unoccupied energy levels). This energy difference is known as the energy band gap (E_g), and represents the minimum amount of energy required for an electron to break free of its bound state.

When photons with energy equal to or greater than E_g are incident upon the semiconductor, they excite the negatively charged electrons from the valence band (VB) to the conduction band (CB), leaving behind positively charged "holes" in the valence band. This process is known as photoexcitation, which leads to the generation of electron-hole pairs. Here, the electrons and holes, known as the charge carriers, become free to move about the semiconductor and participate in conduction. This is depicted in Figure 1.4. Since only photons with energies equal to or greater than E_g can excite electrons into the CB, it is E_g that determines the onset of absorption of sunlight by the material.

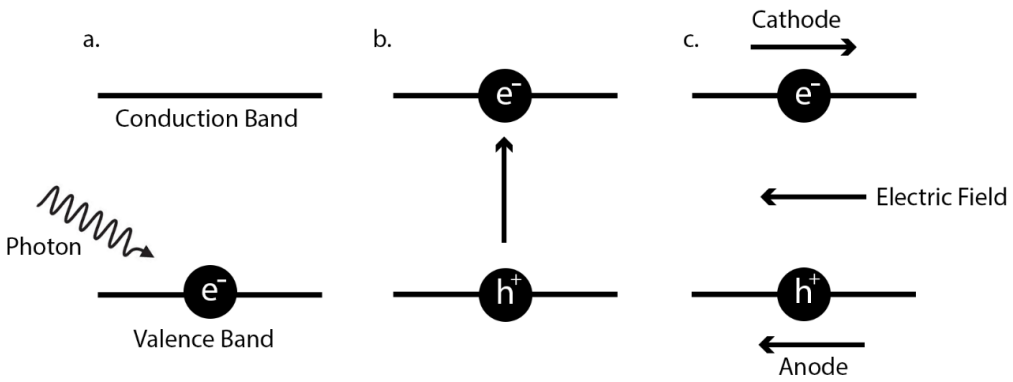

Figure 1.4: Depiction of the basic operation of a solar cell. (a) a photon is absorbed by the semiconductor, (b) an electron is promoted from the VB to the CB, leaving a hole in the VB, (c) the electron and hole are transported to electrodes to be collected.

The Fermi level (E_F) represents the energy level that has a 50% probability of being occupied by an electron at absolute zero temperature in thermal equilibrium and is an important parameter in understanding the behaviour of charge carriers in semiconductor materials. For undoped semiconductors in thermal equilibrium at temperatures > 0 K, E_F is located at the centre of E_g, as undoped semiconductors have an equal concentration of electrons in the conduction band and holes in the valence band. In non-equilibrium conditions, for example under the influence of an external factor such as an applied voltage or illuminated by light, the distribution of carriers deviates from the equilibrium E_F forming separate quasi-Fermi levels used for electrons ($E_{qF,n}$) and holes ($E_{qF,p}$).

The conductivity of the semiconductor can be adjusted to a desired level through a process called doping. This is where impurity atoms with excess valence electrons (negatively charged) or impurity atoms with a deficiency of valence electrons (positively charged) are introduced into the crystal lattice of the semiconductor material through n-type doping or p-type doping, respectively. Through n-type doping the electron (donor) concentration is increased, resulting in an n-type semiconductor, and through p-type doping the hole (acceptor) concentration is increased, resulting in a p-type semiconductor.

For n-type doping, when extra electrons from the donor atoms are introduced into the conduction band this pushes E_F closer to the conduction band, where it is now closer to the energy levels associated with the introduced donor impurities. For p-type doping, when acceptor atoms create holes by accepting electrons from the valence band this pulls E_F closer to the valence band, where it is now closer to the energy levels associated with the introduced acceptor impurities. This is illustrated in Figure 1.5. The concentration of dopants determines

the degree of E_F shift. Therefore, the addition of such impurity atoms enhances electron conductivity in n-type doping and hole conductivity in p-type doping.

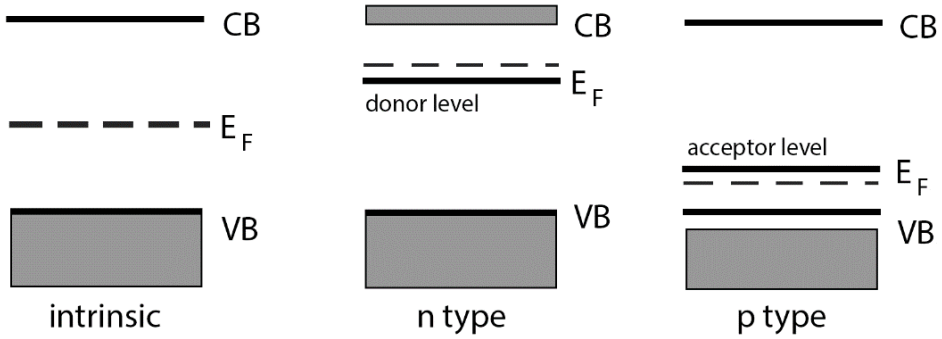

Figure 1.5: Energy level diagrams showing the position of the Fermi level and impurity levels relative to the conduction band and valence band edges, for intrinsic, n-type and p-type semiconductors. The shaded regions indicate levels filled by electrons.

When an n-type semiconductor is joined with a p-type semiconductor, a p-n junction is formed (Figure 1.6). The p-n junction creates an electric field that facilitates the separation of charge carriers generated by the absorption of photons, therefore this structure is commonly used in solar cells.

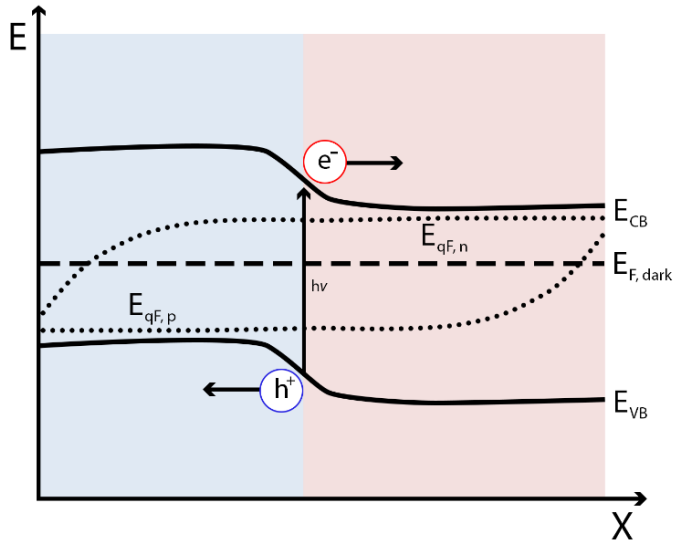

Figure 1.6: Depiction of the absorption of photons followed by the separation of charge carriers at a p-n junction at open circuit, where E represents energy and X represents the distance along the junction.

While p-n junctions can be formed with the same semiconductor material via doping, two different semiconductor materials can be joined together, forming what is known as a heterojunction at their interface. These types of junctions are common in photovoltaic devices

because they are able to facilitate the separation of charge carriers upon incident light. However, solar cells are not limited to these two types of junctions. There are other junctions used in photovoltaics that contain regions of other materials next to the semiconductor region, such as the dye/semiconductor interface in DSCs. The interface of these two regions also forms a junction where phenomena such as charge separation and recombination occur, which plays a fundamental role in the functioning of the solar cell.

1.3.3 The Shockley-Queisser Limit

The Shockley-Queisser limit is the theoretical efficiency limit that can be achieved under ideal conditions. For a single junction, the optimal band gap was found to be around 1.4 eV and would lead to a maximum efficiency of 33.7%. This indicates that around 67% of the solar energy incident on the device does not contribute to solar electricity. The two main sources of energy loss are (1) transmission of photons with energies lower than E_g without absorption, and (2) photos of energy higher than E_g lose energy via vibrations and rotations (Figure 1.7).[13]

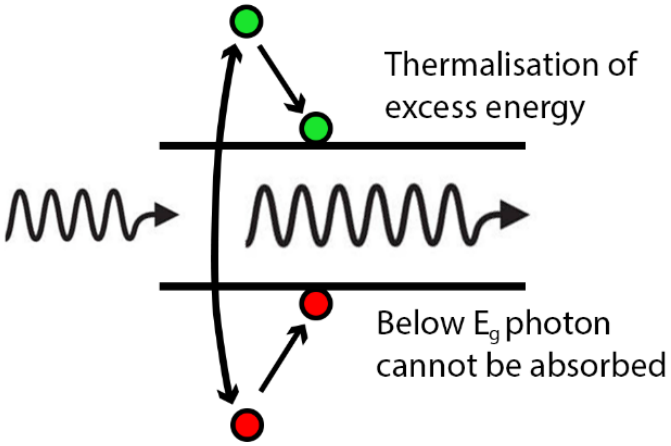

Figure 1.7: Diagram showing the two main sources of incident energy loss in single junction solar cells.

Several advanced approaches have been devised to minimise this energy loss. Among these, the construction of multi-junction devices has demonstrated the potential to surpass this limit. In such devices complimentary band gaps are stacked, leading to increased light collection. For two junctions the maximum efficiency is around 43% and for infinite junctions the maximum efficiency is 65%.[14]

1.3.4 1st Generation PV

Solar cells can be categorised into three generations, the first generation (also known as conventional, traditional or wafer-based cells) consisting of PV technologies based on single-crystal (c-Si) and multi-crystalline (mc-Si) silicon. First produced commercially in 1963 for installation on a light house,[15] mc-Si modules are now the commercially predominant PV technology due to the excellent semiconducting properties of silicon.

There are two main types of first-generation solar cells. The first consist of a p-type silicon wafer (doped with boron) and an n-type silicon wafer (doped with phosphorus), creating a p-n junction. The second consists of separate p-type and n-type layers, forming back-to-back junctions. In back-to-back junctions, each layer acts as an independent solar cell. Although they have proven to provide satisfactory efficiencies whilst maintaining durability, the process of producing high-purity silicon involves multiple steps, including energy-intensive purification methods.[16] Additionally, the record efficiency of c-Si technology (26.1%) is approaching the theoretical Auger efficiency limit of 29.4%.[17]

1.3.5 2nd Generation PV

The development of second-generation PV technologies (known as thin film solar cells) emerged as a response to the limitations and challenges faced with first-generation silicon PV. Second-generation technologies consist of single-junction devices that aim to use new materials, different designs and various assembly techniques while maintaining the efficiencies of first-generation technologies.[18] In addition, the use of flexible substrates opened up new possibilities for integration onto curved surfaces, and the use of lightweight substrates enables portability.[19]

The main types of second-generation solar cells consist of thin films such as amorphous silicon (a-Si), cadmium telluride (CdTe), and copper indium gallium selenide (CIGS). These devices also operate via p-n junctions and exhibit enhanced light harvesting capabilities compared with first-generation solar cells. This is due to the inherent properties of the semiconductors; silicon has an indirect band gap (photoexcitation involving a change in both momentum and energy). However, second-generation solar cells consist of semiconductors that have direct

band gaps (photoexcitation involves only a change in energy, not momentum). This allows for more efficient absorption of photons, enabling them to be produced at a sub-millimetre scale.

1.3.6 3rd Generation PV

The third generation of solar cells comprises several thin-film technologies and is often described as emerging photovoltaics. These technologies include Organic Photovoltaic (OPV) cells, Perovskite Solar Cells (PSCs), Dye-Sensitised Solar Cells (DSCs), and Quantum Dot Solar Cells (QDSCs). The primary goal of third-generation solar cells is often to achieve higher power conversion efficiencies at low cost, using earth abundant materials and innovative technologies such as tandem or multi-junction cells that incorporate different semiconductors.[20] Additionally, the integration of nanotechnology has presented new ways to capture, store, and convert energy.[21] For such technologies, the inclusion of different band gaps allows these devices the potential to surpass the Shockley-Quiesser limit by capturing a broader range of solar wavelengths and converting solar energy more efficiently.

1.4 Dye-Sensitised Solar Cells

1.4.1 Device operation

Dye-sensitised solar cells (DSCs) are a third-generation photovoltaic technology that offer a unique approach to harnessing solar energy. In conventional p-n junction solar cells, the semiconductor undergoes light absorption, as well as charge carrier separation and transportation. However, in DSCs these tasks are separated. The operation of a conventional liquid n-DSC is illustrated in Figure 1.8.

A dye molecule on the semiconductor (TiO_2 in this case) absorbs a photon, exciting it from the ground state to the excited state. This gives rise to the electron injection from the excited dye to the conduction band of the semiconductor, resulting in oxidation of the dye. Electrons then diffuse through the semiconductor to the conductive glass substrate, which acts as an anode. They then pass through an external circuit to perform electrical work until they reach the

conducting glass counter electrode. In the gap between the electrodes is a redox electrolyte and at the counter electrode the electrolyte is reduced. The reduced state of the electrolyte reduces the photo-oxidised dye and the dye is regenerated, completing the circuit. The processes in Figure 1.8 are all electron transfer processes that are beneficial to the performance and efficiency of a DSC. However, there also exists parasitic processes that hinder the performance of the device. These include recombination to the dye, recombination to the redox electrolyte, and the excited state decay of the dye to the ground state. Addressing these issues is crucial for improving the performance of DSCs.

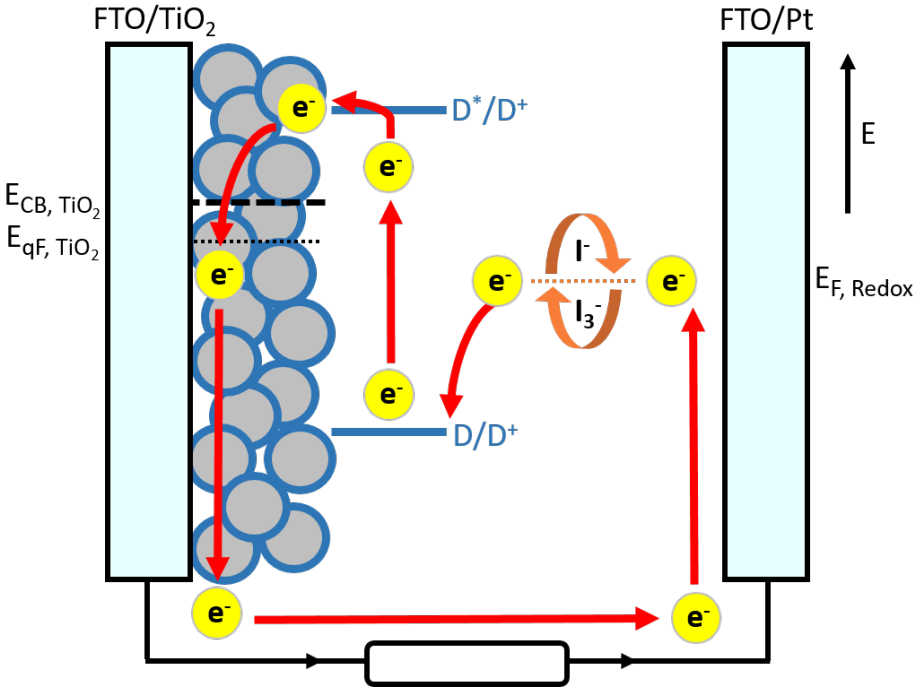

Figure 1.8: Schematic diagram of a liquid n-DSC showing the electron transfer pathway during operation.

1.4.2 Advancements in DSCs

The discovery of DSCs dates back to 1977, when a US patent was submitted by Terje A. Skotheim.[22] It detailed the characteristics of today's dye-sensitised solar cells, describing a substrate of TiO_2 semiconductor with a sensitising dye absorbed on, a transparent reducing agent over the dye, and a layer of metal over the reducing agent. Attempts had been made to synthesise such a device,[23,24] however, these devices exhibited extremely poor light harvesting of less than 1% because of the belief that the semiconductor must have a smooth surface. It wasn't until 1991 when O'Regan and Gratzel used nanometre-sized TiO_2 particles to increase the surface area of the semiconductor film 2000-fold, increasing the light harvesting efficiency

to 46%.[25] The ratio of energy output from the device to energy input from the sun is the power conversion efficiency (PCE) of the device. The PCE of O'Regan and Gratzel's devices was 7.12% under full sunlight and increased to 12% in diffuse sunlight, making them the first commercially viable DSCs of that time.

Nanostructured semiconductor films are a vital component of a DSC, providing support for dye loading and facilitating the transport of photogenerated electrons from the sensitiser to the external circuit. It is important that the photoanode does not absorb any visible light, has sufficient band gap energy to minimise charge carrier recombination, has a conduction band/valence band edge for either n-type/p-type materials, respectively, that matches with that of the excited dye molecules for efficient charge carrier injection, and has high charge carrier mobility.[26] Porous, anatase phase TiO_2 is the most commonly used semiconductor for high-efficiency n-DSCs due to its cost effectiveness, non-toxicity, and abundant availability on Earth.[27] However, other metal oxides such as ZnO, SnO_2, Nb_2O_5, and $SrTiO_3$ have been utilised in attempt to further increase the efficiency of DSCs.[28–31] For p-DSCs, finding a suitable nanostructured semiconductor has proven difficult, with NiO being the most commonly used but coming with drawbacks such as high density of traps and low hole mobility, which leads to fast charge recombination.[32] Other alternatives to NiO include CuO, Cu_2O and ITO[33–35] as well as delafossite Cu(I) ternary oxides such as $CuBO_2$, $CuAlO_2$, and $CuFeO_2$ are being explored, but are yet to outcompete NiO in efficiency.[36–38]

The dye is at the heart of the DSC's functionality. By absorption of photons and injection of the photogenerated charge carriers into the semiconductor on irradiation, the mechanism of the device is initiated. For efficient performance in a DSC the dye sensitiser should fulfil several requirements. This includes broad optical absorption for efficient light harvesting, the incorporation of strong anchoring groups to allow firm adhesion to the semiconductor surface, well-aligned energy levels that are appropriate to the system for efficient charge carrier injection, and high photostability to resist continuous light soaking.[39]

Dye chemistries have undergone significant evolution, which can be categorised into four major phases: the initial use of metal complexes, the transition to organic dyes, the refinement of push-pull dyes, and sensitisation strategies. The first generation of synthetic dyes used in DSCs were primarily based on metal complexes, most notably ruthenium-based dyes. Metal complexes are formed by the coordination of metal ions with ligands. The coordination chemistry allowed for precise control over the metal-to-ligand charge transfer

properties, representing a significant leap in improving the performance and durability of DSCs.[40] However, the limited availability of rare metals such as ruthenium and platinum led researchers to focus their efforts into organic dyes based on carbon-based structures.

Organic dyes offer several advantages over dyes based on metal complexes. These include lower production costs, facile modification, and higher molar absorption coefficients, enabling the design of dyes that could absorb a broader range of the solar spectrum.[41] Thereafter, a push-pull structure was introduced where the electron-donating group and electron-withdrawing group are connected by a π-conjugated bridge. The D-π-A framework can provide better light harvesting due to an extended conjugation, which results in a red-shift in the dye's absorption spectrum. In addition, the push-pull mechanism creates an internal charge transfer within the molecule that reduces charge recombination.[42] More recently, sensitisation techniques such as co-sensitisation have been implemented. This involves using two or more dyes with complementary absorption spectra to allow for broader light absorption. This has proven effective in enhancing the efficiency and inhibiting dye aggregation on the semiconductor surface.[43]

Traditional DSCs were fabricated using a solvent-based iodide-triiodide redox couple electrolyte, where the I_3^- ion acts as the oxidising agent and the I^- ion serves as the reducing agent. These redox reactions are crucial for regenerating the dye molecules after photoexcitation and charge carrier injection into the semiconductor. As well as this, the electrolyte also fundamentally limits the maximum open-circuit voltage (V_{OC}) in a DSC since the V_{OC} is determined by the difference between the Fermi level of the electrons in the TiO_2 and the redox potential of the electrolyte. Iodine-based electrolytes utilised in early DSC technology offered good initial performance, but the redox potential of I_3^-/I^- is not ideal, which limited the photovoltage. As well as this, the corrosive nature of iodine led to stability issues within the device.[44] The introduction of cobalt (Co)-based electrolytes was done to overcome the limitations of iodine-based electrolytes. These are typically based on Co complexes with organic ligands such as bipyridine, for example $[Co(bpy)_3]^{2+/3+}$. The more positive redox potential of Co complexes allowed for higher photovoltages. However, it was found that due to the larger molecular size of Co this led to slower mass transport within the electrolyte, causing a reduction in current density.[45] Building on the success of Co electrolytes, copper (Cu) complexes were introduced instead and were found to show lower mass transport, better diffusion, and a lower driving force required for dye regeneration. As well as this, Cu

complexes offer an even more positive redox potential than Co complexes leading to a further increase in V_{OC}.[46]

In DSCs, the counter electrode (CE) is what facilitates the necessary redox reactions and is vital for completing the electrical circuit. Traditionally, platinum (Pt) was the material of choice for the CE due to its properties such as excellent catalytic activity, stability, and conductivity. However, Pt is a rare and expensive material, causing it to be a significant barrier to the commercialisation of DSCs.[47] As well as this, Pt is not always the most efficient catalyst for the newer Co or Cu redox couples.[48] This caused research to focus on alternatives to Pt, such as carbon-based materials, conducting polymers like poly(3,4-ethylenedioxythiophene (PEDOT), and transition metal compounds like nickel sulfide (NiS), cobalt sulfide (CoS), and iron sulfide (FeS), which are proving to be effective and sustainable replacements to Pt in modern DSC technology.[49–51]

What made DSCs very attractive was that the spectral distribution overlapped with the absorption spectrum of the dye-coated TiO_2 film in diffuse sunlight better than in direct sunlight. This meant that under these conditions the DSCs performed better than conventional silicon cells. As well as this, the long-term stability of cell performance was found to change very little over a period of 2 months due to the chemical stability of the dye.[8] This was a breakthrough for DSCs and ever since research in this field has skyrocketed, with the current record PCE being achieved in 2022, reaching 15.2% when carrying out a hydroxamic acid pre-adsorption that controls the assembly of dye molecules on the surface of TiO_2 to favour charge generation.[52] For p-type DSCs, however, the PCE still lags behind, with the highest efficiency achieved in 2015 of 2.51% when devices containing $Fe(acac)_3$ and a perylene-thiophene-triphenylamine sensitiser (PMI-6T-TPA) were fabricated.[53]

1.5 Solid-State Dye-Sensitised Solar Cells

1.5.1 n-type ssDSCs

Although DSCs are inexpensive and simple to manufacture, after increasing research it became clear that the electrolyte in them is prone to degradation and can be corrosive to the dye molecules over time, which results in a loss of cell performance. As well as this, the devices

need perfect encapsulation to reach long-term stability, and leakage of the electrolyte also may pose a safety hazard due to the toxicity of certain materials. To overcome the limitations of conventional liquid DSCs, in 1995, Tennakone and co-workers developed the concept of solid-state DSCs (ssDSCs) where the liquid electrolyte usually present in DSCs was instead replaced with a solid p-type semiconductor CuI.[54] The end result was a nanoporous TiO_2 electrode for electron conduction, coated in cyanidin for light absorption, with CuI occupying the pores for the transport of holes. The TiO_2/cyanidin/CuI device delivered a short circuit current of 1.5-2.0 mA cm^{-2} in sunlight (about 800 W m^{-2}). Tennakone's special features of the device included a p-type material with a wide band gap, and no dissolving of the monolayer of dye upon deposition of the p-type material. This was pioneering work in the field of DSCs, and since then a vast number of ssDSCs have been made out of many different materials in attempt to fabricate a device as efficient as liquid DSCs that no longer suffer from stability issues.

Over the years different solid-state materials have been used in DSCs for the transportation of holes through the device. This layer is known as the hole transporting material (HTM). Choosing a material with a high mobility for holes is an important factor when fabricating solar cells. In 1997, Hagen and co-workers fabricated a TiO_2/ruthenium/triphenyldiamine device. Triphenyldiamines (TPDs) show mobilities of around 10^{-3} cm^2 V^{-1} s^{-1} at room temperature. TPD was vapor-deposited onto the ruthenium coated TiO_2 nanoparticles with various thicknesses. They found that lower short-circuit currents were observed for cells with thicker TPD layers. This was due to holes having longer trajectories, resulting in higher recombination losses. Therefore, HTM thickness as well as mobility are both important factors to consider when fabricating a device.

In 1998, Bach et al published a paper describing a device where 2,2',7,7'-tetrakis(N,N-di-p-methoxyphenyl-amine)9,9'-spirobifluorene (Spiro-OMeTAD) was used as the organic HTM,[55] which has the hole mobility of 1.69 x 10^{-6} cm^2 V^{-1} s^{-1}.[56] Spiro-OMeTAD was synthesised based on the TPD structure, and the evolution of the synthesis is shown in Figure 1.9. For Spiro-OMeTAD hole mobility is much greater than TPDs due to the addition of *p* -methoxy groups. These groups lower the oxidation potential by 0.22 V compared to TPD, causing the injection barrier height to be lowered.[57]

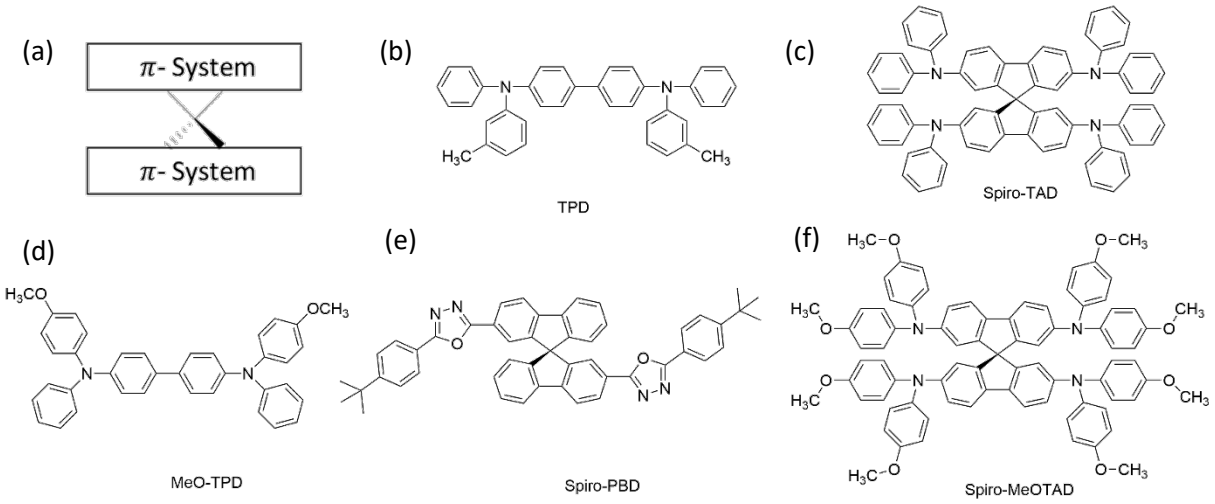

Figure 1.9: The evolution of the synthesis of Spiro-OMeTAD – (a) Spiro-linked systems, (b) TPD HTM, (c) Spiro-TAD HTM, (d) MeO-TPD HTM, (e) Spiro-PBD ETM, and (f) Spiro-OMeTAD.[82]

In Bach's paper an electron-transfer scheme was introduced which is similar to liquid DSCs, except the dye is now regenerated by hole injection into the HTM rather than a redox reaction in the liquid electrolyte. Holes move across the HTM layer through intermolecular hopping as opposed to ion diffusion. This is depicted in Figure 1.10.

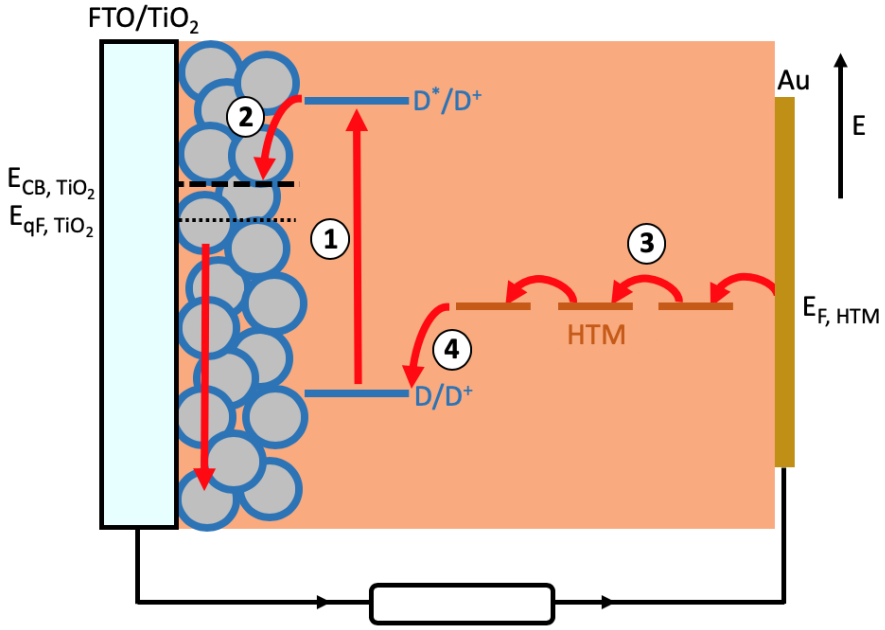

Figure 1.10: Schematic diagram of a solid-state DSC with the electron transfer process depicting (1) photoexcitation of the dye molecule, (2) electron injection into the conduction band of the TiO_2 (femto- to picoseconds), (3) electron intermolecular hopping and (4) regeneration of the dye (picoseconds).

Incident photon-to-current conversion efficiency (IPCE) is the number of detected electrons per number of incident photons and is a measure of how efficiently the solar cell converts incident photons into charge carriers at a given wavelength. Using Spiro-OMeTAD instead of TPD increased the IPCE from 0.2% to 33%, giving a cell efficiency of 0.74%. This was due to electron injection occurring in the femtosecond domain whilst recapture occurred over several microseconds. As well as this, the dye exhibited extremely fast regeneration via hole transfer to OMeTAD. Cappel et al observed that both electron injection and dye regeneration were both complete after 1 ps for a TiO_2/ID176/Spiro-OMeTAD device.[58]

This was a promising step for ssDSCs, and in 2001 Kruger et al were able to increase the power conversion efficiency (PCE) to 2.56% by addition of 4-tert-butylpyridine (tBP) and $Li[CF_3SO_2]_2N$ (lithium ions) to the HTM precursor solution.[59] Lithium ions were added to improve the current output therefore increase the overall efficiency of the device,[10,60] and in the presence of lithium ions dye regeneration by Spiro-OMeTAD occurs faster than 1 ps.[61] tBP was found to decrease charge recombination by 50%. However, when added together this decreased charge recombination even further. It was also found that tBP improved the wetting of the film with the HTM precursor solution.

Since 1998, Spiro-OMeTAD has been the prominent HTM in ssDSCs. To this date, the most efficient ssDSC containing Spiro-OMeTAD was fabricated in 2017 using the D-A-π-A organic sensitizer AQ310. The AQ310-based ssDSC reached a PCE of 8.0%. However, in 2015 a solid-state 'Zombie cell' was fabricated using molecular copper phenanthroline as a solid hole conductor, with a PCE of 8.2%.[62] This category of ssDSC is formed from a liquid DSC in which the liquid electrolyte solidifies into a solid hole conductor as the solvent evaporates from the surface. These are referred to as Zombie cells because the original liquid DSC can come back to life as a ssDSC and retain its functionality. This device was optimised and later used in conjunction with a novel dye WS-72 and reached 11.7% PCE.[63]

1.5.2 p-type ssDSCs

p-type DSCs were first reported in 1999 by Lindquist et al,[64] where nanostructured NiO was chosen as the photocathode due it being a large band gap p-type semiconductor. However, it wasn't until 2016 when the first p-type ssDSC (p-ssDSC) was fabricated. p-ssDSCs are similar devices to conventional n-ssDSCs except the semiconducting material is now a p-type

semiconductor, the HTM is replaced with an electron transporting material (ETM), and the electron flow is reversed (Figure 1.11).

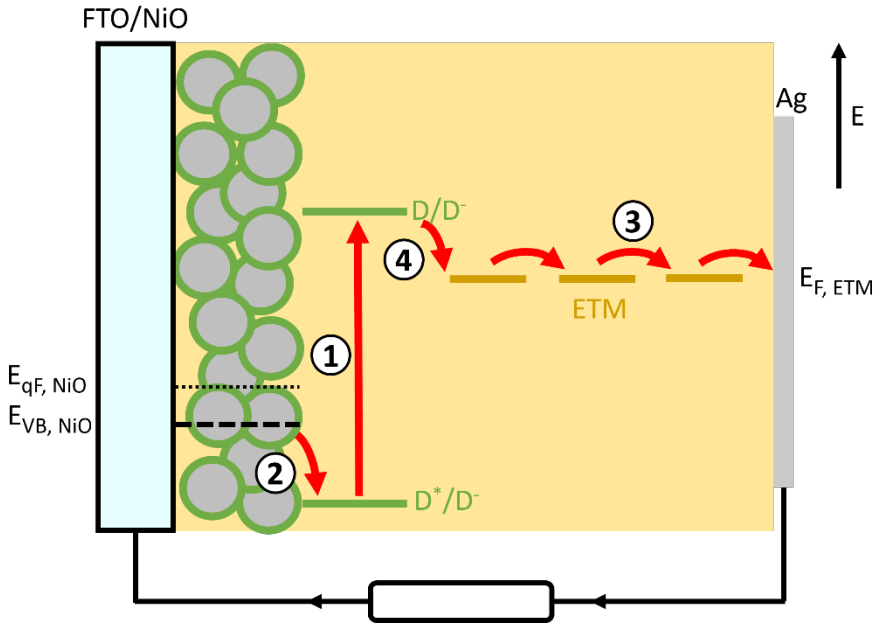

Figure 1.11: Schematic diagram of a p-type ssDSC with the electron transfer process depicting (1) photoexcitation of the dye molecule, (2) hole injection into the valence band of the NiO (< 200 femtoseconds), (3) hole intermolecular hopping and (4) regeneration of the dye (> 8 microseconds for P1).

As with n-ssDSCs, a dye molecule on the semiconductor absorbs the photon, exciting it from the ground state to the excited state. However, as opposed to n-ssDSCs, this gives rise to hole injection from the excited dye to the valence band of the p-type semiconductor. The ground state of the dye is regenerated by the oxidised species of the ETM. At the counter electrode the reduced species in the ETM is regenerated.

Wide bandgap p-type semiconductors are good candidates for photocathodes as they are resistant to photocorrosion.[65] As well as this, in order to fabricate mesoporous films the material must be synthesised as nanoparticles to generate the large surface area. To adsorb the sensitiser onto the surface of the semiconductor it must have high chemical affinity to an organic functional group. NiO is one of the few materials that fits these parameters, which is why it is the most predominant material to use in p-DSCs. The maximum V_{OC} that the device can deliver is governed by the position of the valence band (VB) potential. For NiO, the VB is at 0.54 V vs NHE,[66] making it a good electron donor. However, as it is low lying it is difficult to obtain a large V_{OC}. Therefore, a higher PCE could be obtained with new materials that have a deeper VB potential.

p-ssDSCs use different semiconductors to n-ssDSCs that have different charge transfer kinetics. Compared with n-type metal oxides, p-type are much poorer electronic conductors. The hole diffusion coefficient for NiO ranges from 10^{-8} to 10^{-7} cm^2 s^{-1},[67] 2 orders of magnitude lower than the electron diffusion coefficient in TiO_2. While hole injection into the VB is fast (210 ps), the slow diffusion of holes accounts for the long time delay between hole injection and collection. As well as this, charge recombination is much faster than in TiO_2 devices, meaning the electron must be transferred to the ETM much faster, or recombination must be slowed down. There are a number of methods to increase the electron/hole transport rate, such as using NiO nanorods,[68] as well as methods to reduce charge recombination, such as using recombination barrier layers.[69]

To obtain high PCEs, sensitisers must absorb across a broad range of the solar spectrum so to harvest a larger number of photons. They must be photochemically and electrochemically stable and functionalised with anchoring groups. The anchoring group grafts them onto the surface of the semiconductor, providing a strong electronic coupling. Strong electronic coupling ensures fast hole tunnelling from the excited state of the sensitiser into the VB of the semiconductor.[25] Sensitisers can also be optimised to slow the back recombination reaction. The most efficient sensitisers are linked to an electron acceptor, which increases the separation distance from the NiO surface and results in a longer-lived charge-separated state. An example of this is shown in Figure 1.12.[70]

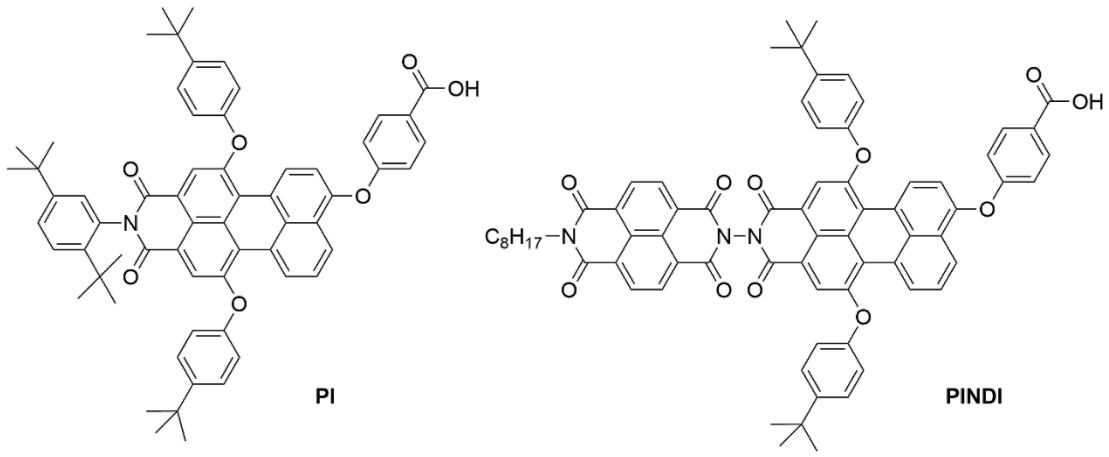

Figure 1.12: Representations of PI and PINDI sensitisers. The lifetime of PI is approximately a few picoseconds, whereas for PINDI is approximately a few microseconds.

The PINDI device achieves a greater performance than the PI device due to the presence of a napthalenediimide (NDI) acceptor. With the presence of the NDI acceptor, the PINDI exhibits recombination approximately 10^5 times slower than PI. Therefore, by extending the length of

the dye and concentrating the electron density onto the NDI acceptor recombination is blocked. Currently, the record p-ssDSC uses a novel indacenodithieno[3,2-b]thiophene (IDTT) linker-based TIP dye with a large π-conjugated system, with PCE of 0.18%.[71] The long alkyl chains and large linker unit attribute to the improved performance of p-ssDSCs. However, this efficiency is still far behind that of n-ssDSCs, therefore much more work must be done to improve this.

In p-ssDSCs an electron-selective material is used instead of an HTM to regenerate the dye and undertake electron transport between the photocathode and the back contact. To transport electrons efficiently the ETM should have good electron mobility. As well as this, the ETM should have good contact with the dye via infiltration in the nanopores of the semiconductor. To allow solution processing the ETM must have good solubility in solvent. Fullerene derivatives have gained more interest as ETMs in photovoltaics as they are strong electron acceptors, with the ability to accept up to 6 electrons. Phenyl-C_{61}-butyric acid methyl ester (PCBM) is a fullerene derivative of buckminsterfullerene, the C_{60} fullerene shown in Figure 1.13,[72] and is one of the most established ETMs that is commercially available with electron mobility of 2 x 10^{-3} cm^2 V^{-1} s^{-1}.[73] As well this, it is reasonably transparent, however, it is not very stable.[74] PCBM derivatives can be blended with the polymer to observe an enhancement in charge separation, carrier mobility, and PCE.

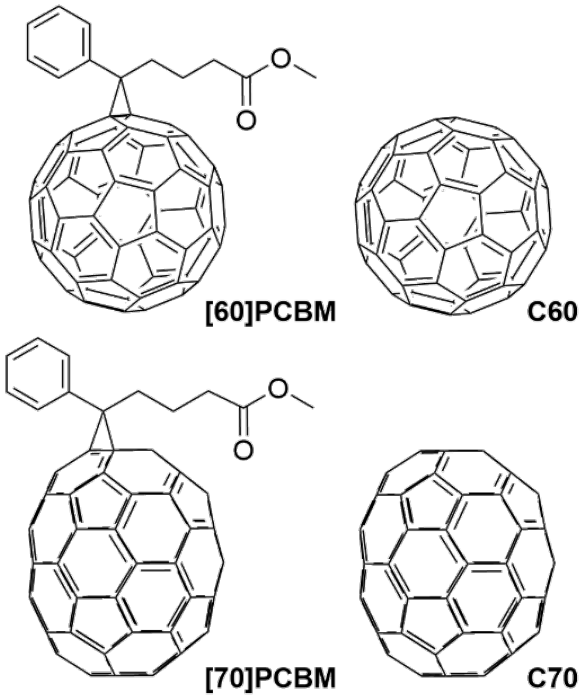

Figure 1.13: Molecular structures of [60]PCBM (LUMO = -3.80 eV), [70]PCBM (LUMO = -3.82 eV), C60 (LUMO = -3.98 eV), and C70 (LUMO = -4.04 eV). Raising the LUMO level can increase the V_{OC}.

Tian and co-workers fabricated the first p-ssDSC using NiO with P1 as the sensitiser along with PCBM as the ETM, their device showed an open circuit voltage of 620 mV.[75] However, electron transfer from the excited state of P1 to the valence band of PCBM competes with charge recombination. This means slow dye regeneration and short lifetime of the reduced dye, which led to a poor photocurrent of around 50 µA cm^{-2}. Later, in 2019, Tian stated that the poor photovoltaic performance was mainly due to the thick PCBM layer (>700nm). Tian calculated that PCBM•⁻ survived on a microsecond timescale, which suggests there is slow charge recombination between the holes and electrons in the NiO and PCBM•⁻.[33]

1.6 Tandem Solid-State Dye-Sensitised Solar Cells

1.6.1 Concept

Research into ssDSCs has been ongoing for over 20 years. This development has effectively addressed the stability concerns that were evident in liquid devices. However, the efficiency of the best devices is still far behind that of other competing third-generation solar cells. A highly effective approach to increase efficiency of devices is to substitute the passive cathode in the cell with a dye-sensitised nanostructured photoactive one, extending it to a tandem device.[76] The diagram in Figure 1.14 depicts a proposed tandem ssDSC.

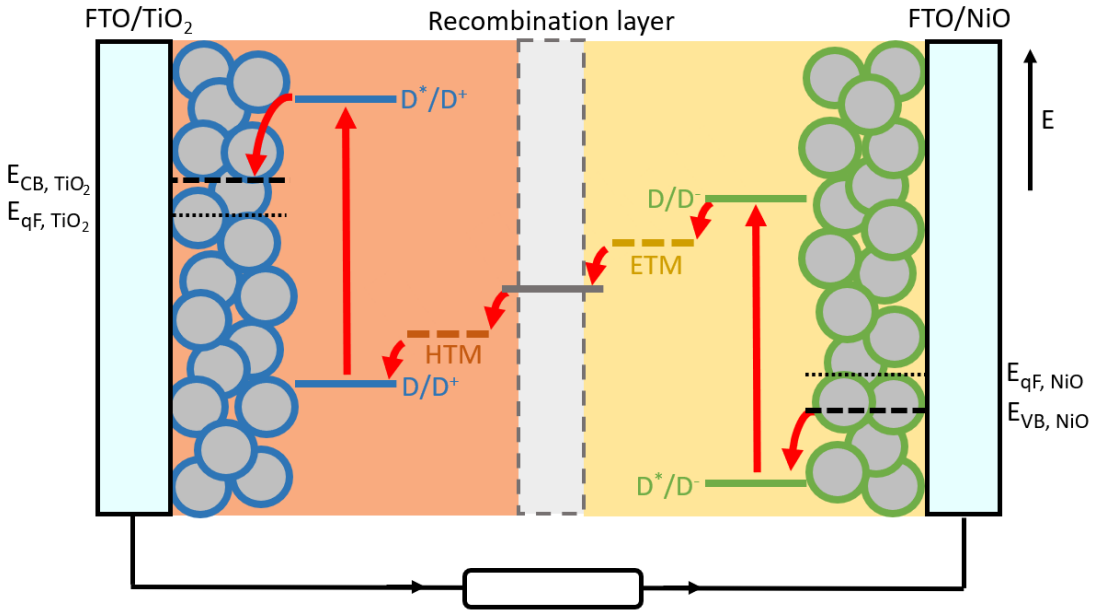

Figure 1.14: Schematic diagram of a p-n tandem ssDSC with two photoactive dye-sensitised electrodes. Device can be illuminated from either side.

In tandem devices, high energy photons are collected at the top electrode and lower energy photons are collected at the bottom electrode, increasing light collection and reducing thermal energy losses.[77] Different ssDSCs with different dyes and absorption regions can be stacked together to construct a tandem device with a broader absorption region, increasing open circuit voltage and short circuit current. An example of adopting this concept in liquid DSCs was demonstrated by Odobel et al.[78] The NiO photocathode was sensitised with Th-DPP-NDI dye with extended absorption into the long wavelengths. When coupled with a TiO_2 photoanode sensitised with D35 dye the tandem device reached a power conversion efficiency of 4.10%, which outperformed that of each subcell.

As the tandem ssDSC will utilise thinner semiconductor layers that liquid tandem DSCs this will enable an increase in light transmission for further enhancement of light absorption. Additionally, the distance that holes and electrons will need to travel will be reduced as the large overstanding layer of the HTM or ETM required for prevention of short circuits is mitigated partly by having the organic/organic interface.

1.6.2 Charge recombination layer

Tandem cells require an interconnecting layer with high transparency and good conductivity to give high efficiencies. In 2013, Chiang et al. fabricated a high-quality indium-doped tin oxide (ITO) film on top of the spiro-OMeTAD HTM as a semi-transparent counter electrode, allowing two n-ssDSCs to be connected in parallel as a three-terminal tandem.[79] The TiO_2 electrodes of the bottom and top cells were sensitised with B1 and Z907, respectively, achieving a PCE of 3.07%. This almost matched the combined PCE of the top (2.65%) and the bottom (0.58%) cells, however incident photon losses might have occurred at the multiple interfaces of the three-terminal tandem device due to scattering reflection of absorption.

To this date no p-n tandem ssDSC has been made, as it wasn't until 2016 that the first p-ssDSC was fabricated. Research for p-ssDSCs is far behind that of n-ssDSCs, with the highest PCE currently at only 0.18%. However, in p-n tandem devices the intermediate oxide films can be omitted and replaced with a charge recombination layer (CRL) to form a two-terminal tandem, which will reduce scattering reflection and absorption. In 2009, Bruder and collaborators used Ag as a CRL in a ssDSC/bulk heterojunction (BJH) organic tandem cell.[80] Each individual cell converted sunlight at about 4.0% PCE, however in tandem they generated an open-circuit

potential of 1.36 V and a PCE of 6.0%. This proves that Ag is an effective serial connection for both subcells.

In 2015, the first bottom-up two-terminal perovskite-perovskite solar cell was constructed by Zhou et al using a novel CRL: spiro-OMeTAD/PEDOT:PSS/PEI/PCBM:PEI.[81] The CRL was prepared at low temperature by orthogonal solvent processing so that processing subsequent layers don't wash away pre-deposited layers. Spiro-OMeTAD and PCBM are common hole/electron transporting materials used in n-ssDSCs/p-ssDSCs, respectively. In this CRL, PEI was used to modify the surface, as well as create a contrast between the work function of the top and bottom sides of the PEDOT:PSS film. Holes flow into the CRL from the bottom subcell, whilst electrons flow out of the CRL to the top subcell, meaning it acts as an efficient site for charge recombination. The tandem cell yielded a V_{OC} of 1.89 V, which is almost equal to the sum of the two subcells, confirming the proof-of-concept success.

1.7 Outline of the Thesis

The focus of this research is to establish a proof of concept for the development of tandem solid-state dye-sensitised solar cells. Monolithic solid-state dye-sensitised solar cells (ssDSCs) have already been shown to have increased stability compared with conventional liquid DSCs. However, their efficiency still lacks in comparison. Therefore, a novel tandem architecture is employed to ssDSCs to increase light absorption and demonstrate a pathway for enhancing the performance of ssDSCs. Additionally, fabrication methods have been chosen with consideration for upscaling of device fabrication.

Chapter 3 introduces the design, fabrication and optimisation of both n-type and p-type ssDSCs that form the constituent parts of the tandem ssDSC. A range of deposition techniques are discussed, considering film homogeneity and ease of upscale.

Chapter 4 details the construction of an Automated Spray Pyrolysis Machine for deposition of thin films, such as blocking layers. This includes building the syringe pump, generating a LabVIEW user interface that controls the ultrasonic spray head and syringe pump properties, and writing GCODE to control the XYZ linear actuators that determines the movement of the spray head and hotplate.

Chapter 5 explores two methods of increasing the charge carrier density for n-type ssDSCs for improved device power conversion efficiency. The first approach discussed was co-sensitisation of a long π-conjugated dye, LEG4, with smaller π-conjugated dyes, L0 and L1, that utilise different absorption spectra. The second approach was investigating the chemical modification of the heterojunction between the TiO_2 and amide-based HTM, TPABT.

Chapter 6 addresses the charge carrier recombination issues in p-type ssDSCs by applying surface modification techniques to the mesoporous NiO film. Surface treatments include the atomic layer deposition of alumina, an aluminium alkoxide solution treatment, and a chenodeoxycholic acid solution treatment. Treatments were characterised using current-voltage measurements and transient absorption spectra, and their kinetic processes were investigated.

Chapter 7 introduces the concept of a tandem ssDSC that employs a charge recombination layer (CRL) that physically and electrically connects an n-type ssDSC subcell with a p-type ssDSC subcell for the efficient charge recombination of majority carriers collected from each subcell. Current-voltage testing was conducted on the CRL to ensure an ohmic contact was established. Following this the tandem device was constructed, initially holding the sub-cells together with pressure, and finally utilising a transparent conductive adhesive. Illumination from both sides of the tandem device was investigated.

References

1 J. F. Kasting, Long-term stability of the earth's climate, *Glob Planet Change*, 1989, **1**, 83–95.

2 *NOAA National Centers for Environmental Information, Monthly Global Climate Report for December 2021, 2022, retrieved from https://www.ncei.noaa.gov/access/monitoring/monthly-report/global/202200.*

3 *HM Government, Net Zero Strategy: Build Back Greener, 2021, retrieved from https://assets.publishing.service.gov.uk/media/6194dfa4d3bf7f0555071b1b/net-zero-strategy-beis.pdf*.

4 *United Nations / Framework Convention on Climate Change, Adoption of the Paris Agreement, 21st Conference of the Parties, Paris: United Nations, 2015, retrieved from https://unfccc.int/sites/default/files/resource/parisagreement_publication.pdf*.

5 *United Kingdom of Great Britain and Northern Ireland's Nationally Determined Contribution, 2022, retrieved from https://unfccc.int/sites/default/files/NDC/2022-09/UK%20NDC%20ICTU%202022.pdf*.

6 L. A. Omeiza, M. Abid, A. Dhanasekaran, Y. Subramanian, V. Raj, K. Kozak, U. Mamudu and A. K. Azad, Application of solar thermal collectors for energy consumption in public buildings – An updated technical review, *Journal of Engineering Research*, DOI:10.1016/j.jer.2023.09.011.

7 *IEA, World Energy Investment 2023, 2023, retrieved from https://www.iea.org/reports/world-energy-investment-2023*.

8 Quirin Schiermeier, Jeff Tollefson, Tony Scully, Alexandra Witze and Oliver Morton, Electricity without carbon., *Nature*.

9 *IEA (2023), Solar PV power generation in the Net Zero Scenario, 2015-2030, IEA, Paris https://www.iea.org/data-and-statistics/charts/solar-pv-power-generation-in-the-net-zero-scenario-2015-2030*.

10 Marina Freitag, Joël Teuscher, Yasemin Saygili, Xiaoyu Zhang, Fabrizio Giordano, Paul Liska, Jianli Hua, Shaik M. Zakeeruddin, Jacques-E. Moser, Michael Grätzel and Anders Hagfeldt, Dye-sensitized solar cells for efficient power generation under ambient lighting, *Nat Photonics*, 2017, **11**, 372–378.

11 I. Mathews, S. N. Kantareddy, T. Buonassisi and I. M. Peters, Technology and Market Perspective for Indoor Photovoltaic Cells, *Joule*, 2019, **3**, 1415–1426.

12 H. Michaels, M. Rinderle, R. Freitag, I. Benesperi, T. Edvinsson, R. Socher, A. Gagliardi and M. Freitag, Dye-sensitized solar cells under ambient light powering machine learning: towards autonomous smart sensors for the internet of things, *Chem Sci*, 2020, **11**, 2895–2906.

13 Q. Wali, N. K. Elumalai, Y. Iqbal, A. Uddin and R. Jose, Tandem perovskite solar cells, *Renewable and Sustainable Energy Reviews*, 2018, **84**, 89–110.

14 W. Shockley and H. J. Queisser, Detailed Balance Limit of Efficiency of p-n Junction Solar Cells, *J Appl Phys*, 1961, **32**, 510–519.

15 A. A. Hossam-Eldin, Mostafa Refaey and Abdelrahman Farghly, in *17th International Middle-East Power System Conference (MEPCON'15)*, Mansoura University, Egypt., 2015.

16 C. Ballif, F.-J. Haug, M. Boccard, P. J. Verlinden and G. Hahn, Status and perspectives of crystalline silicon photovoltaics in research and industry, *Nat Rev Mater*, 2022, **7**, 597–616.

17 M. A. Fazal and S. Rubaiee, Progress of PV cell technology: Feasibility of building materials, cost, performance, and stability, *Solar Energy*, 2023, **258**, 203–219.

18 M. A. Scarpulla, B. McCandless, A. B. Phillips, Y. Yan, M. J. Heben, C. Wolden, G. Xiong, W. K. Metzger, D. Mao, D. Krasikov, I. Sankin, S. Grover, A. Munshi, W. Sampath, J. R. Sites, A. Bothwell, D. Albin, M. O. Reese, A. Romeo, M. Nardone, R. Klie, J. M. Walls, T. Fiducia, A. Abbas and S. M. Hayes, CdTe-based thin film photovoltaics: Recent advances, current challenges and future prospects, *Solar Energy Materials and Solar Cells*, 2023, **255**, 112289.

19 P. M. Mwenda, W. Njoroge, S. Mirenga and D. M. Kinyua, Review: Advances in the CIGS Thin Films for Photovoltaic Applications, *Smart Grid and Renewable Energy*, 2022, **13**, 75–87.

20 N. Shah, A. A. Shah, P. K. Leung, S. Khan, K. Sun, X. Zhu and Q. Liao, A Review of Third Generation Solar Cells, *Processes*, 2023, **11**, 1852.

21 S. M. Mousavi, Z. S. Alborzi, S. Raveshiyan and Y. Amini, in *Nanotechnology Applications for Solar Energy Systems*, Wiley, 2023, pp. 239–256.

22 US 4105470, 1978.

23 H. Gerischer and H. Tributsch, Elektrochemische Untersuchungen zur spektralen Sensibilisierung von ZnO-Einkristallen, *Berichte der Bunsengesellschaft für physikalische Chemie*, 1968, **72**, 437–445.

24 H. Gerischer, M. E. Michel-Beyerle, F. Rebentrost and H. Tributsch, Sensitization of charge injection into semiconductors with large band gap, *Electrochim Acta*, 1968, **13**, 1509–1515.

25 B. O'Regan and M. Grätzel, A low-cost, high-efficiency solar cell based on dye-sensitized colloidal TiO2 films, *Nature*, 1991, **353**, 737–740.

26 C. Cavallo, F. Di Pascasio, A. Latini, M. Bonomo and D. Dini, Nanostructured Semiconductor Materials for Dye-Sensitized Solar Cells, *J Nanomater*, 2017, **2017**, 1–31.

27 R. Sasikumar, S. Thirumalaisamy, B. Kim and B. Hwang, Dye-sensitized solar cells: Insights and research divergence towards alternatives, *Renewable and Sustainable Energy Reviews*, 2024, **199**, 114549.

28 J. A. Anta, E. Guillén and R. Tena-Zaera, ZnO-Based Dye-Sensitized Solar Cells, *The Journal of Physical Chemistry C*, 2012, **116**, 11413–11425.

29 W. M. N. M. B. Wanninayake, K. Premaratne and R. M. G. Rajapakse, High Efficient Dye-Sensitized Solar Cells Based on Synthesized SnO2 Nanoparticles, *J Nanomater*, 2016, **2016**, 1–8.

30 B. N. Nunes, L. A. Faustino, A. V. Muller, A. S. Polo and A. O. T. Patrocinio, in *Nanomaterials for Solar Cell Applications*, Elsevier, 2019, pp. 287–322.

31 S. Gholamrezaei and M. Salavati-Niasari, An efficient dye sensitized solar cells based on SrTiO3 nanoparticles prepared from a new amine-modified sol-gel route, *J Mol Liq*, 2017, **243**, 227–235.

32 S. Wrede and H. Tian, Towards sustainable and efficient p-type metal oxide semiconductor materials in dye-sensitised photocathodes for solar energy conversion, *Physical Chemistry Chemical Physics*, 2020, **22**, 13850–13861.

33 H. I. Alabdan, A. Alwabsi, A. M. Alsagrey, F. H. AlKhulaif, M. E. Abdelgawad, N. J. AlQahtani, A. Al-Malki, A. Alfahad, W. S. Alrubaian, F. M. Alsahli and T. K. Mallick, Usage of CuO in Dye-Sensitized Solar Cells and CuO-Based Dyesensitized Solar Cells: A Review, *IEEE J Photovolt*, 2022, **12**, 1445–1452.

34 S. Du, P. Cheng, P. Sun, B. Wang, Y. Cai, F. Liu, J. Zheng and G. Lu, Highly efficiency p-type dye sensitized solar cells based on polygonal star-morphology Cu2O material of photocathodes, *Chem Res Chin Univ*, 2014, **30**, 661–665.

35 Z. Yu, I. R. Perera, T. Daeneke, S. Makuta, Y. Tachibana, J. J. Jasieniak, A. Mishra, P. Bäuerle, L. Spiccia and U. Bach, Indium tin oxide as a semiconductor material in efficient p-type dye-sensitized solar cells, *NPG Asia Mater*, 2016, **8**, e305–e305.

36 T. Jiang, M. Bujoli-Doeuff, Y. Farré, E. Blart, Y. Pellegrin, E. Gautron, M. Boujtita, L. Cario, F. Odobel and S. Jobic, Copper borate as a photocathode in p-type dye-sensitized solar cells, *RSC Adv*, 2016, **6**, 1549–1553.

37 M. Yu, T. I. Draskovic and Y. Wu, Cu(I)-based delafossite compounds as photocathodes in p-type dye-sensitized solar cells, *Physical Chemistry Chemical Physics*, 2014, **16**, 5026.

38 T. Zhu, Z. Deng, X. Fang, Z. Huo, S. Wang, W. Dong, J. Shao, R. Tao, C. Song and L. Wang, High photovoltages of CuFeO2 based p-type dye-sensitized solar cells, *J Alloys Compd*, 2016, **685**, 836–840.

39 A. Carella, F. Borbone and R. Centore, Research Progress on Photosensitizers for DSSC, *Front Chem*, DOI:10.3389/fchem.2018.00481.

40 M. K. Nazeeruddin and M. Grätzel, 2007, pp. 120–121.

41 Y. Ooyama and Y. Harima, Molecular Designs and Syntheses of Organic Dyes for Dye-Sensitized Solar Cells, *European J Org Chem*, 2009, **2009**, 2903–2934.

42 B. Kim, K. Chung and J. Kim, Molecular Design Principle of All-organic Dyes for Dye-Sensitized Solar Cells, *Chemistry – A European Journal*, 2013, **19**, 5220–5230.

43 G. Saritha, S. Anandan and M. Ashokkumar, in *Rational Design of Solar Cells for Efficient Solar Energy Conversion*, Wiley, 2018, pp. 18–19.

44 H. Iftikhar, G. G. Sonai, S. G. Hashmi, A. F. Nogueira and P. D. Lund, Progress on Electrolytes Development in Dye-Sensitized Solar Cells, *Materials*, 2019, **12**, 1998.

45 S. C. Pradhan, A. Hagfeldt and S. Soman, Resurgence of DSCs with copper electrolyte: a detailed investigation of interfacial charge dynamics with cobalt and iodine based electrolytes, *J Mater Chem A Mater*, 2018, **6**, 22204–22214.

46 Masud and H. K. Kim, Redox Shuttle-Based Electrolytes for Dye-Sensitized Solar Cells: Comprehensive Guidance, Recent Progress, and Future Perspective, *ACS Omega*, 2023, **8**, 6139–6163.

47 M. Wu and T. Ma, Recent Progress of Counter Electrode Catalysts in Dye-Sensitized Solar Cells, *The Journal of Physical Chemistry C*, 2014, **118**, 16727–16742.

48 S. Carli, E. Busatto, S. Caramori, R. Boaretto, R. Argazzi, Cliff. J. Timpson and C. A. Bignozzi, Comparative Evaluation of Catalytic Counter Electrodes for Co(III)/(II) Electron Shuttles in Regenerative Photoelectrochemical Cells, *The Journal of Physical Chemistry C*, 2013, **117**, 5142–5153.

49 M. Kouhnavard, N. A. Ludin, B. V. Ghaffari, K. Sopian and S. Ikeda, Carbonaceous Materials and Their Advances as a Counter Electrode in Dye-Sensitized Solar Cells: Challenges and Prospects, *ChemSusChem*, 2015, **8**, 1510–1533.

50 E. Marchini, S. Caramori, C. A. Bignozzi and S. Carli, On the Use of PEDOT as a Catalytic Counter Electrode Material in Dye-Sensitized Solar Cells, *Applied Sciences*, 2021, **11**, 3795.

51 L. H. Kharboot, N. A. Fadil, T. A. A. Bakar, A. S. M. Najib, N. H. Nordin and H. Ghazali, A Review of Transition Metal Sulfides as Counter Electrodes for Dye-Sensitized and Quantum Dot-Sensitized Solar Cells, *Materials*, 2023, **16**, 2881.

52 Y. Ren, D. Zhang, J. Suo, Y. Cao, F. T. Eickemeyer, N. Vlachopoulos, S. M. Zakeeruddin, A. Hagfeldt and M. Grätzel, Hydroxamic acid pre-adsorption raises the efficiency of cosensitized solar cells, *Nature*, 2023, **613**, 60–65.

53 I. R. Perera, T. Daeneke, S. Makuta, Z. Yu, Y. Tachibana, A. Mishra, P. Bäuerle, C. A. Ohlin, U. Bach and L. Spiccia, Application of the Tris(acetylacetonato)iron(III)/(II) Redox Couple in p-

Type Dye-Sensitized Solar Cells, *Angewandte Chemie International Edition*, 2015, **54**, 3758–3762.

54 K. Tennakone, G. R. R. A. Kumara, A. R. Kumarasinghe, K. G. U. Wijayantha and P. M. Sirimanne, A dye-sensitized nano-porous solid-state photovoltaic cell, *Semicond Sci Technol*, 1995, **10**, 1689–1693.

55 U. Bach, D. Lupo, P. Comte, J. E. Moser, F. Weissörtel, J. Salbeck, H. Spreitzer and M. Grätzel, Solid-state dye-sensitized mesoporous TiO2 solar cells with high photon-to-electron conversion efficiencies, *Nature*, 1998, **395**, 583–585.

56 D. Shi, X. Qin, Y. Li, Y. He, C. Zhong, J. Pan, H. Dong, W. Xu, T. Li, W. Hu, J.-L. Brédas and O. M. Bakr, Spiro-OMeTAD single crystals: Remarkably enhanced charge-carrier transport via mesoscale ordering, *Sci Adv*, DOI:10.1126/sciadv.1501491.

57 Z. Hawash, L. K. Ono and Y. Qi, Recent Advances in Spiro-MeOTAD Hole Transport Material and Its Applications in Organic–Inorganic Halide Perovskite Solar Cells, *Adv Mater Interfaces*, DOI:10.1002/admi.201700623.

58 U. B. Cappel, E. A. Gibson, A. Hagfeldt and G. Boschloo, Dye Regeneration by Spiro-MeOTAD in Solid State Dye-Sensitized Solar Cells Studied by Photoinduced Absorption Spectroscopy and Spectroelectrochemistry, *The Journal of Physical Chemistry C*, 2009, **113**, 6275–6281.

59 J. Krüger, R. Plass, L. Cevey, M. Piccirelli, M. Grätzel and U. Bach, High efficiency solid-state photovoltaic device due to inhibition of interface charge recombination, *Appl Phys Lett*, 2001, **79**, 2085–2087.

60 C. A. Kelly, F. Farzad, D. W. Thompson, J. M. Stipkala and G. J. Meyer, Cation-Controlled Interfacial Charge Injection in Sensitized Nanocrystalline TiO_2, *Langmuir*, 1999, **15**, 7047–7054.

61 U. B. Cappel, A. L. Smeigh, S. Plogmaker, E. M. J. Johansson, H. Rensmo, L. Hammarström, A. Hagfeldt and G. Boschloo, Characterization of the Interface Properties and Processes in Solid State Dye-Sensitized Solar Cells Employing a Perylene Sensitizer, *The Journal of Physical Chemistry C*, 2011, **115**, 4345–4358.

62 M. Freitag, Q. Daniel, M. Pazoki, K. Sveinbjörnsson, J. Zhang, L. Sun, A. Hagfeldt and G. Boschloo, High-efficiency dye-sensitized solar cells with molecular copper phenanthroline as solid hole conductor, *Energy Environ Sci*, 2015, **8**, 2634–2637.

63 W. Zhang, Y. Wu, H. W. Bahng, Y. Cao, C. Yi, Y. Saygili, J. Luo, Y. Liu, L. Kavan, J.-E. Moser, A. Hagfeldt, H. Tian, S. M. Zakeeruddin, W.-H. Zhu and M. Grätzel, Comprehensive control of voltage loss enables 11.7% efficient solid-state dye-sensitized solar cells, *Energy Environ Sci*, 2018, **11**, 1779–1787.

64 J. He, H. Lindström, A. Hagfeldt and S.-E. Lindquist, Dye-Sensitized Nanostructured p-Type Nickel Oxide Film as a Photocathode for a Solar Cell, *J Phys Chem B*, 1999, **103**, 8940–8943.

65 F. Odobel, L. Le Pleux, Y. Pellegrin and E. Blart, New Photovoltaic Devices Based on the Sensitization of p-type Semiconductors: Challenges and Opportunities, *Acc Chem Res*, 2010, **43**, 1063–1071.

66 J. He, H. Lindström, A. Hagfeldt and S.-E. Lindquist, Dye-sensitized nanostructured tandem cell-first demonstrated cell with a dye-sensitized photocathode, *Solar Energy Materials and Solar Cells*, 2000, **62**, 265–273.

67 S. Mori, S. Fukuda, S. Sumikura, Y. Takeda, Y. Tamaki, E. Suzuki and T. Abe, Charge-Transfer Processes in Dye-Sensitized NiO Solar Cells, *The Journal of Physical Chemistry C*, 2008, **112**, 16134–16139.

68 X. L. Zhang, Z. Zhang, F. Huang, P. Bäuerle, U. Bach and Y.-B. Cheng, Charge transport in photocathodes based on the sensitization of NiO nanorods, *J Mater Chem*, 2012, **22**, 7005.

69 L. Tian, J. Föhlinger, Z. Zhang, P. B. Pati, J. Lin, T. Kubart, Y. Hua, J. Sun, L. Kloo, G. Boschloo, L. Hammarström and H. Tian, Solid state p-type dye sensitized NiO–dye–TiO2 core–shell solar cells, *Chemical Communications*, 2018, **54**, 3739–3742.

70 E. A. Gibson, A. L. Smeigh, L. Le Pleux, J. Fortage, G. Boschloo, E. Blart, Y. Pellegrin, F. Odobel, A. Hagfeldt and L. Hammarström, A p-Type NiO-Based Dye-Sensitized Solar Cell with an Open-Circuit Voltage of 0.35 V, *Angewandte Chemie*, 2009, **121**, 4466–4469.

71 B. Xu, S. Wrede, A. Curtze, L. Tian, P. B. Pati, L. Kloo, Y. Wu and H. Tian, An Indacenodithieno[3,2-b]thiophene-Based Organic Dye for Solid-State p-Type Dye-Sensitized Solar Cells, *ChemSusChem*, 2019, **12**, 3243–3248.

72 Y. Xu, X. Huang, J. Yuan and W. Ma, From PCBM-Polymer to Low-Cost and Thermally Stable C60/C70-Polymer Solar Cells: The Role of Molecular Structure, Crystallinity, and Morphology Control, *ACS Appl Mater Interfaces*, 2018, **10**, 24037–24045.

73 H. Tian, Solid-state p-type dye-sensitized solar cells: progress, potential applications and challenges, *Sustain Energy Fuels*, 2019, **3**, 888–898.

74 A. Distler, T. Sauermann, H. Egelhaaf, S. Rodman, D. Waller, K. Cheon, M. Lee and D. M. Guldi, The Effect of PCBM Dimerization on the Performance of Bulk Heterojunction Solar Cells, *Adv Energy Mater*, DOI:10.1002/aenm.201300693.

75 L. Zhang, G. Boschloo, L. Hammarström and H. Tian, Solid state p-type dye-sensitized solar cells: concept, experiment and mechanism, *Physical Chemistry Chemical Physics*, 2016, **18**, 5080–5085.

76 A. Kolay, P. Ghosal and M. Deepa, Novel Integration of Nickel Phthalocyanine/Nickel Oxide-Based Photocathodes and Copper-Encapsulated Carbon-Dot-Cosensitized Photoanodes in Tandem for a Highly Efficient Solar Cell, *ACS Sustain Chem Eng*, 2020, **8**, 8593–8603.

77 J.-F. Lefebvre, X.-Z. Sun, J. A. Calladine, M. W. George and E. A. Gibson, Promoting charge-separation in p-type dye-sensitized solar cells using bodipy, *Chem. Commun.*, 2014, **50**, 5258–5260.

78 Y. Farré, M. Raissi, A. Fihey, Y. Pellegrin, E. Blart, D. Jacquemin and F. Odobel, A Blue Diketopyrrolopyrrole Sensitizer with High Efficiency in Nickel-Oxide-based Dye-Sensitized Solar Cells, *ChemSusChem*, 2017, **10**, 2618–2625.

79 Y.-F. Chiang, R.-T. Chen, A. Burke, U. Bach, P. Chen and T.-F. Guo, Non-color distortion for visible light transmitted tandem solid state dye-sensitized solar cells, *Renew Energy*, 2013, **59**, 136–140.

80 I. Bruder, M. Karlsson, F. Eickemeyer, J. Hwang, P. Erk, A. Hagfeldt, J. Weis and N. Pschirer, Efficient organic tandem cell combining a solid state dye-sensitized and a vacuum deposited bulk heterojunction solar cell, *Solar Energy Materials and Solar Cells*, 2009, **93**, 1896–1899.

81 F. Jiang, T. Liu, B. Luo, J. Tong, F. Qin, S. Xiong, Z. Li and Y. Zhou, A two-terminal perovskite/perovskite tandem solar cell, *J Mater Chem A Mater*, 2016, **4**, 1208–1213.

82 Z. Hawash, L. K. Ono and Y. Qi, Recent Advances in Spiro-MeOTAD Hole Transport Material and Its Applications in Organic–Inorganic Halide Perovskite Solar Cells, *Adv Mater Interfaces*, DOI:10.1002/admi.201700623.

Chapter 2.

Experimental Techniques

2.1 Current density-voltage (J-V) characteristics

The current density flowing through the device is measured at a series of voltages to create a J-V curve, as shown in Figure 2.1. Without illumination a solar cell has the same electrical characteristics as a diode. This is seen when measuring a dark current curve. Under illumination, the J-V curve becomes the superposition of the dark current curve with the light-generated current. A greater light intensity generates a greater amount of shift. Therefore, an ideal solar cell can be electronically modelled by a current source (photogenerated) in parallel with a diode.

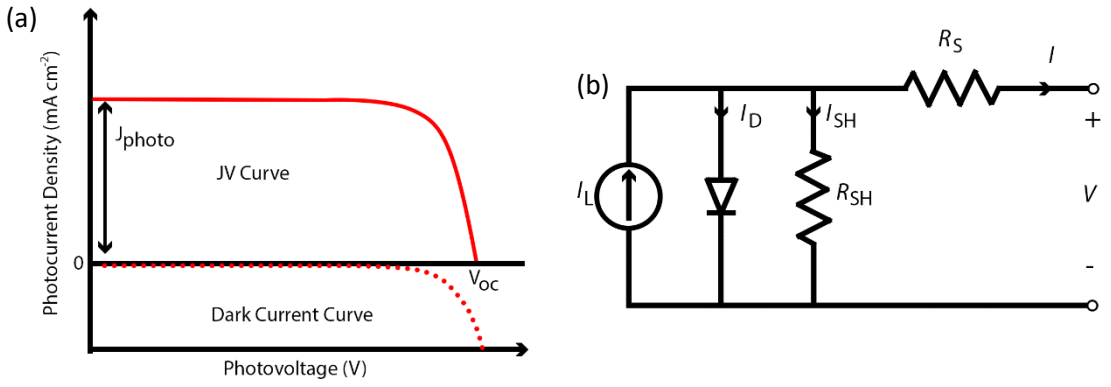

Figure 2.1: An ideal solar cell's (a) example JV curve (solid line) and dark current curve (dashed line) and (b) the equivalent circuit considering the single diode model.

In practice, a shunt resistance component (R_{SH}) and a series resistance component (R_S) are added to the model. Thus, the current produced by the solar cell (I) is equal to the

photogenerated current (I_L) minus the diode current (I_D), minus the shunt current (I_{SH}), which is shown as:

$$I = I_L - I_D - I_{SH}. \tag{2.1}$$

Taking into consideration the diode current described by the Shockley diode equation,[1] Equation 2.1 can be re-written as follows:

$$I = I_L - I_0\left[e^{\frac{V+IR_S}{nV_T}} - 1\right] - \frac{V + IR_S}{R_{SH}}, \tag{2.2}$$

where I_0 is the reverse saturation current, n is the diode quality factor (1 for ideal diode), and $V_T = k_B T/q$ is the thermal voltage. At room temperature (temperature T = 300 K, Boltzmann constant k_B = 1.38 x 10^{-23} m^2 kg s^{-2} K^{-1}, electron charge q = 1.6 x 10^{-19} C) the thermal voltage is around 25.9 mV. Plotting Equation 2.2 gives the IV curve shown in Figure 2.2. To remove the dependence of the solar cell area, it is more common to write as current density rather than current.

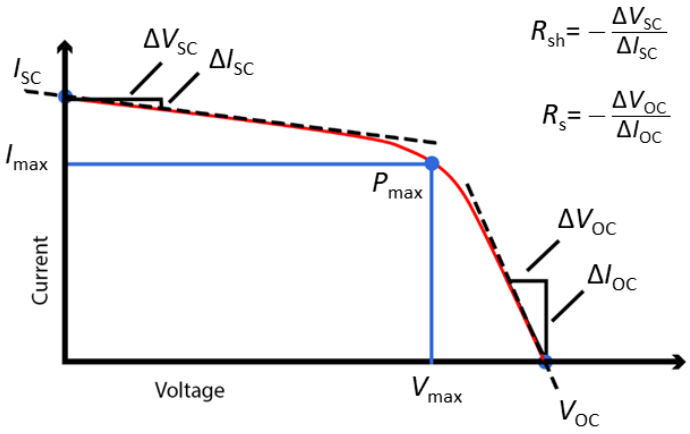

Figure 2.2: Current voltage (I-V) curve of a solar cell with relevant points labelled.

Several key properties can be extracted from the J-V curve of a solar cell. The maximum current density of a solar cell occurs when the voltage across the solar cell is zero, the device is said to be at short circuit and the current density flowing through is called the short circuit photocurrent density (J_{SC}). This can be extracted from the intercept with the y-axis. The maximum voltage from a solar cell occurs when the applied voltage cancels out the built-in electric field, at which the current is zero, and is called the open-circuit voltage (V_{OC}). This can be extracted from the intercept with the x-axis. The fill factor (FF) is the ratio of the actual maximum power output of the solar cell (P_{MP}) to the power output if there were no parasitic resistances. FF can be written as follows:

$$FF = \frac{P_{MP}}{V_{OC}J_{SC}} = \frac{V_{MP}J_{MP}}{V_{OC}J_{SC}}, \quad (2.3)$$

where V_{MP} and J_{MP} are the voltage and current density at maximum power, respectively. Finally, the power conversion efficiency (PCE) of the solar cell is the ratio of incident light power (P_{in}) to output electrical power (P_{out}). The PCE can be calculated using the following equation:

$$PCE = \frac{P_{out}}{P_{in}} = \frac{V_{OC}J_{SC}FF}{P_{in}}. \quad (2.4)$$

As PCE considers all the key properties extracted from the solar cell's J-V curve, it is one of the most common values to use when comparing overall performance of differing devices.

2.2 Incident photon-to-current conversion efficiency (IPCE)

When comparing solar cells with different absorption spectra, a useful parameter to measure is the incident photon-to-electron conversion efficiency (IPCE). IPCE describes how many of the incoming photons at one wavelength are converted to electrons. A monochromator is used to output light at varying wavelengths and the resulting current density is measured. IPCE values as a function of wavelength can be calculated as follows:

$$IPCE(\lambda) = \frac{\text{electrons}_{\text{out}}(\lambda)}{\text{photons}_{\text{in}}(\lambda)} = \frac{hc}{e} \cdot \frac{J_{Ph}(\lambda)}{\lambda \cdot P_{in}(\lambda)}, \quad (2.5)$$

where J_{Ph} is the photocurrent density. The constants (Planck's constant (h), the speed of light (c), and the elementary charge (e)) can be summarised as 1240 V nm. The measurement is usually carried out under short circuit conditions, although can also be done at an applied potential. Considering the process of how current is generated, IPCE can also be written as a product of the efficiency of different processes in the solar cell:

$$IPCE(\lambda) = \text{LHE}(\lambda)\phi_{inj}\eta_c, \quad (2.6)$$

where LHE (light harvesting efficiency) is the fraction of incident photons that are absorbed by the dye, ϕ_{inj} is the quantum yield for charge injection, and η_c is the efficiency of collecting the injected charge at the back contact.[2]

2.3 Ultraviolet-Visible (UV-Vis) spectroscopy

Ultraviolet (UV) radiation refers to wavelengths ranging between 280-400 nm, while visible radiation encompasses wavelengths between 400-700 nm on the electromagnetic spectrum. We can study how matter interacts with or emits electromagnetic radiation using spectroscopy. When radiation interacts with matter there are several processes that can occur, such as reflection, scattering and absorbance. Absorption occurs when the energy of the incident photon is equal to or greater than the energy difference between the highest occupied molecular orbital (HOMO) and the lowest unoccupied molecular orbital (LUMO). If this is satisfied, the photon can be absorbed by an electron in the HOMO and excited into a higher energy state. This means the wavelength of light absorbed corresponds to a measure of energy separation between electronic states. Therefore, it is useful to measure the absorbance of a material to determine the nature of such transitions.

If a beam of light is passed through the sample, the amount of light absorbed can be quantified by the ratio of transmitted radiation (I) to incident radiation (I_0). This ratio is called transmittance (T). Therefore, absorbance (A) can be calculated as follows:

$$A = \log \frac{I_0}{I} = -\log T \, . \qquad (2.7)$$

By plotting absorbance against the wavelength of incident light, a UV-vis spectrum can be obtained.

2.4 Cyclic Voltammetry (CV)

Cyclic voltammetry (CV) is a useful electrochemical technique that allows us to study the thermodynamics of redox processes, estimate energy levels, and investigate electron transfer reaction kinetics. A setup of a three-electrode system is used consisting of a working electrode, a reference electrode, and a counter electrode. Potential of the working electrode is ramped linearly versus time in cyclical phases, scanning between two set voltages in forward and reverse directions. The potentials are relative to a reference electrode. The resulting current change between the working and counter probes is recorded. The resulting current is plotted as a function of potential to form a cyclic voltammogram. CV is used in this thesis to

investigate the mechanism of interfacial electron transfer in an n-ssDSC to minimise interfacial recombination between the FTO and HTM.

2.5 Photoinduced Absorption Spectroscopy (PIA)

Photoinduced absorption spectroscopy (PIA) can be used to study the dynamics of excited states in dyes, allowing processes such as charge separation and recombination to be examined. A probe light is focused onto the sample by a series of optics, and the transmission (T) through a sample is measured (Figure 2.3). A pump light consisting of a square-modulated monochromatic light beam causes electronic excitations that induce small changes in transmission (ΔT). The ratio of $\Delta T/T$ is proportional to the absorbance change (ΔA) as follows:

$$-\frac{\Delta T}{T} = \ln 10 \cdot \Delta A \, . \qquad (2.8)$$

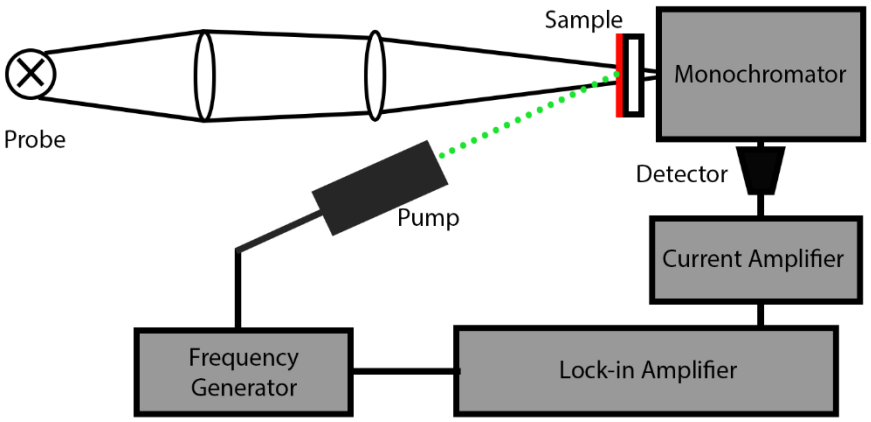

Figure 2.3: Schematic diagram of the PIA setup.

2.6 Transient Absorption Spectroscopy (TAS)

In contrast to square-modulation used in PIA, transient absorption spectroscopy (TAS) excites the sample with short laser pulses to investigate kinetic processes that occur after excitation on the time scales of femtoseconds to nanoseconds. Femtosecond TAS is often used to probe singlet excited states in processes such as charge injection, whereas nanosecond TAS is often used to study back electron transfer. A monochromatic laser pulse (pump) is used to excite

the sample and, after a certain time delay, a polychromatic laser pulse (probe) is used to measure the transmission through a sample. The probe beam passes through the sample and then through a monochromator, which allows the ground state and excited state absorbance changes of the sample to be measured at a particular wavelength. The change in absorbance (ΔA) is calculated according to the following equation:

$$\Delta A = -\log\left(\frac{I_{\text{pumped}}}{I_{\text{unpumped}}}\right), \qquad (2.9)$$

where I_{pumped} is the intensity of the transmitted probe beam in the presence of the pump, and I_{unpumped} is the intensity of the transmitted probe beam in the absence of the pump. In ultrafast transient absorption spectroscopy, operating within femtosecond timescales, a single laser source is used to generate both the pump and the probe pulses, achieving time resolution through adjusting the relative arrival times of these pulses at the sample.

2.7 Scanning Electron Microscopy (SEM) and Energy-Dispersive X-ray spectroscopy (EDX)

Scanning electron microscopy (SEM) uses an electron microscope that generates magnified images of a sample through scanning of its surface using a focused beam of high-energy electrons. Signals are produced that contain information about the surface topography and composition of the solid sample. The electrons are emitted from a filament at the top of a column, accelerated down, and passed through a combination of lenses and apertures to produce a focused beam which then strikes the surface of the sample. The electrons interact with atoms in the sample, generating several electron and X-ray signals.

Once the beam hits the sample, several types of electron signals are produced, including backscattered electrons (BSE) and secondary electrons (SE). BSE are high-energy electrons that occur as a result of elastic collisions of the beam electrons with atoms in the sample. They emerge from deep within the sample and contribute to compositional details, producing lower resolution images. SE are low-energy electrons that occur due to inelastic collisions of the beam electrons and the atoms on the sample surface. SE are sensitive to surface structure and generate high resolution images of surface topography.

Core-shell electrons are ejected from the sample upon excitation by the high-energy electron beam. A higher energy outer-shell electron transitions to the lower energy levels to fill the vacancy, releasing the difference in energy as an X-ray. These X-rays have characteristic spectra of the atom it originated from; the position of the peaks reveals the element, and the intensity of the peak provides information about the concentration of that element. This analysis of the X-rays is called Energy-Dispersive X-ray spectroscopy (EDX) and works in conjunction with SEM.

References

1 W. Shockley, The Theory of p-n Junctions in Semiconductors and p-n Junction Transistors, *Bell System Technical Journal*, 1949, **28**, 435–489.

2 B. O'Regan and M. Grätzel, A low-cost, high-efficiency solar cell based on dye-sensitized colloidal TiO2 films, *Nature*, 1991, **353**, 737–740.

Chapter 3.

Device Fabrication and Optimisation

3.1 Introduction

The widespread commercialisation of solar cells relies on achieving a high power conversion efficiency (PCE). However, other crucial factors contributing to their successful deployment for real world applications involve developing ultra-low-cost device architectures that are stable over 20 years. Conventional liquid state DSCs are constructed by sandwiching two conducting glass substrates together and inserting the liquid electrolyte in between. The conducting glass substrate accounts for most of the materials cost,[1] therefore the advantage of monolithic solid-state DSCs is that the inherent cost of fabrication can be reduced by removing at least one glass substrate. The device is fabricated on a single substrate, creating what is known as a monolithic device. Moreover, monolithic solid-state DSCs are attractive as they require simpler manufacturing processes; they eliminate the need for hole drilling to allow the insertion of the electrolyte, as well as the sealing process.

In this chapter the fabrication of monolithic n-type and p-type solid-state DSCs used in this work is discussed and various deposition techniques are compared, highlighting crucial aspects such as uniformity, reproducibility and scalability. Film uniformity helps minimise any charge transport losses by ensuring efficient charge collection and transport throughout the device, reproducibility of each film deposition ensures that device performance can be replicated across multiple batches for accurate benchmarking, and scalability is important to consider for commercial viability. Furthermore, the optimisation of specific layers within each device is showcased, and the impact on the resulting device's performance is highlighted.

3.2 Solar cell design

3.2.1 Device layout

A solar cell consists of several key components and layers that play a crucial role in converting sunlight into energy. For monolithic solid-state DSCs (ssDSCs) the component architecture usually consists of a transparent conductive substrate, a compact blocking layer, a dye-sensitised mesoporous semiconductor, a charge transporting material and a grid of metal contacts. The layout of each component is essential for establishing an electrical circuit, however it is also important to take into account the deposition techniques for each layer when designing the layout as this can impact uniformity across the substrate as well as device reproducibility. It is also worth considering how easy the design is to upscale.

Figure 3.1 shows 3 cell designs with differing component layouts, all containing 8 rectangular pixels. Figure 3.1(a) shows the design of perovskite solar cells (PSCs) constructed at Newcastle University. PSC architecture is similar to that of monolithic ssDSCs as they both contain 1 transparent conductive substrate and employ a solid charge transporting material, thus this layout was chosen as a starting point to form the initial ssDSC layout shown in Figure 3.1(b).

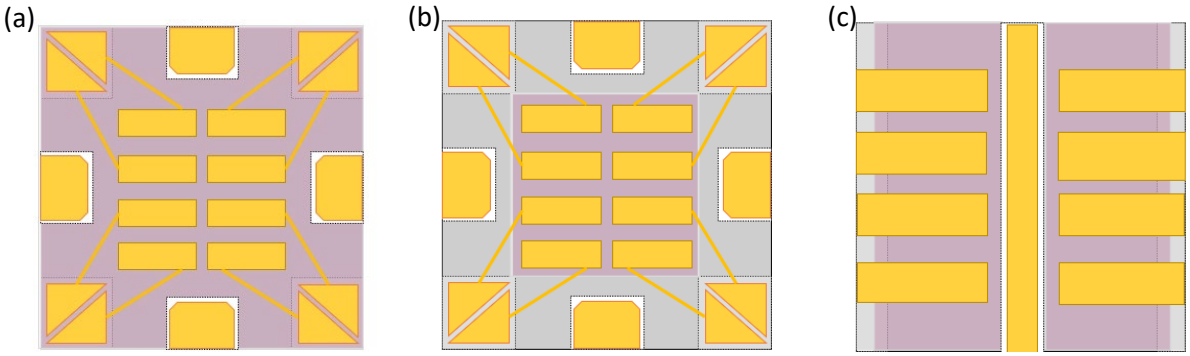

Figure 3.1: (a) Perovskite solar cell layout, (b) initial ssDSC layout, and (c) redesigned ssDSC layout, where the grey area represents the conducting glass substrate, the pink area represents the photoactive area and the yellow area represents the metal contacts.

For PSCs, the photoactive perovskite layer is generally deposited via spin coating. This deposition technique results in the centre of the substrate having the highest uniformity, with non-uniformity arising at the corners of the substrate where solution builds up during the spin coating process. For this reason the metal contacts were positioned in the centre of the substrate. However, when implementing layout 3.1(b) for ssDSCs, the intricate design of the

metal contacts proved difficult to align with other layers. This led to many devices short circuiting and reproducibility was challenging.

For ssDSCs the photoactive dye-sensitised mesoporous semiconductor is typically deposited via screen printing, which is uniform across the whole deposited area. This eliminates the desire to position the metal contacts in the centre of the device. Therefore, a new layout shown in Figure 3.1(c) was chosen that consists of the photoactive area positioned in 2 stripes along the substrate and a much simpler metal contact arrangement that minimises alignment issues, making device fabrication more reproducible and upscalable.

3.2.2 Electrode patterning

To create the electrical circuit in a solar cell there must be a metal contact on the transparent conductive substrate (the front of the solar cell) and a metal contact on the HTM (the rear of the solar cell). The contacts on the conductive substrate and the HTM collect electrons and holes generated within the cell, respectively. Therefore, it is crucial that the HTM contact must not be touching the conductive substrate, as this will result in the device short circuiting. One approach to manage this is to etch the conductive glass in a specific pattern so there are areas of conductivity for the front electrode and areas of non-conductivity for the rear electrode. The solar cells in this work employ a transparent glass substrate coated with fluorine-doped tin oxide (FTO). Three different methods were tested to etch the FTO; acid etch using etch-resistant tape, acid etch using a wax resist, and laser etching.

In photovoltaics the most common etching method is to chemically etch away the FTO using zinc powder and 2 M solution of hydrochloric acid (HCl). The areas to remain unetched are covered with etch-resistant Scotch tape, which is placed on the substrate by hand. This conventional method has its disadvantages as occasionally HCl and zinc powder can infiltrate underneath the tape edges, as seen in Figure 3.2(a), resulting in non-uniformly etched areas. More importantly, it is time consuming and reproducibility depends upon the accuracy of the researcher. The wax resist method uses the same acid reaction as the conventional method, but instead of using etch-resistant tape that is manually placed down a more reproducible technique is used, where an acid-resistant wax is screen printed onto the substrate using a pre-designed mesh shown in Figure 3.2(b). Although this method would have saved time and

is well-matched for upscaling purposes, in practice this method did not yield the desired results as the wax adhered to the mesh.

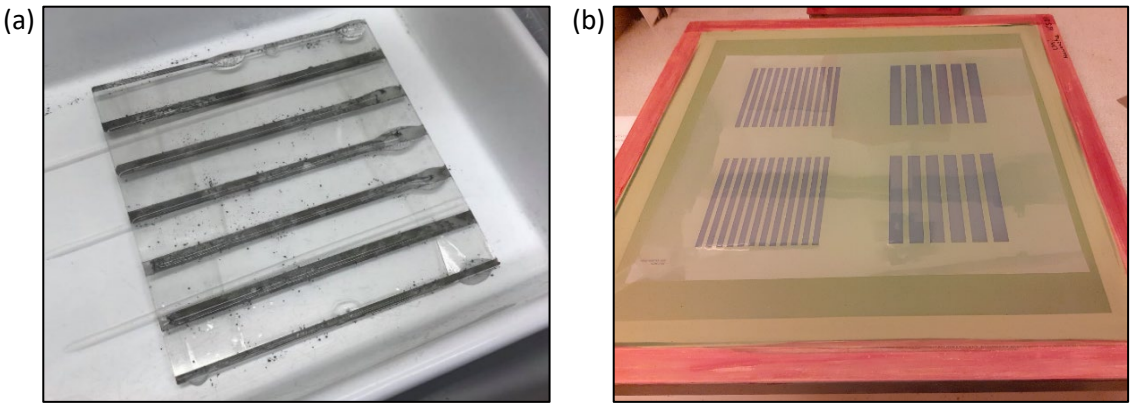

Figure 3.2: Two methods used to chemically etch FTO-coated glass substrates using (a) Scotch tape deposited by hand and (b) wax resist deposited via screen printing mesh. Both methods involve an acid etch using HCl and zinc powder, shown in (a).

The final method tested to etch the electrode pattern was by laser etching using an Ulyxe laser source. High heat from the laser beam melts the conductive material in areas that are pre-defined in the etching pattern sent to the laser system. Different laser parameters were tested such as laser power, frequency, and scan speed. Different filling parameters were also tested such as filling angle, filling interline, and filling direction. Parameters shown in Table 3.1 gave the optimal results for etching the FTO.

Laser Parameters		**Filling Parameters**	
Laser Power:	80%	Interline:	0.04 mm
Frequency:	15 kHz	Angle:	90 degrees
Scan Speed:	500 mm/s	Direction:	Bidirectional
Dot Delay:	5 µs	Outline:	Filling first
Shot Time:	1.5 µs	Tolerance:	0.00 mm
		Fill By:	Object

Table 3.1: Laser and filling parameters used to etch FTO on 3 mm thick glass substrates.

Although screen printing a wax resist would have been compatible with roll-to-roll fabrication, the laser etcher provides a quick etching time of less than 3 min for a 6x6 cm glass substrate, is much less laborious than manually placing down Scotch tape, and is the most reproducible method discussed here since it is an automated technique.

3.3 n-type ssDSC

3.3.1 Spray coating the TiO_2 blocking layer

In n-ssDSCs the HTM and FTO form an ohmic contact, meaning electrons in the FTO and holes in the HTM will recombine at this interface, resulting in an inefficient solar cell. A way to overcome this issue is to deposit a thin, compact, pin-hole free layer of TiO_2 between the FTO and mesoporous TiO_2 to block direct contact between the FTO and HTM. The inclusion of this TiO_2 blocking layer (bl-TiO_2) is essential to avoid short circuiting and loss of current through recombination, yielding a higher current output and device efficiency. Spin coating or spray coating are common methods used to deposit the bl-TiO_2. In this work, spray coating was chosen as the deposition method (Figure 3.3) as it generates thin films with higher uniformity than spin coating and can be automated to enhance reproducibility and scalability.

Obtaining the correct thickness of the bl-TiO_2 is crucial for device performance. If the film is not thick enough, holes from the HTM can pass through and reach the FTO. If the film is too thick, this can hinder electron transport from the mesoporous TiO_2 to the FTO due to inclusion of traps and impurities, which has a negative effect on solar cell performance.[2] For this reason, it is important to find the optimal thickness that is as thin as possible while still effectively blocking holes.

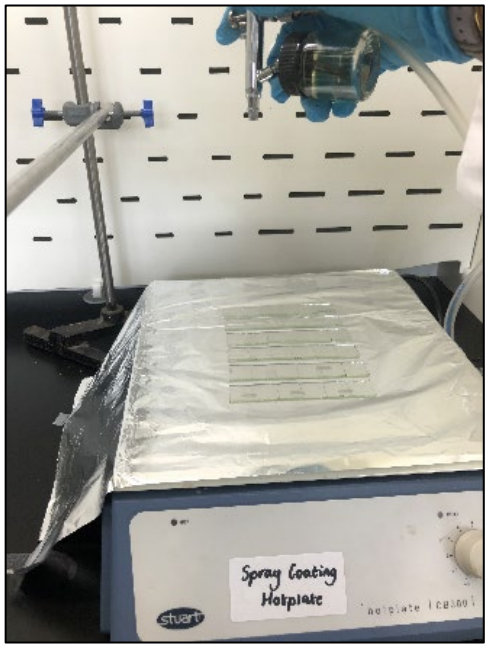

Figure 3.3: Manual spray coating of the TiO_2 blocking layer via an airbrush and N_2 carrier gas.

A series of samples with increasing blocking layer thickness was prepared by varying the number of spraying cycles in the preparation of each TiO_2 blocking layer. In an initial experiment, the distance from the surface of the substrate to the spray nozzle was 18 cm, 1.5 bar N_2 carrier gas was used, and the spray speed was 5 cm s^{-1}. The number of repetitive spraying cycles was varied between 5 and 20, where 5 spraying cycles form the thinnest film and 20 spraying cycles form the thickest.

Cyclic voltammetry (CV) measurements were performed using a three-electrode system in 0.1 M $TBAPF_6$/MeCN with $Fe(C_5H_5)_2$ to see the blocking effect (Figure 3.4). The working electrode was either bare or bl-TiO_2 coated FTO, the counter electrode was Pt wire, and the reference electrode was Ag/$AgNO_3$. The voltammogram obtained from bare FTO shows a quasi-reversible response, suggesting that the redox reaction on $Fe(C_5H_5)_2$ ions is electrochemically reversible and consequently no blocking effect exists. Voltammograms obtained for all samples spray coated with bl-TiO_2 show a decrease in the anodic and cathodic currents with respect to the bare FTO electrode, indicating that some blocking was successful for all samples, even with just 5 spraying cycles. This suggests that the spray coating parameters used to deposit the films needed to be altered to generate thinner bl-TiO_2 films.

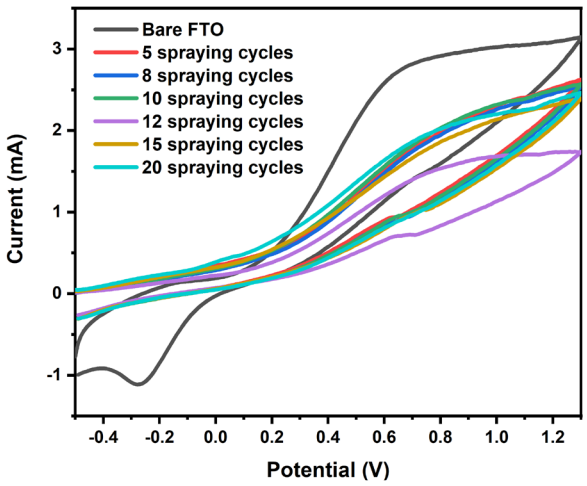

Figure 3.4: Cyclic voltammograms of spray coated TiO_2 films with varying number of spraying cycles, with bare FTO included as a reference. The analyses were recorded at a scan rate of 0.1 V s^{-1} in a 0.1 M $TBAPF_6$/MeCN solution with $Fe(C_5H_5)_2$. Spray coating parameters; carrier gas pressure of 1.5 bar, a spraying height of 18 cm, and spray speed of 5 cm s^{-1}.

Therefore, the spray coating parameters were adjusted so that 1 bar N_2 carrier gas was used with a spray speed of 12 cm s^{-1}, with the distance from substrate surface to nozzle kept at 18 cm. The number of repetitive spraying cycles was varied between 1 and 15, and their resulting voltammograms measured using the same system described previously are shown in Figure 3.5.

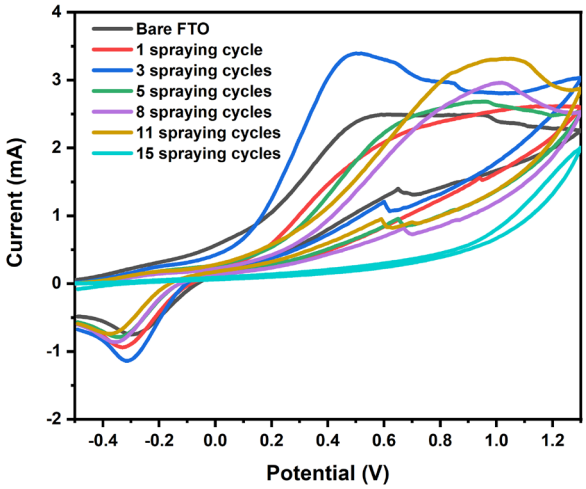

Figure 3.5: Cyclic voltammograms of spray coated TiO_2 films with varying number of spraying cycles, with bare FTO included as a reference. The analyses were recorded at a scan rate of 0.1 V s^{-1} in a 0.1 M $TBAPF_6$/MeCN solution with $Fe(C_5H_5)_2$. Spray coating parameters; carrier gas pressure of 1 bar, a spraying height of 18 cm, and spray speed of 12 cm s^{-1}.

A quasi-reversible response is exhibited for FTO coated with 1-11 spraying cycles, showing that the blocking effect is negligible. However, at 15 spraying cycles this shape disappears and the current is almost completely supressed. This indicates a high density, pinhole-free blocking layer.[3] To confirm this, SEM images were obtained of the FTO coated with 15 spraying cycles of bl-TiO_2, shown in Figure 3.6(b). Bare FTO with irregular grain boundaries forms a rough surface, seen in Figure 3.6(a). When overlayed by the bl-TiO_2 film, the sharpness of FTO grains reduces, becoming slightly blurred. This implies that the film deposited via 15 spraying cycles is extremely thin.[4] Figure 3.6(b) confirms the bl-TiO_2 is thin, and the blocking effect seen in the cyclic voltammogram verifies that it is compact. Therefore, 15 spraying cycles deposited using 1 bar N_2 carrier gas at a spray speed of 12 cm s^{-1} and a spraying height of 18 cm are the optimum conditions to deposit a suitable bl-TiO_2 film.

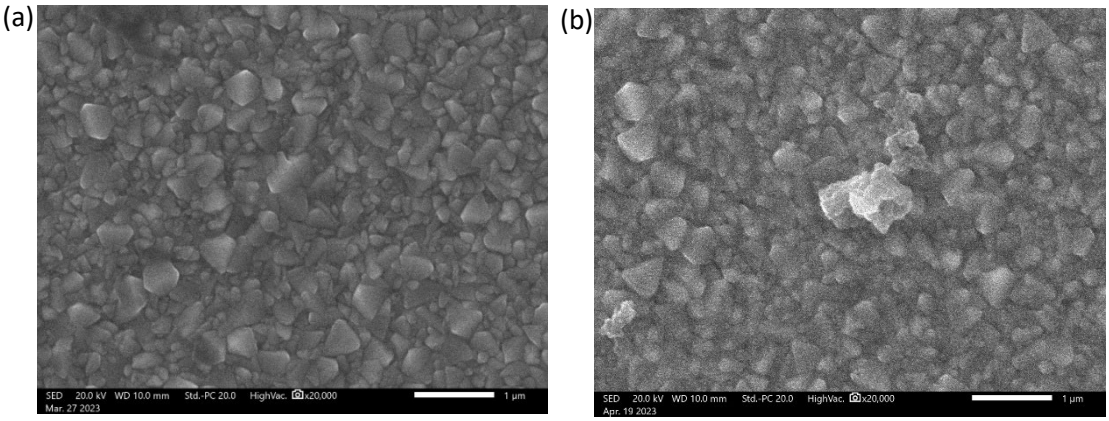

Figure 3.6: SEM topographies of (a) bare FTO, and (b) 15 spraying cycles of bl-TiO_2 on FTO (x20,000).

3.3.2 Deposition of mesoporous TiO_2 film

The mesoporous TiO_2 layer is the most common semiconductor that serves as an electron transport material in n-ssDSCs. Due to its nanocrystalline structure, a high grain-boundary-to-volume ratio provides a large surface area for a monolayer of sensitiser molecules to adsorb onto, enhancing light absorption.[5] The mesoporous TiO_2 (mes-TiO_2) layer is commonly deposited via techniques such as screen printing, doctor blading and spin coating. For this work a highly dispersed titania nanoparticle paste consisting of anatase titania particles of size 15-20 nm was used to deposit a transparent mes-TiO_2 film. Initially, the layout in Figure 3.1(b) was used and the mes-TiO_2 layer was deposited in the centre of the device via doctor blading (Figure 3.7(a)). This involved manually placing Scotch tape on the substrate surface to leave the square active area exposed. Like the conventional etching method mentioned in Section 3.2.2, taping was time consuming and difficult to reproduce. Therefore, a screen printing mesh that employed the layout in Figure 3.1(c) was designed that led to increased reproducibility (Figure 3.7(b)). This method of depositing the mes-TiO_2 allows for scalability and is compatible with roll-to-roll device fabrication.

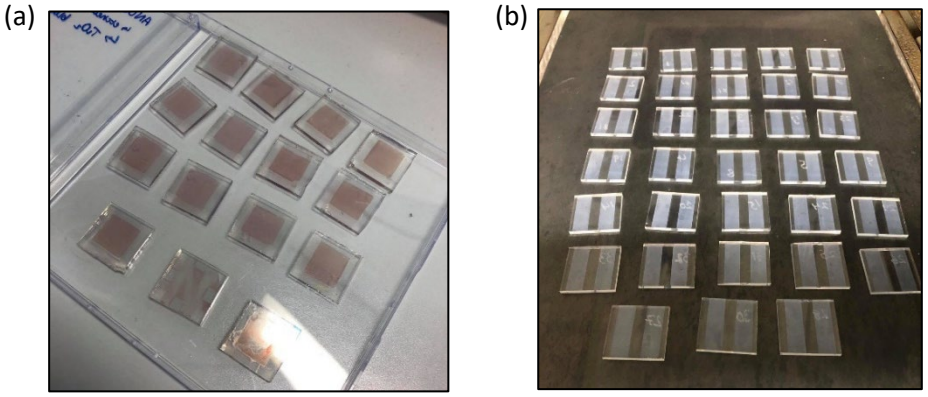

Figure 3.7: Mes-TiO_2 films deposited via (a) doctor blading, and (b) screen printing using the screen printing mesh design (165.31 polyester).

A Dektak^{3}ST profilometer was used to measure the thickness of the screen printed mes-TiO_2 film for a number of samples across the larger screen printed substrate to see whether the deposition was uniform. Table 3.2 shows the thicknesses that were measured.

Sample	1	2	3	4	5	6	7	8	9	10	11
Thickness (µm)	1.82	1.73	1.75	1.96	2.10	1.93	1.99	2.01	2.08	1.96	1.87

Table 3.2: Thickness of screen printed mes-TiO_2 film at different points across the substrate, measured with a Dektak^{3}ST profilometer.

The results in Table 3.2 show that screen printing was relatively uniform, with thicknesses being measured between 1.7-2.1 µm. To enable sufficient pore-filling and low series resistance by the HTM, the optimum TiO_2 thickness for solid-state DSCs is around 2 µm,[6] therefore these results show that screen printing using this mesh was successful in depositing a suitable mes-TiO_2 layer for these devices.

3.3.3 Spiro-OMeTAD HTM optimisation of pore filling

In ssDSCs, a solid charge transport material is used to facilitate the movement of charges between the dye and the counter electrode through inter-molecular hopping processes.[7] In the case of n-ssDSCs this charge is a photogenerated hole. A suitable HTM is one that fills the pores of the mesoscopic scaffold and leaves a solid capping layer on top of the mes-TiO_2 once all solvent has evaporated. Figure 3.8 depicts this process occurring during spin coating, a common technique used to deposit the HTM.

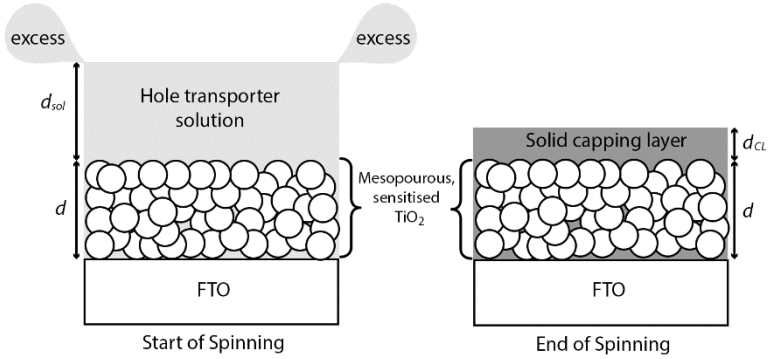

Figure 3.8: Schematic representation of the spin-coating process for depositing a HTM. After evaporation of all solvent, a solid capping layer remains on top of the infiltrated network.

An important factor influencing ssDSC performance is the quality of the pore filling with the HTM as this influences the performance of dye regeneration. A well-filled pore structure increases the coverage of dye with the HTM, which yields a higher charge injection efficiency. As well as this, the average spatial separation between electrons in the TiO_2 and holes in the HTM is increased, slowing down recombination. Finally, the percolation pathway of holes in the HTM is improved, which increases the ambipolar diffusion coefficient for charges in the device.[8] Increasing the concentration of HTM will improve pore filling, however if the concentration is too high this will increase the capping layer thickness and result in a rise in

series resistance. The concentration of HTM at which the pores are optimally filled corresponds to the concentration at which the capping layer starts to form.

Photoinduced absorption spectroscopy (PIA) can be used to investigate the quality of pore filling as it monitors the effectiveness of dye regeneration by recording the spectral shift in absorption upon excitation, which closely matches the absorption spectrum of the oxidised dye species. For this work, the concentration of the HTM Spiro-OMeTAD was varied between 60 and 120 mg ml^{-1} and deposited on separate LEG4-sensitised TiO_2 photoanodes. Figure 3.9 shows the PIA spectra of LEG4/TiO_2 (black line) with the oxidised dye molecules visible at the absorption range between 700 – 800 nm.[9] Upon infiltration of the pores with Spiro-OMeTAD a decrease in absorption intensity is observed. This reveals that the HTM is regenerating the dye as the oxidised dye molecules are quenched. At lower concentrations of HTM (60 – 70 mg ml^{-1}), the decrease in absorption intensity is lower than the that of higher concentrations of HTM (≥ 80 mg ml^{-1}). This indicates that the pores are not optimally filled at lower concentrations.

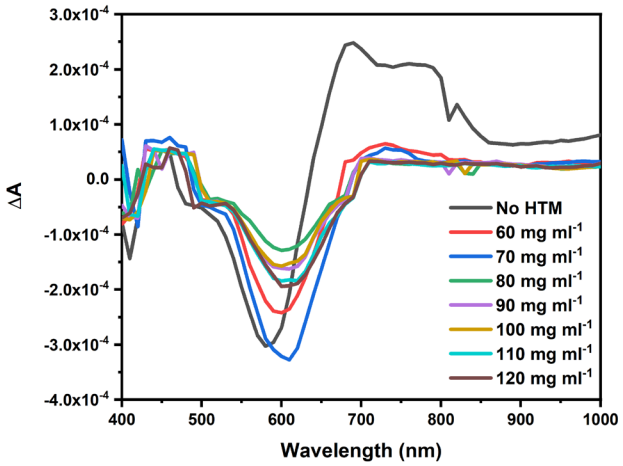

Figure 3.9: Photoinduced absorption spectra of LEG4-sensitised TiO_2 films with varying concentration of Spiro-OMeTAD filling the pores. LiTFSI (25 mM) and tBP (76 mM) additives were included.

In order to see the effect that insufficient pore filling has on device performance, J-V cures were measured for devices with concentrations of Spiro-OMeTAD ranging from 60 to 120 mg ml^{-1}. Figures 3.10 and 3.11 show that when the concentration of Spiro-OMeTAD is varied between 60 and 100 mg ml^{-1}, an increase in J_{SC}, V_{OC} and FF is observed with increasing pore-filling, leading to better device performance. However, at concentrations higher than 100 mg ml^{-1} Spiro-OMeTAD, a reduction in J_{SC} and FF is seen, implying that at 100 mg ml^{-1} the pores are optimally filled and any further increase in concentration of Spiro-OMeTAD will result in a thicker capping layer, leading to resistive losses and a negative impact on device performance.

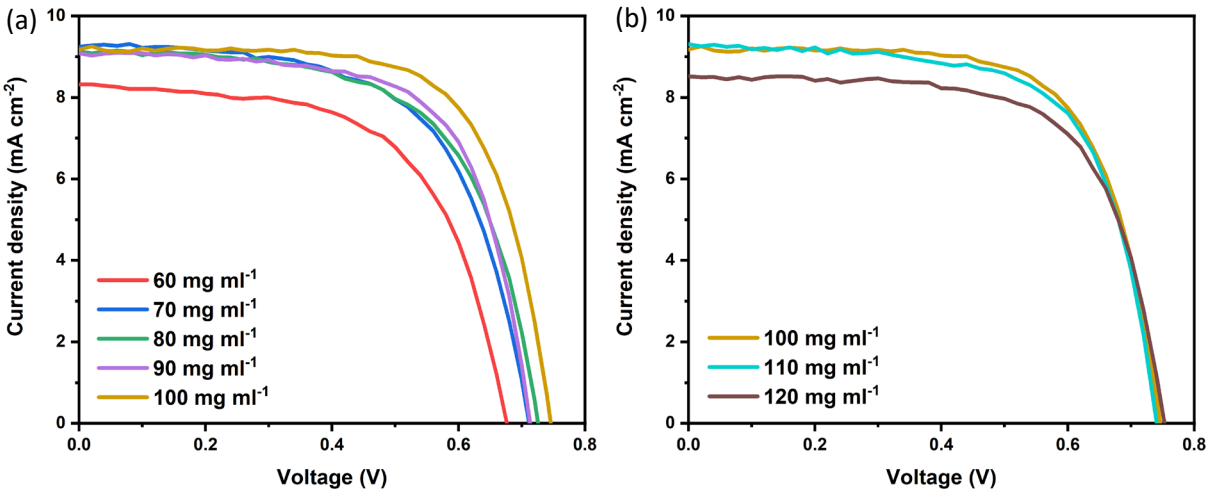

Figure 3.10: J-V curves of champion FTO/TiO_2/LEG4/spiro-OMeTAD/Ag n-ssDSCs fabricated with varying concentrations of spiro-OMeTAD, measured under AM1.5 simulated sun light of 100 mW cm^{-2} irradiance at 0.2 V s^{-1}. The curves have been separated into 2 graphs, (a) concentrations before optimum pore filling, and (b) concentrations after optimum pore filling.

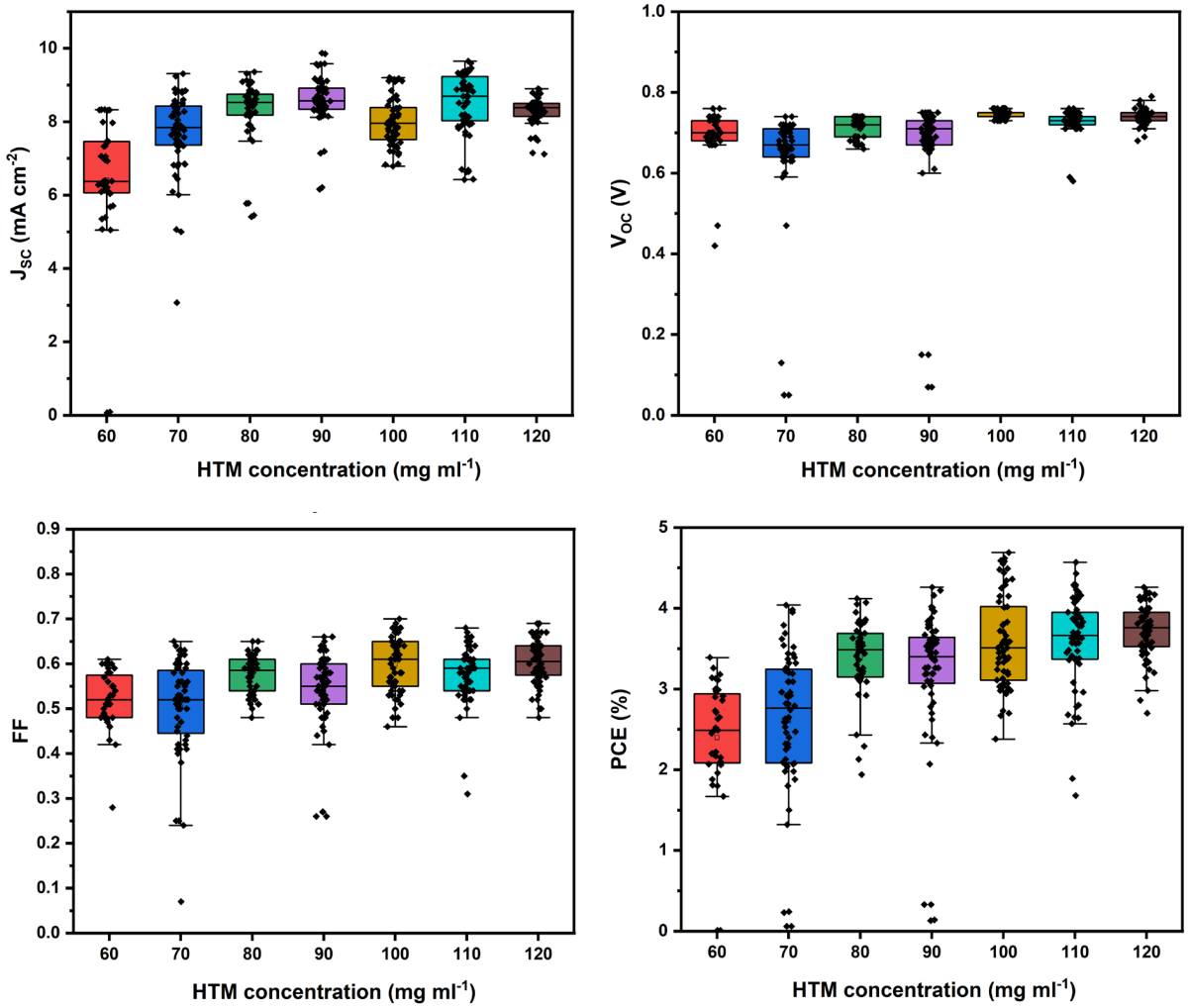

Figure 3.11: Box plots showing J-V characteristics of FTO/TiO_2/LEG4/spiro-OMeTAD/Ag n-ssDSCs fabricated with varying concentrations of spiro-OMeTAD, measured under AM1.5 simulated sun light of 100 mW cm^{-2} irradiance at 0.2 V s^{-1}.

3.4 p-type ssDSC

3.4.1 Deposition of mesoporous NiO film

For all previously reported p-ssDSC, the nanoporous metal oxide used was NiO, the most widely researched p-type semiconductor. Deposition techniques include spin coating[10,11] and screen printing[12] of homemade NiO pastes, and doctor blading of $NiCl_2$ gel.[13] In this section screen printing of a commercial NiO paste is assessed in addition to spin coating and slot-die coating $NiCl_2$ sol gel, and techniques are compared using UV-Vis spectroscopy.

NiO nanoparticle paste is commercially available through Solaronix, where NiO films can be deposited by screen printing and firing at 300°C to form a mesoporous layer of NiO with a semi-transparent grey appearance. Figure 3.12 shows the UV-Vis spectra of screen printed NiO films before and after being submerged in a P1 dye bath overnight.

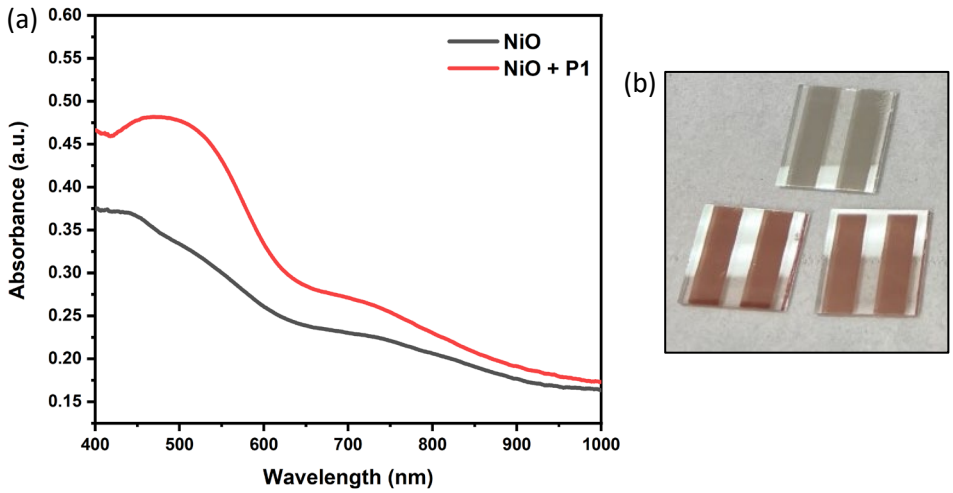

Figure 3.12: (a) UV-Vis spectra of screen printed NiO paste shown in (b), before and after P1 dye loading

After sintering at 300°C, the NiO film exhibited a matte appearance. This indicates scattering due to a large NiO particle size, which explains the relatively low dye adsorption. Therefore, an in-house $NiCl_2$ sol-gel was tested to assess whether increased dye loading could be achieved. Suzuki et al. described a method of synthesising nanoporous NiO films using a series of polyethyleneoxide-polypropyleneoxide-polyethyleneoxide (PEO-PPO-PEO) triblock co-polymers as a template for preparing a nanoporous NiO membrane.[14] They found that particle and pore sizes of the membrane could be adjusted by altering the PEO/PPO ratio. For triblock co-polymer templates with a high PEO/PPO ratio the NiO membrane was formed by the

uniform distribution of NiO nanoparticles with small interparticle voids, which gives a larger surface area for dye adsorption, whereas low PEO/PPO ratio templates resulted in larger interparticle voids and less surface area. High PEO/PPO ratio led to two-fold higher dye-sensitisation IPCE and three-fold higher photocurrent in comparison with low PEO/PPO ratio polymers. In attempt to increase the dye adsorption, a $NiCl_2$ sol-gel was prepared using the polymer templating method described by Suzuki et al.

A preliminary experiment was run to see if the $NiCl_2$ sol-gel could be successfully deposited via spin coating. Both dynamic and static spin coating was tested at 700 rpm, as well as dynamic spin coating at 600 rpm, and the resulting films are seen in Figure 3.13(b). The spectra show that the absorbance of P1 dye at λ_{max} (468 nm) was (0.532-0.314=) 0.218 a.u. for dynamic spin coating at 600 rpm, (0.394-0.268=) 0.126 a.u. for dynamic spin coating at 700 rpm, and (0.438-0.26=) 0.178 a.u. for static spin coating at 700 rpm. This indicates that static spin coating facilitates increased dye adsorption, similarly observed when lowering the spin speed. Nonetheless, Figure 3.13(b) reveals that spin coating $NiCl_2$ sol-gel results in a non-uniform film, suggesting that this deposition technique might not be optimal method to fabricate mesoporous NiO films for p-ssDSCs

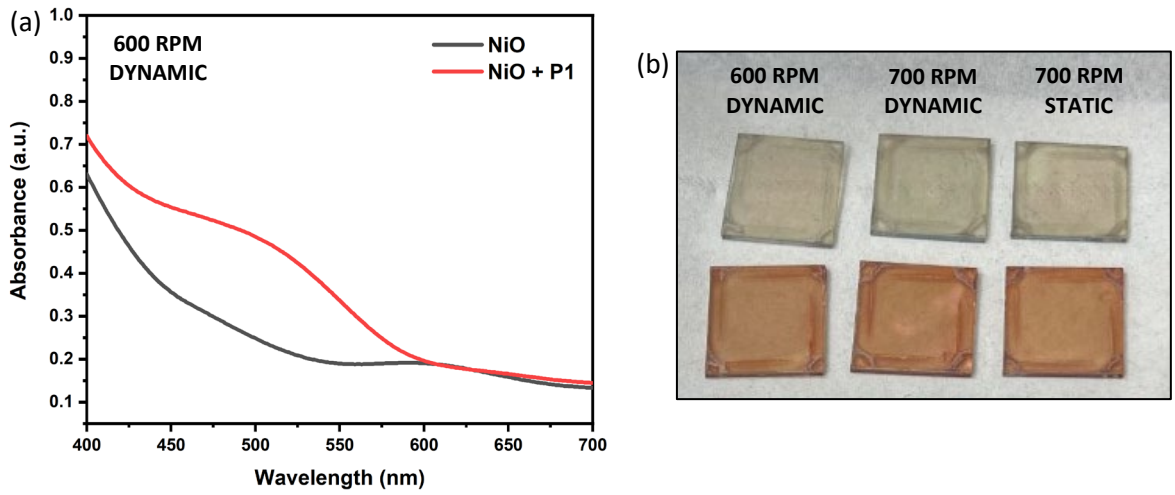

Figure 3.13: (a) UV-Vis spectra of spin coated $NiCl_2$ sol-gel film with the highest dye loading, with and without sensitisation with P1 dye. (b) Spin coated $NiCl_2$ sol-gel films fabricated at different spin coating parameters, before and after dye loading

The next deposition technique assessed was slot-die coating of $NiCl_2$ sol-gel. Slot-die coating offers precise deposition of thin films onto substrates through an automated coating procedure, where the coating speed and dispense rate can be adjusted to control film thickness. A range of coating speeds (1 – 6 mm s^{-1}) and dispense rates (0.145 – 1 µl s^{-1}) were tested. For slower coating speeds and dispense rates, the total volume of sol-gel deposited

was too large that, once sintered, the thick NiO would no longer be adhered to the substrate and flake off. Therefore, the parameters that resulted in the largest absorbance while staying adhered to the substrate was a coating speed of 2.5 mm s^{-1} and a dispense rate of 0.435 µl s^{-1} (Figure 3.14(a)).

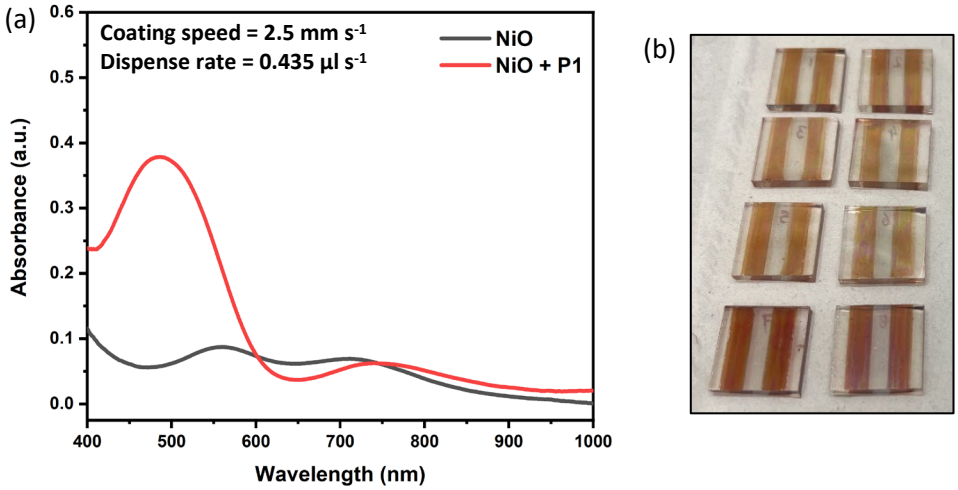

Figure 3.14: (a) UV-Vis spectra of slot-die coated $NiCl_2$ sol-gel film with the highest dye loading, with and without sensitisation with P1 dye. (b) Slot-die coated $NiCl_2$ sol-gel films fabricated at different coating speeds and dispense rates.

Using the same coating speed of 2.5 mm s^{-1} and a dispense rate of 0.435 µl s^{-1}, another layer of NiO was deposited onto the sintered NiO film and the UV-Vis spectra were measured to see how the thickness of NiO film increases dye adsorption (Figure 3.15(a)). The spectra show that the absorbance at λ_{max} for 1 layer of slot-die coated NiO was 0.321 a.u. and for 2 layers of slot-die coated NiO was 0.772 a.u., indicating that slot-die coating 2 layers of $NiCl_2$ sol gel fabricates a mesoporous NiO film that exhibits the largest amount of dye adsorption for increased light absorption.

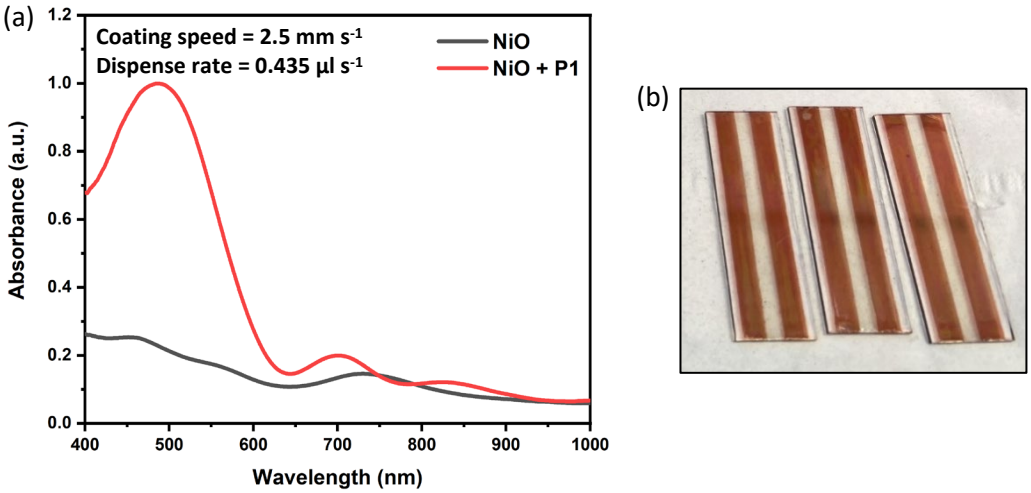

Figure 3.15: (a) UV-Vis spectra of slot-die coated $NiCl_2$ sol-gel film with the highest dye loading, with and without sensitisation with P1 dye. (b) Slot-die coated $NiCl_2$ sol-gel films fabricated at different coating speeds and dispense rates.

References

1 B. E. Hardin, H. J. Snaith and M. D. McGehee, The renaissance of dye-sensitized solar cells, *Nat Photonics*, 2012, **6**, 162–169.

2 B. Peng, G. Jungmann, C. Jäger, D. Haarer, H.-W. Schmidt and M. Thelakkat, Systematic investigation of the role of compact TiO2 layer in solid state dye-sensitized TiO2 solar cells, *Coord Chem Rev*, 2004, **248**, 1479–1489.

3 A. Sangiorgi, R. Bendoni, N. Sangiorgi, A. Sanson and B. Ballarin, Optimized TiO2 blocking layer for dye-sensitized solar cells, *Ceram Int*, 2014, **40**, 10727–10735.

4 T.-S. Su, T.-Y. Hsieh, C.-Y. Hong and T.-C. Wei, Electrodeposited Ultrathin TiO2 Blocking Layers for Efficient Perovskite Solar Cells, *Sci Rep*, 2015, **5**, 16098.

5 C. J. Barbé, F. Arendse, P. Comte, M. Jirousek, F. Lenzmann, V. Shklover and M. Grätzel, Nanocrystalline Titanium Oxide Electrodes for Photovoltaic Applications, *Journal of the American Ceramic Society*, 1997, **80**, 3157–3171.

6 I. Benesperi, H. Michaels and M. Freitag, The researcher's guide to solid-state dye-sensitized solar cells, *J Mater Chem C Mater*, 2018, **6**, 11903–11942.

7 I. Yavuz and K. N. Houk, Mesoscale Ordering and Charge-Transport of Crystalline Spiro-OMeTAD Organic Semiconductors, *The Journal of Physical Chemistry C*, 2017, **121**, 993–999.

8 P. Docampo, A. Hey, S. Guldin, R. Gunning, U. Steiner and H. J. Snaith, Pore Filling of Spiro-OMeTAD in Solid-State Dye-Sensitized Solar Cells Determined Via Optical Reflectometry, *Adv Funct Mater*, 2012, **22**, 5010–5019.

9 P. Liu, B. Xu, K. M. Karlsson, J. Zhang, N. Vlachopoulos, G. Boschloo, L. Sun and L. Kloo, The combination of a new organic D–π–A dye with different organic hole-transport materials for efficient solid-state dye-sensitized solar cells, *J Mater Chem A Mater*, 2015, **3**, 4420–4427.

10 L. Zhang, G. Boschloo, L. Hammarström and H. Tian, Solid state p-type dye-sensitized solar cells: concept, experiment and mechanism, *Physical Chemistry Chemical Physics*, 2016, **18**, 5080–5085.

11 T. T. T. Pham, S. K. Saha, D. Provost, Y. Farré, M. Raissi, Y. Pellegrin, E. Blart, S. Vedraine, B. Ratier, D. Aldakov, F. Odobel and J. Bouclé, Toward Efficient Solid-State p-Type Dye-Sensitized Solar Cells: The Dye Matters, *The Journal of Physical Chemistry C*, 2017, **121**, 129–139.

12 H. Tian, Solid-state p-type dye-sensitized solar cells: progress, potential applications and challenges, *Sustain Energy Fuels*, 2019, **3**, 888–898.

13 L. Tian, J. Föhlinger, P. B. Pati, Z. Zhang, J. Lin, W. Yang, M. Johansson, T. Kubart, J. Sun, G. Boschloo, L. Hammarström and H. Tian, Ultrafast dye regeneration in a core–shell NiO–dye–TiO2 mesoporous film, *Physical Chemistry Chemical Physics*, 2018, **20**, 36–40.

14 S. Sumikura, S. Mori, S. Shimizu, H. Usami and E. Suzuki, Syntheses of NiO nanoporous films using nonionic triblock co-polymer templates and their application to photo-cathodes of p-type dye-sensitized solar cells, *J Photochem Photobiol A Chem*, 2008, **199**, 1–7.

Chapter 4.

Automated Spray Pyrolysis Machine Build

4.1 Introduction

Spray pyrolysis is a thin-film deposition technique that is commonly used in solar cell fabrication to deposit a thin, compact blocking layer. The technique involves the atomisation of a precursor solution into thin droplets that are directed onto a heated substrate (Figure 4.1). The droplets decompose under high temperature and what is left on the substrate is a thin coating of the desired solid material.

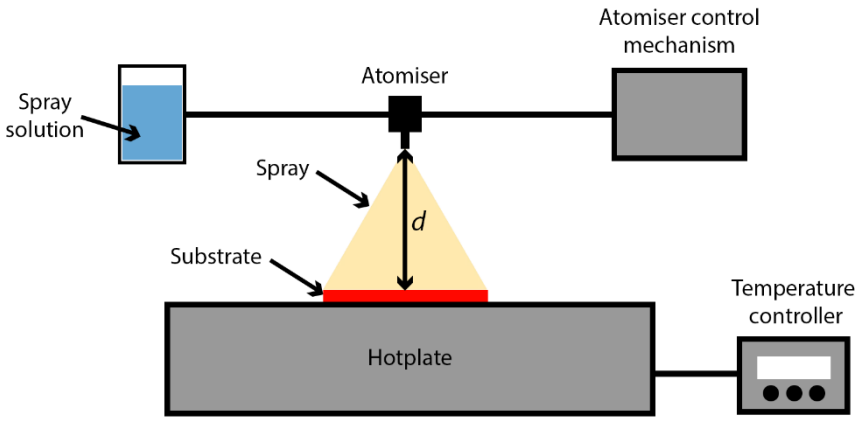

Figure 4.1: Schematic diagram of deposition of a precursor solution via spray pyrolysis.

The way in which the droplets decompose is dependent upon the temperature of the substrate (Figure 4.2). For low temperature depositions, the droplet lands on the substrate and decomposes on the surface. At higher temperature depositions, the solvent within the droplet evaporates during the flight to form a precipitate. The precipitate lands on the substrate, where it decomposes on the surface. At even higher temperatures, after solvent

evaporation the precipitate melts and vaporises mid-flight. The vapour diffuses to the substrate and undergoes chemical vapour deposition onto the surface. At the highest temperatures, before reaching the substrate droplet vaporises to form solid particles.[1] This illustrates that the temperature of the substrate has a great effect on the composition and crystallinity of the film. Consequently, spray pyrolysis is a highly temperature dependent deposition technique.

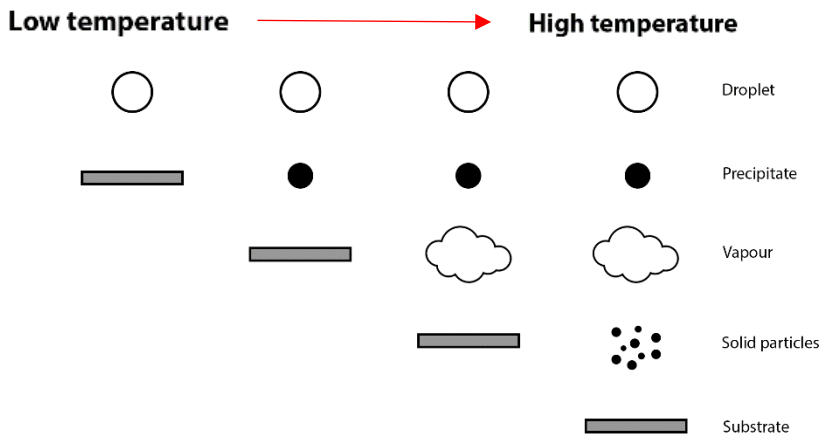

Figure 4.2: Deposition processes that occur at different substrate temperatures, where temperature increases from left to right.

Other key parameters in spray pyrolysis include concentration of precursor solution, spraying rate, carrier gas used and distance from nozzle to substrate. For example, if the distance between the nozzle and the substrate is larger the droplet has more time to undergo the chemical reactions mentioned earlier, thus affecting the characteristics of the thin film. A way in which we can sustain the optimal key parameters and minimise batch-to-batch variation in film characteristics is to automate the spray pyrolysis technique. Automated spray pyrolysis uses advanced instrumentation to control the deposition, thereby reducing variation between batches, as well as between users. A computer-controlled system creates reproducible, uniform films and can also be scaled up to accommodate large-scale production.

There are a number of different atomisers that can be used in spray pyrolysis and the choice of atomiser determines the droplet size and distribution. One example is an ultrasonic frequency atomiser where high-frequency ultrasonic vibrations cause the liquid surface to oscillate to a certain amplitude, which leads to the ejection of tiny droplets. An advantage of ultrasonic spray pyrolysis is that droplet size can be precisely controlled via the ultrasonic amplitude, forming very fine and uniform droplets that result in a highly uniform and homogeneous thin film.

In this work, an automated spray pyrolysis machine that utilises an ultrasonic frequency atomiser was built to perform the thin film deposition of blocking layers in solid-state dye-sensitised solar cells.

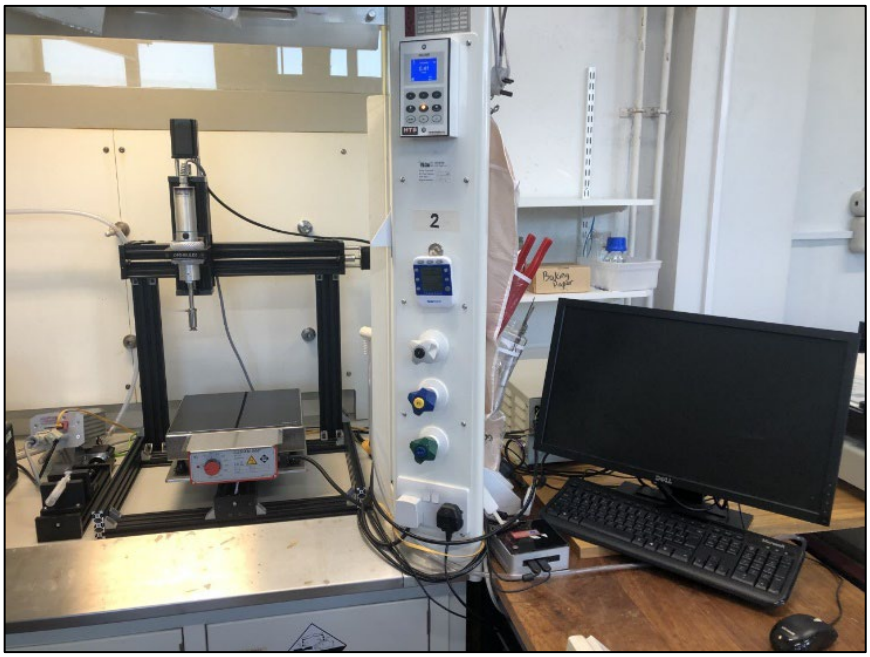

Figure 4.3: Set up of Automated Spray Pyrolysis Machine.

4.2 Construction and Automation

4.2.1. Machine design

The OpenBuilds® C-Beam Machine was chosen to house the spray nozzle and hotplate as it consists of three linear actuators that allow movement along 3 axes; x and y to move the spray nozzle across the hotplate, and z to change the height of the spray nozzle. The machine, as originally purchased, was too short in the z-direction to accommodate the hotplate underneath the spray nozzle with sufficient height for deposition. To address this issue, the four vertical v-slot linear rails of length 250 mm were replaced with longer rails of length 550 mm to raise the height of the spray nozzle. Additionally, the gantry plate in the y-direction was not large enough to accommodate the entire footprint of the hotplate. Therefore, a custom-made gantry plate with a larger area was attached to the existing one.

Three NEMA23 stepper motors are used to move the gantry plates that transport the spray nozzle and hotplate. 4-lead bipolar stepper motors are used over unipolar stepper motors to allow greater torque output to be achieved. An OpenBuilds® BlackBox controller connects the motors with the computer and allows XYZ motion to be controlled using the OpenBuilds® CONTROL software. The machine is powered by a 24V power supply.

A spray head holder was designed, 3D printed and attached to the z axis gantry plate (Figure 4.4). The holder was designed with a cylindrical shape to snugly fit the spray head and featured a gap in the centre of the bottom to accommodate the spray nozzle. The top of the holder was designed as a rectangle to fit over the existing holder that came with the machine, and included two side panels with slots for screws, allowing it to be secured into the pre-existing holes in the original holder. A later design feature was added to the spray head holder; two small holes in the side of the cylinder to allow ventilation from the ventilation holes of the spray head. These holes must remain uncovered to prevent the device from overheating.

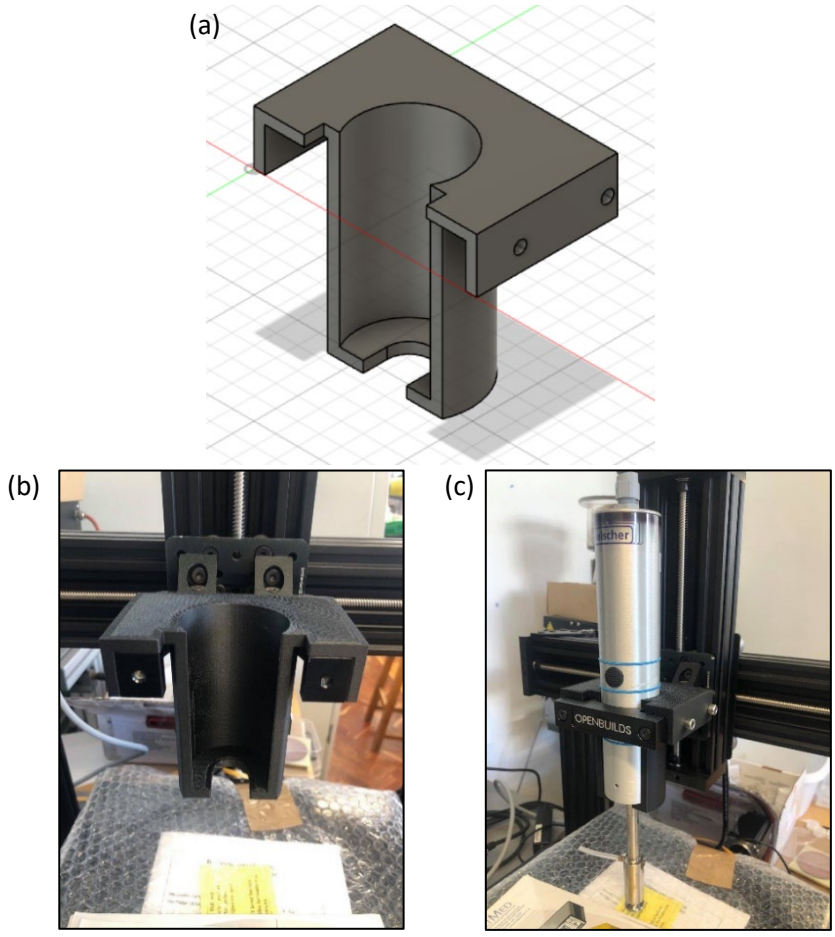

Figure 4.4: (a) Autodesk Fusion 360 design of the spray head holder. Once 3D printed the holder attaches onto the linear actuator, as shown in (b), and secure the spray head in place, shown in (c).

4.2.2. Syringe pump design

A syringe pump was built from a linear actuator to ensure constant flow rate of the precursor solution to the ultrasonic atomiser. A syringe holder (Figure 4.5) was designed, 3D printed and connected to the gantry plate with a NEMA23 stepper motor used to slowly move the syringe plunger into the syringe barrel to create a constant flow. To accommodate various volumes of solution, a variety of syringe holders were designed in different sizes to accommodate 5 ml, 10 ml, 20 ml and 60 ml syringes.

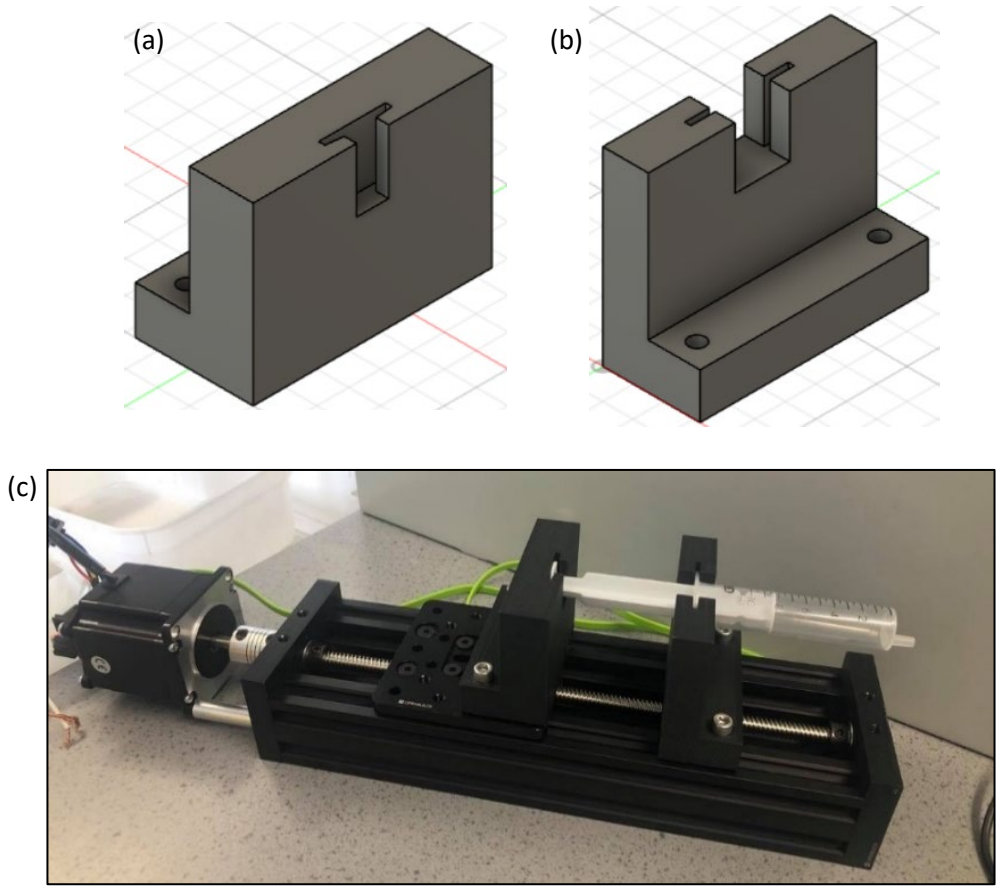

Figure 4.5: Autodesk Fusion 360 designs of the (a) syringe plunger holder and (b) syringe flange holder. Once 3D printed, they attach onto the linear actuator, as shown in (c).

A uStepper S controller with an embedded Arduino platform was used to communicate with the NEMA23 stepper motor. In order to control the embedded platform a LabVIEW programme was written that incorporated LINX virtual instruments, providing a user interface to manage syringe pump parameters such as the acceleration, speed and direction.

4.2.3. Controlling spray distribution

Geometric code (G-code) was written and opened in the OpenBuilds® CONTROL software to instruct the machine motors where to move, at what speed to move, and which path to follow. The machine was instructed to move in straight lines along the x and y axes from given coordinates, as shown in Figure 4.6.

a)

```
G1 F3000 X345.0000 Y0.0000 ;      left to right
G1 F3000 X345.0000 Y65.0000 ;     up
G1 F3000 X0.0000 Y65.0000 ;       right to left
G1 F3000 X0.0000 Y130.0000 ;      up
G1 F3000 X345.0000 Y130.0000 ;    left to right
G1 F3000 X345.0000 Y195.0000 ;    up
G1 F3000 X0.0000 Y195.0000 ;      right to left
G1 F3000 X0.0000 Y0.0000 ;        return to start
```

b)

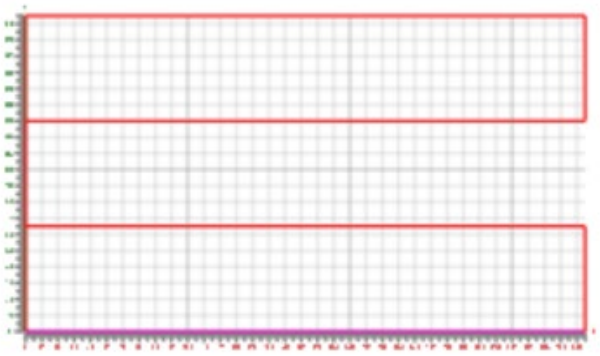

Figure 4.6: (a) G-code written for one spraying cycle, where G1 instructs the machine to move in a straight line, F3000 sets the speed to 3000 mm/min, and X## Y## specifies the end position. (b) The resulting pathway of the spray head (for movement in the X direction) and the hotplate (for movement in the Y direction), where the spraying height is kept constant (in the Z direction).

The x and y coordinates were chosen such that spraying begins to the left of the hotplate and stops to the right of the hotplate, ensuring consistent coverage across the entire surface.

4.2.4. Controlling spray rate and droplet size

A UP200St ultrasonic system consisting of an ultrasonic transducer and generator converts electrical power into mechanical oscillations and transfers these to the S26d18S nebulizer sonotrode. When electrically powered, the ultrasonic processor generates longitudinal mechanical oscillations (reversed piezoelectric action) with a 26 KHz frequency. Adjustment of the processor's power output allows selection of the mechanical amplitude between 20% and 100%. The duty cycle between pause and ultrasonic action can be set from 10% to 100%, which allows pulse operation (10% is 0.1 second of ultrasonic action followed by 0.9 second pause, 100% is continuous operation).

A LAN-interface was set up to enable the monitoring and configuration of all important ultrasonic processor settings via a computer. LabVIEW virtual instruments were written that called on the network IP address specific to the ultrasonic system, which allowed the device to be switched on and off, and for the amplitude and pulse to all be set through a user interface. These virtual instruments were written in a while loop along with the LINX virtual instruments so that the ultrasonic spray and the syringe pump worked in unison. The LabVIEW user interface created to control the spray rate and droplet size is shown in Figure 4.7.

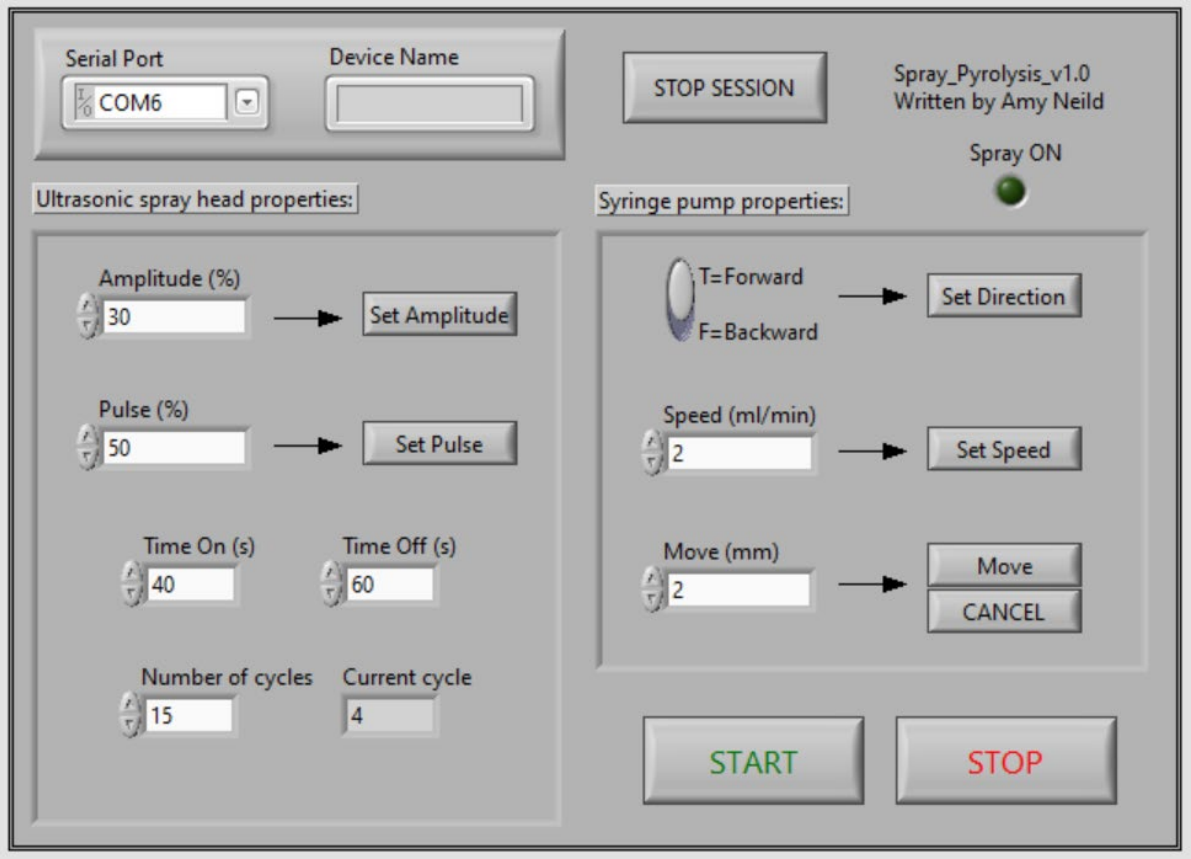

Figure 4.7: LabVIEW programme user interface to control the spray head parameters, syringe pump parameter, and spray cycle parameters.

References

1 E.-K. Oh and S.-G. Kim, Modeling and measurement of aerosol deposition on a heated substrate, *J Aerosol Sci*, 1996, **27**, 1143–1154.

Chapter 5.

Improving the performance of the n-type ssDSC

5.1 Introduction

Interfacial charge transfer plays a pivotal role in solid-state dye-sensitised solar cells (ssDSCs) due to its direct influence on the overall device performance. There are several approaches that can be taken to enhance the processes that occur at each interface within the device in order to improve the charge transfer between various materials within the solar cell structure. Some of the key factors that affect interfacial charge transfer includes light absorption and excitation, injection of electrons into the semiconductor material, transport through the semiconductor and interfacial recombination.

In this chapter, two different approaches to enhancing interfacial charge transfer in n-type ssDSCs will be discussed. The first approach focuses on promoting efficient charge transfer by utilising a fabrication method known as co-sensitisation, which aims to expand the light absorption of the solar cell to increase the density of charge carriers in the device. Absorption spectra of the co-sensitised system are compared with the spectra of single dye systems, and their J-V characteristics are analysed to determine the impact on device performance. The second approach investigates the use of an alternative hole transporting material (HTM) with enhanced conductivity and mobility, as well as improved molecular packing compared with the commonly employed Spiro-OMeTAD HTM. The objective is to improve the flow of holes through the material so that the likelihood of recombination is reduced, thus leading to the more efficient extraction of photogenerated charges.

5.2 Co-sensitisation of LEG4 with L0 and L1

5.2.1 Background

To improve the efficiency of DSCs, researchers have not only investigated novel materials but have also explored innovative methodologies and approaches to utilise existing materials. A main drawback of organic sensitisers is their sharp and narrow absorption bands.[1] One idea that has been proven as a promising approach to combat the partial absorption coverage of the solar spectrum is co-sensitisation of the photoelectrode, a fabrication method that uses two or more different dyes with complementary optical absorption characteristics to produce the DSC working electrode.[2] When two or more different dyes absorb photons in different regions of the solar spectrum the optical absorption of the device is broadened (Figure 5.1), which can lead to more effective power conversion. This was successfully employed in a liquid DSC with the collaborative sensitisation of ADEKA-1 and LEG4, resulting an improvement of the PCE by a factor of 1.3, achieving a 14% PCE.[3]

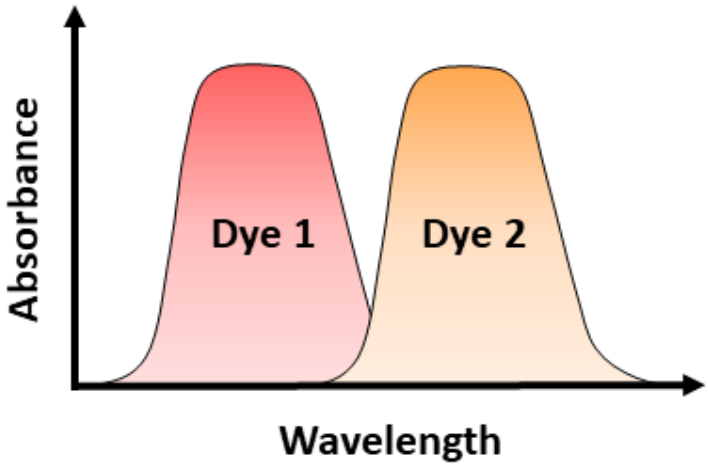

Figure 5.1: Extension of the absorption spectra through co-sensitisation.

As well as extending the absorption spectrum, co-sensitisation can also result in a denser monolayer of dyes[4] (Figure 5.2). This can effectively prevent charge recombination and lead to an increase in V_{OC} of the device.[5] This was observed in ssDSC, where the addition of GBA or ABA as co-adsorbents was shown to inhibit charge transfer from electrons in the TiO_2 conduction band to holes in Spiro-OMeTAD.[6]

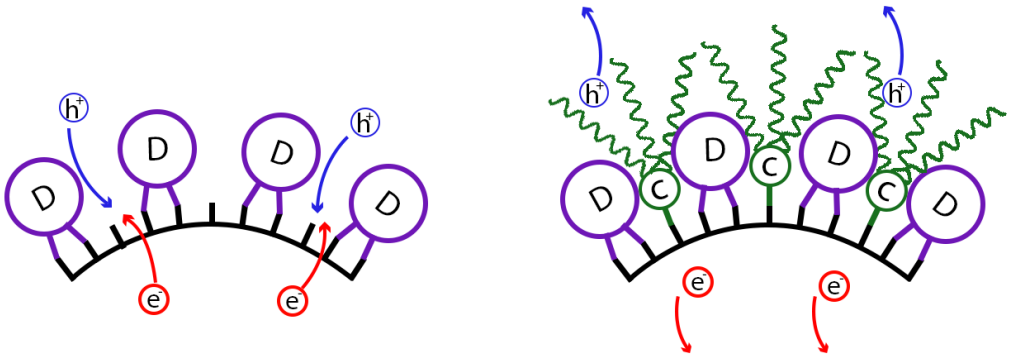

Figure 5.2: Illustration of reduced charge recombination of a co-sensitised TiO_2 surface.

There are two principal techniques for dye co-sensitisation; the cocktail approach and the sequential approach. For the cocktail approach, co-sensitisation occurs in one step through immersing the mesoporous metal semiconductor in a 'cocktail' of two or more dyes, whereas for the sequential approach the mesoporous metal semiconductor surface is sensitised using one dye at a time. The cocktail approach offers the advantage of simplified fabrication, however when sensitisation occurs at the same time unwanted dye competition can occur, meaning one dye may adsorb more favourably onto the semiconductor surface and occupy most of the available anchoring sites. On the other hand, the sequential approach has a more complex fabrication process but offers a high level of control over dye loading, as the order of sensitisation and sensitisation time can be adjusted to modify dye loading for each dye. In this work, the cocktail approach was utilised to co-sensitise mesoporous TiO_2 using LEG4 with either L0 and L1 dyes. The structures of the dyes are shown in Figure 5.3.

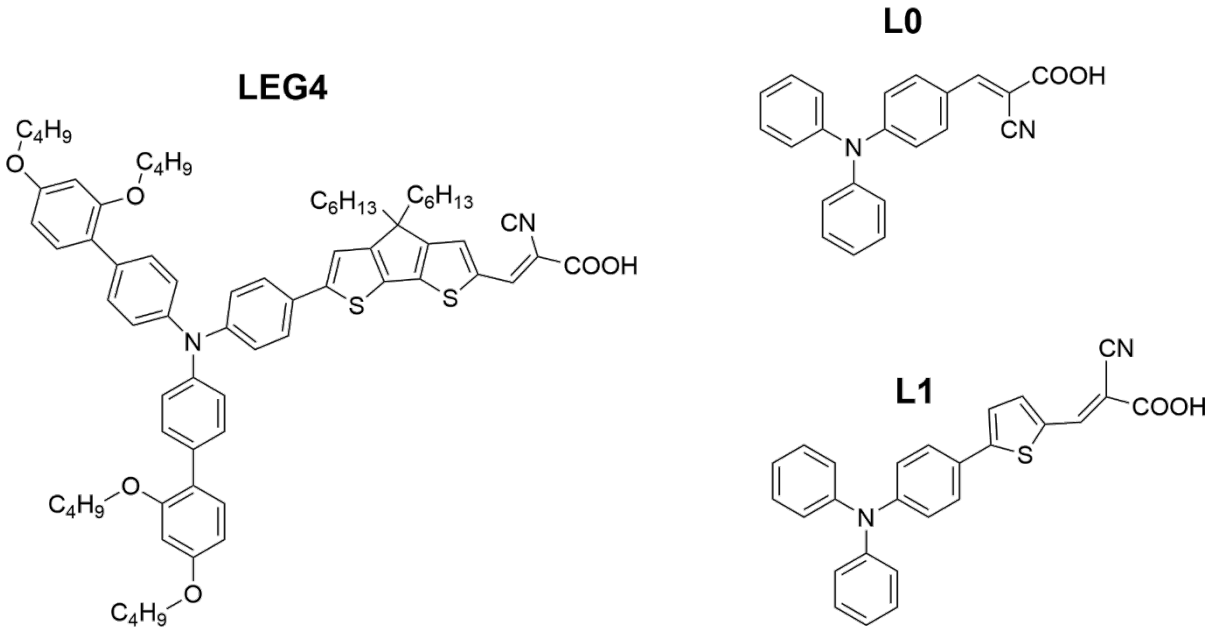

Figure 5.3: Structures of LEG4, L0 and L1 dyes.

As ssDSCs are limited to thin mesoporous metal semiconductor layers due to difficulty surrounding pore filling, donor-(π-linker)-acceptor (D-π-A) dyes with high molar extinction coefficients have been designed to achieve sufficient light harvesting using only a small amount of dye. LEG4 is a carboxy-anchor D-π-A dye that was designed for high photocurrents by extension of the linker fragment. However, long π-conjugation renders elongated and rodlike molecules that tend to form aggregates at the interface of the semiconductor substrate, which results in a lower efficiency.[7] Therefore, it is expected that co-sensitisation of LEG4 with a smaller molecule will not only improve absorption but also fill in any vacant anchoring sites to create a denser monolayer of dye molecules on the surface of the TiO_2 to prevent charge recombination between the TiO_2 and the HTM.

L0 and L1 are small dye molecules that have been reported to have an absorption band in the shorter wavelength region than LEG4. Both dyes form part of a set of dyes with increasing π-conjugation. By increasing the π-conjugation the HOMO and LUMO energy level gap is decreased.[8] By visualising the HOMO and LUMO energy levels in the energy level diagram (Figure 5.4) and comparing to the conduction band of TiO_2, it is clear that a decrease in the HOMO and LUMO energy level gap will lead to a gain in photovoltaic current.[3,8] This is because it becomes easier for electrons to move between these states, promoting a more efficient separation of charge.

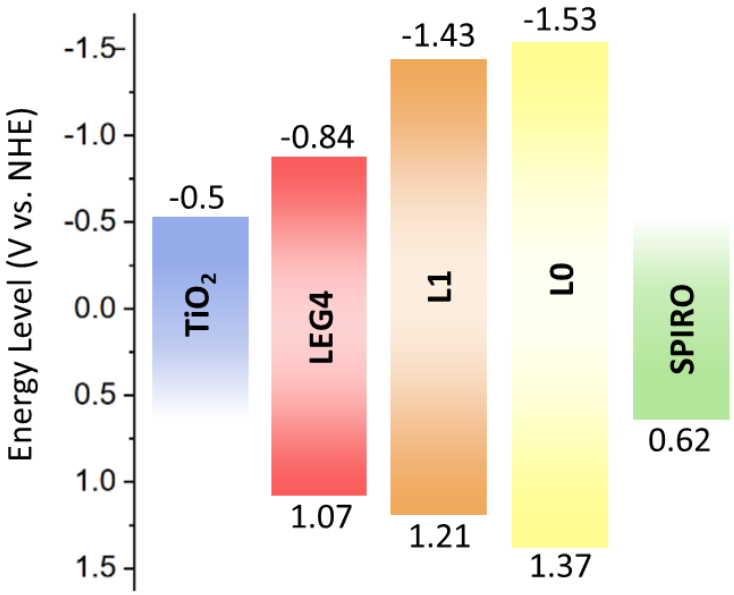

Figure 5.4: Energy level diagram of the components in the n-ssDSC, comparing organic dyes LEG4, L0 and L1. Energy levels for TiO_2, LEG4, L1, L0 and Spiro-OMeTAD were taken directly from literature.

5.2.2 Results and Discussion

Normalised absorption spectra of mesoporous TiO_2 films with each of the three dyes used in this work was measured, using bare mesoporous TiO_2 film as reference (Figure 5.5). The absorption maxima for L0, L1 and LEG4 dyes adsorbed onto TiO_2 films is 406 nm, 427 nm and 475 nm respectively. This is in agreement with literature that reports a redshift in emission spectra upon increasing π-conjugation.[8]

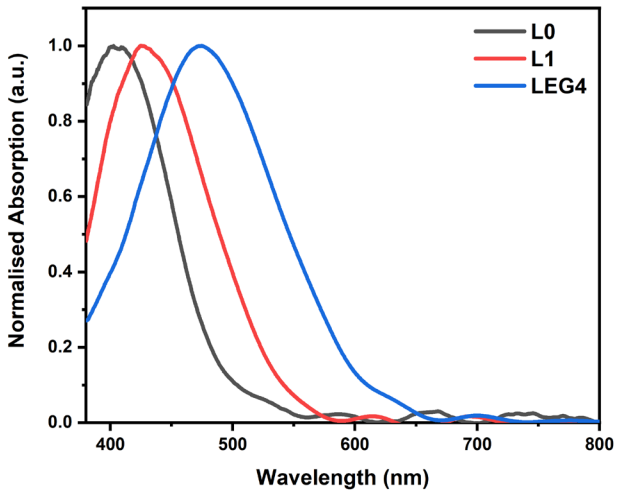

Figure 5.5: Normalised absorption spectra of TiO_2 films with L0, L1 and LEG4 organic dyes employed as sensitisers.

The absorption spectra indicates how co-sensitisation with LEG4 and either L0 or L1 can broaden the absorption spectrum of the solar cell. The absorption maximum for L0 is at a lower wavelength than the absorption maximum for L1. Consequently, for L0 there is a reduced overlap with the absorption spectrum of LEG4. This implies that, when co-sensitised with LEG4, L0 will exhibit a greater enhancement in absorption compared to L1. However, as the cocktail approach to co-sensitisation is used here, how favourable each dye adsorbs onto the mesoporous TiO_2 can affect the absorption of the final device. To account for this, a range of relative concentrations for each co-adsorbent was employed in a series of devices and their absorption spectra and current density-voltage characteristics were compared. Two sets of solar cells were fabricated, the first set containing LEG4:L0 co-sensitised ssDSCs and the second set containing LEG4:L1 co-sensitised ssDSCs. For each set the relative concentration of LEG4:co-adsorbent used was 1:0, 0.75:0.25, 0.5:0.5, 0.25:0.75, 0:1. Figure 5.6 shows the red colour of the LEG4 dye (left) and the yellow colour of the L1 dye (right), and their appearance at each co-sensitised relative concentration on mesoporous TiO_2 films.

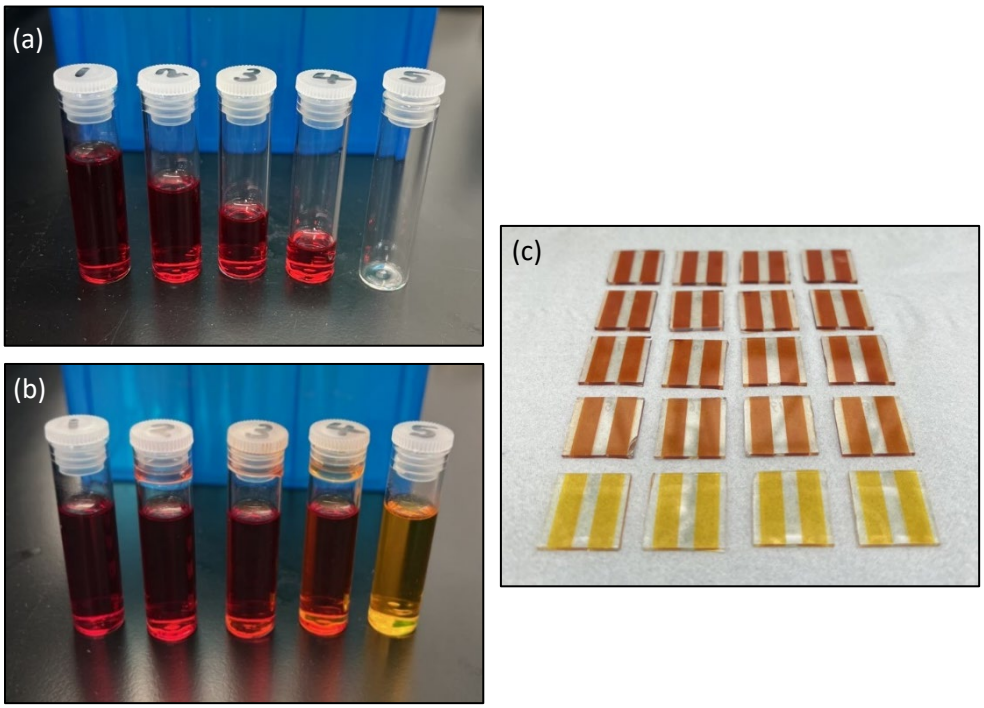

Figure 5.6: Dye baths with (a) varying volumes of LEG4 dye and (b) varying volumes of L1 dye added to LEG4 dye to create co-sensitisers and (c) TiO_2 co-sensitised films of the following concentrations: (1) $LEG4_1$ (2) $LEG4_{0.75}$:$L1_{0.25}$ (3) $LEG4_{0.5}$:$L1_{0.5}$ (4) $LEG4_{0.25}$:$L1_{0.75}$ (5) $L1_1$.

As anticipated, the absorption spectra for co-sensitised devices is broader than that of LEG4, L0 and L1 only, with LEG4:L0 co-sensitised devices extending further than LEG4:L1 devices (Figure 5.7). For both sets of co-sensitised devices the maximum absorbance is reduced upon addition of the co-adsorbent, as well as the absorbance onset shifting to lower wavelengths. This indicates that, rather than only binding to sites unoccupied by LEG4 on the TiO_2 surface, the co-adsorbent attached to sites that LEG4 would have bound to, signifying unwanted dye competition.

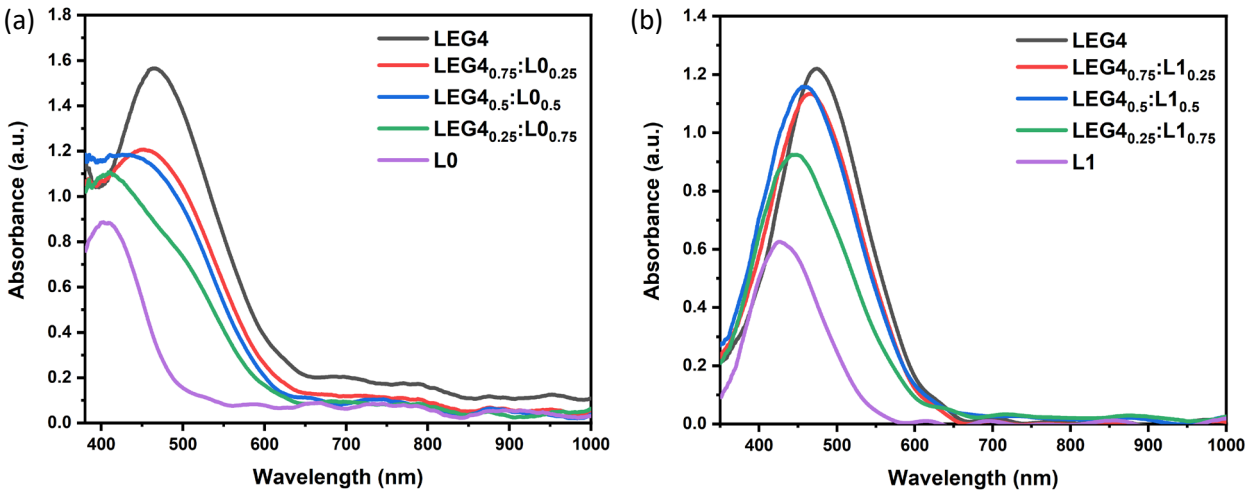

Figure 5.7: Absorption spectra of (a) LEG4, L0 and LEG4:L0 sensitised TiO_2 films and (b) LEG4, L1 and LEG4:L1 sensitised TiO_2 films.

To investigate the effects of co-sensitisation on device performance, J-V characteristics were measured using an AM1.5G and 100 mW cm^{-2} solar simulator, as shown in Figures 5.8 – 5.10.

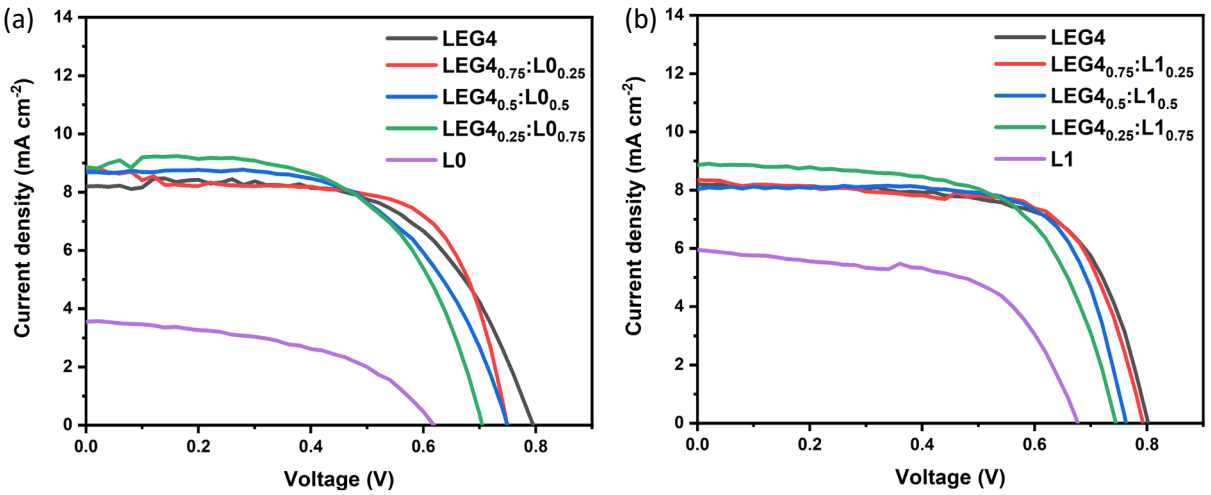

Figure 5.8: J-V curves of champion FTO/TiO_2/dye/Spiro-OMeTAD/Ag n-ssDSCs, where LEG4 is co-sensitised with (a) L0 dye and (b) L1 dye at various relative concentrations, measured under AM1.5 simulated sun light of 100 mW cm^{-2} irradiance at 0.2 V s^{-1}.

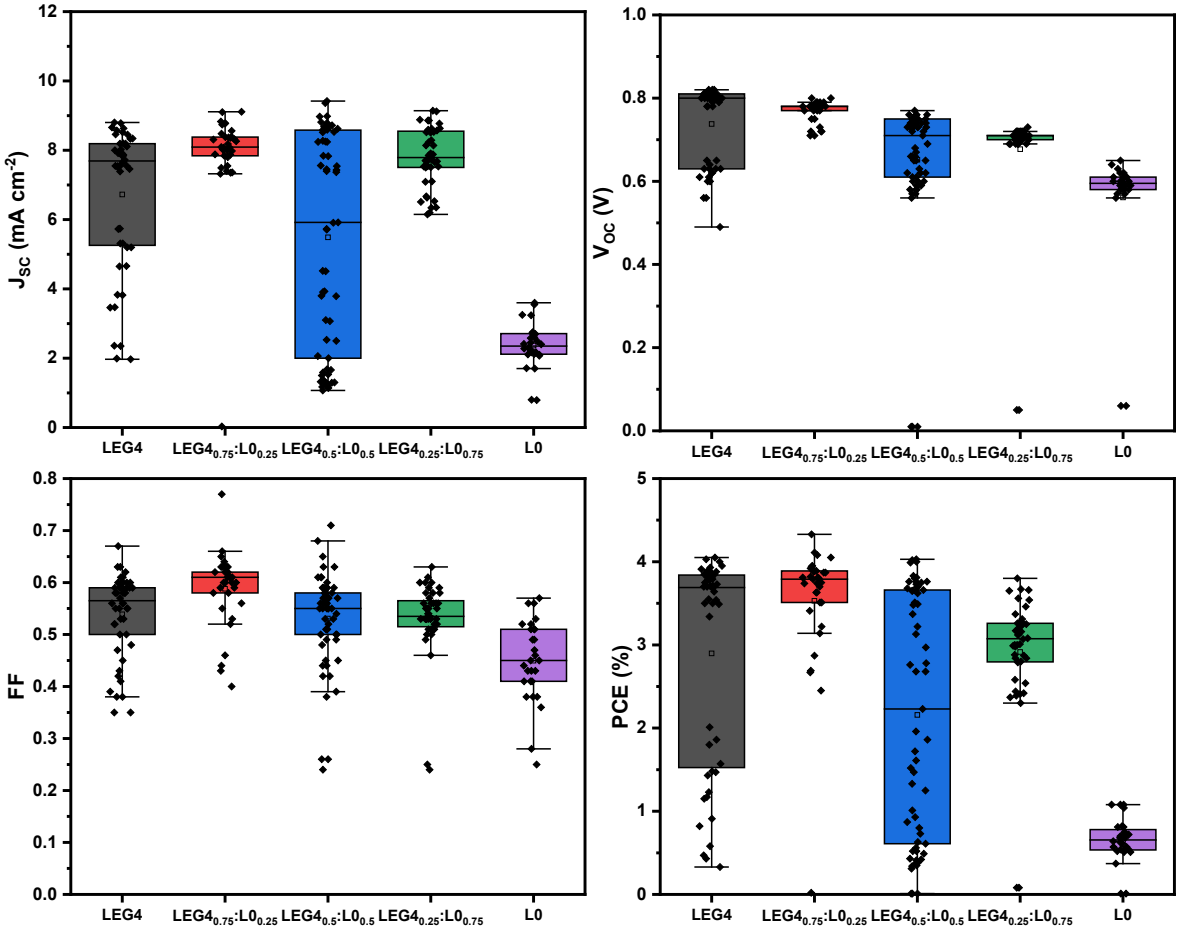

Figure 5.9: Box plots showing the J_{SC}, V_{OC}, FF and PCE of LEG4:L0 co-sensitised TiO_2 based ssDSCs employing Spiro-OMeTAD as the HTM (with 76 mM tBP and 25 mM LiTFSI), measured under AM1.5 simulated sun light of 100 mW cm^{-2} at a scan rate of 0.2 V s^{-1}.

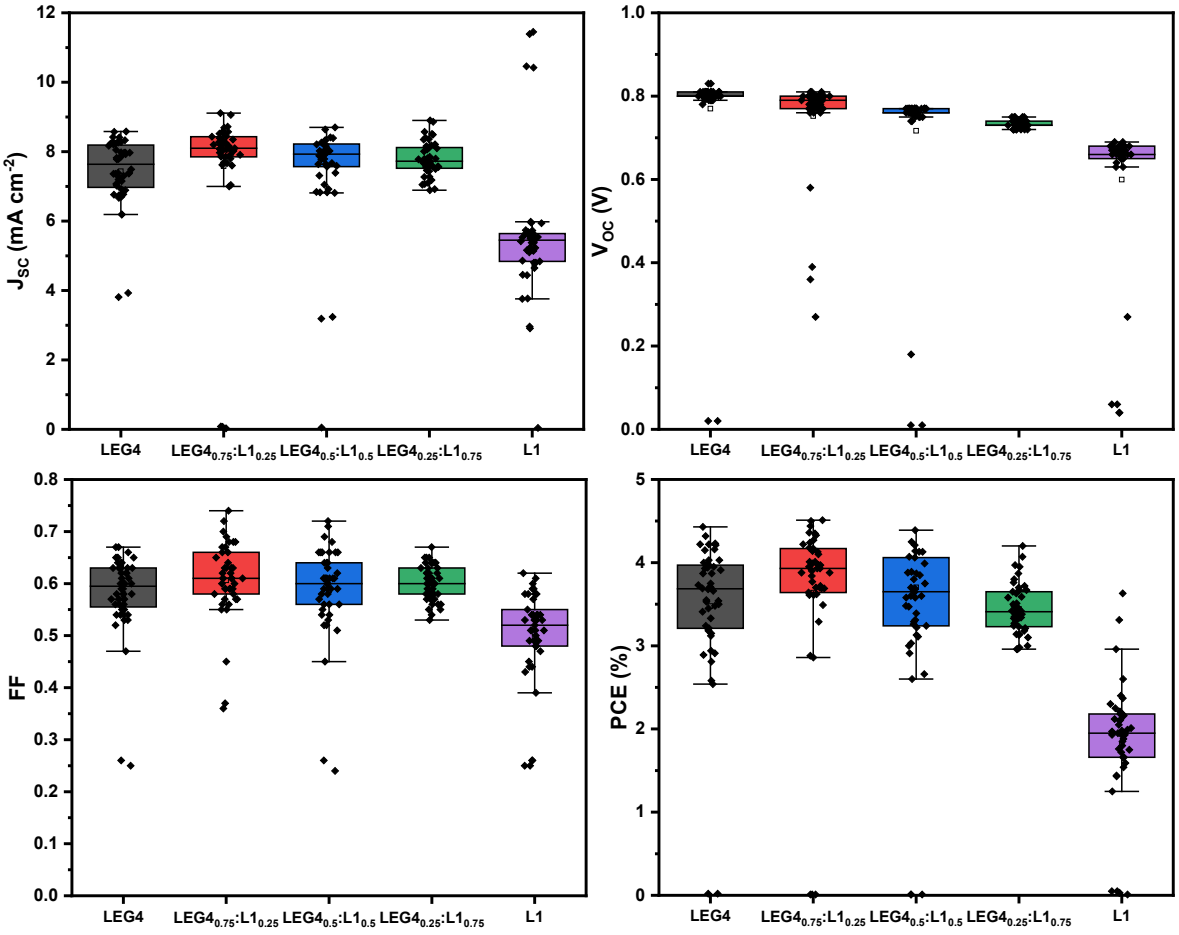

Figure 5.10: Box plots showing the J_{SC}, V_{OC}, FF and PCE of LEG4:L1 co-sensitised TiO_2 based ssDSCs employing Spiro-OMeTAD as the HTM (with 76 mM tBP and 25 mM LiTFSI), measured under AM1.5 simulated sun light of 100 mW cm^{-2} at a scan rate of 0.2 V s^{-1}.

The J-V curves of the champion devices in the two sets of solar cells containing co-sensitised TiO_2 are reported (Figure 5.8). The J_{SC}, V_{OC}, FF and PCE of all devices in each set are shown in Figures 5.9 (LEG4:L0) and 5.10 (LEG4:L1). The J_{SC} is dependent upon the number of photons absorbed by the dye molecules. As mentioned previously, co-sensitisation of LEG4 with L0 or L1 was shown to broaden the absorption spectra and absorb a wider range of photons across the solar spectrum, thus increase the J_{SC}. This is seen in the J-V characteristics as the mean J_{SC} is increased for all but one of the co-sensitised device sets.

For both sets of devices, co-sensitisation results in a lower V_{OC}, and as the concentration of the co-adsorbent (L0 or L1) is increased, the V_{OC} decreases further. The V_{OC} is determined by the difference in potential energy between the Fermi level of the HTM (close to the valence band) and the Fermi level of the TiO_2 (close to the conduction band). The more carriers present in the TiO_2 conduction band, the higher the Fermi level and therefore the higher the V_{OC}. Since co-sensitisation of L0 and L1 with LEG4 has resulted in an increase in J_{SC} but a decrease in V_{OC} these devices must be exhibiting an increase in recombination compared with LEG4 alone.

This is confirmed by the work of Wiberg et al. where the recombination kinetics of L0 and L1 dyes were studied and the results showed ultrafast injection and a following rapid recombination. Recombination rates were also found to increase when adding tBP, which was attributed to an increase in tendency to inject electrons into reactive surface states.[9] This is also reflected in the decrease in FF for L0 and L1 devices, and a reduction in the PCE of co-sensitised devices, as the mean PCE is reduced upon co-sensitisation for all but one ratio of LEG4:co-adsorbent, 0.75:0.25.

For $LEG4_{0.75}$:$L0_{0.25}$ devices, the mean PCE is greater than the individual LEG4 and L0 devices, showing successful co-sensitisation. The same can be said for $LEG4_{0.75}$:$L1_{0.25}$ devices. The two sets of devices were fabricated in separate batches to allow for a range of co-adsorbent concentrations to be tested. Although the highest PCE was achieved from the LEG4:L1 co-sensitisation, the champion PCE only exhibited a 2% enhancement with respect to the PCE of LEG4 alone, whereas for the LEG4:L0 co-sensitisation the champion PCE exhibited a 7% enhancement. Therefore, L0 proved to be a more suitable co-adsorbent for LEG4 compared to L1.

The decrease in PCE for devices with 0.5:0.5 and 0.25:0.75 ratios of LEG4:co-adsorbent indicates unfavourable molecular packing, suggesting that instead of the smaller molecule (co-adsorbent) occupying vacant anchoring sites around LEG4 sensitisation on the TiO_2 surface, at ratios of 0.5 co-adsorbent and above the number of LEG4 molecules adsorbed onto the TiO_2 is reduced, which leads to a negative impact on the device performance. If the sequential approach had been taken, where LEG4 was sensitised first, then a more favourable molecular packing may have been achieved for higher concentrations of coadsorbent.

5.2.3 Conclusion

The co-sensitisation of large organic dye LEG4 with smaller organic dyes L0 or L1 has shown to extend the absorption spectra to lower wavelengths. As the absorption maximum of L0 is further away than that of LEG4 compared with L1, the absorption spectra exhibited less overlap, therefore enhanced broadening. When tested in devices, most co-sensitised devices demonstrate an enhancement in J_{SC} due to improved light absorption, however this comes with a trade-off: a decrease in V_{OC} as a result of recombination losses.

An increase in PCE was only achieved for a 0.75:0.25 ratio of LEG4 to co-adsorbent. This was a result of utilising the cocktail approach, where co-sensitisation occurs in one step through immersion of the films in a 'cocktail' of dyes. This led to unwanted dye competition at larger concentrations of co-adsorbent, where the co-adsorbent occupied more than the optimal number of anchoring sites on the TiO_2 surface. Since LEG4 has a favourable injection efficiency this dye should occupy the most available anchoring sites and the co-adsorbent with less favourable characteristics should 'fill the gaps' to create a denser monolayer of dye for reduced recombination, without having a negative impact on device performance. Therefore, future work should include testing the sequential approach and varying the dipping times in each dye bath to ensure optimal molecular packing. As well as this, the concentration of tBP could also be reduced, as when used in conjunction with L0 and L1 this is thought to cause injection into reactive surface states, leading to an increase in charge recombination.[9]

Overall, L0 outcompeted L1 as a co-adsorbent to LEG4, generating a 7% increase in PCE for the champion device compared with LEG4 alone, whereas the use of L1 as a co-adsorbent only generated a 2% increase in PCE for the champion device. However, optimising the combination of dyes and their interactions with the semiconductor is critical to mitigate the adverse effects on V_{OC} and overall device efficiency.

5.3 Investigating amide-based hole transport material TPABT

5.3.1 Background

The most well known HTM for monolithic solid-state DSCs is the organic material 2,2′,7,7′-tetrakis-(N,N-di-4-methoxyphenylamino)-9,9′-spirobifluorene (Spiro-OMeTAD) (Figure 5.9). However, with spiro-biflourene being an expensive starting material the cost of manufacturing Spiro-OMeTAD is estimated to be ~$90 per gram.[10] This significant contribution to the total device cost, coupled with the complex synthesis, hinders the commercialisation of devices that contain the material. The alternatives that have been published, although compete in performance with Spiro-OMeTAD, are also synthesised in multi-step procedures with extensive product purification.[11] To tackle this issue a new generation of hole transporting materials has surfaced in perovskite solar cells (PSCs) that reach power conversion efficiencies comparable to Spiro-OMeTAD based devices, but are synthesised in a simple, low-cost condensation reaction.[12] This new generation of HTMs introduce a functional amide-based backbone that demonstrate properties such as fast hole injection rate, reduced interfacial recombination, and improved device stability, that can compete with conjugated state-of-the-art HTMs that are currently used in PSCs.

Aromatic amides are being utilized as hole transporting materials due to their ease of manufacture via condensation chemistry. The reactions can be done under ambient conditions, and purification is simple as water is the only side product. As well as this, no expensive metal catalysts are needed, keeping synthesis costs to less than $10 per gram.[10] It is generally believed that amide-bonds that are non-conjugated make poor linkers for the preparation of semiconducting materials, since non-conjugation is said to hinder charge transport.[13] However, bulk materials exhibit enhanced intermolecular interactions due to close molecular packing and good intermolecular orbital overlap. This leads to more satisfactory charge transport properties, which can overcome the loss in charge transport due to non-conjugation.

N^3,N^4-bis(4-(bis(4-methoxyphenyl)amino)phenyl)thiophene-3,4-dicarboxamide (TPABT) is an example of an amide-based small molecule that exhibits improved molecular packing[14] (Figure 5.11). The shorter hole-hopping distance between molecules results in an electrical conductivity of ~10^{-5} S cm^{-1}, whereas Spiro-OMeTAD exhibits a poor conductivity of

~10^{-8} S cm^{-1}.[15] As well as this, TPABT has a higher bandgap therefore more transparent in the visible range of the solar spectrum than Spiro-OMeTAD, which leads to lower parasitic absorption losses.[14] This suggests that TPABT might possess the capability to exceed Spiro-OMeTAD in terms of both performance and cost-effectiveness.

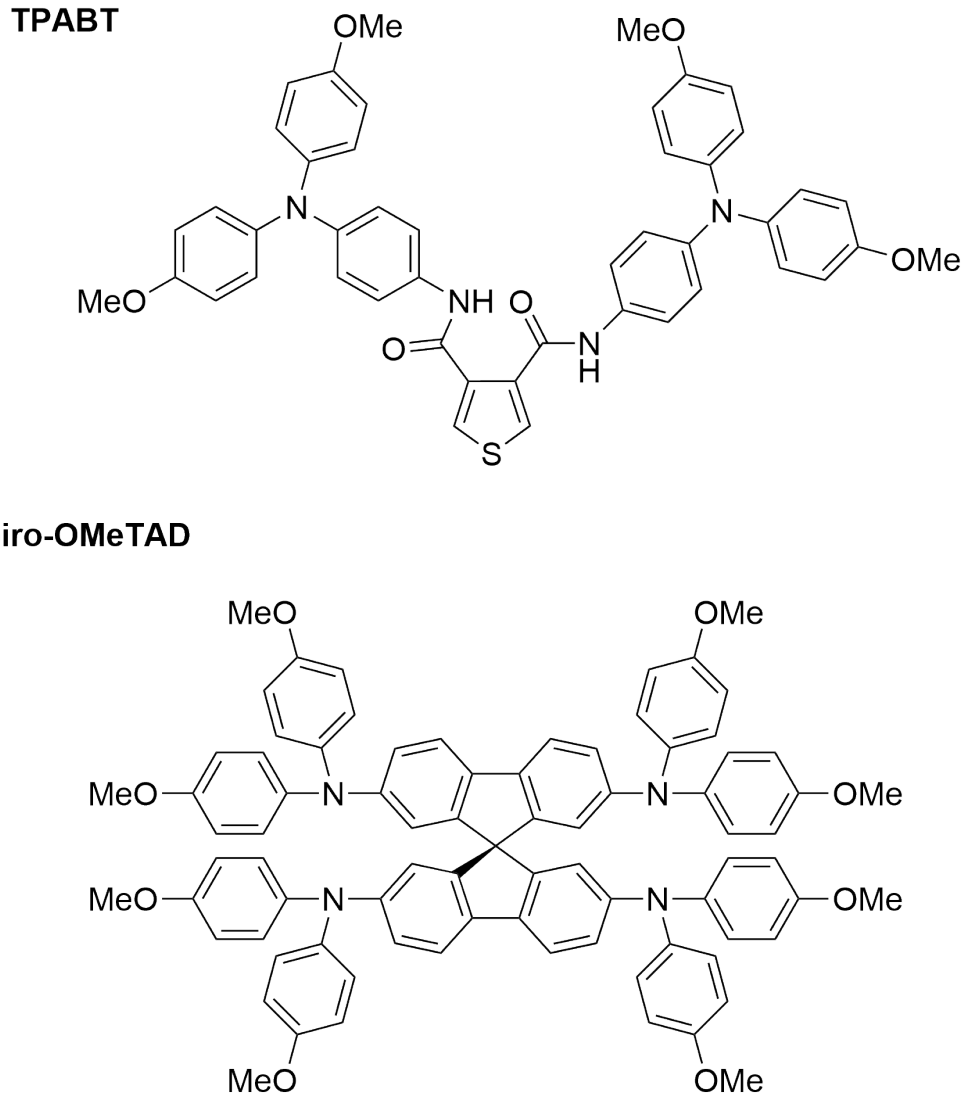

Figure 5.11: Structures of TPABT and Spiro-OMeTAD HTMs.

Several strategies have been used to improve the hole mobility and charge transport properties of HTMs to achieve high performing solar cells. A well-established method that is most widely employed is the inclusion of additives to the HTM. The most common additives used to dope Spiro-OMeTAD are lithium bistrifluoromethanesulfonimidate (LiTFSI) and 4-tertbutylpyridine (tBP) (Figure 5.12). LiTFSI is seen to increase conductivity of Spiro-OMeTAD up to ~10^{-5} S cm^{-1}.[16] This is because Li^+ is an effective p-dopant in the presence of oxygen, facilitating the oxidation of Spiro-OMeTAD. This results in positive charge transfer to the Spiro-

OMeTAD molecules, increasing the hole density in the film. Therefore, holes fill the deepest trap states and enhancement in hole mobility is observed.[17] As well as this, the Fermi level (E_F) shifts towards the HOMO level,[18] promoting efficient hole transport.

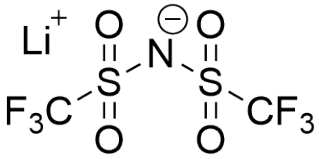

LiTFSI

Lithium bis(trifluoromethane)sulfonimide

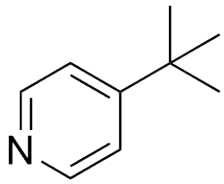

tBP

4-tert-Butylpyridine

Figure 5.12: Structures of LiTFSI and tBP HTM additives.

Upon the addition of LiTFSI to Spiro-OMeTAD there appears to be a concentration gradient of Li^+ ions throughout the HTM.[18] This can mean the interface between the Spiro-OMeTAD/LiTFSI and the counter electrode can be dominated by LiTFSI rather than Spiro-OMeTAD for high concentrations of LiTFSI. To control this gradient other additives can be used in conjunction with LiTFSI, such as tBP. tBP is said to improve the homogeneity of LiTFSI throughout the film, as well as improve the hole collection efficiency at the absorber/HTM interface and improve the steady state performance.[19] As such additives have a dramatic effect on device performance, it is important to ensure the optimal concentration is used.

The aim of this research is to explore the application of the aromatic amide TPABT as a HTM in ssDSCs. TPABT is low cost and the synthesis procedure is simple in comparison to the state-of-the-art HTM Spiro-OMeTAD, both of which are characteristics that can facilitate commercialisation of ssDSCs. This study will focus on how changing the concentration of the additives tBP and LiTFSI to TPABT affects the device performance and dye regeneration, which will be determined via J-V characterisation, UV-Vis, PIA and TAS measurements. In addition to this, a self-attenuation of hysteric behaviour present in the devices will be discussed.

5.3.2 Results and Discussion

To improve the conductivity of TPABT for enhanced PCE a series of devices were fabricated where the concentration of tBP and LiTFSI in TPABT were varied. The initial experiment undertaken varied the concentration of the additives with respect to TPABT but kept the ratio

of the additives tBP:LiTFSI constant. Two ratios of tBP:LiTFSI were investigated; the first was the ratio of tBP:LiTFSI used in Spiro-OMeTAD based ssDSCs in Section 3.3.3 (S), and the second was the ratio of tBP:LiTFSI used in TPABT based PSCs (T).[14] These ratios were 1:0.33 (S) and 1:0.22 (T) of tBP:LiTFSI. The molar concentration of tBP:LiTFSI was increased in uniform multiples from 114:38 mM to 570:190 mM for the S ratio (1:0.33), and from 114:25 mM to 570:125 mM for the T ratio (1:0.22) (Table 5.1). The concentration of TPABT was 50 mg ml^{-1} for all devices, as this is the concentration at which the solubility limit of TPABT is reached.

Units of additive	tBP (mM)	LiTFSI (mM)	Reverse scan PCE (%)	Forward scan PCE (%)
S1	114	38	0.047	0.046
S2	228	76	0.226	0.044
S3	342	114	0.175	0.025
S4	456	152	0.189	0.017
S5	570	190	0.189	0.007
T1	114	25	0.018	0.012
T2	228	50	0.070	0.021
T3	342	75	0.222	0.052
T4	456	100	0.238	0.036
T5	570	125	0.154	0.026

Table 5.1: Molar concentrations of the additives tBP and LiTFSI to 50 mg ml^{-1} TPABT for two sets of samples (S and T, where S = 114:38 mM and uses the tBP:LiTFSI ratio 1:0.33, and T = 114:25 and uses the ratio 1:0.22). PCE for reverse and forward scans are included. Devices were measured under AM1.5 simulated sun light of 100 mW cm^{-2} irradiance at 0.2 V s^{-1}.

J-V scans were taken to investigate the effect of varying the concentration of additives to TPABT on the device performance. Forward bias to short-circuit (reverse) and short-circuit to forward bias (forward) scans yielded highly different results (Figure 5.13). When scan direction influences the shape of a J-V curve this is known as hysteresis.[20] It was found that increasing the concentration of additives to TPABT has a significant influence on hysteresis; hysteresis seems to intensify with an increase in additives. It should be noted that for devices S3-S5 and T4-T5 (where LiTFSI concentration is above 76 mM) the FF for reverse scans is above 1. These curves in specific exhibit an unusual shape after a certain reduction in applied voltage. Instead of the current beginning to plateau after maximum current has been reached (as observed in a typical J-V curve) the current experiences a steep decline and then starts to plateau. A similar observation is evident for S2 and T3, when LiTFSI molar concentration is 76 mM and 75 mM respectively. However, the decrease in current happens at a much lower applied voltage and no plateau is observed. It is clear that the higher the concentration of additives, the higher the applied voltage is at which the current begins to reduce. For forward scans, all resemble typical J-V curves except for S2 and T3. For these devices, at low applied voltages the opposite to

their corresponding reverse scan is seen, where the current experiences a steep decline as the voltage is increased.

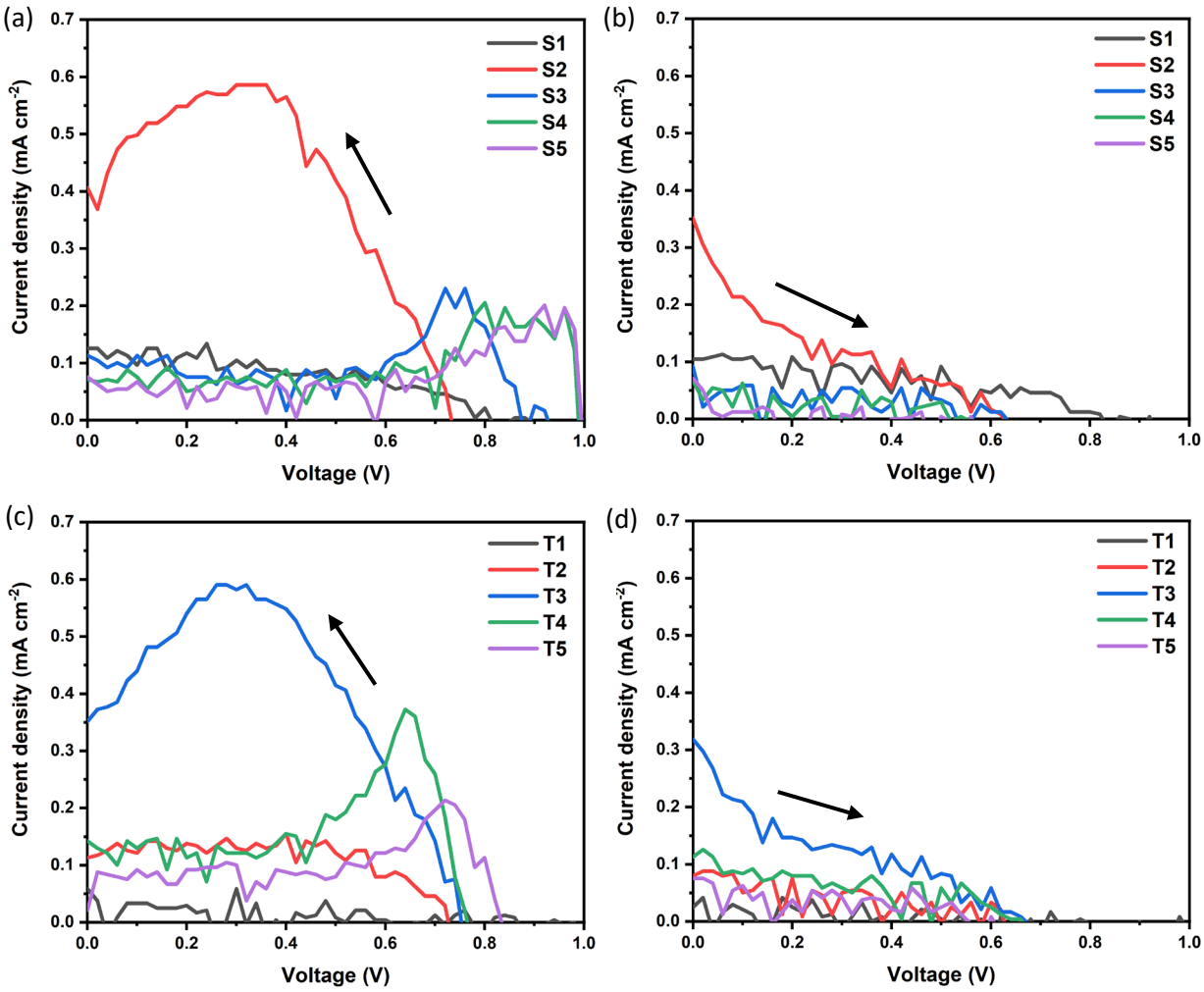

Figure 5.13: J-V curves showing (a) reverse scans and (b) forward scans for champion devices from sample set S, and (c) reverse scans and (d) forward scans for champion devices from sample set T. Both sets contain 5 samples with increasing concentration of tBP and LiTFSI additives to TPABT, where set S has a 1:0.33 ratio and set T has a 1:0.22 ratio of tBP:LiTFSI (see Table 5.3 for exact concentrations). Devices were measured under AM1.5 simulated sun light of 100 mW cm^{-2} irradiance at 0.2 V s^{-1}.

These devices exhibit a sufficient V_{OC} but suffer from low $J_{SC,}$ FF and PCE. This could be due to low electron injection into the conduction band of the TiO_2, poor hole extraction from the dye to TPABT, or poor conductivity of TPABT. It is evident that LiTFSI has a greater effect on solar cell performance compared with tBP, as S2 and T3 devices yielded similar J-V curves and output efficiency even though the latter has an additional 114 mM tBP. Therefore, to investigate the effects of LiTFSI alone another experiment was undertaken, this time keeping the concentration of tBP constant. The concentration of tBP was kept at 76 mM for all devices to keep consistent with the concentration used in ssDSCs employing Spiro-OMeTAD as a HTM in Section 3.3.3. Additionally, a lower concentration of tBP could reduce the conduction band

edge of the TiO_2, therefore increase electron injection into the mesoporous scaffold.[19] The concentration of LiTFSI was varied between 25 mM and 100 mM and their J-V characteristics were measured (Figure 5.14).

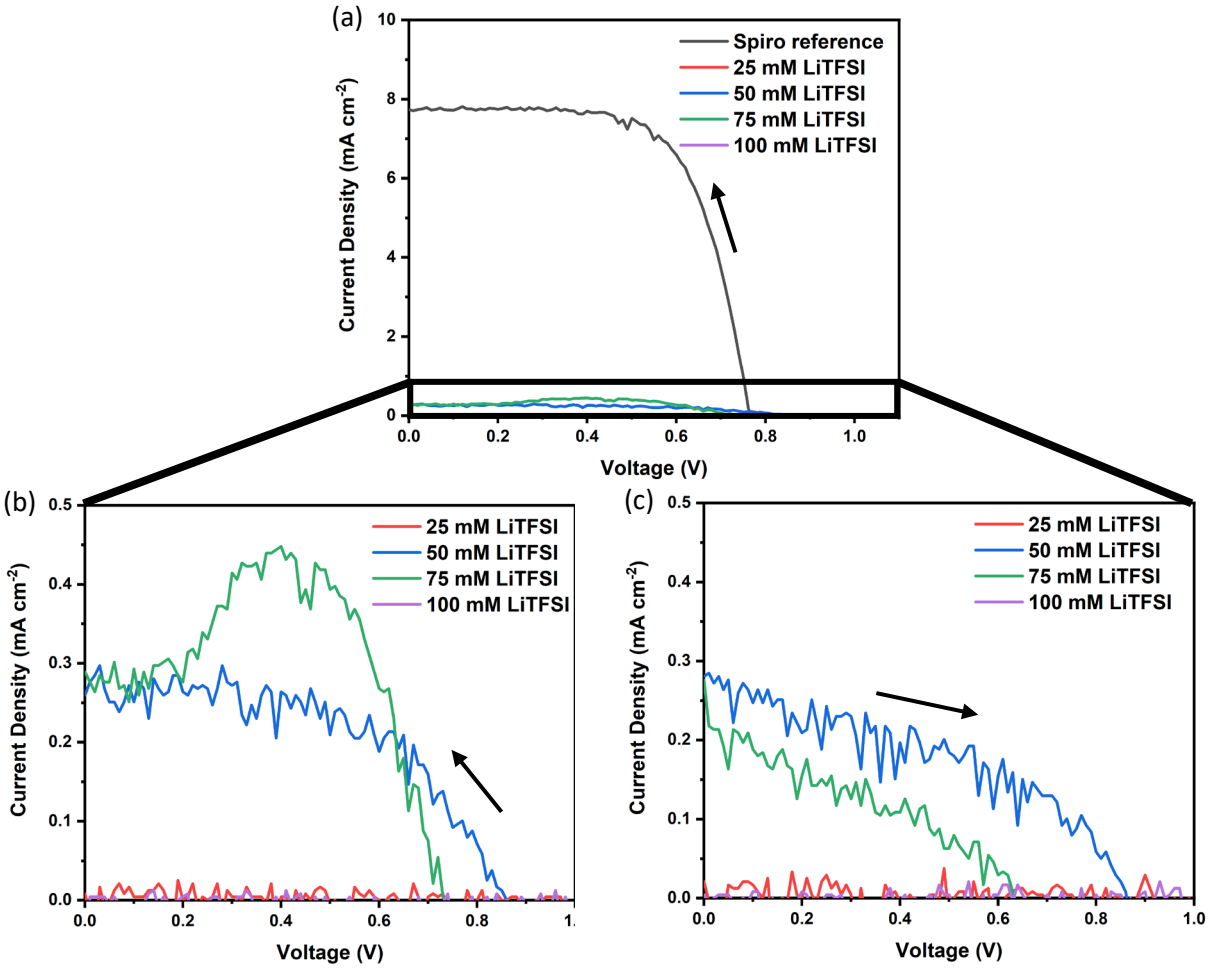

Figure 5.14: J-V curves of champion devices showing (a) reverse scans of all devices, (b) reverse scans of TPABT devices only, and (c) forward scans of TPABT devices only, with varying LiTFSI concentration to 50 mg ml^{-1} TPABT, keeping tBP concentration constant to 76 mM. A reference device employing a 100 mg ml^{-1} Spiro-OMeTAD HTM with 25 mM LiTFSI and 76 mM tBP is shown. Devices were measured under AM1.5 simulated sun light of 100 mW cm^{-2} irradiance at 0.1 V s^{-1}.

For devices containing LiTFSI concentrations of 25 mM and 100 mM there is no photocurrent generated and no output J-V curve is observed. For 25 mM LiTFSI, there is insufficient p-doping and for 100 mM there is likely an excess of p-doping; an abundance of holes could act as a recombination centre for photo-generated electrons, which would lead to the loss of charge carriers.[21] When the concentration of LiTFSI is 50 mM the output J-V curve displays little hysteresis. However, for 75 mM significant hysteresis is observed, which follows the same trend observed in the previous batch (Figure 5.13); the J-V curves exhibit a consistent shape for 76 mM, 228 mM and 342 mM of tBP when the molar concentration of LiTFSI is ~ 75 mM. As the LiTFSI molar concentration is increased from 50 mM to 75 mM, the maximum current

density measured is enhanced. This is due to an increase in hole mobility which can be attributed to a greater reduction in the barrier height for charge hopping between TPA units.[14] A decrease in V_{OC} is also observed with increasing molar concentration of LiTFSI, where Spiro-OMeTAD devices containing 25 mM LiTFSI exhibits the highest V_{OC} and TPABT devices containing 75 mM exhibits the lowest V_{OC} out of the working devices, which may be due to a shift in the TiO_2 energy levels due to more Li^+ ions.

Upon remeasuring the J-V characteristics of the same solar cells after 3 months of being stored in a desiccator (Figure 5.15), the J_{SC} of the Spiro-OMeTAD reference device decreased from 7.73 mA cm^{-2} to 3.70 mA cm^{-2} due to degradation. Furthermore, the V_{OC} increased from 0.76 V to 0.89 V. This indicates oxygen-induced degradation that can be ascribed to the creation of $O2^{-\bullet}$ at the TiO_2 surface, leading to an upward shift of the TiO_2 conduction band thus an increase in cell voltage.[22] On the other hand, the J_{SC} of the TPABT device containing 75 mM

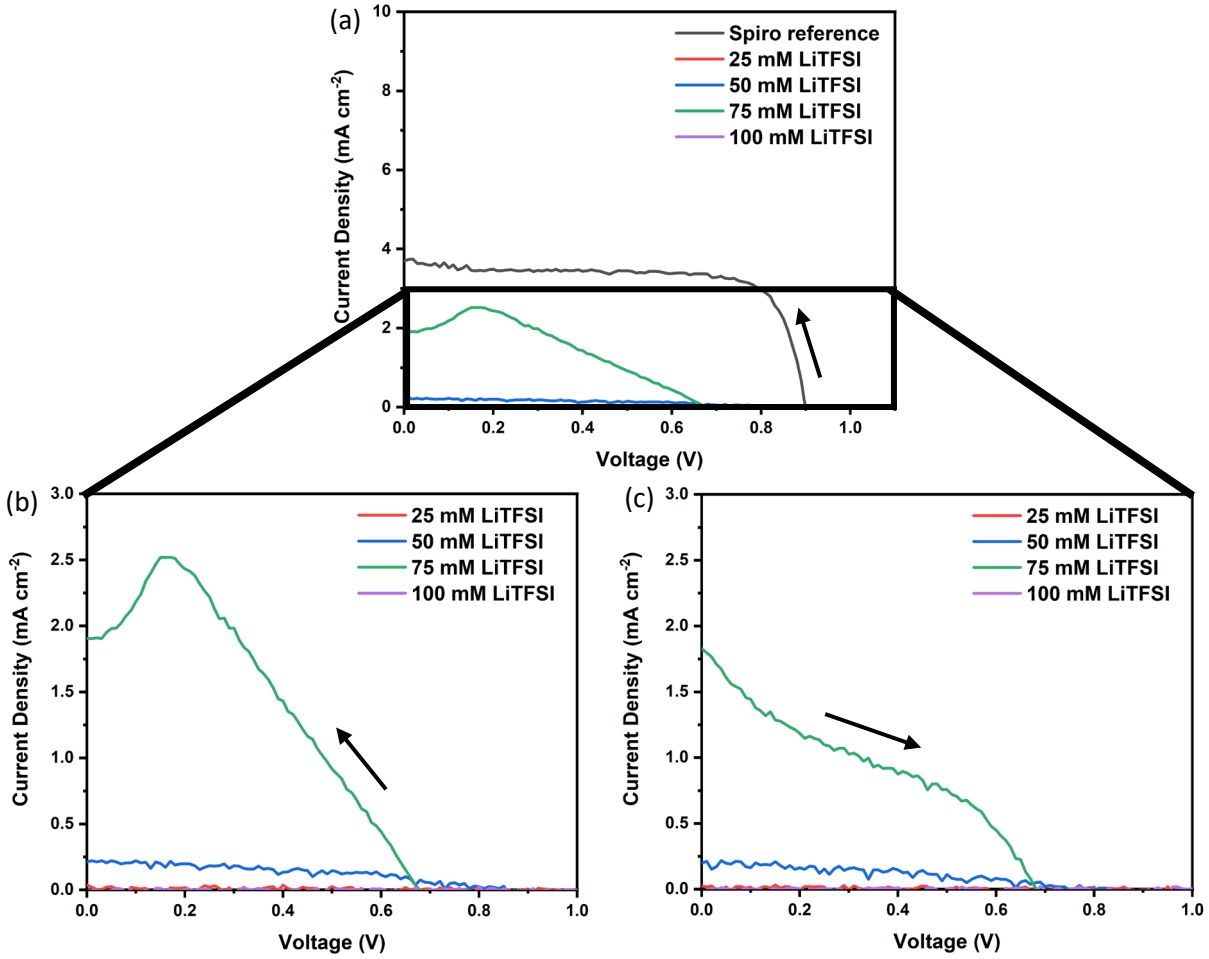

Figure 5.15: J-V curves of champion devices shown in Figure 5.12, 3 months after device fabrication, showing (a) reverse scans of all devices, (b) reverse scans of TPABT devices only, and (c) forward scans of TPABT devices only, with varying LiTFSI concentration to 50 mg ml^{-1} TPABT, keeping tBP concentration constant to 76 mM. A reference device employing a 100 mg ml^{-1} Spiro-OMeTAD HTM with 25 mM LiTFSI and 76 mM tBP is shown. Devices were measured under AM1.5 simulated sun light of 100 mW cm^{-2} irradiance at 0.1 V s^{-1}.

LiTFSI increased from 0.29 mA cm^{-2} to 1.90 mA cm^{-2}, whereas the V_{OC} only slightly decreased from 0.73 V to 0.68 V. This indicates that the oxidation time for Spiro-OMeTAD-based ssDSCs and TPABT-based ssDSCs differs, which could be due to the closer packing of TPABT molecules requiring more time for oxygen to penetrate through the HTM. This is supported by PIA measurements (Figure 5.16) of devices in Table 5.3, where sample series S was measured 3 days after device fabrication and sample series T was measured 23 days after device fabrication.

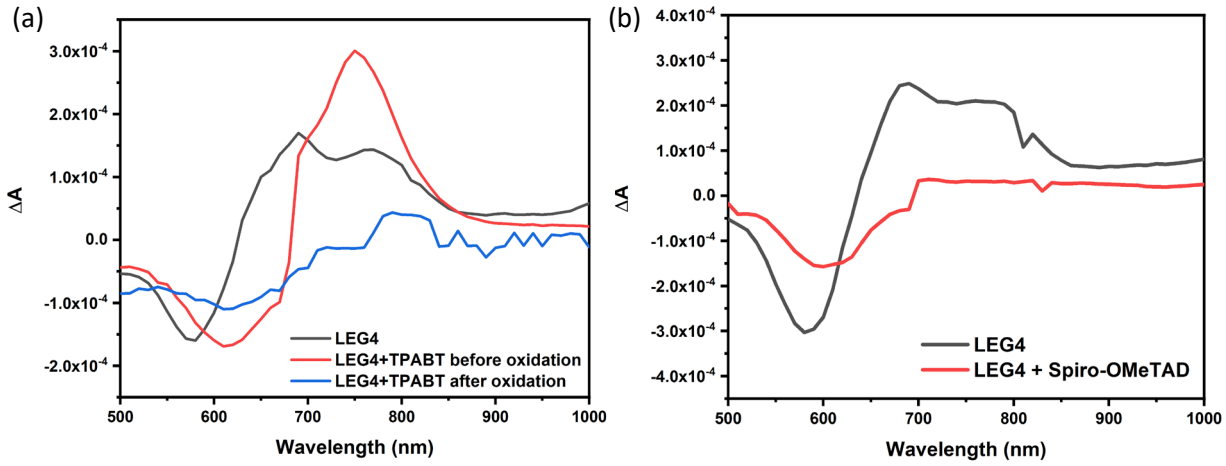

Figure 5.16: (a) PIA spectra of a device from sample set S2 (tBP:LiTFSI = 1:0.33) measured 3 days after device fabrication and again after prolonged aging to demonstrate how oxidation time affects dye regeneration. (b) PIA spectra of reference spiro-OMeTAD device measured 3 days after device fabrication.

The PIA spectrum for LEG4 shows a negative ΔA signal centred around 590 nm due to the decreased light absorption from the ground state dye (D). The positive ΔA signal in the range of 650 to 800 nm is ascribed to the oxidised dye state (D^+).[23] The PIA spectrum for S2 device measured 3 days after device fabrication shows a bleach with a minimum around 610 nm and a positive absorption feature with a maxima centred around 750 nm. The PIA spectrum for the same device measured after prolonged aging also shows a bleach with a minimum around 610 nm. However, a quenching of the oxidised dye state is observed. This indicates dye regeneration occurs only after a prolonged duration of oxidation, affirming the observation that TPABT oxidation time is much longer than Spiro-OMeTAD oxidation time, which is seen to quench the oxidised dye state after only 3 days.

The 3 month aged devices were studied further through exposure to a light soaking treatment. This was done by carrying out repetitive scan cycles (a reverse scan followed by a forward scan is equivalent to 1 scan cycle) while subject to simulated AM 1.5G illumination. Interestingly,

after repeated scan cycles the observed hysteresis reduces until it is almost negligible for all devices. In conjunction with this, the Jsc and PCE both increase up until a certain scan number (differing for each LiTFSI concentration). For 75 mM LiTFSI where this is observed the most, the Jsc increases from 0.9 mA cm^{-2} in the first scan to 5.1 mA cm^{-2} in the fifth scan, and the PCE increases from 0.33% to 1.48% (Figure 5.17). After the fifth scan both Jsc and PCE begin to reduce. In contrast, this behaviour was not observed for Spiro-OMeTAD based devices.

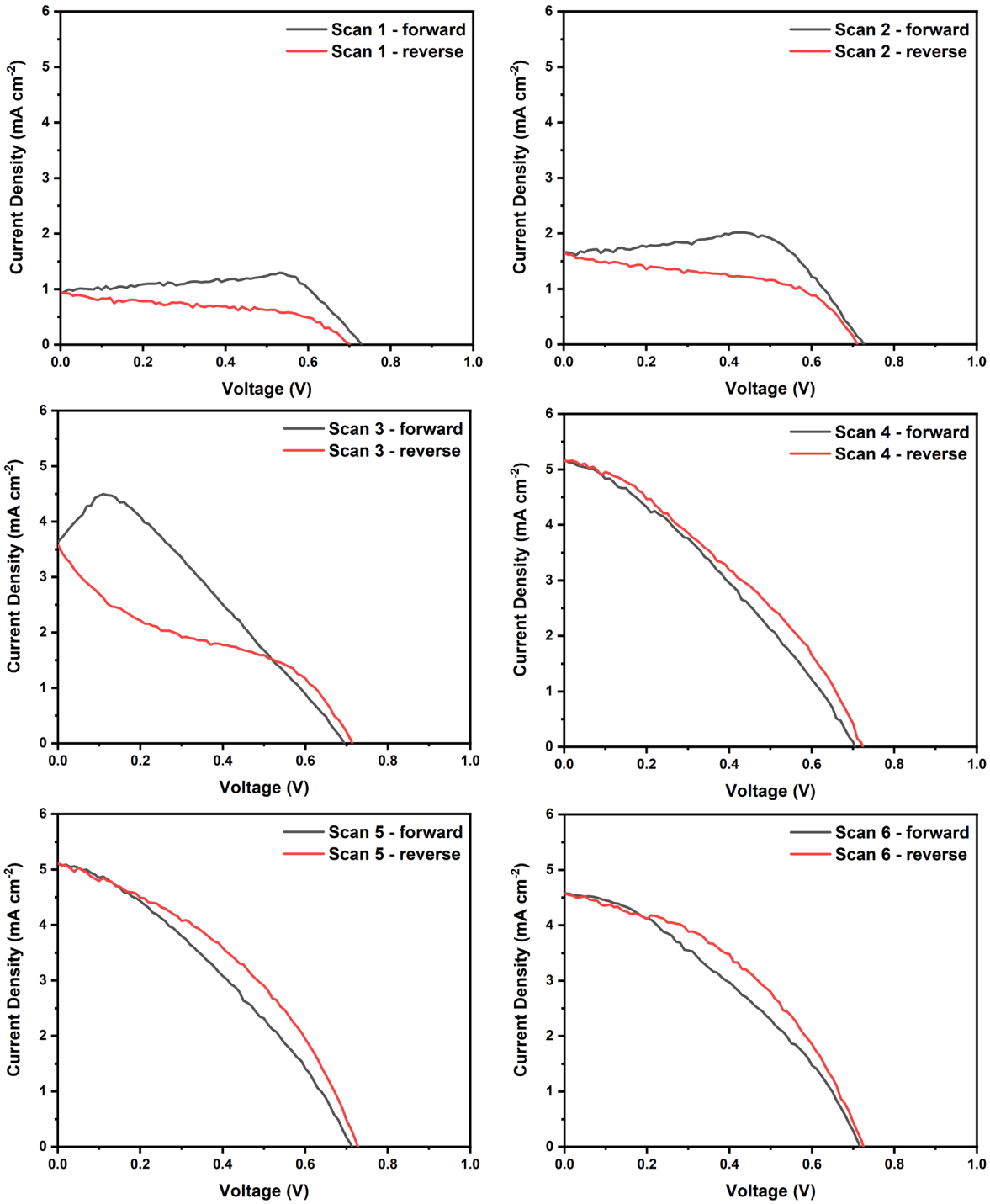

Figure 5.17: Successive J-V curves for 3 month aged FTO/TiO_2/LEG4/TPABT/Ag ssDSC with 75 mM LiTFSI and 76 mM tBP additives to 50 mg ml^{-1} TPABT, showing a significant reduction in hysteresis and improvement of device performance with successive scans. Devices were measured under AM1.5 simulated sun light of 100 mW cm^{-2} irradiance at 0.1 V s^{-1}.

The proposed hypothesis is that the significant increase in photovoltaic performance is due to Li^+ ion migration from coordinates inside the pores toward the TiO_2/LEG4 interface. The positively charged Li^+ ions have a tendency to adsorb onto the negatively charged TiO_2 surface,[24] which is driven by a local electric field that is induced after photoexcitation and charge separation. This local electric field is established when the two quasi-Fermi levels are shifted in opposite directions due to electron and hole injections upon light absorption.[25] The presence of Li^+ at the TiO_2/LEG4 interface alters the space charge formed by the electron injection into the TiO_2[26] and screens conduction band electrons after injection, thus supressing charge recombination and enhancing the photocurrent and solar cell performance.[27]

One factor that is interlinked with J-V hysteresis in perovskite solar cells is the Fermi level alignment between the electron transport material (ETL) and the perovskite absorber, and it was shown that the depth of trap states correlates to the energy difference between the Fermi level and conduction band minimum in the ETL.[28] Deep trap states are likely to trigger charge accumulation at the interface, which leads to enhanced charge recombination at the ETL/absorber interface. For the 75 mM LiTFSI device shown in Figure 5.18 it is reasonable to assume that at the beginning of the light soaking treatment before the suggested Li^+ ion migration, hysteresis is most prominent due to an unfavourable Fermi level alignment. However, upon light soaking the Li^+ ions likely migrate towards the surface of the ETL, resulting in a more favourable Fermi level alignment and minimising the presence of deep trap states; the photocurrent is increased and hysteresis is reduced.

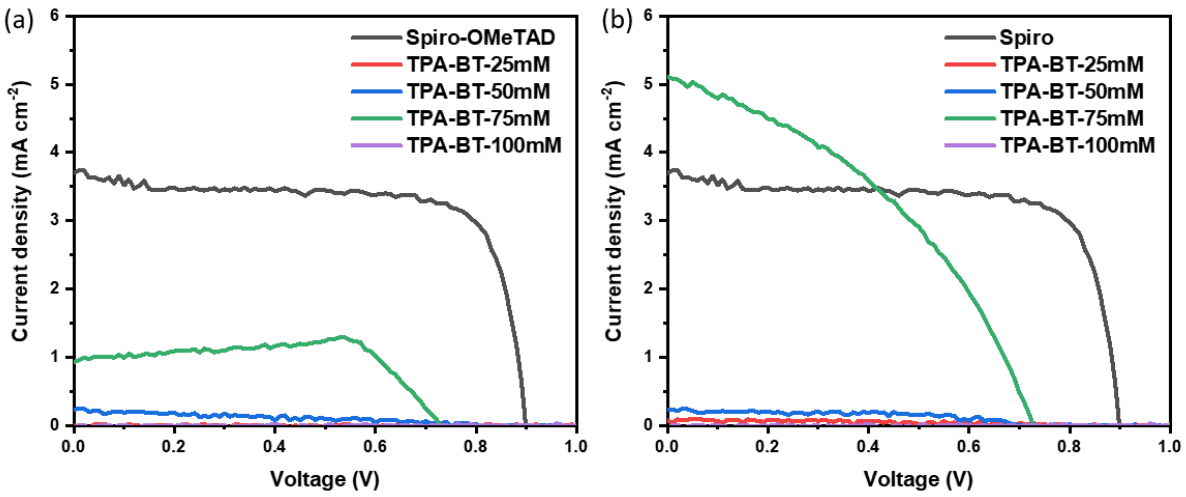

Figure 5.18: J-V curves for 3 month aged FTO/TiO_2/LEG4/TPABT/Ag ssDSC for varying concentrations of LiTFSI and 76 mM tBP additives to 50 mg ml^{-1} TPABT for (a) before light soaking treatment and (b) after light soaking treatment. A reference device employing a 100 mg ml^{-1} Spiro-OMeTAD HTM with 25 mM LiTFSI and 76 mM tBP is shown. Devices were measured under AM1.5 simulated sun light of 100 mW cm^{-2} irradiance at 0.1 V s^{-1}.

5.3.3 Conclusion

In summary, TPABT has been successfully utilised as a HTM in TiO_2 based ssDSCs, achieving a PCE of 1.48% for a 3 month aged device. Aging was found to be essential for dye regeneration to allow for oxidation of TPABT, which requires a longer oxidation time than Spiro-OMeTAD. This could be due to the denser molecular packing of TPABT. Once aged, it is critical to subject the devices to a light soaking treatment for optimal device performance, as all devices exhibited an increase in PCE upon light soaking, with the largest improvement observed being from 0.33% to 1.48%. This is due to the presence of a local electric field that arises after photoexcitation and charge separation, causing the Li^+ ions to adsorb onto the TiO_2 surface. Here, the Li^+ ions screen conduction band electrons after injection, inhibiting charge recombination and minimising J-V hysteresis due to a preferential Fermi level alignment in the TiO_2, therefore enhancing J_{SC} and overall device performance.

Modification of the heterojunction between the TiO_2 and TPABT through addition of tBP and LiTFSI additives revealed that the optimum molar concentration of LiTFSI was around 75 mM, for concentrations of tBP ranging from 76 mM to 342 mM. However, further optimisation is required. This includes determining the optimal oxidation time, as the devices were only measured after 3 months aging in a desiccator. Therefore, further investigation could reveal promising efficiencies from the low-cost, easily synthesised amide-based HTM.

5.4 Experimental Methods

5.4.1 Chemical reagents

All chemicals were used as received without further purification. Titanium(IV) isopropoxide (97%), acetylacetone (≥99%), transparent titania paste, titanium(IV) chloride tetrahydrofuran complex (97%), tert-Butanol (≥99.5%), acetonitrile (≥99.9%), spiro-OMeTAD (99%), and tBP (98%) were purchased from Sigma-Aldrich. Ethanol (99.8%) was purchased from Fisher Chemical. LEG4 (DN-F05), L0 (DNF01), and L1 (DNF02) were purchased from Dyenamo. Anhydrous chlorobenzene (99.5%, extra dry), anhydrous chloroform (99.9%, extra dry),

anhydrous isopropanol (99.8%, extra dry), and LiTFSI (99%) were purchased from Acros Organics. Anhydrous acetonitrile (>99.8%) was purchased from Alfa Aesar.

5.4.2 Device fabrication

Preparation of FTO/c-TiO_2/mes-TiO_2:

Fluorine-doped tin oxide (FTO, Pilkington, 7 Ω sq^{-1}) coated glass substrates were cleaned in ultrasonic baths of detergent diluted in tap water (15 min), de-ionised water (15 min), and ethanol (15 min) in sequence. The substrates were then blown dry using a nitrogen flow. The FTO was then etched using a Ulyxe laser etcher to create the electrode pattern (parameters specified in Section 3.2.2), and then exposed to UV-ozone for 15 min to remove the last traces of organic residues. A compact TiO_2 blocking layer was deposited via 15 spray cycles of spray pyrolysis on a hotplate at 450°C using an airbrush and N_2 as the carrier gas. The solution used in the spray pyrolysis was 3.6 ml acetylacetone and 2.4 ml titanium(IV) isopropoxide dissolved in 54 ml ethanol. To deposit the mesoporous TiO_2 film (~ 1.9 µm), transparent titania paste was screen printed onto the compact layer. After sintering on a hotplate at 450°C for 30 min the substrates were cooled to room temperature and immersed into a 40 mM aqueous solution of titanium(IV) chloride tetrahydrofuran complex for 20 min at 70°C. The substrates were then rinsed with de-ionised water and ethanol successively, and then annealed on a hotplate at 500°C for 30 min.

Dye sensitisation:

Co-sensitisation of LEG4 with L0 and L1: Once cooled to 70°C the substrates were immersed into a 0.1 mM solution of sensitiser in a mixture of tert-butanol and acetonitrile (1:1 volume ratio). The sensitiser solution varied from 100% LEG4, 75% LEG4 + 25% co-adsorbent, 50% LEG4 + 50% co-adsorbent, 25% LEG4 + 75% co-adsorbent, and 100% co-adsorbent. The substrates were left in the solution overnight and then the sensitised electrodes were rinsed with acetonitrile.

Investigating amide-based hole transporting material TPABT: Once cooled to 70°C the substrates were immersed into a 0.1 mM solution of LEG4 sensitiser in a mixture of tert-butanol and acetonitrile (1:1 volume ratio). The substrates were left in the solution overnight and then the sensitised electrodes were rinsed with acetonitrile.

Hole transporting material deposition:

The preparation and deposition of the HTM solutions were carried out in a nitrogen-filled glovebox. The HTM solution was homogeneously spread by means of a pipette onto the sensitised electrode and left to penetrate into the mesoporous network for 30 s, followed by a two-step spin coating for 40 s at 700 rpm then 2 s at 2000 rpm.

Co-sensitisation of LEG4 with L0 and L1: The formulation of the HTM solution was 100 mg ml^{-1} Spiro-OMeTAD in anhydrous chlorobenzene, with the addition of 76 mM tBP and 25 mM LiTFSI (LiTFSI was pre-dissolved in anhydrous acetonitrile at 170 mg ml^{-1}). The solution was filtered through a 0.45 µm polytetrafluoroethylene (PTFE) syringe filter and 50 µl was dispensed onto the substrate. The films were left overnight in a desiccator.

Investigating amide-based hole transporting material TPABT: The formulation of the Spiro-OMeTAD HTM solution was 100 mg ml^{-1} Spiro-OMeTAD in anhydrous chlorobenzene, with the addition of 76 mM tBP and 25 mM LiTFSI (LiTFSI was pre-dissolved in acetonitrile at 170 mg ml^{-1}). The solution was filtered through a 0.45 µm PTFE syringe filter and 50 µl was dispensed onto the substrate. The formulation of the TPABT HTM was 50 mg ml^{-1} TPABT (synthesised as previously reported)[14] dissolved in a mixture of anhydrous chloroform and anhydrous chlorobenzene (2:1 volume ratio) along with various concentrations of LiTFSI and tBP (concentrations are specified in figure captions). The TPABT solution was heated for 10 min at 70°C until transparent, then passed hot through a 0.45 µm PTFE syringe filter and 60 µl was dispensed onto the substrate. The films were left overnight in a desiccator.

Metal electrode deposition:

The substrates were placed in a BOC-Edwards Auto thermal evaporator where 120 nm of silver was deposited through a mask under high vacuum (10^{-6} Torr) at a rate of 1 $Å s^{-1}$ to form the silver electrodes.

5.4.3 Characterisation

UV-Vis measurements were taken using an Ocean Optics USB2000+ Fiber Optic Spectrometer. J-V measurements were taken using a Keysight U2722A source meter with a HelioSim-CL60 solar simulator (Voss electronic GmbH). PIA measurements were taken using square-wave-

modulated (Signal Recovery 650) blue light (405 nm, 3 mW, Thorlabs) for excitation, while as a probe a white light (ASB-W-030 Spectral Products) was used, which focussed on a monochromator (Digikröm CM110). A circular photodiode (Thorlabs) initially recorded a DC±AC signal, which was amplified and split into its components using a pre-amplifier (Model 5182 Signal Recovery). The lock-in amplifier (Model 7225 Signal Recovery) locked onto the reference phase from the chopper unit and extracted amplitude and phase of the AC signal.[29]

References

1 M. R. Elmorsy, S. A. Badawy, E. Abdel-Latif, M. A. Assiri and T. E. Ali, Significant improvement of dye-sensitized solar cell performance using low-band-gap chromophores based on triphenylamine and carbazole as strong donors, *Dyes and Pigments*, 2023, **214**, 111206.

2 J. M. Cole, G. Pepe, O. K. Al Bahri and C. B. Cooper, Cosensitization in Dye-Sensitized Solar Cells, *Chem Rev*, 2019, **119**, 7279–7327.

3 K. Kakiage, Y. Aoyama, T. Yano, K. Oya, J. Fujisawa and M. Hanaya, Highly-efficient dye-sensitized solar cells with collaborative sensitization by silyl-anchor and carboxy-anchor dyes, *Chemical Communications*, 2015, **51**, 15894–15897.

4 Y. S. Kwon, I. Y. Song, J. Lim, S.-H. Park, A. Siva, Y.-C. Park, H. M. Jang and T. Park, Reduced charge recombination by the formation of an interlayer using a novel dendron coadsorbent in solid-state dye-sensitized solar cells, *RSC Adv*, 2012, **2**, 3467.

5 M. Freitag, J. Teuscher, Y. Saygili, X. Zhang, F. Giordano, P. Liska, J. Hua, S. M. Zakeeruddin, J.-E. Moser, M. Grätzel and A. Hagfeldt, Dye-sensitized solar cells for efficient power generation under ambient lighting, *Nat Photonics*, 2017, **11**, 372–378.

6 M. Wang, C. Grätzel, S. Moon, R. Humphry-Baker, N. Rossier-Iten, S. M. Zakeeruddin and M. Grätzel, Surface Design in Solid-State Dye Sensitized Solar Cells: Effects of Zwitterionic Co-adsorbents on Photovoltaic Performance, *Adv Funct Mater*, 2009, **19**, 2163–2172.

7 W. Sharmoukh, J. Cong, J. Gao, P. Liu, Q. Daniel and L. Kloo, Molecular Engineering of D–D–π–A-Based Organic Sensitizers for Enhanced Dye-Sensitized Solar Cell Performance, *ACS Omega*, 2018, **3**, 3819–3829.

8 D. Hagberg, KTH Royal Institute of Technology, 2009.

9 J. Wiberg, T. Marinado, D. P. Hagberg, L. Sun, A. Hagfeldt and B. Albinsson, Distance and Driving Force Dependencies of Electron Injection and Recombination Dynamics in Organic Dye-Sensitized Solar Cells, *J Phys Chem B*, 2010, **114**, 14358–14363.

10 M. L. Petrus, K. Schutt, M. T. Sirtl, E. M. Hutter, A. C. Closs, J. M. Ball, J. C. Bijleveld, A. Petrozza, T. Bein, T. J. Dingemans, T. J. Savenije, H. Snaith and P. Docampo, New Generation Hole Transporting Materials for Perovskite Solar Cells: Amide-Based Small-Molecules with Nonconjugated Backbones, *Adv Energy Mater*, DOI:10.1002/aenm.201801605.

11 U. Díaz and A. Corma, Organic-Inorganic Hybrid Materials: Multi-Functional Solids for Multi-Step Reaction Processes, *Chemistry – A European Journal*, 2018, **24**, 3944–3958.

12 M. L. Petrus, T. Bein, T. J. Dingemans and P. Docampo, A low cost azomethine-based hole transporting material for perovskite photovoltaics, *J Mater Chem A Mater*, 2015, **3**, 12159–12162.

13 C. R. Kemnitz and M. J. Loewen, "Amide Resonance" Correlates with a Breadth of C−N Rotation Barriers, *J Am Chem Soc*, 2007, **129**, 2521–2528.

14 E. A. A. Alkhudhayr, D. Sirbu, M. Fsadni, B. Vella, B. T. Muhammad, P. G. Waddell, M. R. Probert, T. J. Penfold, T. Hallam, E. A. Gibson and P. Docampo, Improving the Conductivity of Amide-Based Small Molecules through Enhanced Molecular Packing and Their Application as Hole Transport Mediators in Perovskite Solar Cells, *ACS Appl Energy Mater*, 2023, **6**, 11573–11582.

15 L. Nakka, Y. Cheng, A. G. Aberle and F. Lin, Analytical Review of Spiro-OMeTAD Hole Transport Materials: Paths Toward Stable and Efficient Perovskite Solar Cells, *Advanced Energy and Sustainability Research*, DOI:10.1002/aesr.202200045.

16 A. Abate, T. Leijtens, S. Pathak, J. Teuscher, R. Avolio, M. E. Errico, J. Kirkpatrik, J. M. Ball, P. Docampo, I. McPherson and H. J. Snaith, Lithium salts as "redox active" p-type dopants for organic semiconductors and their impact in solid-state dye-sensitized solar cells, *Physical Chemistry Chemical Physics*, 2013, **15**, 2572.

17 Z. Hawash, L. K. Ono and Y. Qi, Recent Advances in Spiro-MeOTAD Hole Transport Material and Its Applications in Organic–Inorganic Halide Perovskite Solar Cells, *Adv Mater Interfaces*, , DOI:10.1002/admi.201700623.

18 R. Schölin, M. H. Karlsson, S. K. Eriksson, H. Siegbahn, E. M. J. Johansson and H. Rensmo, Energy Level Shifts in Spiro-OMeTAD Molecular Thin Films When Adding Li-TFSI, *The Journal of Physical Chemistry C*, 2012, **116**, 26300–26305.

19 S. N. Habisreutinger, N. K. Noel, H. J. Snaith and R. J. Nicholas, Investigating the Role of 4-Tert Butylpyridine in Perovskite Solar Cells, *Adv Energy Mater*, DOI:10.1002/aenm.201601079.

20 H. J. Snaith, A. Abate, J. M. Ball, G. E. Eperon, T. Leijtens, N. K. Noel, S. D. Stranks, J. T.-W. Wang, K. Wojciechowski and W. Zhang, Anomalous Hysteresis in Perovskite Solar Cells, *J Phys Chem Lett*, 2014, **5**, 1511–1515.

21 H. J. Snaith and M. Grätzel, Enhanced charge mobility in a molecular hole transporter via addition of redox inactive ionic dopant: Implication to dye-sensitized solar cells, *Appl Phys Lett*, , DOI:10.1063/1.2424552.

22 U. B. Cappel, T. Daeneke and U. Bach, Oxygen-Induced Doping of Spiro-MeOTAD in Solid-State Dye-Sensitized Solar Cells and Its Impact on Device Performance, *Nano Lett*, 2012, **12**, 4925–4931.

23 J. Zhang, N. Vlachopoulos, M. Jouini, M. B. Johansson, X. Zhang, M. K. Nazeeruddin, G. Boschloo, E. M. J. Johansson and A. Hagfeldt, Efficient solid-state dye sensitized solar cells: The influence of dye molecular structures for the in-situ photoelectrochemically polymerized PEDOT as hole transporting material, *Nano Energy*, 2016, **19**, 455–470.

24 G. Redmond and D. Fitzmaurice, Spectroscopic determination of flatband potentials for polycrystalline titania electrodes in nonaqueous solvents, *J Phys Chem*, 1993, **97**, 1426–1430.

25 L. Yang, B. Xu, D. Bi, H. Tian, G. Boschloo, L. Sun, A. Hagfeldt and E. M. J. Johansson, Initial Light Soaking Treatment Enables Hole Transport Material to Outperform Spiro-OMeTAD in Solid-State Dye-Sensitized Solar Cells, *J Am Chem Soc*, 2013, **135**, 7378–7385.

26 J. Krüger, R. Plass, L. Cevey, M. Piccirelli, M. Grätzel and U. Bach, High efficiency solid-state photovoltaic device due to inhibition of interface charge recombination, *Appl Phys Lett*, 2001, **79**, 2085–2087.

27 Y. S. Kwon, I. Y. Song, J. Lim, S.-H. Park, A. Siva, Y.-C. Park, H. M. Jang and T. Park, Reduced charge recombination by the formation of an interlayer using a novel dendron coadsorbent in solid-state dye-sensitized solar cells, *RSC Adv*, 2012, **2**, 3467.

28 M. F. Aygüler, A. G. Hufnagel, P. Rieder, M. Wussler, W. Jaegermann, T. Bein, V. Dyakonov, M. L. Petrus, A. Baumann and P. Docampo, Influence of Fermi Level Alignment with Tin Oxide on the Hysteresis of Perovskite Solar Cells, *ACS Appl Mater Interfaces*, 2018, **10**, 11414–11419.

29 H. Michaels, Uppsala University, 2022.

Chapter 6.

Improving the performance of the p-type ssDSC

6.1 Introduction

Charge recombination in solar cells results in a loss of the generated electrical current, thereby exerting a significant effect on the power conversion efficiency (PCE) of the device. The maximum open circuit voltage (V_{OC}) is restricted by charge recombination as it is controlled by the concentration of the injected charges in the semiconductor, which impacts the Fermi level of the semiconductor.[1] There are several recombination pathways that exist within the device, such as bulk recombination, interfacial recombination and trap-assisted recombination, which may require different strategies for minimising their impact on device performance. The work in this chapter focusses on minimising interfacial recombination in NiO based p-type ssDSCs at the ETM/FTO interface (1) and at the ETM/NiO interface (2), depicted in Figure 6.1.

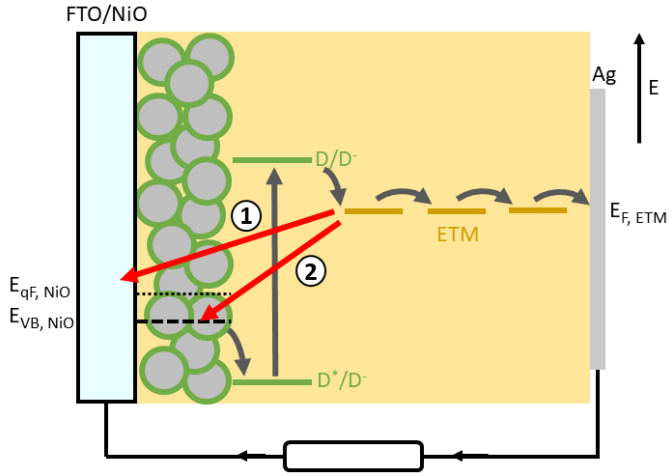

Figure 6.1: Schematic diagram of a p-type ssDSC with the electron transfer process depicted in grey and interfacial charge recombination process (1) at the ETM/FTO interface and (2) at the ETM/NiO interface depicted in red.

To supress recombination between the highly concentrated holes in the FTO and the reduced ETM, a thin compact blocking layer is deposited directly onto the conductive substrate. For all previously reported p-ssDSCs, a 60-200 nm compact NiO blocking layer was deposited via spin coating,[2] spray pyrolysis[3] and sputter coating.[4,5] To prevent recombination of electrons and holes the blocking layer must be pinhole free, which can be investigated using scanning electron microscopy (SEM). In addition, the blocking effect can be analysed using cyclic voltammetry (CV). In this section a NiO blocking layer is deposited via two separate techniques, spin coating and spray coating, and their suitability to mitigate recombination will be discussed.

Another critical factor that limits the performance in p-type DSCs is charge recombination between the reduced ETM and holes in NiO valence band. Due to the lower dielectric constant of NiO compared with TiO_2 (NiO: ~ 11.9, TiO_2: 30-170), Coulombic screening between the charged dye and the carrier in the semiconductor is weaker.[6,7] This causes greater charge recombination in devices utilising NiO compared with TiO_2. Furthermore, it was previously suggested that the charge transport mechanism in NiO occurs via hole hopping over potential barriers at the surface of the NiO nanocrystals.[8] However, the existence of excess Ni^{3+} at the surface of the film can lead to low charge transfer resistances and high rates of charge recombination.[9] This is attributed to oxidised Ni^{3+} surface states that trap a hole to "Ni^{4+}" – a mixed valence state of Ni higher than 3.[10,11] This process is known as hole shallow-trapping (Figure 6.2). Once trapped, the "Ni^{4+}" holes are able to interact with the reduced dye and the electrolyte in DSCs or the ETM in ssDSCs.

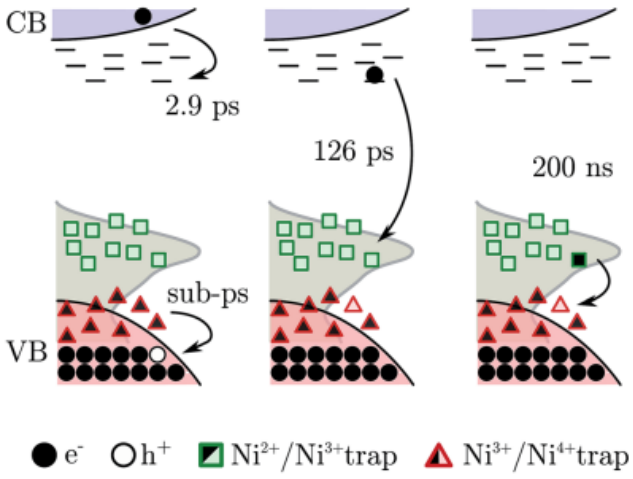

Figure 6.2: Schematic diagram of the electron-hole dynamics after band gap excitation. The pink area represents the VB, the light blue area represents the CB, the squares and triangles represent trap states, and the grey area represents the experimental reference of the density of states. Arrows indicate the movement of an electron.
Figure taken from DOI: 10.1039/c7sc03442c

One method proven useful in reducing charge recombination losses is by passivation of the NiO surface states to insulate the NiO surface.[12,13] Therefore, in the latter half of this chapter three different NiO surface treatments tested at various concentrations are employed to form a barrier layer with the objective of suppressing recombination, and current density-voltage (J-V) characteristics are assessed to determine the blocking effect. Transient absorption spectra of the devices are compared to provide insights into charge carrier dynamics, and the lifetimes associated with various kinetic processes are extracted to determine the timescales of different transitions occurring within the device. Utilising this data, a comparison is made to assess how effectively each treatment minimises charge recombination.

6.2 SEM and EDX Analysis of compact NiO blocking layer

6.2.1 Spin coating

A blocking layer solution of 0.5 M nickel acetate tetrahydrate in 2-methoxyethanol was deposited via spin coating onto clean FTO glass at 2000 rpm for 30 s. The process was repeated 2 and 3 times to obtain different film thicknesses for comparison. The spin coated films were annealed at 450 °C for 30 min to allow thermal decomposition of nickel acetate tetrahydrate into compact NiO.[14] These films are shown in Figure 6.3.

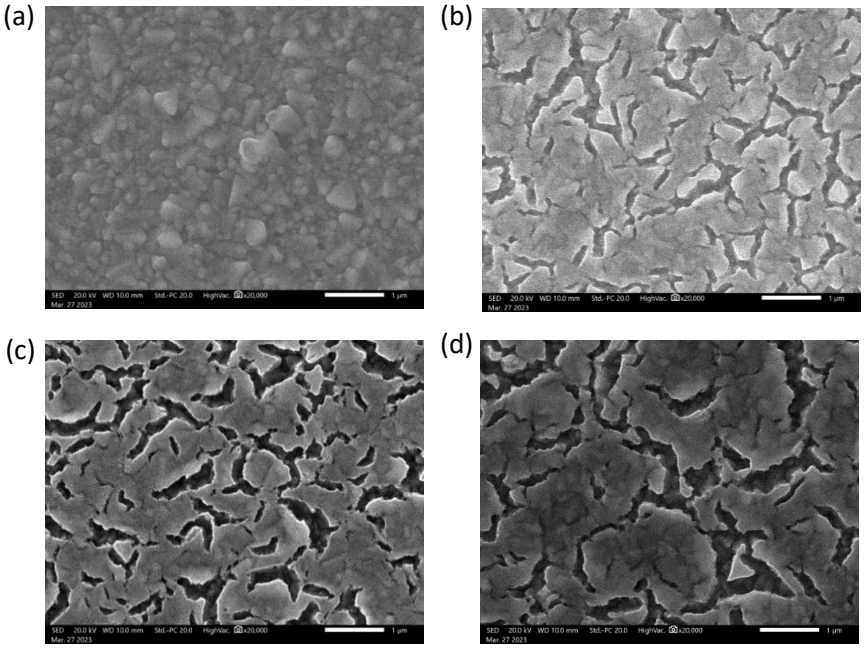

Figure 6.3: SEM images of (a) bare FTO substrate, (b) 6x6cm FTO substrate with 2 NiO spin coating cycles, (c) 6x6cm FTO substrate with 3 NiO spin coating cycles, and (d) 2x2cm FTO substrate with 3 NiO spin coating cycles, where all images are taken at x20,000 magnification.

Figure 6.3 shows SEM images that display the morphology of (a) bare FTO, and (b), (c), and (d) FTO coated with a NiO film. For images (b), (c), and (d), the compact NiO film was deposited via spin coating, where (b) uses a 6x6cm glass substrate with 2 spin coating cycles, (c) uses a 6x6cm glass substrate with 3 spin coating cycles, and (d) uses a 2x2cm substrate with 3 spin coating cycles. For bare FTO, a rough surface comprised of irregular grain boundaries is observed. For all spin coated substrates the surface appears smoother, indicating there is a film of NiO overlaying the FTO. However, large cracks are present on the surface. This suggests that these films are not compact, therefore not suitable for use as a blocking layer in p-type ssDSCs as the ETM can come into contact with the FTO, facilitating charge recombination at the ETM/FTO interface. This would lead to the devices short circuiting.

EDX analysis was undertaken to confirm that the lines on the surface of the films in Figure 6.3(b)-(d) are in fact cracks in the NiO film. Figure 6.4(a) shows a x50,000 magnification of the NiO coated FTO, where visibility inside the crack is higher. Here, the morphology looks similar

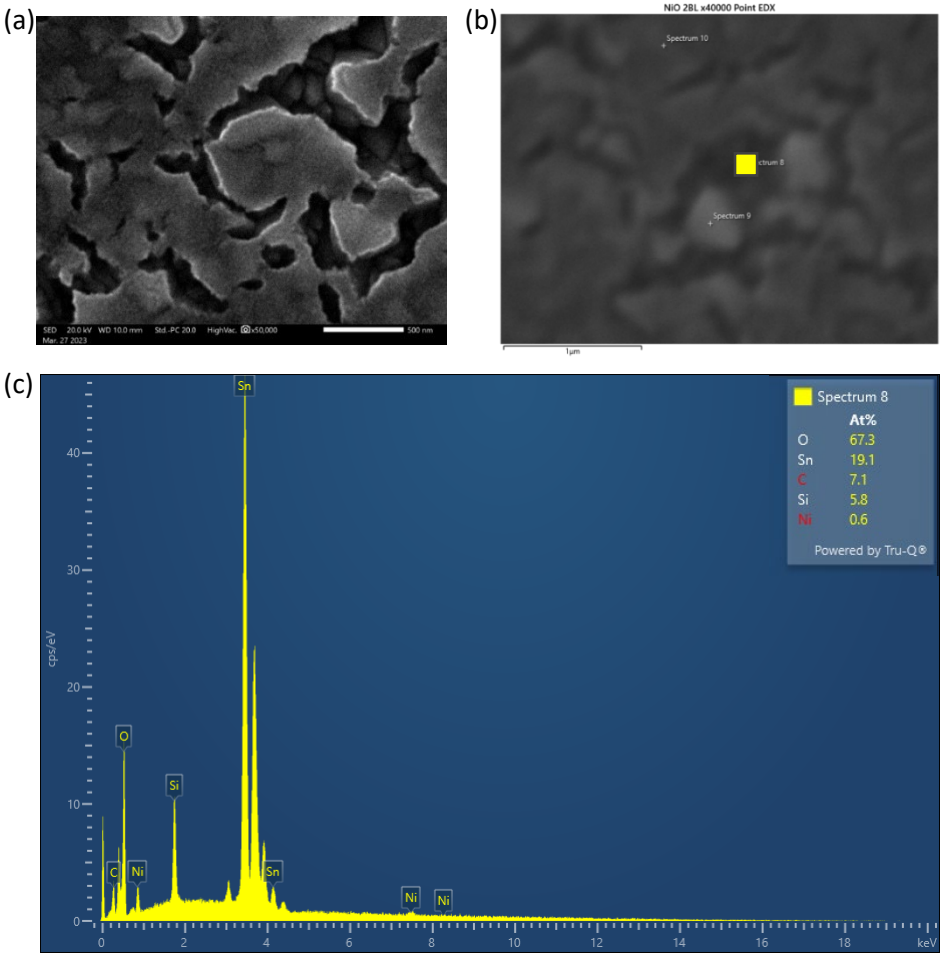

Figure 6.4: SEM image of FTO coated with 2 NiO spin coating cycles at (a) x50,000 magnification and (b) x40,000 magnification for EDX analysis, where (c) shows the EDX spectrum obtained at the yellow square from inside the crack.

to that of bare FTO shown in Figure 6.3(a). Point analysis was taken both inside outside of the crack. The spectrum outside the crack, where the NiO film should be compact, shows an atomic weight percentage (At%) of Ni to be 3.7%, and Sn to be 14.6%. When EDX point analysis was taken inside the crack, the At% of Ni reduced to 0.6% and Sn increased to 19.1%, confirming that the feature is a crack. The presence of the cracks shows that spin coating with this NiO blocking layer recipe is incompatible. This is supported by the photocurrent density-photovoltage (J-V) characteristics of p-ssDSCs employing a spin coated NiO blocking layer, as they show the devices have short circuited.

In attempt to fabricate a film that blocks direct contact between the FTO and ETM, annealing steps were carried out between each spin coating cycle. This was to see whether the subsequent cycle would fill in the cracks from the previous cycle. SEM images shown in Figure 6.5 reveal surfaces with features that resemble cracks but on a much smaller scale than observed in Figure 6.3, with a larger distance between each crack. Therefore, annealing after each successive spin coating cycle does reduce the width and quantity of the cracks in the NiO film.

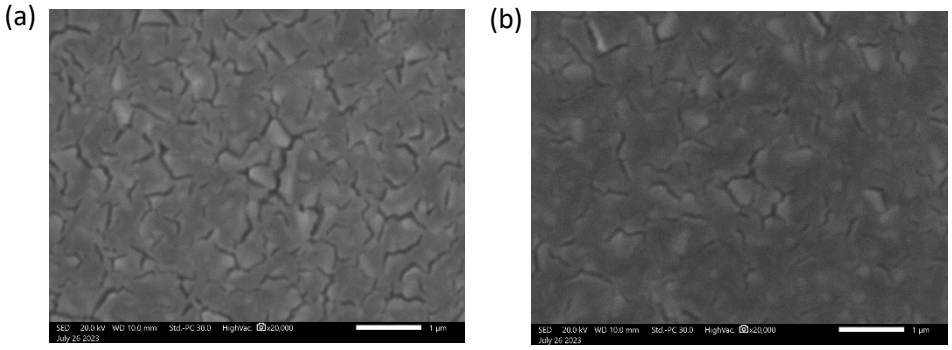

Figure 6.5: SEM images of FTO coated with (a) 2 NiO spin coating cycles and (b) 3 NiO spin coating cycles with annealing steps carried out after each cycle, where both images are taken at x20,000 magnification.

Since there has been 3 successive NiO films deposited on top of one another, the cracks present at the surface might not actually be exposing FTO, instead it could be exposing the underlying NiO film. To investigate this, these films were utilised as blocking layers in p-ssDSC FTO/bl-NiO/mes-NiO/P1/PCBM/BCP/Ag devices. However, the results show that the devices showing little to no variation between the number of annealing cycles (Figure 6.6), therefore there must be a pathway through the cracks in each layer for electrons from the ETM to flow to the FTO, rendering this deposition technique unsuitable to deposit a compact, pinhole free NiO film from this precursor solution.

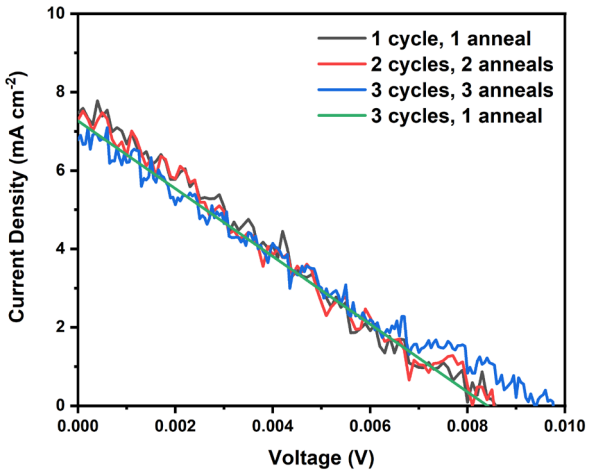

Figure 6.6: Current density-voltage (J-V) scans of FTO/c-NiO/mes-NiO/P1/PCBM/BCP/Ag devices, where the c-NiO has been fabricated with varying number of spin coating cycles and annealing steps. Devices were measured under AM1.5 simulated sun light of 100 mW cm^{-2} irradiance at 0.01 V s^{-1} (black, red, blue) or 0.2 V s^{-1} (green).

6.2.2 Spray coating

The NiO blocking layer precursor solution used previously in Section 6.2.1 was diluted to 37 mM nickel acetate tetrahydrate in 2-methoxyethanol. The solution was sprayed using an in-house built Automated Spray Pyrolysis Machine (see Chapter 4). Due to the toxicity of NiO in aerosol form, it was important to have this automated so that the deposition could take place inside a closed fume hood. An ultrasonic spray head was fed the precursor solution at a rate of 6.7 ml min^{-1}. The spray head was positioned at 18 cm above the substrates, which were kept heated at 450 °C. The processor's mechanical amplitude was set to 49% and pulse set to 100% (100% is continuous operation). The speed at which the ultrasonic spray head moved was set to 2000 mm min^{-1}. After each spraying cycle, a wait time of 60 s was used to allow thermal decomposition of the precursor solution.

Initially, the total number of spraying cycles used was 17 and 30 cycles to compare the coverage and surface morphology. Figure 6.7 shows SEM images and their corresponding EDX area analysis for NiO films deposited using 17 and 30 spraying cycles at 2 sites per film. Bare FTO is also shown for comparison. When 17 spraying cycles of precursor solution were deposited, EDX shows that for Site 1 the At% of Ni was 0.4% and for Site 2 was negligible. This suggests that 17 spraying cycles was insufficient for complete coverage.

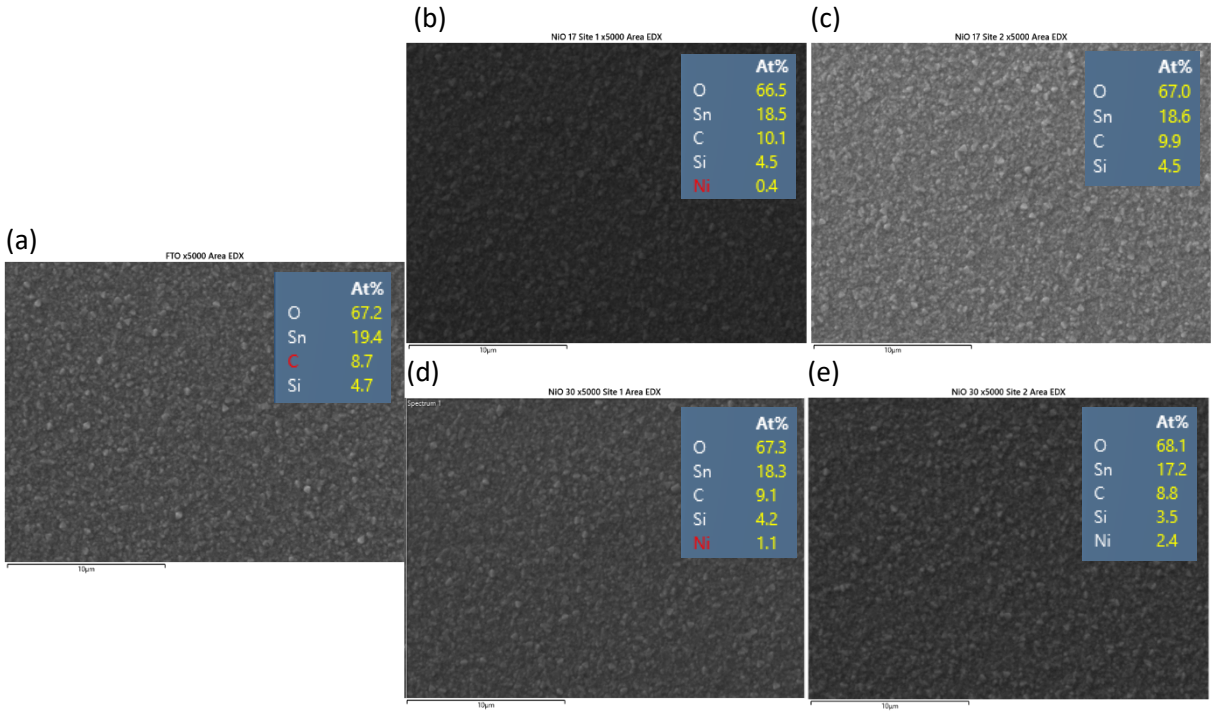

Figure 6.7: SEM images of (a) bare FTO, (b) site 1 and (c) site 2 of FTO coated with 17 NiO spraying cycles, and (d) site 1 and (e) site 2 of FTO coated with 30 NiO spraying cycles.

When 30 spraying cycles of precursor solution were deposited, EDX shows that the At% of Ni was 1.1% for Site 1 and 2.4% for Site 2. For both films there is a variation of At% of Ni, which indicates that the film being deposited is not uniform. This could be due to a number of factors such as the speed of the spray head, the heigh of the spray head and also the temperature of the hotplate during deposition, as discussed in Chapter 4: Automated Spray Pyrolysis Build. However, on inspection of the film fabricated with 30 spraying cycles at a magnification of x30, large clusters of solid material are visible on the FTO substrate. An EDX line scan was performed to verify the material forming the large clusters. In Figure 6.8, when the intensity of Sn detected decreases the intensity of Ni detected increases. This occurs at areas between 900-1200 µm across the substrate, at around 2000 µm across the substrate, and at around 3350 µm across the substrate. These areas correspond to where the yellow line in Figure 6.8(a) crosses the large clusters. This verifies that the ultrasonic spray coating of this specific NiO precursor solution at this set of spray coating parameters has led to a non-uniform coating of NiO that consists of large and small clusters of solid material. Consequently, carrying out optimisation of the spray coating parameters was required. However, due to the toxicity of NiO in aerosol form this was ruled out in the interest of safety for lab users. As well as this, recombination at the PCBM/NiO interface cannot be disregarded. Therefore, different approaches to supressing recombination are discussed in the remainder of this chapter.

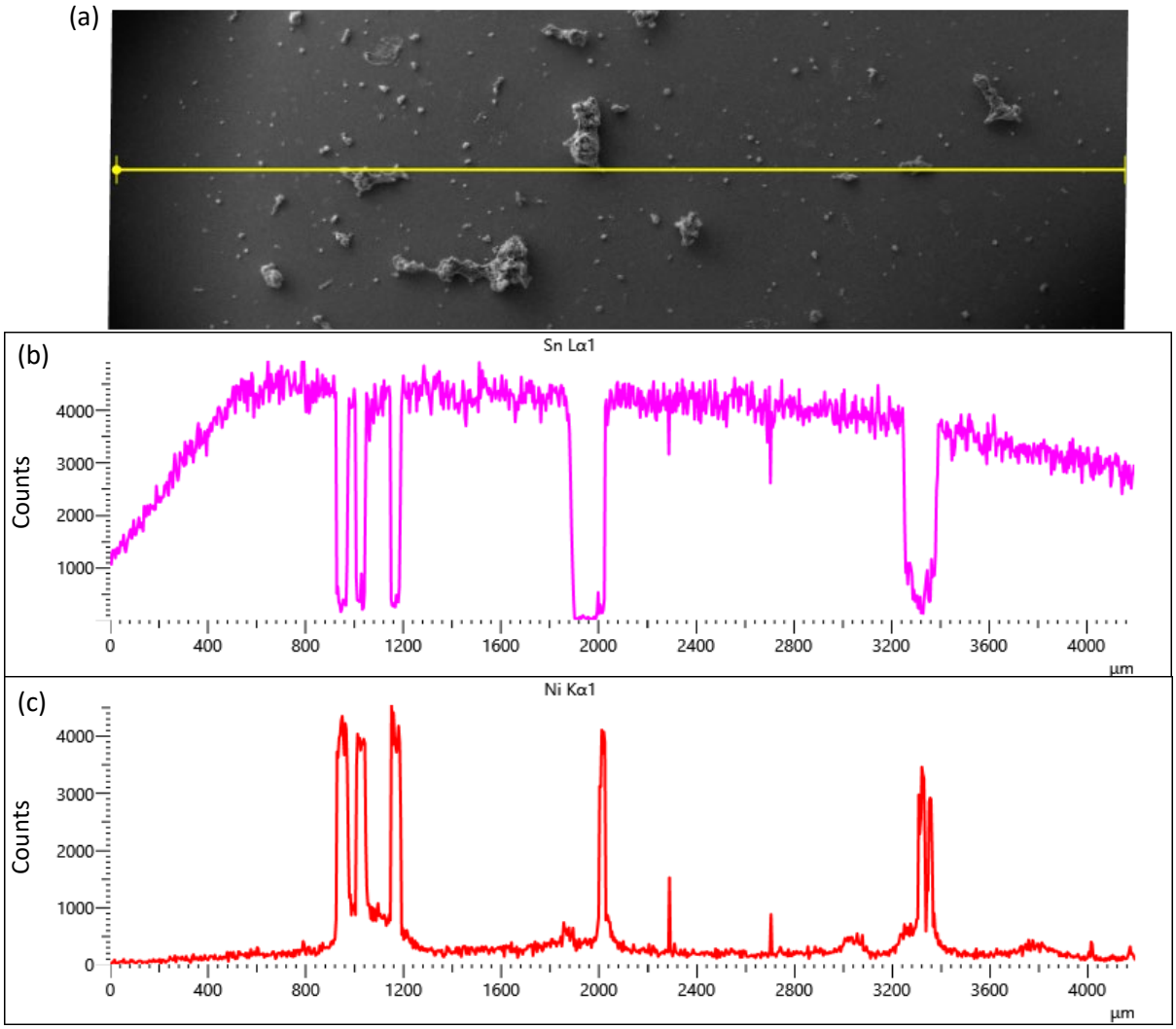

Figure 6.8: (a) SEM image of FTO coated with 30 NiO spraying cycles at x30 magnification for EDX line analysis, where (b) the EDX spectrum of Sn and (c) the EDX spectrum of Ni are obtained along the yellow line.

6.3 NiO surface treatments as blocking layers in p-type ssDSCs

6.3.1 Atomic layer deposition of alumina

Minimising the recombination of the highly concentrated holes in the FTO and the reduced ETM is vital for solar cell performance. Since the blocking layers deposited on FTO described in Section 6.2 were unsuccessful in stopping enough recombination at the ETM/electrode interface for a working device, the use of an additional thin layer of an insulating material on the surface of NiO can also be deposited to act as a blocking layer to minimise charge carrier

recombination at the ETM/NiO interface (Figure 6.9). The first material tested was the atomic layer deposition (ALD) of alumina (AlO_xH_y).

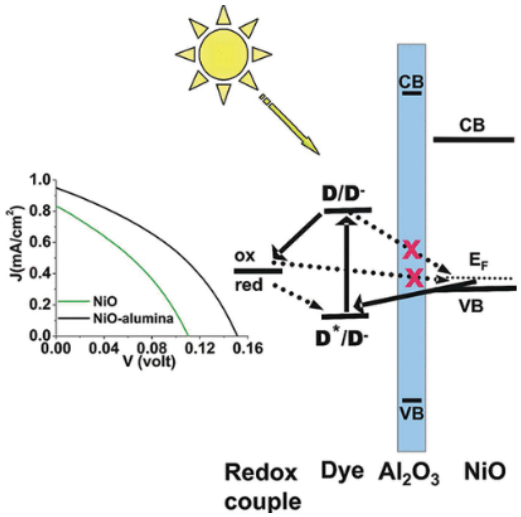

Fig 6.9: Schematic representation of the interfacial electron transport processes in NiO-based liquid DSCs and the effect of an alumina coating. Figure taken from DOI: 10.1021/la203534s

Due to the large band gap of aluminium oxide (Al_2O_3), the utilisation of an Al_2O_3 coating on the NiO surface has been shown to increase overall conversion efficiency by 74% for a NiO-based DSC, resulting from an increase in J_{SC} due to an increased efficiency of carrier collection at the semiconductor-FTO interface, and an increase in V_{OC} due to a higher resistance for electron-hole recombination across NiO surface locally.[15] This process was undertaken for NiO-based ssDSCs in this work, testing 1-3 ALD cycles.

Due to a low number of ALD cycles the overall reaction (shown in equation 6.1) may not go to completion, meaning aluminium could exist in the form of Al_2O_3, AlO(OH), or $Al(OH)_3$ phases. Therefore, the word 'alumina' has been used to describe the mixture of phases of unknown composition, AlO_xH_y.

$$2Al(CH_3)_3 + 3H_2O \rightarrow Al_2O_3 + 6CH_4 \qquad (6.1)$$

The impact of the deposited alumina layers was assessed by constructing NiO p-type ssDSCs, both with and without undergoing ALD treatment, followed by the evaluation of their photo-conversion properties. Figure 6.10(b) shows a box plot of the J_{SC} of FTO/c-NiO/mes-NiO/P1/PCBM/BCP/Ag ssDSCs with and without ALD alumina coating on the mesoporous NiO surface (note that c-NiO is the spin coated NiO film mentioned in Section 6.2.1 with cracks present in the film). These results convey an initial drop in J_{SC} after ALD treatment and a recovery of J_{SC} with more ALD cycles. Devices that have undergone ALD treatment exhibit an

overall reduction in J_{SC} compared to untreated devices. However, as the number of ALD cycles increases, the J_{SC} shows a corresponding increase. This differs to the results obtained for liquid DSCs that underwent ALD treatment, where the J_{SC} increased for 1 ALD cycle but reduces for 2 and 3 ALD cycles, which is attributed to poor hole injection across the alumina interface into NiO.[15] This suggests that the number of ALD cycles in this study could have been increased up to a point where the J_{SC} begins to increase.

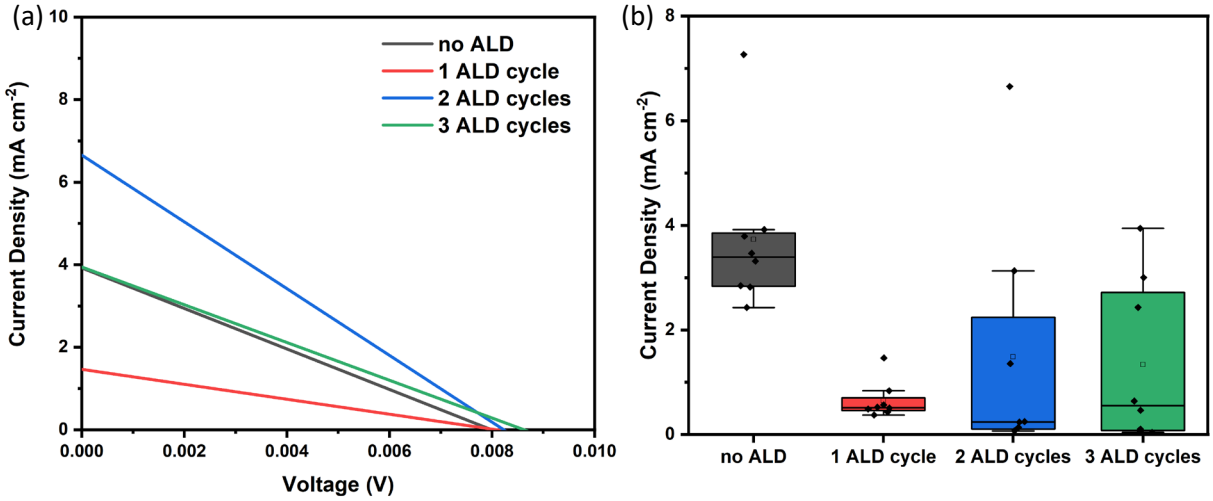

Fig 6.10: (a) Current density - voltage (J-V) curves of champion NiO-based ssDSCs (excluding outliers) with and without utilisation of an ALD alumina coating, with varying number of ALD cycles from 1 cycle to 3 cycles, and (b) a box plot representing the J_{SC} of all devices. Devices were measured under AM1.5 simulated sun light of 100 mW cm^{-2} irradiance at 0.1 V s^{-1}.

An additional factor contributing to the overall decrease in J_{SC} could be due to the precursors used during the ALD treatment, trimethylaluminum (TMA) and deionised water (H_2O). The presence of water adsorbed on the surface of mesoporous NiO can lead to the formation of Ni-OH groups, which impact the surface states the NiO film ($Ni^{2+} \rightarrow Ni^{3+}$). Surface states dominate the conductivity in mesoporous NiO films as hole hopping occurs mainly at the NiO/ETM interface.[16] With the presence of such Ni^{3+} states, the valence band may shift upwards in energy, which can lead to greater charge recombination.[9] Therefore, this could explain why the J_{SC} of almost all ALD treated devices is lower than untreated devices. A successive thermal treatment of T > 600 K after ALD treatment and before submersion into the P1 dye bath would remove any residual moisture on the mesoporous NiO surface.[17] Due to the cost and availability of the ALD equipment, testing an increased number of ALD cycles as well as testing a thermal treatment after the ALD treatment could not be performed. Therefore, alternative surface treatments were carried out and discussed in the remainder of this section.

6.3.2 Aluminium alkoxide solution treatment

Chemical surface treatment by aluminium alkoxide solution onto the surface of mesoporous NiO is another method seen to form a thin insulating layer to prevent electron injection into the NiO and minimise recombination in p-type DSCs.[18] This is represented with the same diagram as seen for ALD of alumina (Figure 6.9). For this treatment, mesoporous NiO films were submerged in a solution of aluminium-tri-*sec*-butoxide in dry iso-propanol at 60°C for 20 minutes, followed by sintering at 200°C for 30 minutes. This treatment was chosen as it can be carried out in a dry solvent, avoiding any reaction with NiO and water.

To control the thickness of the insulating layer several concentrations of aluminium alkoxide solution were tested, from 5 mM to 20 mM. Initially, cyclic voltammetry (CV) of FTO coated with aluminium alkoxide treatment was measured to investigate the blocking effects of the films fabricated from the range of concentrations, comparing films that were rinsed with dry iso-propanol prior to sintering and those that were left unrinsed. CV measurements were performed using a three-electrode system in 3 M KCl/DI water with 20 mM $[Co(en)_3]Cl_3$. This redox couple was chosen as the potential is within the NiO band gap and was shown to be an excellent mediator for p-DSCs.[19] Here, the working electrode was either bare or treated FTO, the counter electrode was Pt wire, and the reference electrode was Ag/AgCl. The voltammograms are shown in Figure 6.11.

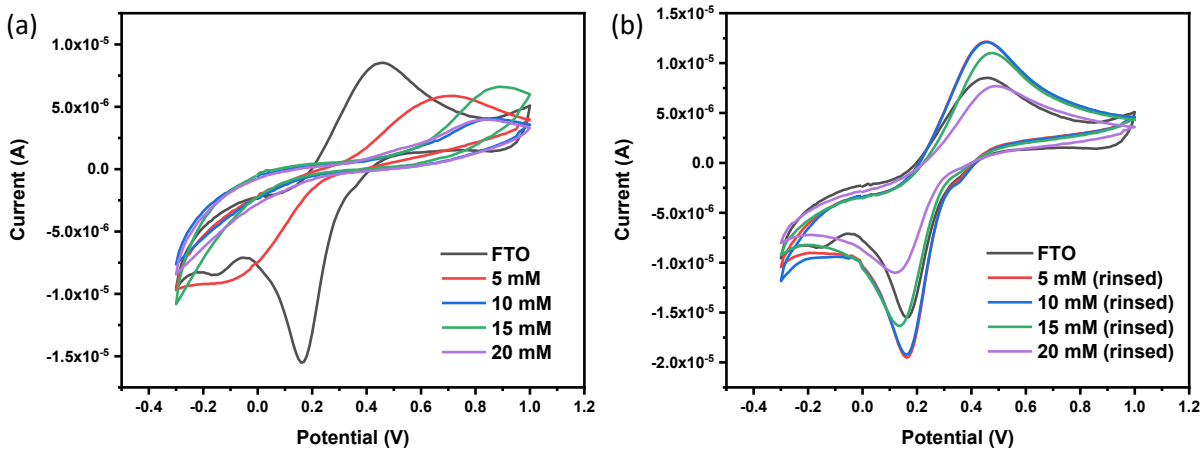

Figure 6.11: Cyclic voltammograms of FTO films that underwent aluminium alkoxide solution treatment at various concentrations (a) without a rinsing step and (b) with a rinsing step, with bare FTO included as a reference. The analyses were recorded at a scan rate of 0.1 V s^{-1} in a 3 M KCl/DI water solution with 20 mM $[Co(en)_3]Cl_3$.

The CV obtained from a bare FTO working electrode shows a quasi-reversible response. For all cases where the working electrode used was treated FTO where a rinsing step was included, clear anodic and cathodic peaks are still apparent. In all cases except for the highest

concentration, 20 mM, the peak current actually increases. This shows that the rinsing step removes some of the deposited aluminium alkoxide, resulting in a non-compact insulating layer therefore only a small blocking effect is seen. The increase in redox signal may be due to the deposited film creating an increased surface area of the electrode. For CV measured for treated FTO where a rinsing step was omitted, the quasi-reversible response is only visible for the lowest concentration of aluminium alkoxide solution tested, which was 5 mM. For all other concentrations, almost all of the current is supressed. This demonstrates that 5 mM concentration is too low to form a fully insulating layer of aluminium alkoxide. To test the impact of the blocking layer on solar cell performance, J-V curves were measured and their photoconversion properties were analysed (Figure 6.12).

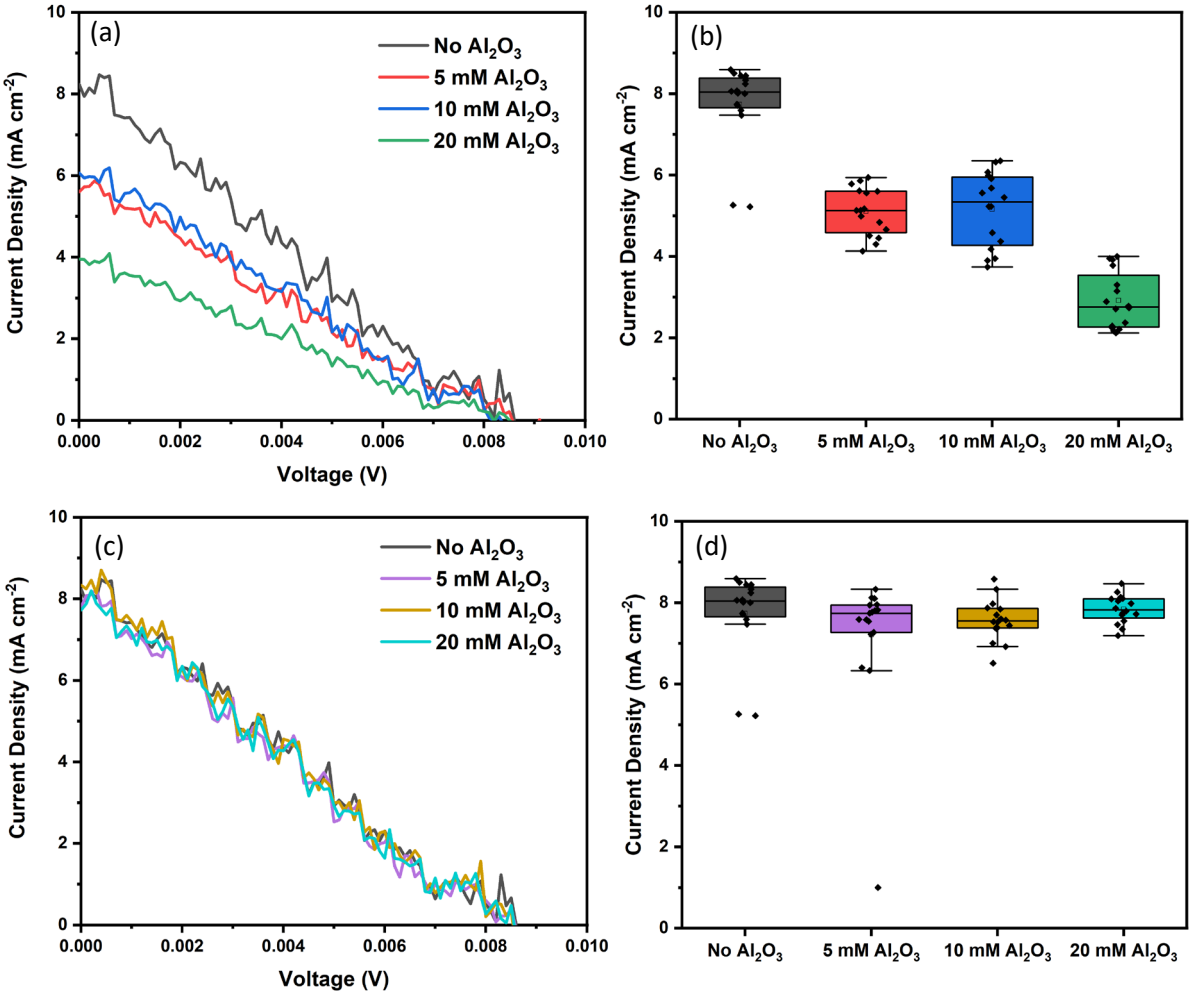

Figure 6.12: Current density - voltage (J-V) curves of champion NiO-based ssDSCs with and without utilisation of an aluminium alkoxide surface treatment on NiO, for varying concentrations of solution, for (a) treatments with no rinsing step and (b) the box plot showing J_{SC} for the whole batch, and (c) treatments with a rinsing step and (d) the boxplots showing J_{SC} for the whole batch. Outliers have been omitted.

From the J-V scans it was shown that the photoconversion properties remained relatively unchanged after chemical surface treatment when a rinsing step was included. However, when the rinsing step was omitted the J_{SC} of the devices were affected. Again, rather than experiencing an enhancement as seen in literature,[18] the surface treatment led to a 32%, 26% and 52% reduction in J_{SC} for 5 mM, 10 mM and 20 mM Al_2O_3 solution treatments, respectively. This indicates that, for both ALD and chemical Al_2O_3 surface treatments, the hole injection into NiO was being inhibited by the presence of the insulating films, or charge transport through NiO was supressed.

6.3.3 Chenodeoxycholic acid treatment

The two previous surface treatments involving the deposition of alumina onto the mesoporous NiO surface were found to decrease the J_{SC} as they were unable to reduce charge recombination within the device and instead potentially inhibited hole injection into NiO or supressed charge transport through the NiO electrode. Therefore, a third and final surface treatment was tested utilising a different material, chenodeoxycholic acid (CDCA). In n-type TiO_2 based DSCs, CDCA has often been used as a co-adsorbent to break up the π-π aggregates between organic sensitisers and create a physical barrier on the semiconductor to reduce recombination at the TiO_2/electrolyte interface.[20] However, Odobel et al. found that co-adsorption of CDCA with the dye did not reduce charge recombination in a liquid p-type DSC.[12] Consequently, CDCA was utilised in an alternative manner by performing dye chemisorption first and then spin coating an ethanol solution of CDCA onto the already dyed photocathode. This, in turn, created a physical barrier shown to prevent charge recombination. Therefore, rather than using an insulating layer of alumina, this method was utilised for CDCA to form an insulating organic layer after dye chemisorption.

Several concentrations of ethanol solutions of CDCA were tested; 2 mM, 5 mM and 10 mM. As well as this, the conventional method of using CDCA as a co-adsorbent to P1 was also tested for comparison. The performance of the resulting devices is shown in Figure 6.13. The J_{SC} increased by 2.47 mA cm^{-2} upon addition of a 2 mM CDCA insulating layer, and by 0.29 mA cm^{-2} with a 5 mM CDCA layer. However, when the concentration was increased to 10 mM, the J_{SC} decreased by 0.45 mA cm^{-2}. This suggests that with low concentrations of CDCA the charge recombination is reduced, but when the concentration is too high a different process is

supressed, having a negative impact on device performance. When CDCA is utilised as a co-adsorbent in P1 J_{SC} is increased by 0.73 mA cm^{-2}, which is less than a third of the increase generated via spin coating onto the already dyed NiO. However, as only one concentration of co-adsorbent was tested no definitive conclusion can be drawn regarding which method is superior.

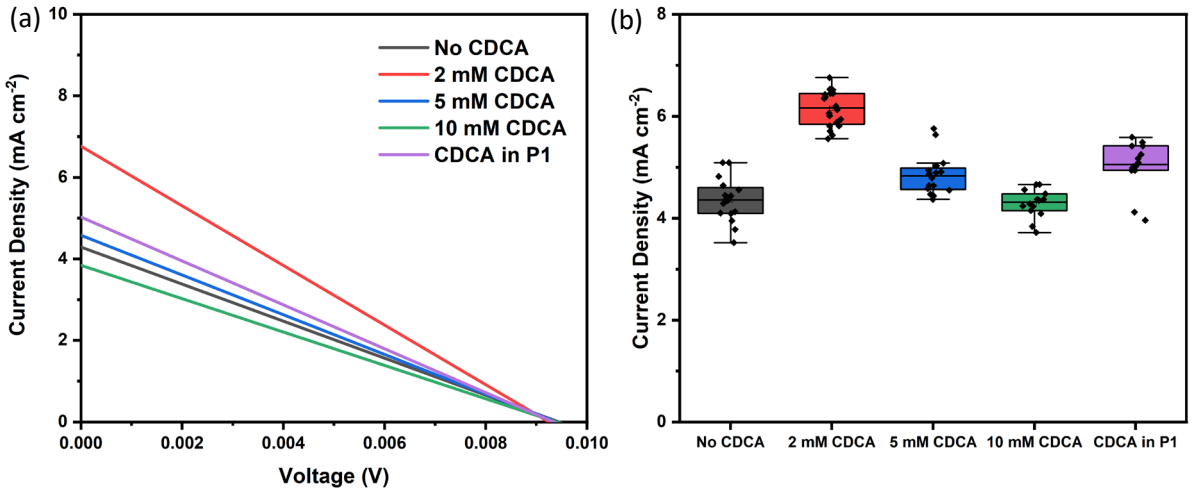

Figure 6.13: (a) Current density - voltage (J-V) curves of champion NiO-based ssDSCs with and without utilisation of CDCA surface treatment on NiO, for varying concentrations of solution, and (b) the boxplots showing J_{SC} for the whole batch. Outliers have been omitted.

6.4 Using Transient Absorption Spectroscopy to determine the blocking effects of various NiO surface treatments

Transient absorption spectroscopy (TAS) is an experimental technique used to study the dynamics of photo-excited states in materials. For ssDSCs, TAS can provide crucial insights into several aspects of device operation, such as photoexcited states, charge carrier dynamics and interfacial processes. The transient absorption spectra (chirp-corrected) for NiO based p-type ssDSCs utilising ALD of alumina, aluminium alkoxide solution treatment, and chenodeoxycholic acid (CDCA) treatment were measured, and the extent to which they inhibit recombination in the device is discussed.

This portion of the chapter is divided into sub-sections; the first three (6.4.1 to 6.4.3) contain the transient absorption spectra for each surface treatment accordingly. Also included in these sub-sections are two graphs that contain the transient spectrum for all concentrations of the

surface treatment at two specific time delays, one fast (300 ps) and one slow (1 ns), to examine how the spectral response changes at varying concentrations. The last three sub-sections (6.4.4 to 6.4.6) present the kinetic information obtained from the transient absorption spectra. The sub-sections are divided into the kinetics studied at each wavelength: first the ground state bleach of the dye around 510 nm, and secondly the excited state of the dye around 580 nm (these characteristics show a similar result to TAS measurements obtained for P1 in solution, as documented in previous publications),[21,22] and finally the reduced state of the dye around 630 nm (which is in close agreement with spectroelectrochemistry measurements by Qin et al).[22] These sub-sections allow a straightforward comparison of how each surface treatment affects various processes within the device. Kinetic data has been normalised and exponential functions, shown in Equation 6.2, have been used to model the decay or rise of the transient signal. From this, the lifetimes associated with each kinetic process has been extracted to provide insight into the timescales of the different transitions occurring within the device.

$$y = A_1 e^{\frac{-x}{\tau_1}} + A_2 e^{\frac{-x}{\tau_2}} + y_0 \qquad (6.2)$$

Where τ_1 and τ_2 are the lifetimes of the process, $A_1$and A_2 are the amplitudes corresponding to the initial value of the decay, y_0 represents the offset parameter, y is the observed data point and x is time.

6.4.1 Transient absorption spectra – ALD of alumina

For no ALD treatment when P1 is directly bound to NiO and PCBM is utilised as the ETM, TAS measurements (Figure 6.14) are in agreement with those obtained by Zhang et al., with an absorption peak centred around 630 nm corresponding to the reduced state of the dye, which diminishes within 500 ps.[3] When varying the number of ALD cycles, differences in TAS measurements are observed, namely a faster decay as well as the characteristics of the isosbestic point. An isosbestic point occurs at a specific wavelength where the absorbance remains constant across different time delay, resulting in all time traces intersecting at exactly the same wavelength. For no ALD there is one clear isosbestic point around 550 nm, implying a simple two-state process where two well-defined states interconvert, such as ground and excited states. For 1, 2 and 3 ALD cycles there are multiple crossover points at different

wavelengths. This suggests these systems involve more complex dynamics, potentially with intermediate states or multiple pathways for relaxation. Kinetic fits are shown in Sections 6.4.4 to 6.4.6.

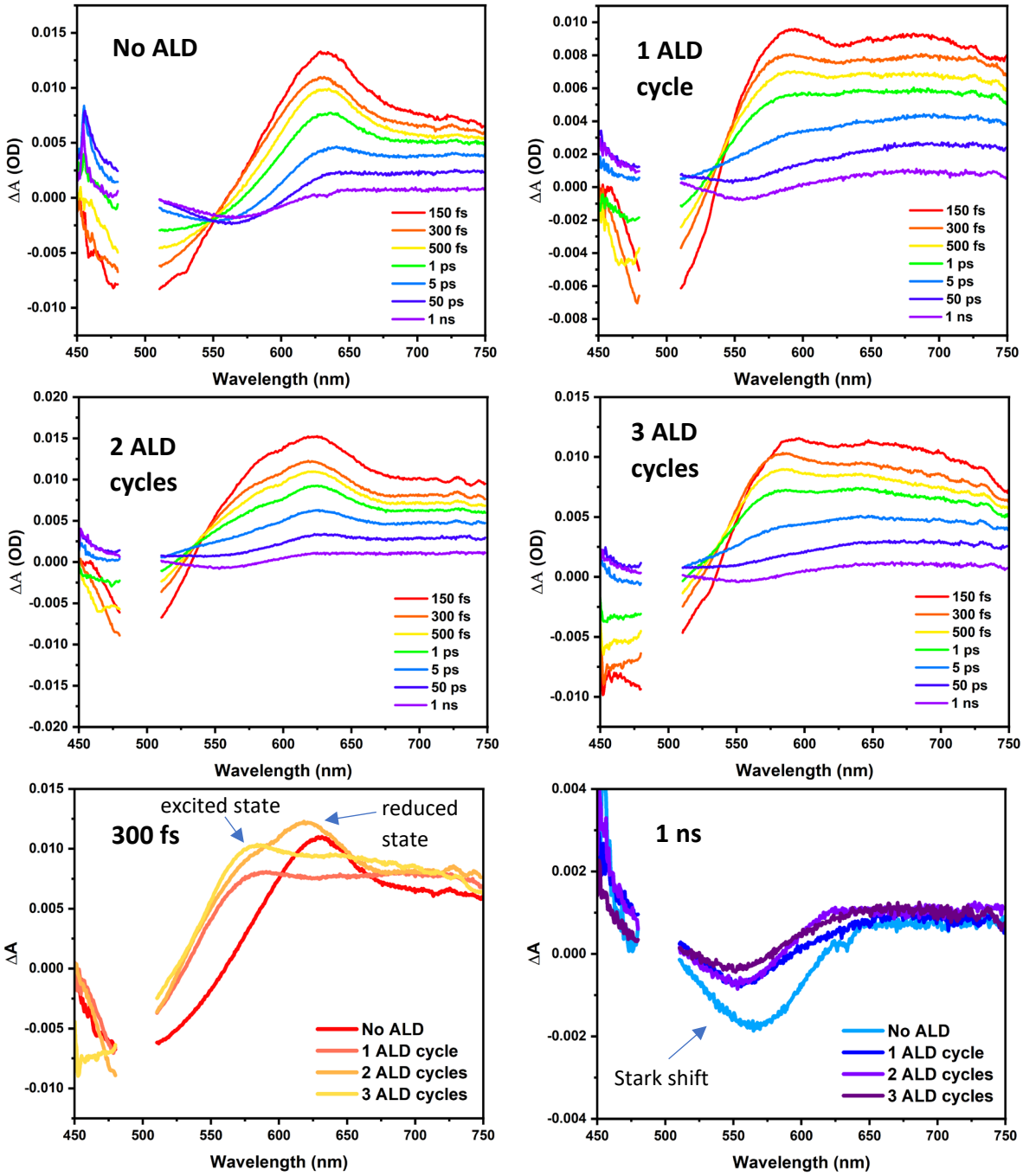

Figure 6.14: Transient absorption spectra upon excitation at 490 nm of FTO/NiO/Alumina/PCBM.

6.4.2 Transient absorption spectra – Aluminium alkoxide solution treatment

Generally, the TAS measurements for the aluminium alkoxide (Al_2O_3) solution treatment (Figure 6.15) are similar to those for the ALD treatment, showing an absorption peak centred

around 630 nm and an isosbestic point at around 550 nm. However, for all concentrations of Al_2O_3 there remains one clear isosbestic point around 550 nm, implying a simple two-state process. The absorption intensity increases with increasing concentration of Al_2O_3, showing a more significant absorption peak around 630 nm at faster timescales (300 fs). This suggests that higher concentrations of Al_2O_3 prolong the lifetime of the excited state. Kinetic fits are shown in Sections 6.4.4 to 6.4.6.

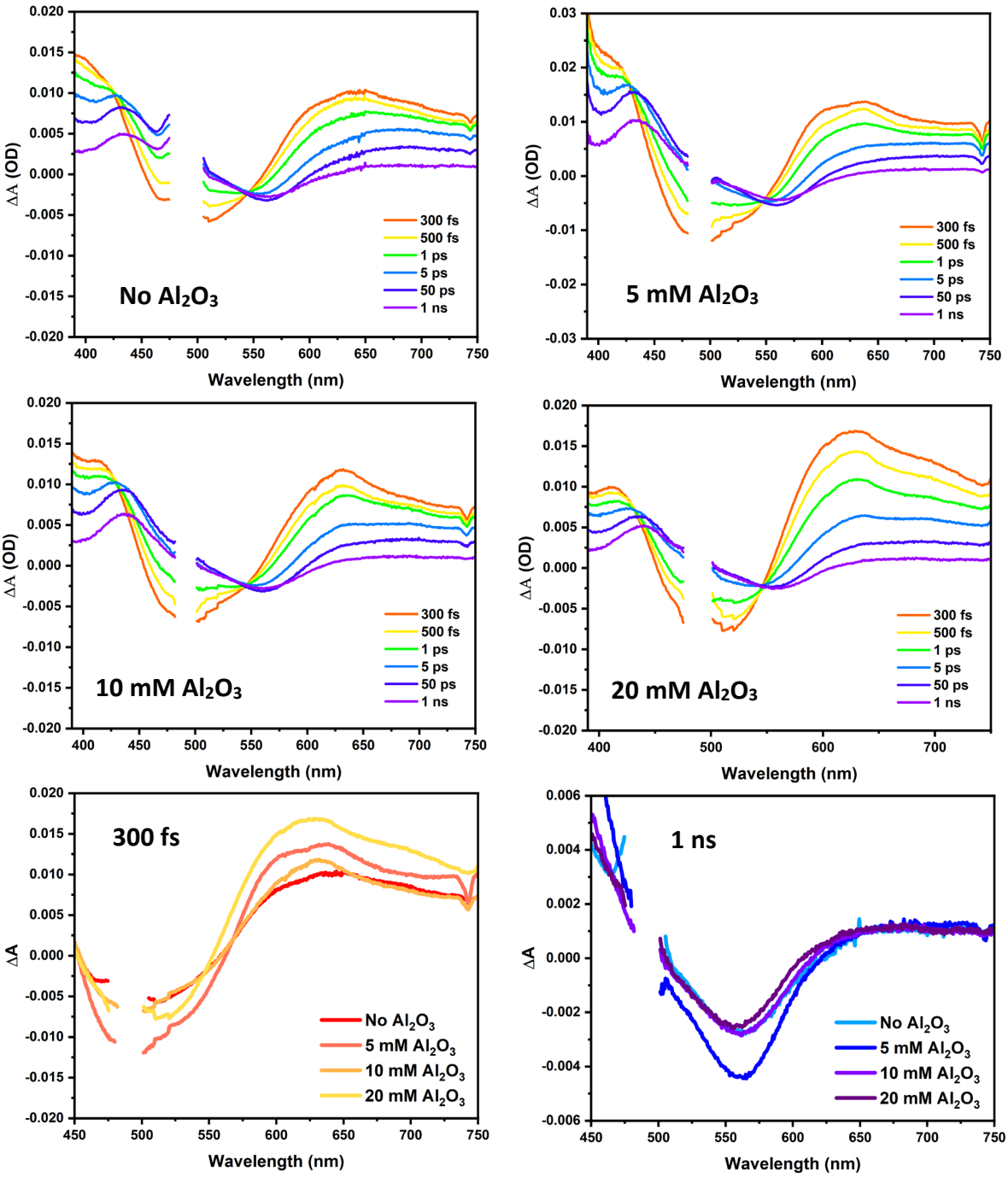

Figure 6.15: Transient absorption spectra upon excitation at 490 nm of FTO/NiO/Al_2O_3/PCBM.

6.4.3 Transient absorption spectra – Chenodeoxycholic acid treatment

TAS measurements for devices employing the CDCA treatment (Figure 6.16) show across all samples, the absorption peak centred around 630 nm remains. Higher CDCA concentrations prolong the excited-state lifetime, which suggests that less recombination occurs at the NiO/PCBM interface. When CDCA is incorporated into the P1 dye bath a stronger signal is observed. This could indicate that CDCA in P1 enhances the separation of charge carriers and promotes more effective charge transport. Kinetic fits are shown in Sections 6.4.4 to 6.4.6.

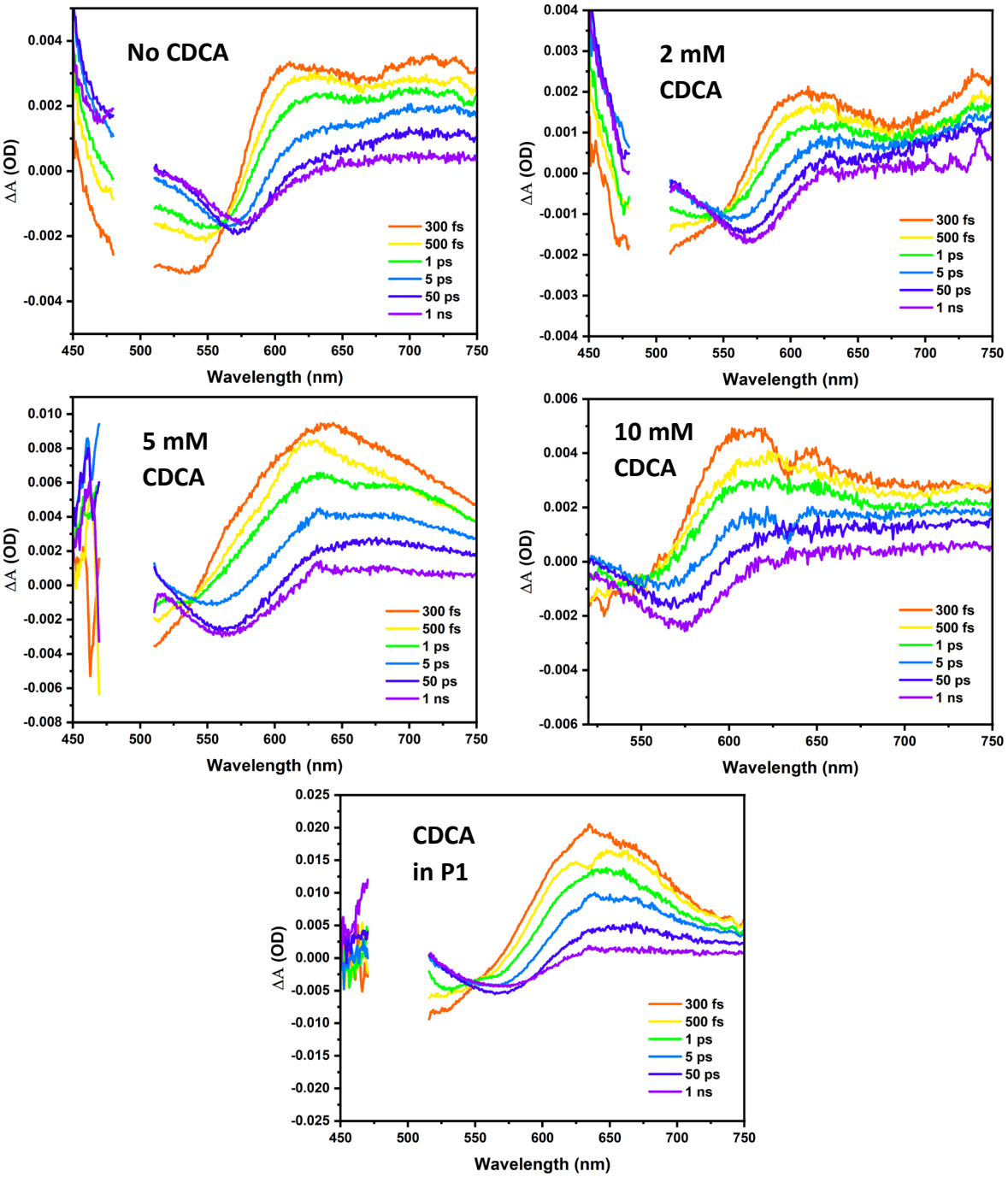

Figure 6.16(a): Transient absorption spectra upon excitation at 490 nm of FTO/NiO/P1/CDCA/PCBM.

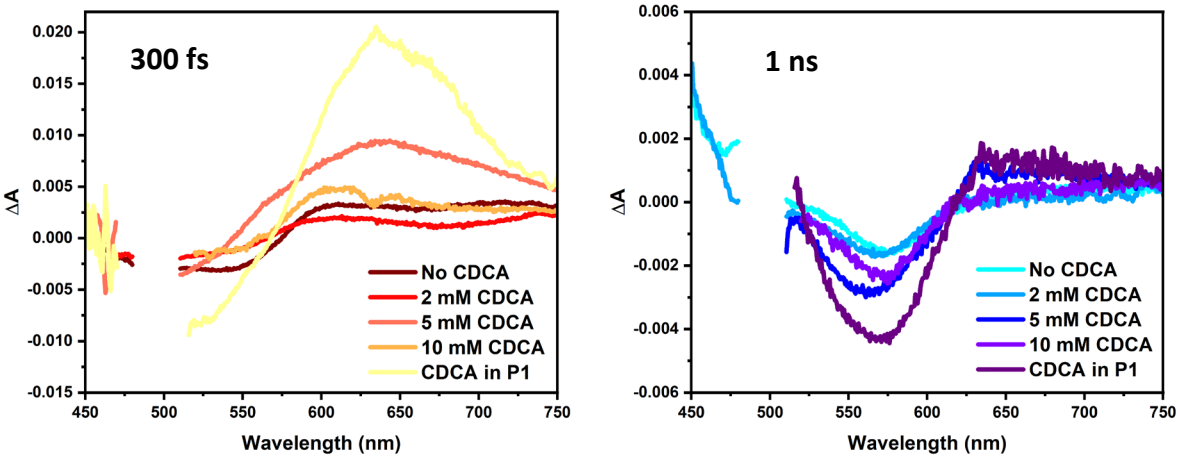

Figure 6.16(b): Transient absorption spectra upon excitation at 490 nm of FTO/NiO/P1/CDCA/PCBM.

6.4.4 Kinetics at 510 nm – ground state bleach of the dye

Molecules in their ground state typically absorb light at specific wavelengths. When a dye molecule absorbs a photon and transitions from its ground state (HOMO) to an excited state (LUMO) this leads to a reduction in the number of molecules in the ground state. This ground state depopulation causes a bleach in absorption spectrum at the wavelengths where the ground state absorbs. For these devices, the P1 ground state bleach is at ~ 510 nm.[21]

Figure 6.17 shows that for all surface treatments, the lifetimes associated with the fast decay (within several picoseconds) are consistent for all concentrations of each surface treatment (τ_1= < 1 ps, τ_2 is a few picoseconds). This indicates that the presence of the insulating layer does not affect the ground state bleach. The only difference is exhibited when CDCA is used as a co-adsorbent in P1. This stands to reason, as co-sensitisation directly impacts light absorption.

For the slower decay (tens of picoseconds to nanoseconds) the kinetic data show that there is little difference between ALD and Al_2O_3 treatments (τ_3= 100 – 200 ps) and the number of ALD cycles or concentration of Al_2O_3 solution has little effect on the ground state bleach, indicating there is little impact on injection and recombination. For CDCA, the kinetic data does not display an exponential behaviour. This suggests that CDCA treatment has a different effect on the ground state bleach of the dye compared with the two other treatments.

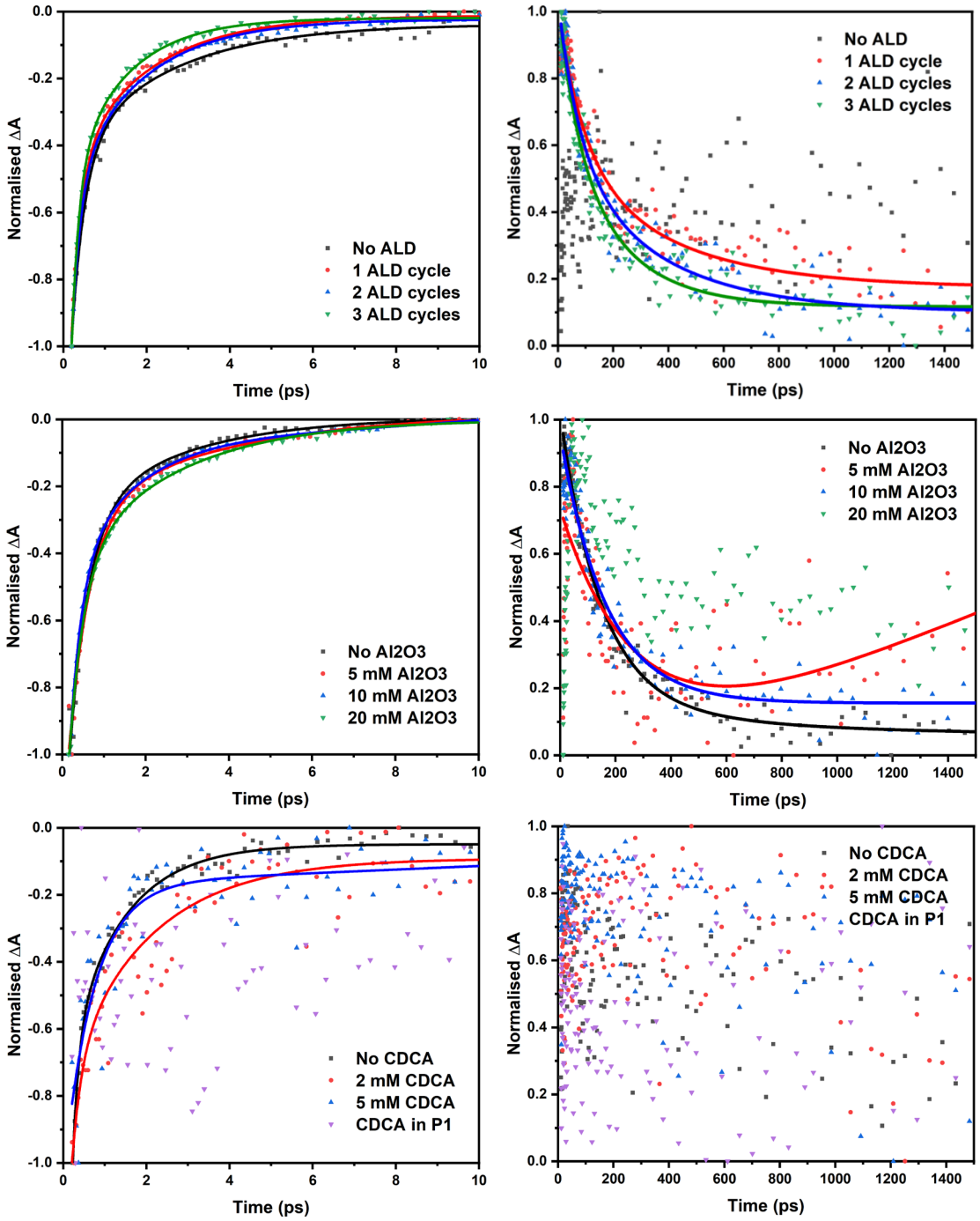

Figure 6.17: Kinetic traces obtained at 510 nm, corresponding to the ground state bleach of the dye, for various NiO surface treatments. Data was extracted from TAS measurements upon excitation at 490 nm.

510 nm (0-10 ps)			
	τ_1 ps (A_1)	τ_2 ps (A_2)	y_0
NiO|P1	0.32 ± 0.03 (-1.04)	2.34 ± 0.30 (-0.41)	-0.04
NiO|**1 ALD cycle**|P1	0.23 ± 0.01 (-1.21)	1.85 ± 0.08 (-0.49)	-0.01
NiO|**2 ALD cycles**|P1	0.22 ± 0.01 (-1.20)	1.71 ± 0.06 (-0.54)	-0.02
NiO|**3 ALD cycles**|P1	0.18 ± 0.01 (-1.54)	1.33 ± 0.06 (-0.53)	-0.02

Table 6.1(a): Fitted lifetimes (τ) of the ground state bleach with corresponding amplitudes (A) and offset (y_0) for various NiO surface treatments.

510 nm (10-1500 ps)			
	τ_3 ps (A_3)	---	y_0
NiO|**1 ALD cycle**|P1	152.22 ± 9.26 (0.79)	---	0.23
NiO|**2 ALD cycles**|P1	157.12 ± 10.30 (0.85)	---	0.15
NiO|**3 ALD cycles**|P1	129.52 ± 6.19 (0.89)	---	0.14

510 nm (0-10 ps)			
	τ_1 ps (A_1)	τ_2 ps (A_2)	y_0
NiO|P1	0.46 ± 0.06 (-1.03)	2.62 ± 0.94 (-0.32)	0.01
NiO|**5 mM Al_2O_3**|P1	0.52 ± 0.06 (-0.97)	3.67 ± 1.47 (-0.31)	0.02
NiO|**10 mM Al_2O_3**|P1	0.29 ± 0.02 (-0.98)	1.66 ± 0.33 (-0.45)	-0.05
NiO|**20 mM Al_2O_3**|P1	0.36 ± 0.02 (-0.89)	2.52 ± 0.17 (-0.47)	$3x10^{-4}$
510 nm (10-1500 ps)			
	τ_3 ps (A_3)	---	y_0
NiO|P1	154.20 ± 5.88 (0.94)	---	0.09
NiO|**5 mM Al_2O_3**|P1	66.03 ± 11.50 (1.22)	---	0.26
NiO|**10 mM Al_2O_3**|P1	145.05 ± 9.92 (0.85)	---	0.16
NiO|**20 mM Al_2O_3**|P1	117.20 ± 22.86 (0.88)	---	0.45

510 nm (0-10 ps)			
	τ_1 ps (A_1)	τ_2 ps (A_2)	y_0
NiO|P1	0.15 ± 0.03 (-1.74)	1.29 ± 0.12 (-0.68)	-0.05
NiO|**2 mM CDCA**|P1	0.23 ± 0.20 (-0.76)	1.98 ± 0.69 (-0.67)	-0.09
NiO|**5 mM CDCA**|P1	0.55 ± 0.53 (-0.43)	1.01 ± 0.41 (-0.49)	-0.13

Table 6.1(b): Fitted lifetimes (τ) of the ground state bleach with corresponding amplitudes (A) and offset (y_0) for various NiO surface treatments.

6.4.5 Kinetics at 580 nm – excited state of the dye

The transient absorption spectra show a positive absorption feature at around 580 nm. This is assigned to the excited state of the dye, P1*. Figure 6.18 shows that for the decay occurring within the first 10 ps, all three surface treatments make almost no difference to the lifetime of the excited state of the dye. However, for the slower decay there are clear differences between the data. For all samples without any surface treatment, CDCA as a co-adsorbent in P1, and for the lower concentrations of Al_2O_3 treatment, rather than showing a decay the data points begin to rise. This could indicate two overlapping processes, such as the decay of the excited state overlapping with the rise of the charge separated state. On the other hand, for all numbers of ALD cycles, the highest concentration of Al_2O_3 treatment and for all concentrations of spin coated CDCA, the data show an exponential decay. These differences propose that the surface treatments at these concentrations might influence hole injection into the NiO.

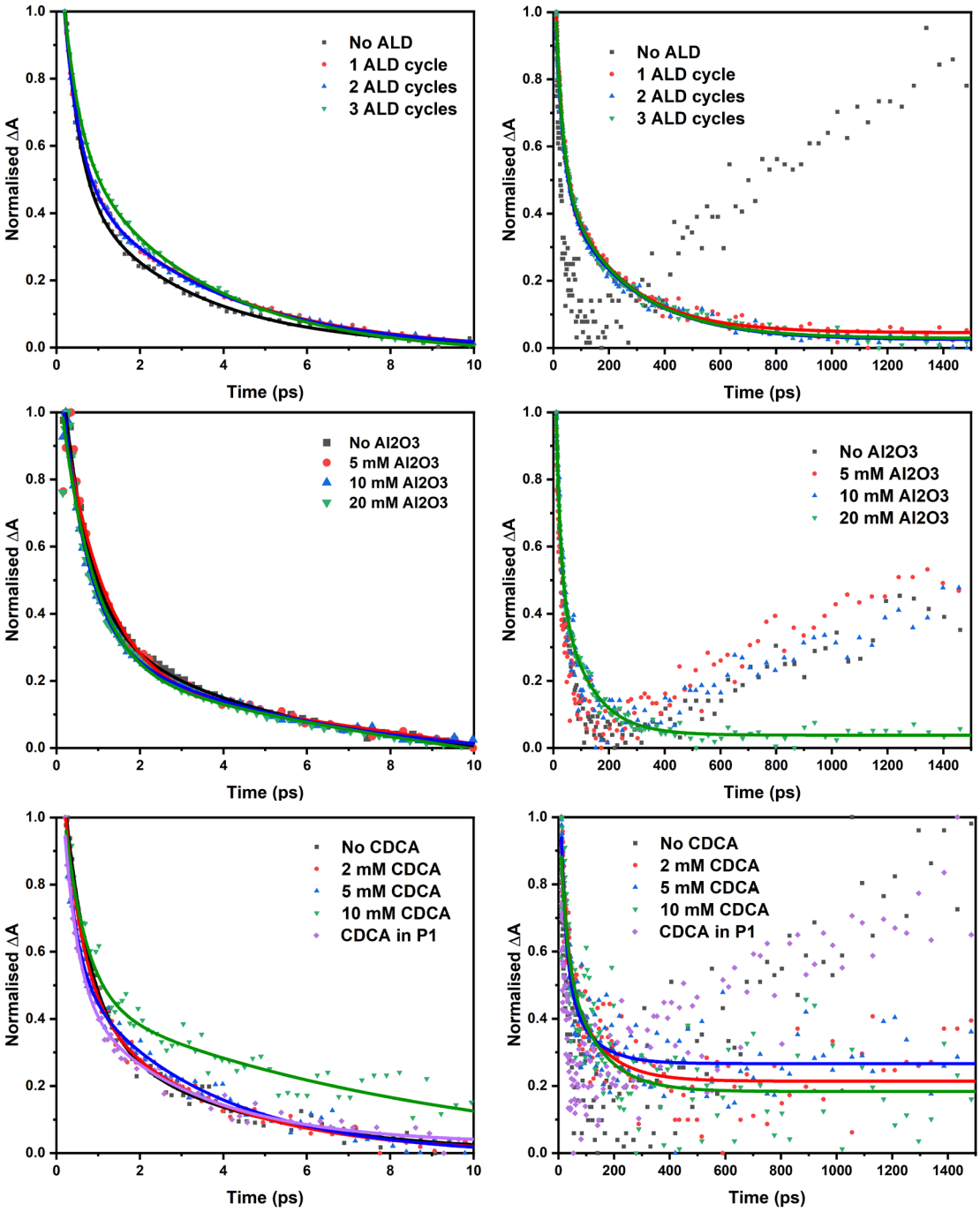

Figure 6.18: Kinetic traces obtained at 580 nm, corresponding to the excited state of the dye, for various NiO surface treatments. Data was extracted from TAS measurements upon excitation at 490 nm.

580 nm (0-10 ps)			
	τ_1 ps (A_1)	τ_2 ps (A_2)	y_0
NiO|P1	0.36 ± 0.02 (0.95)	2.81 ± 0.22 (0.51)	$4x10^{-4}$
NiO|**1 ALD cycle**|P1	0.37 ± 0.01 (0.83)	3.40 ± 0.13 (0.55)	-0.01
NiO|**2 ALD cycles**|P1	0.36 ± 0.02 (0.83)	3.28 ± 0.16 (0.55)	-0.01
NiO|**3 ALD cycles**|P1	0.40 ± 0.02 (0.68)	3.15 ± 0.11 (0.65)	-0.02

Table 6.2(a): Fitted lifetimes (τ) of the excited state of the dye with corresponding amplitudes (A) and offset (y_0) for various NiO surface treatments.

580 nm (10-1500 ps)			
	τ_3 ps (A_3)	τ_4 ps (A_4)	y_0
NiO|**1 ALD cycle**|P1	24.86 ± 1.21 (0.72)	218.07 ± 10.40 (0.49)	0.05
NiO|**2 ALD cycles**|P1	26.89 ± 1.08 (0.71)	249.07 ± 11.01 (0.47)	0.02
NiO|**3 ALD cycles**|P1	26.49 ± 1.09 (0.70)	238.01 ± 10.03 (0.49)	0.02

580 nm (0-10 ps)			
	τ_1 ps (A_1)	τ_2 ps (A_2)	y_0
NiO|P1	0.62 ± 0.05 (0.90)	5.00 ± 1.48 (0.45)	-0.05
NiO|**5 mM Al_2O_3**|P1	0.40 ± 0.03 (1.18)	2.84 ± 0.24 (0.54)	0.01
NiO|**10 mM Al_2O_3**|P1	0.45 ± 0.02 (0.98)	3.54 ± 0.35 (0.46)	-0.01
NiO|**20 mM Al_2O_3**|P1	0.40 ± 0.02 (1.12)	3.39 ± 0.23 (0.48)	-0.01
580 nm (10-1500 ps)			
	τ_3 ps (A_3)	τ_4 ps (A_4)	y_0
NiO|**20 mM Al_2O_3**|P1	16.28 ± 1.00 (0.93)	109.16 ± 6.12 (0.50)	0.04

580 nm (0-10 ps)			
	τ_1 ps (A_1)	τ_2 ps (A_2)	y_0
NiO|P1	0.59 ± 0.07 (0.92)	3.60 ± 1.04 (0.42)	-7.4×10^{-4}
NiO|**2 mM CDCA**|P1	0.46 ± 0.05 (0.85)	3.18 ± 0.52 (0.50)	-0.001
NiO|**5 mM CDCA**|P1	0.31 ± 0.05 (0.81)	3.23 ± 0.43 (0.57)	-0.008
NiO|**10 mM CDCA**|P1	0.52 ± 0.11 (0.78)	8.49 ± 7.32 (0.50)	-0.028
NiO|**CDCA in P1**|P1	0.34 ± 0.04 (0.89)	2.85 ± 0.39 (0.47)	0.027
580 nm (10-1500 ps)			
	τ_3 ps (A_3)	τ_4 ps (A_4)	y_0
NiO|**2 mM CDCA**|P1	22.74 ± 10.32 (0.56)	115.39 ± 47.06 (0.38)	0.21
NiO|**5 mM CDCA**|P1	19.17 ± 7.28 (0.71)	92.56 ± 48.59 (0.29)	0.27
NiO|**10 mM CDCA**|P1	21.32 ± 15.26 (0.46)	117.11 ± 50.26 (0.45)	0.18

Table 6.2(b): Fitted lifetimes (τ) of the excited state of the dye with corresponding amplitudes (A) and offset (y_0) for various NiO surface treatments.

6.4.6 Kinetics at 630 nm – reduced state of the dye

The transient absorption spectra show a positive absorption feature at around 630 nm. This is assigned to the reduced state of the dye, $P1^-$. In Figure 6.19, it is evident that the recombination process for devices with and without ALD and Al_2O_3 treatments is very similar. For the fast decay, τ_1= < 1 ps and τ_2 is a few picoseconds, and for the slower decay, τ_1 is around 30 ps and τ_2 is around 300 ps. This is in line with measurements obtained by Qin et al. who observed a decay within a few hundred picoseconds.[22] However, for CDCA surface treatment the recombination process seems to be affected. This supports the J-V characteristics obtained in Section 6.3.3, where CDCA was the only treatment seen to increase the J_{SC}.

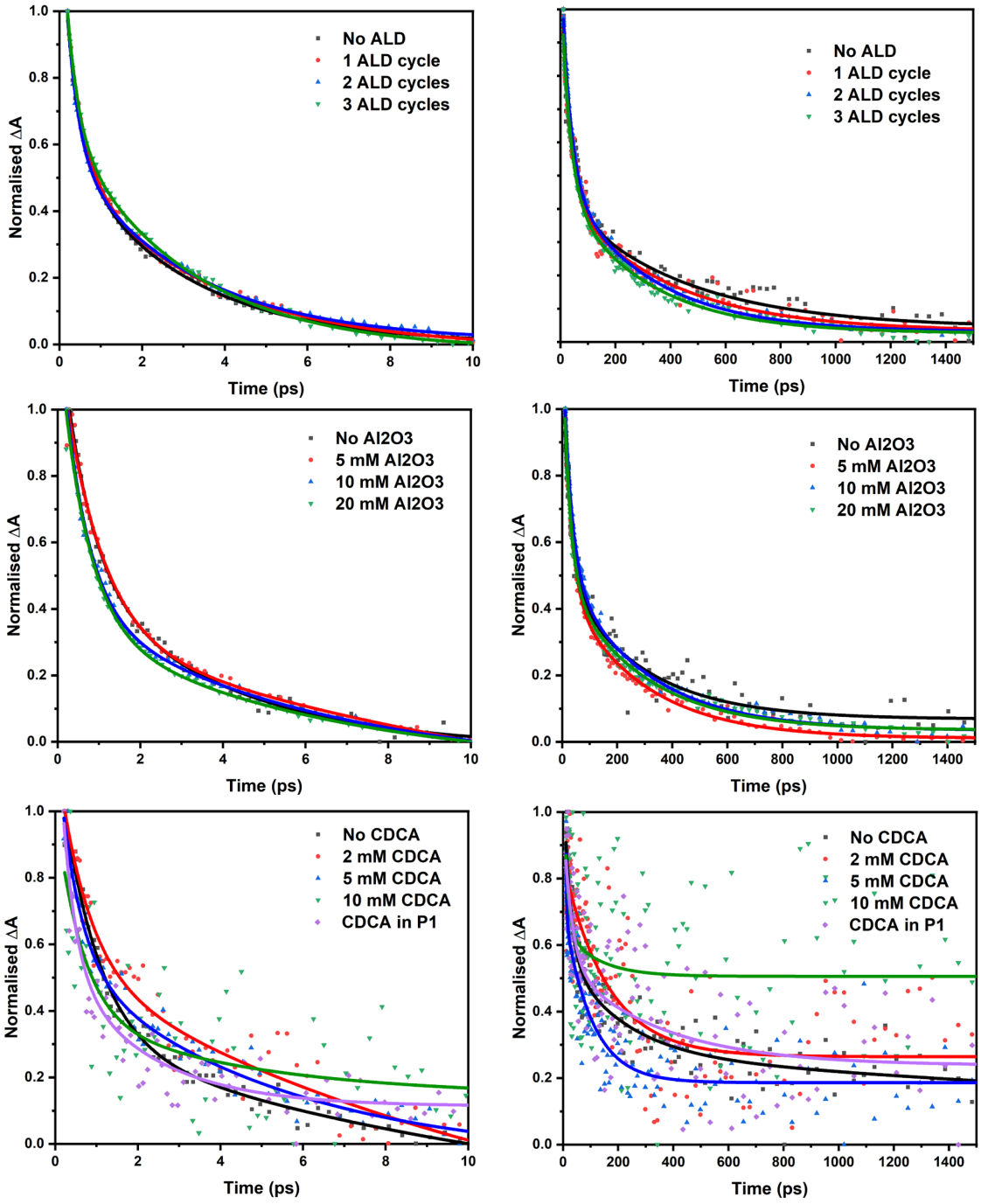

Figure 6.19: Kinetic traces obtained at 630 nm, corresponding to the reduced state of the dye, for various NiO surface treatments. Data was extracted from TAS measurements upon excitation at 490 nm.

630 nm (0-10 ps)			
	τ_1 ps (A_1)	τ_2 ps (A_2)	y_0
NiO|P1	0.34 ± 0.02 (0.75)	2.84 ± 0.16 (0.59)	5.6×10^{-4}
NiO|**1 ALD cycle**|P1	0.38 ± 0.02 (0.76)	3.30 ± 0.20 (0.58)	-0.01
NiO|**2 ALD cycles**|P1	0.28 ± 0.02 (0.86)	3.00 ± 0.14 (0.59)	0.01
NiO|**3 ALD cycles**|P1	0.28 ± 0.02 (0.74)	2.90 ± 0.11 (0.70)	-0.02

Table 6.3(a): Fitted lifetimes (τ) of the reduced state of the dye with corresponding amplitudes (A) and offset (y_0) for various NiO surface treatments.

630 nm (10-1500 ps)			
	τ_3 ps (A_3)	τ_4 ps (A_4)	y_0
NiO|P1	36.03 ± 2.92 (0.68)	431.67 ± 66.89 (0.39)	0.04
NiO|**1 ALD cycle**|P1	33.10 ± 2.60 (0.69)	377.34 ± 47.58 (0.41)	0.03
NiO|**2 ALD cycles**|P1	32.75 ± 1.21 (0.68)	311.85 ± 14.70 (0.46)	0.03
NiO|**3 ALD cycles**|P1	31.58 ± 1.53 (0.67)	301.73 ± 18.90 (0.43)	0.03

630 nm (0-10 ps)			
	τ_1 ps (A_1)	τ_2 ps (A_2)	y_0
NiO|P1	0.71 ± 0.10 (0.77)	3.78 ± 1.00 (0.55)	-0.02
NiO|**5 mM Al_2O_3**|P1	0.94 ± 0.12 (0.90)	15.88 ± 27.01 (0.68)	-0.36
NiO|**10 mM Al_2O_3**|P1	0.59 ± 0.04 (0.88)	6.08 ± 1.34 (0.51)	-0.09
NiO|**20 mM Al_2O_3**|P1	0.65 ± 0.07 (0.88)	5.92 ± 2.42 (0.45)	-0.08
630 nm (10-1500 ps)			
	τ_3 ps (A_3)	τ_4 ps (A_4)	y_0
NiO|P1	29.96 ± 3.81 (0.64)	283.94 ± 43.27 (0.43)	0.07
NiO|**5 mM Al_2O_3**|P1	26.57 ± 1.35 (0.80)	280.83 ± 18.32 (0.46)	0.01
NiO|**10 mM Al_2O_3**|P1	29.85 ± 1.54 (0.70)	292.96 ± 17.34 (0.49)	0.03
NiO|**20 mM Al_2O_3**|P1	25.11 ± 1.20 (0.74)	282.65 ± 15.99 (0.46)	0.04

630 nm (0-10 ps)			
	τ_1 ps (A_1)	τ_2 ps (A_2)	y_0
NiO|P1	0.90 ± 0.14 (0.90)	13.01 ± 22.42 (0.59)	-0.27
NiO|**2 mM CDCA**|P1	0.74 ± 0.25 (0.66)	12.23 ± 18.01 (0.93)	-0.40
NiO|**5 mM CDCA**|P1	0.49 ± 0.13 (0.67)	5.12 ± 2.10 (0.61)	-0.05
NiO|**10 mM CDCA**|P1	0.63 ± 0.63 (0.62)	4.29 ± 13.66 (0.26)	0.14
NiO|**CDCA in P1**|P1	0.32 ± 0.14 (0.85)	2.06 ± 0.85 (0.46)	0.11
630 nm (10-1500 ps)			
	τ_3 ps (A_3)	τ_4 ps (A_4)	y_0
NiO|P1	21.10 ± 5.32 (0.65)	279.17 ± 66.27 (0.36)	0.21
NiO|**5 mM CDCA**|P1	3.35 ± 1.89 (4.34)	100.18 ± 13.81 (0.53)	0.19
NiO|**CDCA in P1**|P1	27.53 ± 19.53 (0.46)	339.37 ± 216.57 (0.31)	0.24

Table 6.3(b): Fitted lifetimes (τ) of the reduced state of the dye with corresponding amplitudes (A) and offset (y_0) for various NiO surface treatments.

6.5 Conclusion

The first half of this chapter aimed to minimise recombination at the ETM/FTO interface by implementing two different techniques for depositing a compact NiO blocking layer onto the conductive substrate. For spin coating of the NiO blocking layer, three spin coating cycles were carried out in succession followed by one annealing step. SEM and EDX analysis revealed large cracks in the blocking layer and J-V scans showed devices had short circuited. As a result, the experiment was repeated with three annealing steps, one after each successive spin coating

cycle. SEM showed a reduction in the size and frequency of the cracks. However J-V scans revealed no difference in J-V parameters, indicating the presence of a continuous electron pathway across each subsequent layer. Therefore, spray coating was utilised as an alternative deposition technique to deposit the NiO blocking layer. Spray coating was carried out on the in-house built Automated Spray Pyrolysis Machine (Chapter 4). SEM and EDX analysis showed small and large clusters of material on the surface of the FTO, indicating non-uniform coating of the NiO blocking layer. This could have been due to the spray coating parameters used during deposition, such as the speed of the spray head, the height of the spray head and the temperature of the hotplate. Further optimisation of these parameters is required, however due to the toxicity of NiO in aerosol form this optimisation was ruled out in the interest of safety for lab users. Consequently, another approach was used to minimise recombination within the device.

In the second half of this chapter, three NiO surface treatments were tested as blocking layers to minimise the recombination at the ETM/NiO interface; atomic layer deposition of alumina, aluminium alkoxide solution treatment, and chenodeoxycholic acid treatment. The aim here was to passivate Ni^{3+} surface states which may facilitate charge recombination. Out of the three treatments only CDCA was seen to increase $J_{SC.}$ However, the J-V curve still resembled straight lines. In NiO based DSCs, a similar J-V response was observed depicting straight lines when using 100% water as the electrolyte solvent.[13] This resistive behaviour was attributed to the localised electronic states centred on surface -OH groups associated with Ni vacancies. To investigate this further, transient absorption spectroscopy was carried out for all three surface treatments and their lifetimes of various processes was extracted from their kinetics. Overall, the change in kinetics arising from each surface treatment was not enough to make an impact on the performance of the solar cell, and devices still exhibited resistive behaviour. The lifetimes associated with the reduced state of the dye showed little to no variation between surface treatments and concentrations of each treatment tested, indicating recombination rates remained unaffected. However, a clear difference was observed between the slower process (tens of picoseconds to nanoseconds) that occurs at 580 nm, which is assigned to the excited state of the dye. This suggests that rather than mitigating recombination, the insulating layers had possibly contributed to the formation of non-injecting dyes anchored onto the Al_2O_3 sites, which could be associated with hole-shallow trapping. D'Amario et al. used transient absorption spectroscopy to analyse the trapping of electrons and holes by band gap excitation of NiO nanoparticle films and revealed that after a femtosecond pulse the hole

is trapped on a sub-picosecond time scale in a "Ni^{4+}" state – a shallow trap for holes since they are located close to the valence band.[11] This is visible for the p-ssDSCs in this work, as kinetic data displays fast processes that are < 1 ps. Therefore, once trapped the hole survives until it recombines within the nanosecond timeframe.

It was also uncovered that there are two kinds of holes that recombine with electrons in the reduced dye, both with very different kinetics.[23] Biphasic recombination kinetics show a fast pathway (15 nm) and a slow pathway (1 ms). The hole showing fast recombination is assigned to the "Ni^{4+}" trap and is most relevant at positive potentials. The slower recombination is assigned to the Ni^{3+} and is more important at negative potentials. Therefore, the fast recombination has a greater impact on device performance. Since these devices exhibit fast recombination, the poor device performance can be attributed to the "Ni^{4+}" shallow hole trapping.

Overall, it is believed that these devices exhibit fast recombination therefore significantly affecting hole injection into the NiO. It could be possible that other processes are occurring, such as silver ions (Ag^{+}) from the metal contacts have migrated into adjacent layers, including the electron transport material. Here, they could interfere with regeneration processes. However, due to not having working devices parameters such as transport time and recombination resistance from impedance could not be calculated. Future investigations could include employing different sensitisers to increase the lifetime of the charge separated state. If recombination of the trapped hole is slowed down then this could be outcompeted by regeneration.

6.6 Experimental Methods

6.6.1 Chemical reagents

All chemicals were used as received without further purification. Nickel(II) acetate tetrahydrate (99.995%), 2-methoxyethanol (99.8%, anhydrous), nickel(II) chloride (99.9%, anhydrous), poly(ethylene glycol)-*block*-poly*(*propylene glycol*)-block*-poly(ethylene glycol) (F108), aluminium-tri-*sec*-butoxide (97%), acetonitrile (>99.5%), PCBM (>99.5%), and

bathocuproine (96%) were purchased from Sigma-Aldrich. Ethanol (99.8%) was purchased from Fisher Chemical. P1 (DNFP01) was purchased from Dyenamo. Anhydrous isopropanol (99.8%, extra dry) and anhydrous chlorobenzene (99.5%, extra dry) were purchased from Acros Organics. Chenodeoxycholic acid was purchased from Apollo Scientific.

6.6.2 Device fabrication

FTO substrate preparation:

Fluorine-doped tin oxide (FTO, Pilkington, 7 Ω sq^{-1}) coated glass substrates were cleaned in ultrasonic baths of detergent diluted in tap water (15 min), de-ionised water (15 min), and ethanol (15 min) in sequence. The substrates were then blown dry using a nitrogen flow. The FTO was then etched using a Ulyxe laser etcher to create the electrode pattern (parameters specified in Section 3.2.2), and then exposed to UV-ozone for 15 min to remove the last traces of organic residues.

NiO blocking layer deposition:

Spin coating: A blocking layer solution of 0.5 M nickel acetate tetrahydrate in 2-methoxyethanol was deposited via spin coating onto clean FTO glass at 2000 rpm for 30 s. The process was repeated 2 and 3 times to obtain different film thicknesses for comparison. The spin coated films were annealed at 450 °C for 30 min to allow thermal decomposition of nickel acetate tetrahydrate into dense NiO.

Spray coating: A blocking layer solution of 37 mM nickel acetate tetrahydrate in 2-methoxyethanol was deposited using an in-house built Automated Spray Pyrolysis Machine (see Chapter 4). An ultrasonic spray head was fed the precursor solution at a rate of 6.7 ml min^{-1}. The spray head was positioned at 18 cm above the substrates, which were kept heated at 450 °C. The processor's mechanical amplitude was set to 49% and pulse set to 100%. The speed at which the ultrasonic spray head moved was set to 2000 mm min^{-1}. 17 and 30 repetitive spraying cycles were performed. After each spraying cycle, a wait time of 60 s was used to allow thermal decomposition of the precursor solution.

Mesoporous NiO deposition:

A $NiCl_2$ sol-gel was prepared using the polymer templating method described by Suzuki *et al.* A NiO precursor solution was prepared by dissolving anhydrous $NiCl_2$ (1g) and the tri-block co-polymer F108 (poly(ethylene glycol)-*block*-poly*(*propylene glycol*)*-*block*-poly(ethylene glycol)) (1g) into a mixture of ultra-pure deionised water (3g) and ethanol (6g). The solution was stirred overnight and left to rest for 2 weeks. The mixture was centrifuged for 15 min to sediment out undissolved $NiCl_2$ and amorphous NiO. The sol-gel solution was then slot-die coated onto the NiO blocking layer at a coating speed of 2.5 mm s^{-1} and a dispense rate of 0.435 µl s^{-1}, followed by sintering on a hotplate at 450°C for 30 min. This process was repeated twice.

Mesoporous NiO surface treatments:

Atomic layer deposition of alumina: Substrates were heated to 200°C and the sequential deposition of the gaseous reactants of water (H_2O – 50 cycles) and trimethylaluminum (TMA – 5 cycles) was undertaken. The overall reaction is $2Al(CH_3)_3 + 3H_2O \rightarrow Al_2O_3 + 6CH_4$. Aluminium could exist in the form Al_2O_3, AlO(OH), or $Al(OH)_3$. This process was repeated 1 – 3 times to control the thickness of the alumina.

Aluminium alkoxide solution treatment: The aluminium alkoxide solution treatment was carried out in a nitrogen filled glovebox. NiO films were immersed in 5 mM, 10 mM, 15 mM and 20 mM solutions of Aluminium-tri-*sec*-butoxide in anhydrous isopropanol at 60°C for 20 min. Once removed from the solution, half of the substrates underwent a rinsing step with anhydrous isopropanol. All substrates, including non-treated NiO, were heated at 200°C.

Dye sensitisation:

Once cooled to 70°C the substrates were immersed into a solution of P1 sensitiser (0.2 mM) in acetonitrile. The substrates were left in the solution overnight and then the sensitised electrodes were rinsed with acetonitrile.

Co-sensitisation with chenodeoxycholic acid: For the devices where CDCA was utilised as a co-adsorbent, 0.6 mM CDCA was added to the P1 dye bath.

Sensitised mesoporous NiO surface treatment:

Chenodeoxycholic acid treatment: For the cases where chenodeoxycholic acid (CDCA) was utilised as a surface treatment, 2 mM, 5 mM and 10 mM solutions of CDCA in ethanol were prepared and deposited onto the substrates via spin coating at 2000 rpm for 30 s. No rinsing after spin coating was performed.

Electron transport material deposition:

The preparation and deposition of the ETM solution was carried out in a nitrogen-filled glovebox. The ETM solution was homogeneously spread by means of a pipette onto the sensitised electrode and left to penetrate into the mesoporous network for 30 s, followed by a two-step spin coating for 3 s at 1000 rpm and then 30 s at 3000 rpm. The formulation of the ETM solution was 40 mg ml^{-1} PCBM in anhydrous chlorobenzene. The solution was filtered through a 0.45 µm polytetrafluoroethylene (PTFE) syringe filter and 60 µl was dispensed onto the substrate. The substrates were placed on a hotplate at 100°C for 5 min, then left overnight in a desiccator.

Deposition of interlayer:

The preparation and deposition of the interlayer solution was carried out in a nitrogen-filled glovebox. A 0.5 mg ml^{-1} solution of bathocuproine (BCP) in anhydrous isopropanol was left to stir overnight at 70°C. The BCP solution was deposited onto the substrates via spin coating at 5000 rpm for 20 s, then left for 10 min at room temperature.

Metal electrode deposition:

The substrates were placed in a BOC-Edwards Auto thermal evaporator where 120 nm of silver was deposited through a mask under high vacuum (10^{-6} Torr) at a rate of 1 $Å s^{-1}$ to form the silver electrodes.

6.6.3 Characterisation

SEM was performed using a JSM-IT510 InTouchScope Microscope with an Oxford Instruments Ultim Max 100 EDX detector. J-V measurements were taken using a Keysight U2722A source meter with a HelioSim-CL60 solar simulator (Voss electronic GmbH). Cyclic voltammetry measurements were taken using an IviumStat potentiostat (details of the setup are in section 6.3.2). TAS measurements were performed using an Ultrafast Systems TAS Spectrometer. Samples were pumped with Ti:Sapphire laser at 1kHz (800nm source pump). Excitation wavelength was selected using an optical parametric amplifier. For ultrafast measurements a portion of the pump beam was routed through a sapphire crystal to achieve white light continuum to act a probe beam. Excitation of 490 nm was used with a pump power of 60 µW. The pump power was varied to check for linearity and minimised to limit dye photobleaching. Four spectra were taken per sample and averaged to achieve the presented spectra.

References

1 P. Bonhôte, J.-E. Moser, R. Humphry-Baker, N. Vlachopoulos, S. M. Zakeeruddin, L. Walder and M. Grätzel, Long-Lived Photoinduced Charge Separation and Redox-Type Photochromism on Mesoporous Oxide Films Sensitized by Molecular Dyads, *J Am Chem Soc*, 1999, **121**, 1324–1336.

2 T. T. T. Pham, S. K. Saha, D. Provost, Y. Farré, M. Raissi, Y. Pellegrin, E. Blart, S. Vedraine, B. Ratier, D. Aldakov, F. Odobel and J. Bouclé, Toward Efficient Solid-State p-Type Dye-Sensitized Solar Cells: The Dye Matters, *The Journal of Physical Chemistry C*, 2017, **121**, 129–139.

3 L. Zhang, G. Boschloo, L. Hammarström and H. Tian, Solid state p-type dye-sensitized solar cells: concept, experiment and mechanism, *Physical Chemistry Chemical Physics*, 2016, **18**, 5080–5085.

4 B. Xu, S. Wrede, A. Curtze, L. Tian, P. B. Pati, L. Kloo, Y. Wu and H. Tian, An Indacenodithieno[3,2-b]thiophene-Based Organic Dye for Solid-State p-Type Dye-Sensitized Solar Cells, *ChemSusChem*, 2019, **12**, 3243–3248.

5 L. Tian, T. Törndahl, J. Lin, P. B. Pati, Z. Zhang, T. Kubart, Y. Hao, J. Sun, G. Boschloo and H. Tian, Mechanistic Insights into Solid-State p-Type Dye-Sensitized Solar Cells, *The Journal of Physical Chemistry C*, 2019, **123**, 26151–26160.

6 K. V. Rao and A. Smakula, Dielectric Properties of Cobalt Oxide, Nickel Oxide, and Their Mixed Crystals, *J Appl Phys*, 1965, **36**, 2031–2038.

7 E. Thimsen, A. B. F. Martinson, J. W. Elam and M. J. Pellin, Energy Levels, Electronic Properties, and Rectification in Ultrathin p-NiO Films Synthesized by Atomic Layer Deposition, *The Journal of Physical Chemistry C*, 2012, **116**, 16830–16840.

8 P. Lunkenheimer, A. Loidl, C. R. Ottermann and K. Bange, Correlated barrier hopping in NiO films, *Phys Rev B*, 1991, **44**, 5927–5930.

9 L. D'Amario, R. Jiang, U. B. Cappel, E. A. Gibson, G. Boschloo, H. Rensmo, L. Sun, L. Hammarström and H. Tian, Chemical and Physical Reduction of High Valence Ni States in Mesoporous NiO Film for Solar Cell Application, *ACS Appl Mater Interfaces*, 2017, **9**, 33470–33477.

10 A. G. Marrani, V. Novelli, S. Sheehan, D. P. Dowling and D. Dini, Probing the Redox States at the Surface of Electroactive Nanoporous NiO Thin Films, *ACS Appl Mater Interfaces*, 2014, **6**, 143–152.

11 L. D'Amario, J. Föhlinger, G. Boschloo and L. Hammarström, Unveiling hole trapping and surface dynamics of NiO nanoparticles, *Chem Sci*, 2018, **9**, 223–230.

12 L. Favereau, Y. Pellegrin, L. Hirsch, A. Renaud, A. Planchat, E. Blart, G. Louarn, L. Cario, S. Jobic, M. Boujtita and F. Odobel, Engineering Processes at the Interface of p-Semiconductor for Enhancing the Open Circuit Voltage in p-Type Dye-Sensitized Solar Cells, *Adv Energy Mater*, DOI:10.1002/aenm.201601776.

13 A. D. Taggart, J. M. Evans, L. Li, K. J. Lee, J. L. Dempsey, Y. Kanai and J. F. Cahoon, Enabling Aqueous NiO Photocathodes by Passivating Surface Sites That Facilitate Proton-Coupled Charge Transfer, *ACS Appl Energy Mater*, 2020, **3**, 10702–10713.

14 P. Ho, L. Q. Bao, K.-S. Ahn, R. Cheruku and J. H. Kim, P-Type dye-sensitized solar cells: Enhanced performance with a NiO compact blocking layer, *Synth Met*, 2016, **217**, 314–321.

15 G. Natu, Z. Huang, Z. Ji and Y. Wu, The Effect of an Atomically Deposited Layer of Alumina on NiO in P-type Dye-Sensitized Solar Cells, *Langmuir*, 2012, **28**, 950–956.

16 L. Tian, R. Tyburski, C. Wen, R. Sun, M. Abdellah, J. Huang, L. D'Amario, G. Boschloo, L. Hammarström and H. Tian, Understanding the Role of Surface States on Mesoporous NiO Films, *J Am Chem Soc*, 2020, **142**, 18668–18678.

17 D. Cappus, C. Xu, D. Ehrlich, B. Dillmann, C. A. Ventrice, K. Al Shamery, H. Kuhlenbeck and H.-J. Freund, Hydroxyl groups on oxide surfaces: NiO(100), NiO(111) and Cr2O3(111), *Chem Phys*, 1993, **177**, 533–546.

18 S. Uehara, S. Sumikura, E. Suzuki and S. Mori, Retardation of electron injection at NiO/dye/electrolyte interface by aluminium alkoxide treatment, *Energy Environ Sci*, 2010, **3**, 641.

19 S. Powar, T. Daeneke, M. T. Ma, D. Fu, N. W. Duffy, G. Götz, M. Weidelener, A. Mishra, P. Bäuerle, L. Spiccia and U. Bach, Highly Efficient p-Type Dye-Sensitized Solar Cells based on Tris(1,2-diaminoethane)Cobalt(II)/(III) Electrolytes, *Angewandte Chemie International Edition*, 2013, **52**, 602–605.

20 Z.-S. Wang, Y. Cui, Y. Dan-oh, C. Kasada, A. Shinpo and K. Hara, Thiophene-Functionalized Coumarin Dye for Efficient Dye-Sensitized Solar Cells: Electron Lifetime Improved by Coadsorption of Deoxycholic Acid, *The Journal of Physical Chemistry C*, 2007, **111**, 7224–7230.

21 E. Sheibani, L. Zhang, P. Liu, B. Xu, E. Mijangos, G. Boschloo, A. Hagfeldt, L. Hammarström, L. Kloo and H. Tian, A study of oligothiophene–acceptor dyes in p-type dye-sensitized solar cells, *RSC Adv*, 2016, **6**, 18165–18177.

22 P. Qin, J. Wiberg, E. A. Gibson, M. Linder, L. Li, T. Brinck, A. Hagfeldt, B. Albinsson and L. Sun, Synthesis and Mechanistic Studies of Organic Chromophores with Different Energy Levels for p-Type Dye-Sensitized Solar Cells, *The Journal of Physical Chemistry C*, 2010, **114**, 4738–4748.

23 L. D'Amario, L. J. Antila, B. Pettersson Rimgard, G. Boschloo and L. Hammarström, Kinetic Evidence of Two Pathways for Charge Recombination in NiO-Based Dye-Sensitized Solar Cells, *J Phys Chem Lett*, 2015, **6**, 779–783.

Chapter 7.

Tandem ssDSC assembly using a Charge Recombination Layer

7.1 Introduction

Tandem photovoltaic devices are constructed by sandwiching two individual cells (subcells) together. In a tandem device, the incident light that is unabsorbed by the top subcell is passed through and absorbed by the bottom subcell, thereby broadening the light absorption range. This offers the potential to increase the efficiency beyond the Shockley-Queisser limit for a single junction solar cell, as the maximum efficiency for a device with two photoactive dye-sensitised electrodes is 43%.[1] Based on Kirchhoff's law, the theoretical photovoltage of a series connected tandem device is the sum of the voltages generated from the two subcells, whereas the photocurrent equals that of the subcell with the lowest produced current.[2]

Integration of the two subcells requires electrical coupling. In liquid tandem DSCs (t-DSCs) the subcells are electrically connected as they share a redox electrolyte. However, for solid-state tandem DSCs (t-ssDSCs) the liquid electrolyte is replaced with a HTM and an ETM for the n-type subcell and p-type subcell, respectively. External wiring between the separate devices will increase resistance and require additional interconnections. Therefore, the two subcells are joined together by what is known as a charge recombination layer (CRL). The role of this layer is to facilitate the recombination of separated charge carriers that are photogenerated within each subcell. After photoexcitation, electrons and holes are transported to their respective layers, the ETM and the HTM, then undergo recombination and annihilation within the CRL.[2]

In t-ssDSCs, the CRL should form an ohmic contact that minimises energy barriers for the charge carriers to flow across the CRL and facilitates efficient recombination. An ohmic contact also enhances the flow of current between the subcells, which enables efficient transfer of charge carriers from one subcell to the other. This promotes successive photon absorption by the subcells and enhances the overall electrical output of the tandem solar cell. The choice of the CRL is critical to device performance. A work function contrast is required to provide adequate energy level alignment for electron and hole collection. The CRL should be processed at low temperatures with a short annealing time to avoid damaging the underlying organic dye. As well as this, each successive layer of the CRL requires the use of orthogonal solvents. It is also important that the CRL has high optical transparency to allow unabsorbed light from the top subcell to pass through to the bottom sub-cell.

In 2015, Jiang et al. proposed a two-terminal perovskite/perovskite tandem solar cell that uses a CRL consisting of Spiro-OMeTAD/PEDOT:PSS/PEI/PCBM:PEI.[3] This is shown in Figure 7.1. The choice of Spiro-OMeTAD and PCBM enables efficient hole and electron collection, respectively. Additionally, PEI is employed to modify the surface and establish a work function contrast between the upper and lower surfaces of the PEDOT:PSS film.

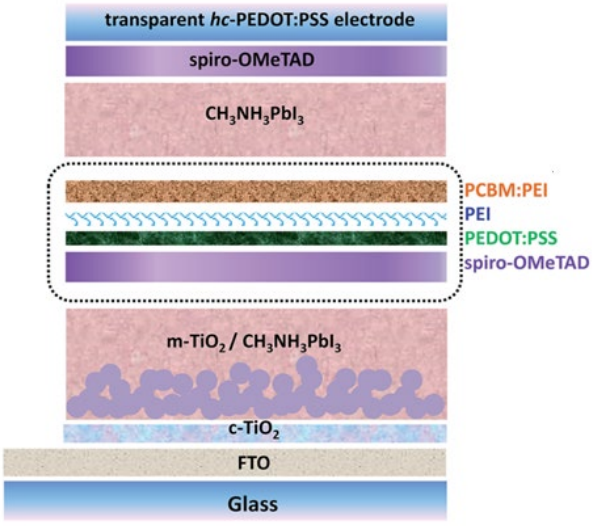

Figure 7.1: Two-terminal bottom-up perovskite/perovskite tandem solar cell utilising a CRL composed of Spiro-OMeTAD/PEDOT:PSS/PEI/PCBM:PEI. Figure obtained from DOI: 10.1039/c5ta08744a

The tandem device in this thesis is comprised of an n-type ssDSC that incorporates spiro-OMeTAD as the HTM, and a p-type ssDSC that incorporates PCBM as the ETM. Therefore, the CRL proposed by Jiang et al. seemed a reasonable starting point for the fabrication of a CRL for such tandem ssDSC.

7.2 Tandem cell design

In earlier chapters, the cell design was arranged to have both top and bottom contacts located on one side of the substrate. However, in the tandem device two glass substrates are joined together. Consequently, the original singular cell design is no longer viable as it would prevent access to the contacts. Therefore, the cell design required modification to allow accessibility to contacts on individual glass substrates. Figure 7.2 shows the tandem cell design, where the grey area represents the area that is etched away. This creates two channels that, when the two subcells are placed together, create 2 pixels per tandem device.

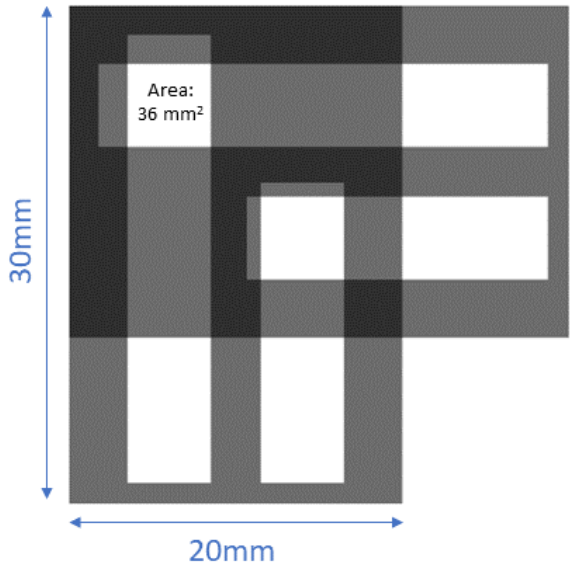

Figure 7.2: Tandem ssDSC device design consisting of two subcells deposited on 30x20 mm FTO substrates. The FTO substrates are etched (grey area) to leave two FTO channels (white areas: 20x6 mm and 10x6 mm) that create two pixels with active area of 36 mm^2.

7.3 Charge Recombination Layer

7.3.1 Spiro-OMeTAD

The thickness of the Spiro-OMeTAD within the CRL employed in the perovskite/perovskite tandem device was 150 nm.[3] A 150 nm overstanding layer was found to guarantee a smooth surface to provide a reliable serial connection between the two subcells in a ssDSC/vacuum deposited bulk heterojunction tandem solar cell.[4] However, spin coating parameters used for

the perovskite/perovskite tandem were for deposition directly onto the perovskite film. Therefore, these parameters needed to be adjusted for deposition onto a mesoporous TiO_2 network in the ssDSC tandem. Consequently, the Spiro-OMeTAD that infiltrates the mesoporous TiO_2 in the n-type subcell requires a 150 nm overstanding layer. Results from Docampo et al. (Figure 7.3) revealing the thickness of the overstanding layer as a function of casting Spiro-OMeTAD concentration (for the same concentration of tBP and LiTFSI additives used in this work) was used to extract the Spiro-OMeTAD concentration required to provide an overstanding layer of suitable thickness for integration into the CRL.[5] A linear fit was employed for the slope containing data after 0.11 vol% and using the equation of the slope the Spiro-OMeTAD concentration that results in a 150 nm overstanding layer was found to be 0.126 vol%, therefore a solution containing 0.126 vol% of Spiro-OMeTAD was deposited onto the photoanode.

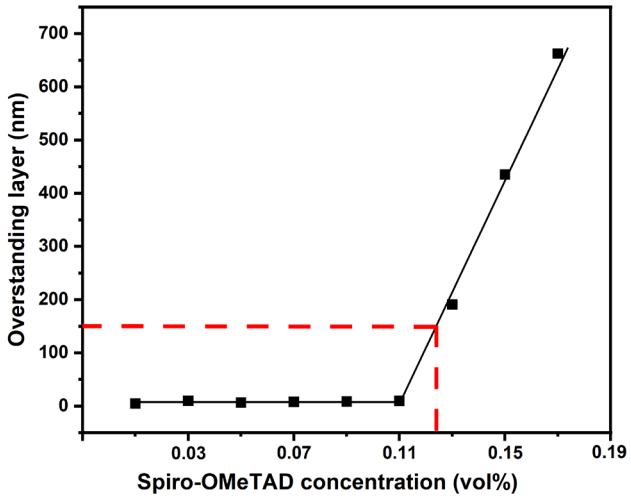

Figure 7.3: Overstanding layer thickness as a function of casting Spiro-OMeTAD concentration, where black squares show data from SEM image analysis, black line represents the prediction from fit, and the red dashed line shows the vol% of Spiro-OMeTAD that results in a 150 nm overstanding layer.
Data retrieved from DOI: 10.1002/adfm.201201223

7.3.2 PCBM:PEI

The CRL utilises a PCBM:PEI mixture that replaced pure PCBM. The presence of PEI was found to increase the conductivity of PCBM from < 10^{-5} S cm^{-2} to around 0.015 S cm^{-2} when a 1:15 ratio of PEI:PCBM by weight was used.[3] To investigate how this will impact device performance transient absorption spectroscopy (TAS) of FTO/NiO/P1/PCBM:PEI/BCP/Ag devices was undertaken for varying concentrations of PEI added to the PCBM.

Figure 7.4 indicates the absorption peak centred around 630 nm differs when varying the concentration of PEI in the PCBM ETM, where a decrease in the amplitude of the absorption peak is observed with increasing concentration of PEI. This absorption peak is attributed to the reduced state of the dye. The impact that PEI has on device performance is discussed in Section 7.4 – Tandem J-V response.

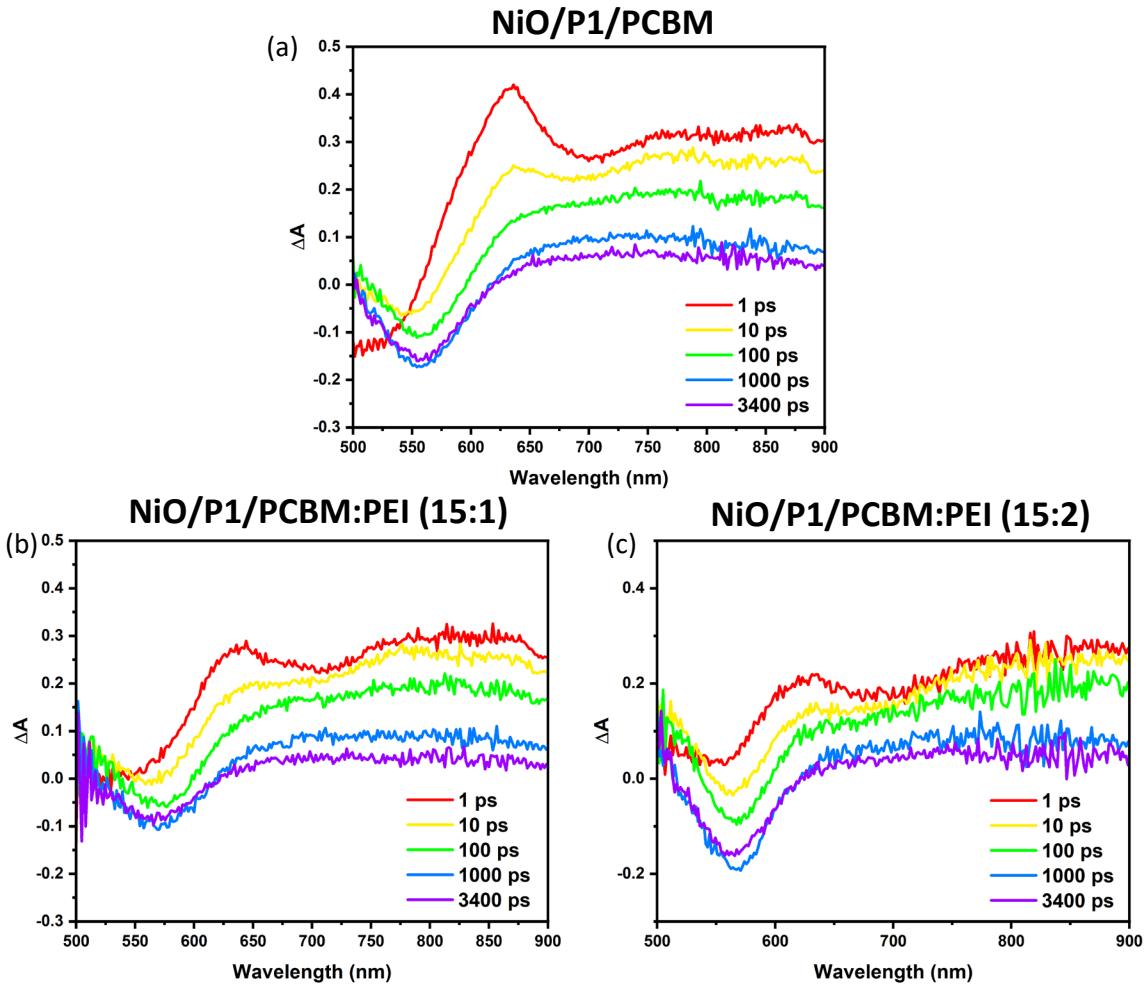

Figure 7.4: Transient absorption spectroscopy upon excitation at 490 nm of NiO/P1 with (a) PCBM, (b) a 15:1 ratio of PCBM:PEI, and (c) a 15:2 ratio of PCBM:PEI by weight utilised as electron transporting materials.

7.3.3 Ohmic contact

Due to wetting difficulties of the PEDOT:PSS, this layer in the CRL was replaced with a 5 nm layer of thermally evaporated silver (Ag), as Ag has been successfully implemented as a recombination site in other tandem PV technologies.[4,6] The work function of PEDOT:PSS used in the perovskite/perovskite tandem is about 5.0 eV,[3] and the work function of Ag deposited on Spiro-OMeTAD is around 4.6 eV.[7] An initial test of the CRL was carried out to ensure an

ohmic contact was achieved. This was performed by depositing Spiro-OMeTAD/Ag onto one FTO substrate and PCBM:PEI/PEI onto another FTO substrate (etched using the pattern shown in Figure 7.2 with silver contacts painted at the end of the FTO channel). I-V scans were performed while the substrates were clamped together. Figure 7.5(a) shows the I-V scan of the CRL without Ag exhibits a rectifying behaviour indicating a non-ohmic contact between the subcells, whereas Figure 7.5(b) shows that the CRL containing Ag forms a favourable ohmic contact. However, the currents obtained are low, indicating further optimisation is required.

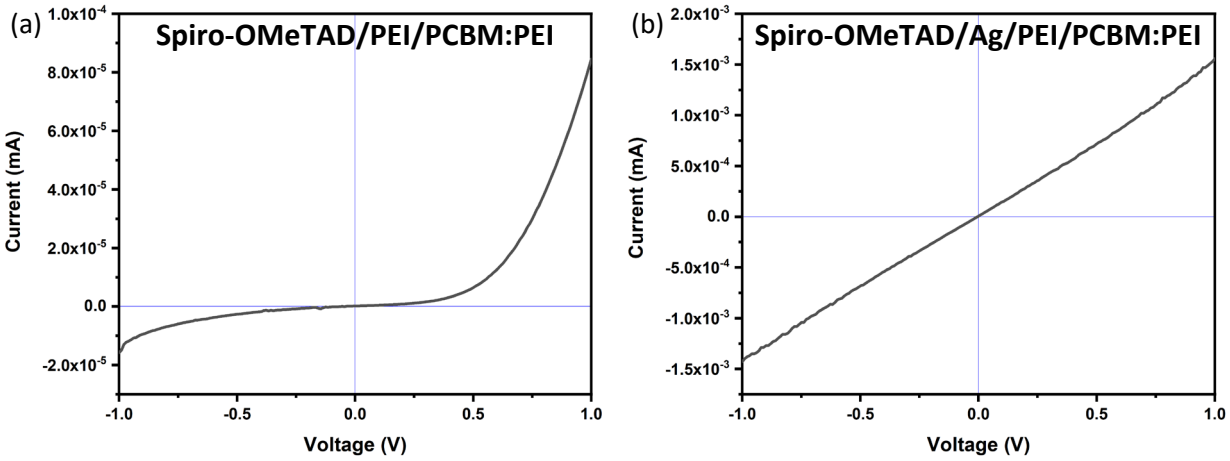

Figure 7.5: I-V response of (a) Spiro-OMeTAD/PEI/PCBM:PEI CRL and (b) Spiro-OMeTAD/Ag/PEI/PCBM:PEI CRL with a 15:1 ratio of PCBM:PEI by weight, measured at a scan rate of 0.5 V s^{-1}.

For devices employing the CRL in Figure 7.5(b), the PCBM:PEI blend will transport electrons to the Ag from the NiO subcell, the Spiro-OMeTAD will transport holes from the TiO_2 subcell, and these photogenerated charges will recombine at the Ag recombination centre. This is assisted by the presence of PEI that will form a work function contrast between the top and bottom sides of the CRL for electron and hole collection and enhance the conductivity of PCBM from < 10^{-5} S cm^{-2} to around 0.015 S cm^{-2} when a 1:15 ratio of PEI:PCBM by weight is used.[3]

7.3.4 Testing a transparent conductive adhesive for future applications in tandem ssDSCs

The tandem ssDSCs in this work were held together with clamps, however, extending the potential of tandem ssDSCs to real-world applications will involve ensuring their structural integrity and proper assembly. Consequently, tandem devices consisting of two glass substrates will require mechanical adhesion of the two subcells. In this work, a UV glue was tested to secure the subcells as one device. However, this resulted in no electrical contact

between the n-type side and the p-type side. Therefore, a transparent conductive adhesive (TCA) was tested within the CRL to electrically and mechanically assemble the subcells as one device. The TCA used is taken from the work by Bryant et al. that is designed to have high transparency (>98%) and conduction paths vertically (z-conduction),[8] making this a suitable option for use in the CRL of the tandem ssDSC. The TCA consists of a blend of PEDOT:PSS and an acrylic adhesive, therefore when testing the CRL with this adhesive layer the evaporated Ag layer formerly used in this work was omitted from the CRL, as the PEDOT:PSS will now act as the recombination site.

To test the TCA in the CRL the experiment in Section 7.3.1 was repeated to verify an ohmic contact is still achieved. The volume fraction of PEDOT:PSS used in the TCA was 0.0175. The ratio of PCBM:PEI was altered between 15:0.5, 15:1 and 15:2 by weight to vary the conductivity of the PCBM:PEI film.[3] Spiro-OMeTAD was deposited onto one pre-etched FTO substrate and the PCBM:PEI, PEI, and TCA were deposited onto another (etched using the pattern shown in Figure 7.2 with silver contacts painted at the end of the FTO channel). The weight of a glass substrate was too heavy to be held by the small channels of TCA deposited, therefore once adhered together the substrates were then secured in place using the UV glue. Figure 7.6 shows the J-V response of CRLs containing TCA with varying ratios of PCBM:PEI.

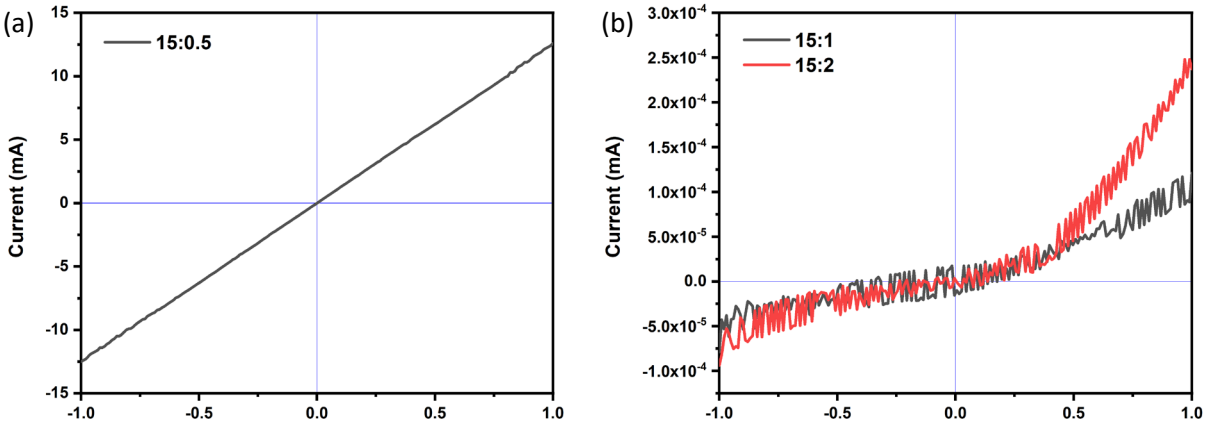

Figure 7.6: I-V response of Spiro-OMeTAD/PEDOT:PSS/PEI/PCBM:PEI CRL containing a TCA with a 0.0175 volume fraction of PEDOT:PSS, for the following ratios of PCBM:PEI: (a) 15:0.5, (b) 15:1 and 15:2 by weight, measured at a scan rate of 0.5 V s^{-1}.

The PEDOT:PSS at the surface of a TCA that contains a 0.0175 volume fraction of PEDOT:PSS is at most ~ 1.75% of the total surface area, therefore current will only be collected from the Spiro-OMeTAD layer from 1.75% directly underneath the PEDOT:PSS. Therefore, to assist charge collection across the whole Spiro-OMETAD surface Bryant et al. spray coated a 50 nm

interlayer of PEDOT:PSS onto the Spiro-OMeTAD.[8] Thus, future investigation will involve testing this interlayer in the CRL to improve charge extraction across the entirety of the Spiro-OMeTAD interface, followed by testing the modified CRL containing the TCA in a tandem ssDSC.

7.4 Tandem ssDSC J-V response

Tandem ssDSCs were constructed employing a Spiro-OMeTAD/Ag/PEI/PCBM:PEI CRL and their J-V response was measured under AM1.5 simulated sunlight of 100 mW cm^{-2}. To reveal the impact of the addition of PEI to the PCBM ETM on device performance, a series of devices were fabricated with varying concentrations of PEI, consisting of a 15:0.5, a 15:1, and a 15:2 ratio of PCBM:PEI by weight.

Figure 7.7 reveals that a higher V_{OC} and J_{SC} were obtained when illuminating from the n-type subcell side. The devices containing a 15:0.5 or 15:1 ratio of PCBM:PEI by weight performed slightly better than the device with no PEI added to PCBM. However, at a larger concentration of PEI where the ratio of PCBM:PEI by weight is 15:2, the device performance is hindered.

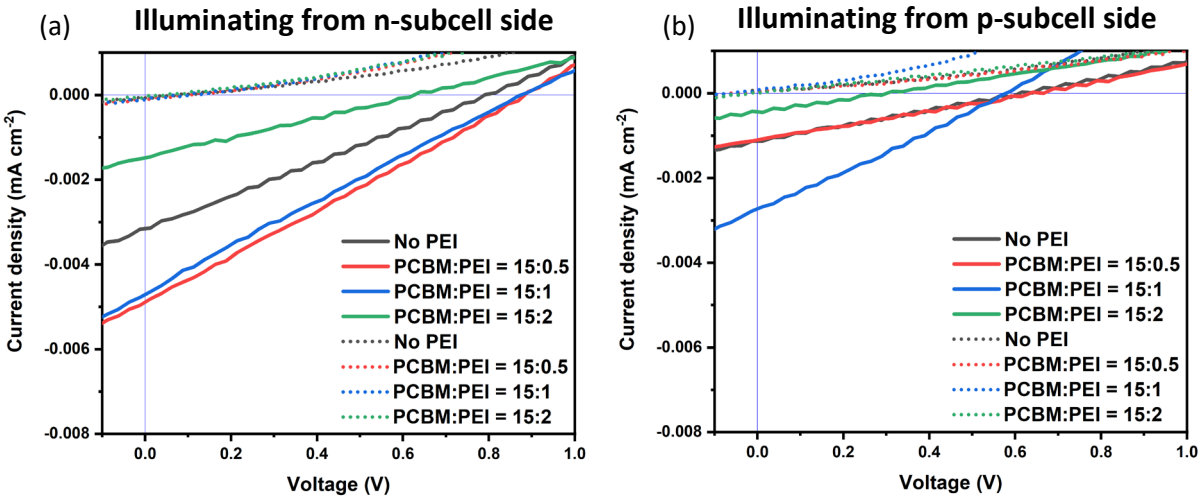

Figure 7.7: J-V response of tandem ssDSCs employing a Spiro-OMeTAD/Ag/PEI/PCBM:PEI CRL for (a) illumination from the n-type subcell side, and (b) illumination from the p-type subcell side, measured under AM1.5 simulated sun light of 100 mW cm^{-2} at a scan rate of 0.5 V s^{-1}. Dotted lines represent dark J-V curves.

Overall, the devices exhibit a poor FF and reveal the effects of parasitic resistances. This is likely due to the poor performance and resistive behaviour of the p-type subcell. A very high series resistance is likely present due to the inadequate blocking layer in the p-type subcell.

Additionally, the J_{SC} of the tandem ssDSCs is two orders of magnitude lower than the p-type and n-type ssDSCs studied in this thesis. This can be attributed to the low current drawn through the CRL (Figure 7.5). However, the V_{OC} reaches an impressive 0.88 V, which is higher than that of the n-type ssDSC and p-type ssDSC alone. Therefore, this study has highlighted the potential of the tandem ssDSC configuration and the ability to utilise the collective open-circuit voltages of the component devices.

7.5 Conclusion

In summary, the employment of a charge recombination layer (CRL) in a p-n tandem ssDSCs has shown to electrically connect the individual subcells and generate a V_{OC} of the tandem device that is higher than that of the individual subcells. The V_{OC} of the champion tandem device was 0.88 V, which is close to that of the highest efficiency liquid tandem DSC (V_{OC} = 0.91 V).[9] This is a promising result considering the substantial set back in performance due to the inability of the p-type ssDSC to perform as expected. However, the low J_{SC} of the tandem devices highlights that further optimisation of the CRL and exploration of alternative materials is required to fully unlock the potential of tandem ssDSCs, as the CRL employed in the tandem ssDSC was seen to reduce the J_{SC} of the tandem device by two orders of magnitude in comparison with the theoretical J_{SC}. Future work should involve testing the CRL employing the transparent conductive adhesive as the current obtained across this CRL was substantially higher. A further study on the effects of PEI on device performance is also required, as the results obtained in this work are insufficient to make any conclusive determinations.

Furthermore, these results signify the importance of improving the performance of p-type ssDSCs; development of new p-type semiconductors that exhibit fast hole-transport properties, as well as the incorporation of dyes with broad absorption spectra and high extinction coefficients will help increase the PCE of the p-type device for improved efficiency of the tandem ssDSC.

7.6 Experimental Methods

7.6.1 Chemical reagents

All chemicals were used as received without further purification. Titanium(IV) isopropoxide (97%), acetylacetone (≥99%), transparent titania paste, titanium(IV) chloride tetrahydrofuran complex (97%), tert-Butanol (≥99.5%), acetonitrile (≥99.9%), spiro-OMeTAD (99%), tBP (98%), nickel(II) acetate tetrahydrate (99.995%), 2-methoxyethanol (99.8%, anhydrous), nickel(II) chloride (99.9%, anhydrous), poly(ethylene glycol)-*block*-poly*(*propylene glycol*)-block*-poly(ethylene glycol) (F108), aluminium-tri-*sec*-butoxide (97%), PCBM (>99.5%), and polyethylenimine (PEI) were purchased from Sigma-Aldrich. Ethanol (99.8%) was purchased from Fisher Chemical. LEG4 (DN-F05) and P1 (DNFP01) were purchased from Dyenamo. Anhydrous chlorobenzene (99.5%, extra dry), anhydrous chloroform (99.9%, extra dry), anhydrous isopropanol (99.8%, extra dry), and LiTFSI (99%) were purchased from Acros Organics. Anhydrous acetonitrile (>99.8%) was purchased from Alfa Aesar. PEDOT:PSS (PH 1000) was purchased from Ossila.

7.6.2 Preparation of the photoanode

Fluorine-doped tin oxide (FTO, Pilkington, 7 Ω sq^{-1}) coated glass substrates were cleaned in ultrasonic baths of detergent diluted in tap water (15 min), de-ionised water (15 min), and ethanol (15 min) in sequence. The substrates were then blown dry using a nitrogen flow. The FTO was then etched using a Ulyxe laser etcher to create the electrode pattern (parameters specified in Section 3.2.2), and then exposed to UV-ozone for 15 min to remove the last traces of organic residues. A compact TiO_2 blocking layer was deposited via 15 spray cycles of spray pyrolysis on a hotplate at 450°C using an airbrush and N_2 as the carrier gas. The solution used in the spray pyrolysis was 3.6 ml acetylacetone and 2.4 ml titanium(IV) isopropoxide dissolved in 54 ml ethanol. To deposit the mesoporous TiO_2 film (~ 1.9 µm), transparent titania paste was screen printed onto the compact layer. After sintering on a hotplate at 450°C for 30 min the substrates were cooled to room temperature and immersed into a 40 mM aqueous solution of titanium(IV) chloride tetrahydrofuran complex for 20 min at 70°C. The substrates were then rinsed with de-ionised water and ethanol successively, and then annealed on a

hotplate at 500°C for 30 min. Once cooled to 70°C the substrates were immersed into a 0.1 mM solution of LEG4 sensitiser in a mixture of tert-butanol and acetonitrile (1:1 volume ratio). The substrates were left in the solution overnight and then the sensitised electrodes were rinsed with acetonitrile.

7.6.3 Preparation of the photocathode

Fluorine-doped tin oxide (FTO, Pilkington, 7 Ω sq^{-1}) coated glass substrates were cleaned in ultrasonic baths of detergent diluted in tap water (15 min), de-ionised water (15 min), and ethanol (15 min) in sequence. The substrates were then blown dry using a nitrogen flow. The FTO was then etched using a Ulyxe laser etcher to create the electrode pattern (parameters specified in Section 3.2.2), and then exposed to UV-ozone for 15 min to remove the last traces of organic residues. A blocking layer solution of 0.5 M nickel acetate tetrahydrate in 2-methoxyethanol was deposited via spin coating onto clean FTO glass at 2000 rpm for 30 s. The process was repeated 3 times. The spin coated films were annealed at 450 °C for 30 min to allow thermal decomposition of nickel acetate tetrahydrate into dense NiO. A $NiCl_2$ sol-gel was prepared using the polymer templating method described by Suzuki *et al.* A NiO precursor solution was prepared by dissolving anhydrous $NiCl_2$ (1g) and the tri-block co-polymer F108 (poly(ethylene glycol)-*block*-poly*(*propylene glycol*)*-*block*-poly(ethylene glycol)) (1g) into a mixture of ultra-pure deionised water (3g) and ethanol (6g). The solution was stirred overnight and left to rest for 2 weeks. The mixture was centrifuged for 15 min to sediment out undissolved $NiCl_2$ and amorphous NiO. The sol-gel solution was then slot-die coated onto the NiO blocking layer at a coating speed of 2.5 mm s^{-1} and a dispense rate of 0.435 µl s^{-1}, followed by sintering on a hotplate at 450°C for 30 min. This process was repeated twice. Once cooled to 70°C the substrates were immersed into a solution of P1 sensitiser (0.2 mM) in acetonitrile. The substrates were left in the solution overnight and then the sensitised electrodes were rinsed with acetonitrile.

7.6.4 Fabrication of the Spiro-OMeTAD/Ag/PEI/PCBM:PEI CRL

The preparation and deposition of the Spiro-OMeTAD solution was carried out in a nitrogen-filled glovebox. The HTM solution was homogeneously spread by means of a pipette onto the sensitised photoanode and left to penetrate into the mesoporous network for 30 s, followed by a two-step spin coating for 40 s at 700 rpm then 2 s at 2000 rpm. The formulation of the HTM solution was 0.126 vol% of Spiro-OMeTAD in anhydrous chlorobenzene, with the addition of 76 mM tBP and 25 mM LiTFSI (LiTFSI was pre-dissolved in anhydrous acetonitrile at 170 mg ml^{-1}). The solution was filtered through a 0.45 µm polytetrafluoroethylene (PTFE) syringe filter and 75 µl was dispensed onto the substrate. The films were left overnight in a desiccator.

The preparation and deposition of the PCBM:PEI and PEI solutions were carried out in a nitrogen-filled glovebox. The ETM solution was homogeneously spread by means of a pipette onto the sensitised photocathode and left to penetrate into the mesoporous network for 30 s, followed by a two-step spin coating for 3 s at 1000 rpm and then 30 s at 3000 rpm. The formulation of the ETM solution was 40 mg ml^{-1} PCBM in anhydrous chlorobenzene with varying concentrations of PEI (15:0.5, 15:1 and 15:2 ratios of PCBM:PEI by weight). The solution was filtered through a 0.45 µm polytetrafluoroethylene (PTFE) syringe filter and 90 µl was dispensed onto the substrate. The substrates were placed on a hotplate at 100°C for 5 min. Following this, a PEI layer was deposited on top of the PCBM:PEI film by spin coating a solution of 0.1 wt% in anhydrous isopropanol at 5000 rpm for 1 min, then substrates were heated on a hotplate at 100°C for 1 min. The substrates were placed in a BOC-Edwards Auto thermal evaporator where 5 nm of silver was deposited through a mask under high vacuum (10^{-6} Torr) at a rate of 1 $Å s^{-1}$.

7.6.5 Characterisation of the tandem ssDSCs

J-V measurements were performed using a 2401 Keithley SourceMeter with a HelioSim-CL60 solar simulator (Voss electronic GmbH) measured under AM1.5 simulated sun light of 100 mW cm^{-2} at a scan rate of 0.5 V s^{-1}.

7.6.6 Characterisation of the Spiro-OMeTAD/Ag/PEI/PCBM:PEI CRL

The ohmic contact of the CRL was verified by constructing a device of FTO/Spiro-OMeTAD/Ag/PEI/PCBM:PEI/FTO. The deposition of these layers was as described in Section 7.5.4, with one substrate consisting of FTO/Spiro-OMeTAD/Ag and another substrate consisting of FTO/PCBM:PEI/PEI. A small spot of silver paint was deposited on the FTO contacts to improve the contact with the crocodile clips during characterisation. I-V measurements were performed while the substrates were clamped together using a 2401 Keithley SourceMeter at a scan rate of 0.5 V s^{-1}.

7.6.7 Characterisation of the Spiro-OMeTAD/PEDOT:PSS/PEI/PCBM:PEI CRL

The ohmic contact of the CRL was verified by constructing a device of FTO/Spiro-OMeTAD/PEDOT:PSS/PEI/PCBM:PEI/FTO. The deposition of all layers except PEDOT:PSS was as described in Section 7.5.4, with one substrate consisting of FTO/Spiro-OMeTAD and another substrate consisting of FTO/PCBM:PEI/PEI. The transparent conductive adhesive (TCA) containing PEDOT:PSS was fabricated as reported by Bryant et al. such that the final volume fraction of PEDOT:PSS in the dry TCA film was 0.0175.[8] The TCA mixture was doctor bladed onto the FTO/PCBM:PEI/PEI substrate and dried for 15 min at 60°C followed by 5 min at 120°C. A hot press heated to 100°C was used to activate the pressure sensitive adhesive using pressure 0.15 MPa, and a UV epoxy was used to hold the glass substrates together. A small spot of silver paint was deposited on the FTO contacts to improve the contact with the crocodile clips during characterisation. I-V measurements were performed using a 2401 Keithley SourceMeter at a scan rate of 0.5 V s^{-1}.

References

1 W. Shockley and H. J. Queisser, Detailed Balance Limit of Efficiency of p-n Junction Solar Cells, *J Appl Phys*, 1961, **32**, 510–519.

2 M. Zhang and Z. Lin, Efficient interconnecting layers in monolithic all-perovskite tandem solar cells, *Energy Environ Sci*, 2022, **15**, 3152–3170.

3 F. Jiang, T. Liu, B. Luo, J. Tong, F. Qin, S. Xiong, Z. Li and Y. Zhou, A two-terminal perovskite/perovskite tandem solar cell, *J Mater Chem A Mater*, 2016, **4**, 1208–1213.

4 I. Bruder, M. Karlsson, F. Eickemeyer, J. Hwang, P. Erk, A. Hagfeldt, J. Weis and N. Pschirer, Efficient organic tandem cell combining a solid state dye-sensitized and a vacuum deposited bulk heterojunction solar cell, *Solar Energy Materials and Solar Cells*, 2009, **93**, 1896–1899.

5 P. Docampo, A. Hey, S. Guldin, R. Gunning, U. Steiner and H. J. Snaith, Pore Filling of Spiro-OMeTAD in Solid-State Dye-Sensitized Solar Cells Determined Via Optical Reflectometry, *Adv Funct Mater*, 2012, **22**, 5010–5019.

6 K. X. Steirer, G. A. MacDonald, S. Olthof, J. Gantz, E. L. Ratcliff, A. Kahn and N. R. Armstrong, Energy Level Alignment and Morphology of Ag and Au Nanoparticle Recombination Contacts in Tandem Planar Heterojunction Solar Cells, *The Journal of Physical Chemistry C*, 2013, **117**, 22331–22340.

7 M. Gholipoor, N. Solhtalab and M. H. Mohammadi, High-performance parallel tandem MoTe2/perovskite solar cell based on reduced graphene oxide as hole transport layer, *Sci Rep*, 2022, **12**, 20455.

8 D. Bryant, P. Greenwood, J. Troughton, M. Wijdekop, M. Carnie, M. Davies, K. Wojciechowski, H. J. Snaith, T. Watson and D. Worsley, A Transparent Conductive Adhesive Laminate Electrode for High-Efficiency Organic-Inorganic Lead Halide Perovskite Solar Cells, *Advanced Materials*, 2014, **26**, 7499–7504.

9 Y. Farré, M. Raissi, A. Fihey, Y. Pellegrin, E. Blart, D. Jacquemin and F. Odobel, A Blue Diketopyrrolopyrrole Sensitizer with High Efficiency in Nickel-Oxide-based Dye-Sensitized Solar Cells, *ChemSusChem*, 2017, **10**, 2618–2625.

Chapter 8.

Conclusion

This thesis aimed to establish the proof of concept for the tandem solid-state DSC, highlighting its potential for improved open-circuit voltages while overcoming the stability issues that surround liquid tandem DSCs. To accomplish this, the two subcells (n-type ssDSC and p-type ssDSC) that constitute the tandem device were designed and fabricated, followed by a study on a charge recombination layer (CRL) that electrically connected the two subcells. In Chapter 7, a tandem ssDSC with V_{OC} of 0.88 V and J_{SC} of 0.005 mA cm^{-2} was achieved. The poor performance of the tandem device was attributed to the ineffective operation of the p-type ssDSC and the and low current measured through the CRL. The subsequent discussion addresses these existing issues and outlines future strategies to overcome them.

The PCE of n-type ssDSCs is generally much lower than traditional DSCs as they utilise TiO_2 films that are around 2 µm, which are much thinner in comparison to liquid DSC. These thin films impact the performance of the device due to recombination between the photoinjected electrons and the holes in the HTM, as well as hinder light absorption. In Chapter 5, experiments aimed at enhancing increasing the light absorption in n-type ssDSCs were conducted through a co-sensitisation approach. This fabrication method has been seen to extend the absorption spectrum for enhanced light harvesting,[1] as well as form a denser monolayer of dyes to prevent charge recombination.[2] The co-sensitisation approach showed that employing LEG4 dye with a smaller co-adsorbent L0, which exhibits an absorption band in the shorter wavelength region compared with LEG4, resulted in a notable 7% increase in PCE. However, further improvements require optimisation of the dye loading by changing the method of co-sensitisation from the cocktail approach (two dyes loading at the same time) to the sequential approach (one day sensitised at a time). This would allow a higher level of

control over the dye loading which could reduce unwanted dye competition. Additionally, other dyes should be tested to extend the absorption region into higher wavelengths.

Another method tested to improve the performance of n-type ssDSCs was the utilisation of an amide-based HTM with enhanced conductivity due to close molecular packing.[3] Employing the amide-based HTM, TPABT, required modification of the heterojunction between the TiO_2 and the TPABT, therefore a series of experiments was undertaken, varying the concentration of additives LiTFSI and tBP to the TPABT in order to adjust the Fermi level alignment between the TiO_2 and the HTM. Interestingly, it was found that a longer oxidation time, as well as light soaking treatment were necessary for devices employing TPABT as the HTM, whereas this was not the case for those employing Spiro-OMeTAD. It was hypothesised that the light soaking treatment induced Li^+ ion migration in TPABT devices, resulting in a more favourable Fermi level alignment and minimisation of the presence of deep trap states. This raises the question of whether this behaviour is exhibited in other HTMs that might be disregarded after insufficient oxidation time or light soaking. Therefore, future work should involve developing a better understanding of such phenomena.

In Chapter 6, an investigation was conducted to address recombination issues at the ETM/electrode interface in p-type ssDSCs. It was found that the spin coated blocking layer that was deposited onto the FTO to prevent recombination at the ETM/FTO interface was not compact. This was evident through SEM and EDX analysis which displayed the presence of cracks in the film, revealing the underlying FTO. Additionally, the spray coated blocking layer displayed non-uniform coverage, which would require extensive optimisation of the spray coating parameters which posed a health and safety risk due to the toxicity of NiO in aerosol form. Furthermore, the recombination at the ETM/NiO interface could not be ruled out, therefore an alternative approach was undertaken in which three surface treatments were tested to passivate the Ni^{3+} surface states that are accountable for charge recombination.[4] However, TAS measurements indicated that the lifetimes associated with the reduced state of the dye showed little to no variation between surface treatments, which implied that recombination rates remained unaffected. However, differences in the lifetimes associated with the excited state of the dye suggested that rather than mitigating recombination, the insulating layers may have generated non-injecting dyes anchored onto the passivated NiO surface. The kinetic data showed recombination in the sub-picosecond timescale. This is in agreement with results from D'Amario et al., who attribute this fast recombination to hole

shallow-trapping in a "Ni^{4+}".[5] To avoid this, electron recombination with the trapped hole in the "Ni^{4+}" state must be retarded to allow relaxation to the hole in the Ni^{3+} state, where recombination is slower. Thus, before employment of p-type ssDSCs into tandem ssDSCs, future work should involve testing a new dye that can exhibit long-lived charge separated excited states. Additionally, pore filling of the ETM into the mesoporous NiO network should be improved, as well as testing a sputtered NiO blocking layer, as this seems to be the effective method to fabricate a compact NiO blocking layer in the literature.[6–8]

In Chapter 7, a charge recombination layer (CRL) was studied to electrically connect the two subcells by creating an energy level cascade that supported the electron transport from the p-type subcell and the hole transport from the n-type subcell into the charge recombination site. There, they recombine to enhance the flow of charge carriers between each subcell, and minimise recombination among the photogenerated charge carriers within each subcell. The CRL employed within the tandem ssDSC consisted of Spiro-OMeTAD/Ag/PEI/PCBM:PEI. A study of this CRL revealed the successful fabrication of an ohmic contact to minimise energy barriers for the charge carriers to flow across the CRL. However, the performance of the tandem ssDSCs was poor due to low current through the CRL and the additional work that is required on the p-type ssDSC. A further study was undertaken to test the adhesion of the CRL to mechanically connect the two subcells for real-world applications, removing the necessity to apply clamping or pressure on the subcells for their operation. A transparent conductive adhesive (TCA) containing PEDOT:PSS dispersed in an acrylic adhesive was employed in place of Ag, which was found to mechanically and electrically connected the CRL, and UV epoxy was used to hold the glass substrates in place. Results obtained for this CRL show that a PCBM:PEI ratio of 15:0.5 was able to form an ohmic contact. Therefore, future work will involve testing the TCA in a fully working tandem device.

Overall, this study has revealed valuable insights into the operation and potential challenges of tandem ssDSCs. The crucial importance of obtaining high electrical conductivity in the CRL has been highlighted. Furthermore, the inability of the p-type ssDSC to perform as expected also had a direct impact on the overall performance of the tandem device as the photocurrent equals that of the subcell with the lowest produced current. This outcome underscores the significance of the p-type ssDSC performance in influencing the efficiency of the tandem device, and future research should place critical importance on studying the p-type electrode.

References

1 K. Kakiage, Y. Aoyama, T. Yano, K. Oya, J. Fujisawa and M. Hanaya, Highly-efficient dye-sensitized solar cells with collaborative sensitization by silyl-anchor and carboxy-anchor dyes, *Chemical Communications*, 2015, **51**, 15894–15897.

2 Y. S. Kwon, I. Y. Song, J. Lim, S.-H. Park, A. Siva, Y.-C. Park, H. M. Jang and T. Park, Reduced charge recombination by the formation of an interlayer using a novel dendron coadsorbent in solid-state dye-sensitized solar cells, *RSC Adv*, 2012, **2**, 3467.

3 E. A. A. Alkhudhayr, D. Sirbu, M. Fsadni, B. Vella, B. T. Muhammad, P. G. Waddell, M. R. Probert, T. J. Penfold, T. Hallam, E. A. Gibson and P. Docampo, Improving the Conductivity of Amide-Based Small Molecules through Enhanced Molecular Packing and Their Application as Hole Transport Mediators in Perovskite Solar Cells, *ACS Appl Energy Mater*, 2023, **6**, 11573–11582.

4 L. D'Amario, R. Jiang, U. B. Cappel, E. A. Gibson, G. Boschloo, H. Rensmo, L. Sun, L. Hammarström and H. Tian, Chemical and Physical Reduction of High Valence Ni States in Mesoporous NiO Film for Solar Cell Application, *ACS Appl Mater Interfaces*, 2017, **9**, 33470–33477.

5 L. D'Amario, J. Föhlinger, G. Boschloo and L. Hammarström, Unveiling hole trapping and surface dynamics of NiO nanoparticles, *Chem Sci*, 2018, **9**, 223–230.

6 B. Xu, S. Wrede, A. Curtze, L. Tian, P. B. Pati, L. Kloo, Y. Wu and H. Tian, An Indacenodithieno[3,2-b]thiophene-Based Organic Dye for Solid-State p-Type Dye-Sensitized Solar Cells, *ChemSusChem*, 2019, **12**, 3243–3248.

7 L. Tian, T. Törndahl, J. Lin, P. B. Pati, Z. Zhang, T. Kubart, Y. Hao, J. Sun, G. Boschloo and H. Tian, Mechanistic Insights into Solid-State p-Type Dye-Sensitized Solar Cells, *The Journal of Physical Chemistry C*, 2019, **123**, 26151–26160.

8 H. Cheng, Y. Liu, B. Cai, C. Hägglund, T. Kubart, G. Boschloo and H. Tian, Atomic Layer Deposition of SnO2 as an Electron Transport Material for Solid-State P-type Dye-Sensitized Solar Cells, *ACS Appl Energy Mater*, 2022, **5**, 12022–12028.

Posters and Oral Contributions

Solid-State Dye-Sensitised Solar Cells: The Push Towards Automating Fabrication Techniques (poster – see Appendix)

Amy Neild, Susanna Stephens, Pablo Docampo and Elizabeth Gibson

International Conference on Hybrid and Organic Photovoltaics, Valencia, 2022

Developing Tandem Solid-State Dye-Sensitised Solar Cells (oral contribution)

Amy Neild

Asia-Pacific International Conference on Perovskite, Organic Photovoltaics and Optoelectronics, Kobe, 2023

Unlocking the potential of alternative hole transporting materials for solid-state dye-sensitised solar cells through prolonged oxidation and light soaking treatment (poster – see Appendix)

Amy Neild, Miriam Fsadni, Pablo Docampo and Elizabeth Gibson

Next Generation Materials for Solar Photovoltaics, London, 2024

Unlocking the potential of alternative hole transporting materials for solid-state dye-sensitised solar cells through prolonged oxidation and light soaking treatment (oral contribution)

Amy Neild, Benjamin Vella, Miriam Fsadni, Pablo Docampo and Elizabeth Gibson

Photovoltaic Science, Applications and Technology Conference, Glasgow, 2024

Appendix. Posters

Solid-State Dye-Sensitised Solar Cells: The Push Towards Automating Fabrication Techniques

Amy Neild[1], Susanna Stephens[1], Pablo Docampo[2], Elizabeth Gibson[1]

1- Energy Materials Laboratory, Newcastle University, Newcastle upon Tyne, NE1 7RU, England
2- School of Chemistry, University of Glasgow, University Pl, G12 8QQ, Glasgow, UK

a.neild1@newcastle.ac.uk

Mixed Metal Oxide Reactor

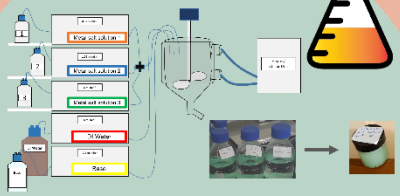

The synthesis of metal oxides at specific stoichiometries is automated using pumps that deliver the reagents to a reaction vessel at specified flow rates. The pH and temperature are kept constant throughout the reaction through the presence of a base pump and a jacketed reaction vessel connected to a heater/chiller unit.

Motivation: Fabricating solar cells manually requires considerable time and effort, but more importantly it demands precision and consistency. Reproducibility is dependent upon the experience and skill of the lab worker, but there is no guarantee that results will be error-free. By automating fabrication techniques involved in making the devices we can significantly improve reproducibility and uniformity, as well as reduce hands-on lab time to allow more time for innovation.

Laser Etching

A laser beam removes the conductive material coated on the glass substrate as well as the blocking layer previously deposited. High heat causes the surface of the material to melt in areas pre-defined in the etching pattern. Any design can be uploaded onto the computer and can consist of channels as thin as 200 µm, allowing more intricate etching patterns to be used in the devices.

Spray Pyrolysis

An ultrasonic spray head atomizes the blocking layer precursor solution and is deposited at a specified height above a substrate on a heated surface to form a thin film. The movement of the spray head and hotplate is controlled using XYZ linear actuators.

The process is controlled via a LabVIEW program and parameters can easily be altered such as:

- Spray head height
- Spray head speed
- Spray amplitude
- Syringe pump flow rate
- Delay between cycles
- Spray pulse

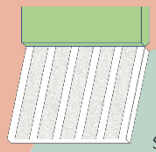

Slot-Die Coating

Solution is delivered onto a substrate at a constant rate through a narrow slot. Striped patterns can be deposited through the design of a shim in the slot die head. The substrate is positioned on a hotplate that can reach a temperature of 120°C.

One of the main advantages of slot-die coating over traditional techniques like spin coating is that it can easily be integrated into scale-up processes.

Outcome:

- **Greater precision**
- **Reduces manual errors**
- **Larger number of devices**
- **Improves uniformity of film**
- **Makes optimisation less laborious**
- **Vital for the upscale of device fabrication**

Unlocking the potential of alternative hole transporting materials for solid-state dye-sensitised solar cells through prolonged oxidation and light soaking treatment

Amy Neild[1], Miriam Fsadni[1], Pablo Docampo[2], Elizabeth Gibson[1]

1 – Energy Materials Laboratory, Newcastle University, Newcastle upon Tyne, NE1 7RU, England
2 – School of Chemistry, University of Glasgow, University Pl, G12 8QQ, Glasgow, UK

a.neild1@newcastle.ac.uk

Introduction

Aromatic amides serve as promising hole transporting materials (HTMs) due to their facile synthesis via condensation chemistry. TPABT is an example of an amide-based small molecule that exhibits high conductivity values (~10^{-5} S cm^{-1} upon the addition of standard ionic additives) at an estimated cost of only $5/g, reaching power conversion efficiencies of ~15% when employed as a HTM in perovskite solar cells.[1]

In this work, TPABT was utilised as a HTM in solid-state dye-sensitised solar cells (ssDSCs) and 2 day old devices generated a poor power conversion efficiency (PCE) of 0.19%. Consequently, the aim of this work was to investigate whether the initial underperformance accurately reflects the capabilities of TPABT as a HTM in ssDSCs, or whether testing alternative HTMs should follow a different approach compared to testing state-of-the-art Spiro-OMeTAD for a more accurate evaluation.

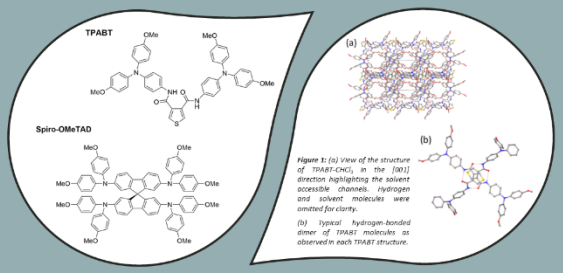

Figure 1: (a) View of the structure of TPABT-$CHCl_3$ in the [001] direction highlighting the solvent accessible channels. Hydrogen and solvent molecules were omitted for clarity. (b) Typical hydrogen-bonded dimer of TPABT molecules as observed in each TPABT structure.

Prolonged oxidation

Upon remeasuring the J-V characteristics of the same solar cells after 3 months of being stored in a desiccator, the PCE of the TPABT device increased from 0.19% to 0.70%, whereas the PCE of the Spiro-OMeTAD device decreased from 4.00% to 2.42%. This indicates that the oxidation time for Spiro-OMeTAD-based ssDSCs and TPABT-based ssDSCs differs, which is ascribed to the closer packing of TPABT molecules requiring more time for oxygen to penetrate through the HTM.

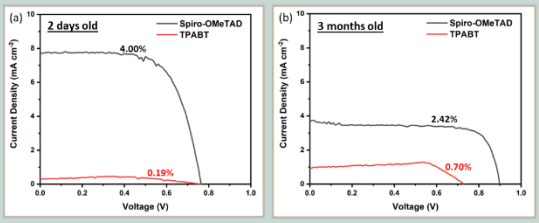

Figure 2: J-V curves of FTO/TiO_2/LEG4/HTM/Ag ssDSC with TPABT (75 mM LiTFSI and 76 mM tBP additives to 50 mg ml^{-1} TPABT) and Spiro-OMeTAD (25 mM LiTFSI and 76 mM tBP additives to 100 mg ml^{-1} Spiro-OMeTAD) measured after (a) 2 days and (b) 3 months. Devices were measured under AM1.5 simulated sun light of 100 mW cm^{-2} irradiance at 0.1 V s^{-1}.

This is also evident in photoinduced absorption (PIA) measurements. The PIA spectra for devices measured 3 days after device fabrication show a bleach with a minimum between 600-620 nm (assigned to the ground state dye – D) and a positive absorption feature with a maxima centred around 750 nm (assigned to the oxidised dye state – D^+). For devices measured 23 days after fabrication, a quenching of the oxidised dye state is observed for all but 1 concentration of additives. This indicates dye regeneration occurs for devices with prolonged duration of oxidation, affirming the observation that TPABT oxidation time is much longer than Spiro-OMeTAD, which is shown to quench the oxidised dye state after only 3 days.

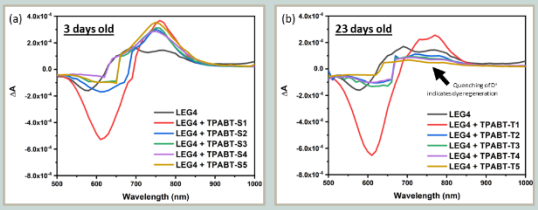

Figure 3: PIA spectra of two series of TPABT devices measured (a) 3 days after device fabrication and (b) 23 days after device fabrication demonstrating how oxidation time affects dye regeneration. Sample series S (tBP:Li-TFSI = 1:0.33) and sample series T (tBP:Li-TFSI = 1:0.22) contain increasing concentration of additives with increasing number in the series.

Light soaking treatment

The 3 month old devices were further studied through exposure to a light soaking treatment. Repetitive scan cycles were carried out while subject to simulated AM1.5 illumination. Interestingly, after repeated scan cycles the observed hysteresis reduces until almost negligible for all devices. In conjunction with this, the J_{SC} and PCE both increase up until a certain scan number (differing for each LiTFSI concentration). This behaviour was not observed for Spiro-OMeTAD based devices.

The proposed hypothesis is that the improvement in performance was due to the presence of a local electric field that arises after photoexcitation and charge separation, causing the Li^+ ions to adsorb onto the TiO_2 surface.[2] Here, the Li^+ ions screened conduction band electrons after injection, inhibiting charge recombination and reducing J-V hysteresis due to a preferential Fermi level alignment of the TiO_2 minimising the presence of deep trap states.[3]

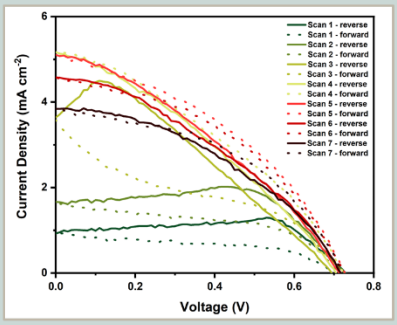

Figure 4: Successive J-V curves for 3 month aged FTO/TiO_2/LEG4/TPABT/Ag ssDSC with 75 mM LiTFSI and 76 mM tBP additives to 50 mg ml^{-1} TPABT, showing a significant reduction in hysteresis and improvement of device performance with successive scans. Devices were measured under AM1.5 simulated sun light of 100 mW cm^{-2} irradiance at 0.1 V s^{-1}.

Conclusion

Overall, these results highlighted that the alternative HTM TPABT required a different length of time to oxidise than state-of-the-art Spiro-OMeTAD, which was important for dye regeneration. However, the optimal oxidation time is yet to be calculated. Additionally, a light soaking treatment was essential for TPABT-based ssDSCs to minimise J-V hysteresis and improve PCE from 0.33% to 1.48%, whereas this was not necessary for Spiro-OMeTAD-based ssDSCs. Therefore, this investigation has underscored that the way in which we assess the performance of alternative HTMs should not be kept consistent to reference HTMs, and instead should follow an individual approach for a more accurate analysis.

*1 – E. A. A. Alkhudhayr, et al., Improving the Conductivity of Amide-Based Small Molecules through Enhanced Molecular Packing and Their Application as Hole Transport Mediators in Perovskite Solar Cells, ACS Appl Energy Mater, 2023, **6**, 11573–11582.*
*2 – L. Yang et al., Initial Light Soaking Treatment Enables Hole Transport Material to Outperform Spiro-OMeTAD in Solid-State Dye-Sensitized Solar Cells, J Am Chem Soc, 2013, **135**, 7378–7385.*
*3 – M. F. Aygüler, et al., Influence of Fermi Level Alignment with Tin Oxide on the Hysteresis of Perovskite Solar Cells, ACS Appl Mater Interfaces, 2018, **10**, 11414–11419.*